GEOCHEMICAL CHARACTERISTICS OF ALUMINUM AND MAGNESIUM SECONDARY MINERAL PHASES IN URANIUM MILL TAILINGS

A Thesis Submitted to the College of

Graduate and Postdoctoral Studies

In Partial Fulfillment of the Requirements

For the Degree of Doctor of Philosophy

In the Department of Geological Sciences

University of Saskatchewan

Saskatoon

By

JARED M. ROBERTSON

PERMISSION TO USE

In presenting this thesis/dissertation in partial fulfillment of the requirements for a Postgraduate degree from the University of Saskatchewan, I agree that the Libraries of this University may make it freely available for inspection. I further agree that permission for copying of this thesis/dissertation in any manner, in whole or in part, for scholarly purposes may be granted by the professor or professors who supervised my thesis/dissertation work or, in their absence, by the Head of the Department or the Dean of the College in which my thesis work was done. It is understood that any copying or publication or use of this thesis/dissertation or parts thereof for financial gain shall not be allowed without my written permission. It is also understood that due recognition shall be given to me and to the University of Saskatchewan in any scholarly use which may be made of any material in my thesis/dissertation.

Requests for permission to copy or to make other uses of materials in this thesis/dissertation in whole or part should be addressed to:

Head of the Department of Geological Sciences
University of Saskatchewan
114 Science Place
Saskatoon, Saskatchewan
S7N 5E2

ABSTRACT

The Athabasca Basin in northern Saskatchewan, Canada is a major source of uranium (U) and an important economic driver for the province and country. The Athabasca Basin U deposits contain elevated concentrations of As, Se, Mo, Ni, and ^{226}Ra (elements of concern; EOCs). The Key Lake U mill uses a stepwise $Ca(OH)_2$ neutralization process (pH 4.0, 6.5, 9.5, and 10.5) to precipitate EOCs from raffinate (acidic, metal-rich wastewater) prior to releasing the effluent to the environment. The neutralization process precipitates a complex mixture of secondary minerals concentrated with EOCs that are deposited to an in-pit tailings management facility (TMF) at pH ≈ 10.1. Extensive studies show adsorption to ferrihydrite is a primary control on aqueous EOC concentrations. Recent studies suggest poorly characterized Al and Mg precipitates could also influence EOC concentrations. The objectives of this thesis were to characterize the Al and Mg secondary mineralogy in the Key Lake neutralization process and quantify controls exerted by these minerals on EOC concentrations. Additionally, a review of all geochemical literature pertaining to in-pit TMFs in the Athabasca Basin was conducted to synthesize the collective science. Laboratory and mill samples were used for the study. The Al and Mg secondary minerals identified were amorphous $AlOHSO_4$ (a hydrobasaluminite-like phase, existing below neutral pH), amorphous $Al(OH)_3$, MgAl-hydrotalcite, and Al-substituted ferrihydrite. In the absence of ferrihydrite, Al and Mg mineral phases sequestered As, Se, Mo, and Ni. Batch adsorption experiments showed MgAl-hydrotalcite adsorbs As, Se, and Mo to the same order of magnitude as ferrihydrite. Arsenic and Ni XAS experiments showed Al and Mg minerals sequester As and Ni in concert with ferrihydrite. Arsenic(V) formed bidentate-binuclear complexes on the surface of ferrihydrite and amorphous $Al(OH)_3$. Hydrotalcite adsorbed As(V) on the mineral surface and/or within the mineral interlayer through bidentate complexation. Nickel was adsorbed to amorphous $Al(OH)_3$ through edge-sharing bidentate-mononuclear complexes and precipitated as a Ni-Al layered double hydroxide at pH 10.5. These results demonstrate that mineralogically complex tailings rich in Fe, Al, and Mg exert multiple mechanisms of controls on EOC solubility and further the understanding of the long-term fate of EOCs in tailings.

ACKNOWLEDGMENTS

I am extremely grateful to my supervisor and mentor Dr. Jim Hendry for extending me this opportunity and continually pushing me to the next level. I am forever indebted for what you have contributed to my growth as a researcher and to my career.

I would like to acknowledge Dr. Joseph Essilfie-Dughan for mentoring me and teaching me most of what I know about geochemistry. In particular, performing experiments with you at the CLS have been a highlight of this experience. I am extremely grateful for your contributions.

I would also like to thank my graduate committee, Dr. Matt Lindsay, Dr. Jeff Warner, Dr. Tom Kotzer, and Dr. Derek Peak, as well as those who chaired my committee meetings, Dr. Jim Merriam and Dr. Samuel Butler. Thank you also to my external examiner, Dr. John Mahoney, for your helpful suggestions and questions regarding my thesis.

I owe Krysta Shacklock and Ryan Frey a great deal of thanks for constructing the synthetic raffinate neutralization system and working out its bugs before I began. This whole process would have taken much longer without your contributions.

I would like to thank Jocelyn Bissonnette for many great conversations on our work and being a wonderful person to travel through this process with.

I am especially grateful to Fina Nelson for getting this whole process started - for taking me on as a summer student and for extending the initial offer to continue my education with the group.

To my amazing fiancée, Maeghan - you have supported me through this entire thesis and have always encouraged me to reach my full potential.

Finally, to my incredible mother, Kathy - this whole educational journey would not have been possible without you. Thank you the countless ways you have supported me through the years.

TABLE OF CONTENTS

LIST OF FIGURES

LIST OF TABLES

LIST OF SYMBOLS AND ABBREVIATIONS

σ^2	Debye-Waller factor ($Å^2$)
χ_v^2	Reduced chi-square
CN	Coordination number
DTMF	Deilmann tailings management facility
E_0	Energy shift (eV)
EMPA	Electron microprobe analysis
EOC	Element of concern
EXAFS	Extended X-ray absorption fine structure
FA	Ferric arsenate
FH	Ferrihydrite
ICP-MS	Inductively coupled plasma mass spectrometry
ICP-OES	Inductively coupled plasma optical emission spectrometry
k	Photoelectron wave vector ($Å^{-1}$)
K_{sp}	Solubility product constant
KLBN	Key Lake bulk neutralization process
LCF	Linear combination fitting
LDH	Layered double hydroxide
HTLC	Hydrotalcite-like compound
MS	Multiple scattering
PCA	Principal component analysis
RLITMF	Rabbit Lake in-pit tailings management facility
R	Interatomic distance (Å)

RSD	Relative standard deviation
S_0^2	Amplitude reduction factor
SRNS	Synthetic raffinate neutralization system
TEM	Transmission electron microscopy
TMF	Tailings management facility
XANES	X-ray absorption near edge spectroscopy
XAS	X-ray absorption spectroscopy
XRD	X-ray diffraction

1.0 INTRODUCTION

The Key Lake uranium mill, located in northern Saskatchewan, Canada, is the largest uranium mill in the world, producing 8.85×10^6 kg U_3O_8 per year from an average mill head grade of 4.61% U_3O_8 in 2012 (Cameco, 2013). Since 1999, the mill has been processing ore from the McArthur River mine, located 80 km north of the mill (Bharadwaj and Moldovan, 2005). The uranium is extracted from the ore using a sulfuric acid leach followed by solvent extraction and refining. A bulk neutralization process (hereafter termed the Key Lake bulk neutralization process; KLBN) is used to treat the acidic uranium-barren waste streams (termed raffinate) prior to the release of the effluent to the environment. Precipitates formed during raffinate neutralization are mixed with leach residue (spent ore) and have been discharged as tailings to the in-pit Deilmann Tailings Management Facility (DTMF) since 1996 (Bharadwaj and Moldovan, 2005).

A primary goal of the KLBN is to sequester elements that can cause adverse health effects to living organisms into tailings solids to minimize their mobility in the receiving environment. In the case of the Key Lake mill tailings, elements of concern (EOCs) include As, Mo, Ni, and Se which are dissolved from the ore during the oxidative leaching process (Shaw et al., 2011). Due to the potential environmental impacts of EOCs, research efforts have focused on defining the mineralogical controls on EOCs in the tailings body. It is well known that Fe in the form of ferrihydrite effectively adsorbs EOCs in the DTMF, thereby preventing mobilization into the surrounding groundwater (Das et al., 2011a; Essilfie-Dughan et al., 2013; Shaw et al., 2011). However, very little research has been directed towards studying the Al and Mg mineral phases in the DTMF system. Evidence has recently been found that Al-Mg mineral phases in the DTMF may play a role in controlling the mobility of EOCs (Gomez et al., 2013a). It is of interest to characterize and understand any type of EOC control these phases may exert in addition to the current ferrihydrite-EOC control system. The hypotheses tested in this thesis are (1) discrete Al and Mg secondary mineral phases precipitate during neutralization of raffinate and (2) these phases exert mineralogical controls on EOCs. This study aims to characterize the Al and Mg secondary mineral phases present in the DTMF.

1.1 Objectives of Study

The objectives of this study were to (1) characterize the Al and Mg mineral phases that are generated from the Key Lake bulk neutralization process; (2) determine if Al and Mg mineral phases exert controls on EOCs (e.g., As, Ni, Se, Mo) in the neutralization process; (3) determine the magnitude of control exerted by the Al and Mg mineral phases on As and Ni concentrations with and without Fe mineral phases; and (4) compile a complete review of the literature on U in-pit tailings management facilities of the Athabasca Basin (Key Lake, Rabbit Lake, and McClean Lake).

The first three objectives were achieved in part with a continuous-flow model of the KLBN called the synthetic raffinate neutralization system (SRNS). Synthetic raffinates of various compositions were processed in the SRNS to investigate Al and Mg precipitation and the resulting controls of EOC concentrations. Aqueous and solid phase samples from the SRNS were analyzed with a suite of analytical techniques (ICP-MS, XRD, ATR-IR spectroscopy, Raman spectroscopy, XAS, and TEM) to determine the geochemical characteristics of the precipitates such as mineralogy, local coordination environment of the sequestered EOCs, and adsorption capacity of the Al and Mg secondary minerals. The final objective was achieved through a critical review of all literature pertaining to U in-pit tailings management facilities of the Athabasca Basin.

This thesis is a manuscript-style thesis consisting of four manuscripts (Chapters 3 to 6) that sequentially build off each other. The first manuscript (Chapter 3) is a validation study of the SRNS that compares the aqueous and solid phase geochemistry of the model to data from the KLBN and verifies that the SRNS is a valid model of the KLBN. The second manuscript (Chapter 4) presents data from the SRNS to characterize the bulk Al and Mg mineralogy that precipitates in the KLBN and identify Al and Mg mineralogical controls of As, Ni, Se, and Mo at various pH values. The third manuscript (Chapter 5) uses the mineralogical characterization from Chapter 4 as a basis to study the local coordination environment of As and Ni in SRNS and KLBN precipitates and quantify the contribution of Al and Mg mineralogical controls of As and Ni relative to Fe mineralogical controls. The final manuscript (Chapter 6) is a review of all literature of the U in-pit tailings management facilities in the Athabasca Basin, including the three previous manuscripts in this thesis. In addition to the four manuscript chapters, a general literature review (Chapter 2) and a summary of conclusions and recommendations (Chapter 7) are presented.

The status of the four manuscripts at the time of defense of this thesis were:

- **Chapter 3 - Modeling the Key Lake uranium mill's bulk neutralization process using a pilot-scale model.** Published by *Hydrometallurgy*, Vol. 149, 210-219, doi: 10.1016/j.hydromet.2014.08.010.
- **Chapter 4 - Precipitation of aluminum and magnesium secondary minerals from uranium mill raffinate (pH 1.0–10.5) and their controls on aqueous contaminants.** Published by *Applied Geochemistry*, Vol. 64, 34-42, doi: 10.1016/j.apgeochem.2015.09.002.
- **Chapter 5 - Coordination of arsenic and nickel to aluminum and magnesium phases in uranium mill raffinate precipitates.** Published by *Applied Geochemistry* 81, 12-22. doi:10.1016/j.apgeochem.2017.03.015.
- **Chapter 6 - Geochemistry of Uranium Mill Tailings in the Athabasca Basin, Saskatchewan, Canada - A Review.** In preparation for submission.

2.0 BACKGROUND AND LITERATURE REVIEW

2.1 Overview of the Key Lake Uranium Mill Process

The Key Lake uranium mill has processed ores from multiple mine sites during its operation. Currently, Key Lake processes ore from the McArthur River mine, while ore from the Gaertner and Deilmann open pit mines was processed prior to 1999. Ore in slurry form is blended with mineralized waste rock to dilute the feed to 4% U_3O_8 before being pumped to an acid leaching process. The leaching process uses 93% sulfuric acid under oxidizing conditions (Eh > 610 mV) and dissolves uranium from the ore along with other elements such as Fe, Al, Mg, As, Ni, Se, and Mo. A counter-current decantation circuit is used to wash the leach residue (refractory uranium-barren gangue minerals) which is pumped to a thickener and discharged to the DTMF. The uranium-rich leachate is pumped to a solvent extraction process where an organic solution of tertiary amines selectively extracts the dissolved uranium from the leachate. The uranium-barren solution, termed raffinate, contains the impurities dissolved during the leaching process and is pumped to the bulk neutralization circuit for treatment, while the uranium-rich organic solution is further purified before being precipitated as yellowcake which is calcined and then packaged. In the bulk neutralization process (Chapter 2.2), the acidic raffinate (~pH 1) is combined with other waste streams (containing relatively minor amounts of contaminants) and neutralized with slaked lime (hydrated CaO) to facilitate precipitation of dissolved metals and other impurities. The precipitates are thickened and combined with the leach residue before being discharged to the DTMF. The treated effluent is held in monitoring ponds until chemical analysis determines the effluent meets environmental regulatory specifications and is discharged to the environment (Bharadwaj and Moldovan, 2005).

2.2 Key Lake Bulk Neutralization Process

The KLBN treats several input streams, including the raffinate solution (which is the primary source of contaminants), using a stepwise neutralization to a terminal pH of 10.5 to

sequester EOCs in secondary mineral phases (Gomez et al., 2013a; Lieu et al., 2010). The chemical composition of the raffinate, and therefore the composition of the solid tailings, is dependent on the ore that is processed (Shaw et al., 2011). For example, Ni-Co-As-S minerals were abundant in the Deilmann ore, but are sparse in the McArthur River ore (Jamieson and Frost, 1997; von Pechmann, 1981). Dissolution and oxidation of these minerals during leaching influences the concentrations of metal(loid)s in the raffinate.

In the KLBN (Figure 2.1), the acidic raffinate (~pH 1) originating from the solvent extraction process is pumped to an air mixed tank called a Pachuca (P1) (Bharadwaj and Moldovan, 2005). The raffinate flows by gravity to the first neutralization step, P2, where slaked lime is added to increase the pH to 3.5-4.2. The solution is pumped to the Se-Mo thickener where flocculant is added to enhance solid agglomeration and settling properties. The aqueous overflow from the Se-Mo thickener is pumped to P3 where lime is added to increase the pH to ~6.5. From P3, the solution is pumped to P4 where more lime is added to increase the pH to ~9.5. The resulting slurry is pumped to the Lamella thickener. The overflow from the Lamella thickener flows to the Radium Removal Circuit where H_2SO_4 incrementally decreases the pH to 6.0 via three reactors (pH 7.5, 6.5, and 6.0). This solution flows by gravity to the Radium Removal thickener where flocculant is added. Barium chloride ($BaCl_2$) is added at P2, P4, and in the Radium Removal circuit to reduce ^{226}Ra activity in the final effluent via co-precipitation with barite (Liu and Hendry, 2011). The overflow from the Radium Removal thickener is the final effluent and is released to monitoring ponds prior to final release to the environment. The slurry underflows from each thickener (Se-Mo, Lamella, and Radium Removal), which contain the secondary mineral precipitates, are combined with the leach residue, raised to a terminal pH of 10.5 (via CaO), and pumped to the TMF (tailings management facility) thickener.

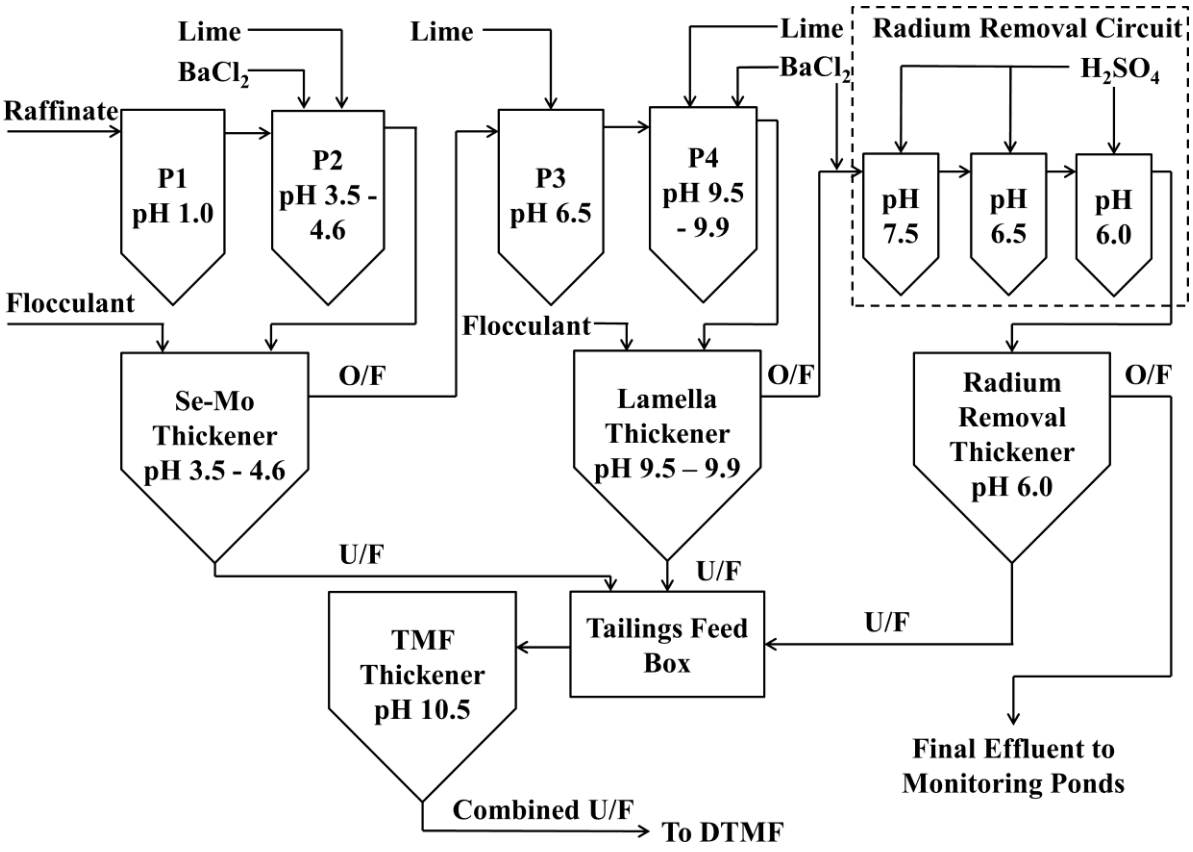

Figure 2.1. Block flow diagram of the Key Lake bulk neutralization process. Only major units of the process are displayed. Overflow and underflow of thickeners are indicated by O/F and U/F, respectively.

2.3 Controls of Elements of Concern

Detailed research on the potential migration of environmental contaminants from various tailings management facilities in the Athabasca Basin has been conducted in recent decades in an effort to understand the long term environmental impact of uranium tailings disposal. In particular, research is focused on the fate of elements such as As, Ni, Se, Mo, and ^{226}Ra (Donahue et al., 2000; Essilfie-Dughan et al., 2011a, 2011b; Langmuir et al., 1999; Liu and Hendry, 2011; Moldovan et al., 2008; Shaw et al., 2011).

Arsenic is the most studied EOC in the uranium tailings environment, partly due to its abundance (up to 10%) in Athabasca Basin ore (Langmuir et al., 1999). Arsenic is liberated from primary minerals, often in the form of sulfides, during the leaching process, as shown by the oxidation of gersdorffite (Eq. 2.1; Essilfie-Dughan et al., 2013):

$$2NiAsS + 3H_2O + \frac{13}{2}O_2 \rightarrow 2SO_4^{2-} + 2AsO_4^{3-} + 2Ni^{2+} + 6H^+ \quad (2.1)$$

Concentrations of As in raffinate solutions are reported to be as high as 526 mg/L (Moldovan and Hendry, 2005). Upon neutralization with slaked lime to pH 3.5-4.2, As concentrations decrease to < 1 mg/L in the neutralized raffinate solution (Gomez et al., 2013a; Moldovan and Hendry, 2005). This results from co-precipitation of AsO_4^{3-} with Fe^{3+} that produces an amorphous 2-line ferrihydrite phase with arsenate adsorbed via inner-sphere bidentate surface complexes (Essilfie-Dughan et al., 2013; Moldovan et al., 2003; Waychunas et al., 1993). Adsorption of arsenate to ferrihydrite is shown to be the dominant mechanism of As removal from aqueous systems, especially when the Fe/As molar ratio exceeds 4 (Donahue and Hendry, 2003). Within the tailings environment itself, As-adsorbed ferrihydrite is an abundant mineral phase in facilities such as the Rabbit Lake TMF and the DTMF (Essilfie-Dughan et al., 2013; Pichler et al., 2001). Under the oxic conditions maintained in these TMFs, ferrihydrite is a metastable phase that can crystalize to other iron oxides such as goethite or hematite and reduce the surface area available for surface complexes (Das et al., 2011b). Studies show, however, the presence of sorbates such as As greatly inhibits the crystallization of ferrihydrite (Das et al., 2011a). This is supported by the lack of goethite and hematite found in tailings samples (Moldovan et al., 2003), as well as Fe and As pore water concentrations that remain stable after 12 years (Shaw et al., 2011). In the McClean Lake TMF, poorly crystalline scorodite (or ferric arsenate) has been identified a control of aqueous As concentrations (Frey et al., 2010; Langmuir et al., 2006; Mahoney et al., 2007). Calcium arsenates have also been proposed as possible controls of As solubility due to high concentrations of Ca from slaked lime, however they are not expected to precipitate in major quantities when Fe minerals are abundant (Becze et al., 2010; Pichler et al., 2001).

The mineralogical controls of other EOCs such as Mo, Se, Ni, and ^{226}Ra are not studied as thoroughly as the controls of As. Within the alkaline (~pH 10) and oxic (~200 mV) tailings pits, Mo and Se are present as MoO_4^{2-} and SeO_3^{2-}, respectively (Donahue and Hendry, 2003; Essilfie-Dughan et al., 2011b; Shaw et al., 2011). Like As, Mo and Se are controlled by adsorption to 2-line ferrihydrite (Essilfie-Dughan et al., 2011b; Lieu et al., 2010). Molybdenum is also controlled by the precipitation of $NiMoO_4$ when the molar ratios of Ni/Mo is high and Fe/Mo is low (Essilfie-Dughan et al., 2011b). Nickel precipitates at higher pH values (> pH 6.5) as $NiMoO_4$ and $Ni(OH)_2$, but is also adsorbed by ferrihydrite (Essilfie-Dughan et al., 2012; Mahoney et al., 2007). Activities

of ^{226}Ra are controlled by the addition of $BaCl_2$ during the neutralization process which results in the precipitation of the sparingly soluble mineral barite ($BaSO_4$). Due to the similar ionic radii of hydrated Ba and ^{226}Ra ions, ^{226}Ra co-precipitates with barite as $(Ba,Ra)SO_4$ as a stable mineral phase (Liu and Hendry, 2011; Lottermoser, 2003).

2.4 Aluminum-Magnesium Mineral Phases

It is evident that ferrihydrite is a critical mineralogical control of EOCs in uranium tailings. However, the Al and Mg mineral phases of neutralized uranium tailings are poorly characterized in the literature, possibly due to the effectiveness of Fe mineral phases as an EOC control. Concentrations of Al and Mg often exceed those of Fe in the Key Lake raffinate (e.g., [Al] = 3510 mg/L, [Mg] = 3020 mg/L, and [Fe] = 2555 mg/L in a raffinate sample taken in 2009; Liu and Hendry, 2011), while concentrations of Al and Mg in the final neutralized raffinate are < 3 mg/L (Gomez et al., 2013a). This concentration reduction indicates that Al and Mg mineral phases should comprise a large fraction of the final tailings.

Due to the high concentrations of Al and Mg, hydrotalcite ($(Mg_6Al_2(OH)_{16})CO_3 \cdot 4H_2O$) is a potential mineral phase in neutralized uranium tailings. Hydrotalcite is a mineral of the layered double hydroxide (LDH) group. The general stoichiometry of an LDH is $[M^{2+}_{1-x}M^{3+}_{x}(OH)_2]^{x+}[A^{n-}]_{x/n} \cdot yH_2O$, where M is a divalent or trivalent cation and A is an anion of charge n. The structure of an LDH consists of layered metal hydroxides sheets with anionic interlayers (Figure 2.2). The metal hydroxide layer takes the form of brucite-like ($Mg(OH)_2$) units where trivalent cations (i.e., Al^{3+}) can substitute for divalent cations (i.e., Mg^{2+}) and cause a net positive charge. Anions and water molecules form layers between the metal hydroxide layers to counterbalance the net positive charge. Divalent cations can be Mg, Ni, Fe(II), Zn, Co, etc.; trivalent cations can be Al, Fe(III), V, etc.; anions can be CO_3^{2-}, SO_4^{2-}, Cl^-, NO_3^-, etc. (Evans and Slade, 2006). Layered double hydroxides have adsorptive properties and anion exchanging capabilities through exchange of their interlayer anions, making LDHs attractive for toxic element uptake (Das et al., 2002; Parker et al., 1995; Yang et al., 2005). Hydrotalcite-like compounds are shown to uptake many anions including AsO_4^{3-}, MoO_4^{2-}, and SeO_3^{2-} through multiple mechanisms such as surface complexation, structural coordination, and interlayer incorporation (Jobbágy and Regazzoni, 2013; Paikaray et al., 2013; Palmer et al., 2009). Hydrotalcite can precipitate in process water from the Ranger U mill via

titration with Na-aluminite (Douglas et al., 2010), and is identified as a major mineralogical component in the DTMF as a Mg/Fe(II)-Al-SO_4/CO_3 type LDH associated with As and Ni (Gomez et al., 2013a). More research is needed to determine the role of potential hydrotalcite-like mineral phases in U tailings and whether they can be considered long-term EOC controls.

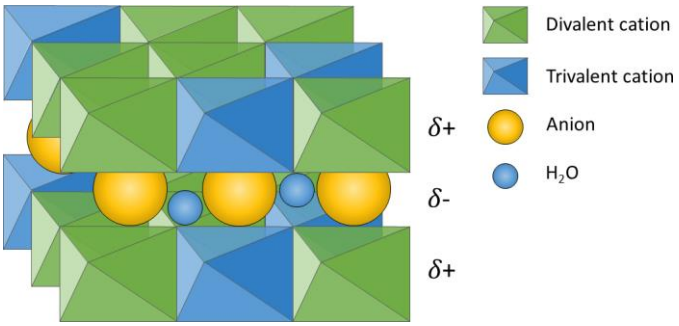

Figure 2.2. Generalized structure of a layered double hydroxide.

Rapid neutralization of Key Lake raffinate results in the precipitation of Al starting at pH 4, while geochemical models indicate amorphous $Al(OH)_3$ begins precipitation at pH 5 (Moldovan and Hendry, 2005). Early experimental results show Al precipitates as early as pH 3.8 in a concentrated Al solution (1635 mg/L), indicating that an amorphous Al phase could be present in the Se-Mo thickener (despite geochemical modeling results) where co-precipitation of ferrihydrite and arsenate occurs. Although amorphous $Al(OH)_3$ is shown to effectively adsorb arsenate from solution (Goldberg, 2002), geochemical modeling of Key Lake raffinate shows amorphous $Al(OH)_3$ to only adsorb minimal amounts of arsenate due to the presence of ferrihydrite (Moldovan and Hendry, 2005). Nonetheless, precipitation of amorphous $Al(OH)_3$ may be an alternative sorbent phase during raffinate neutralization.

2.5 Incorporation of Aluminum and Silicon into the Ferrihydrite Structure

Ferrihydrite is rarely found in a pure state in nature because impurities are easily incorporated into its structure due to its highly disordered structure. These impurities can affect the physical and chemical properties of ferrihydrite, such as the surface structure, particle size, solubility, and how it interacts with EOCs (Cismasu et al., 2011). Aluminum is observed to substitute for Fe^{3+} in the ferrihydrite structure during co-precipitation processes (Cismasu et al., 2012), while other ions such as silicate bind to the reactive ferrihydrite surface sites or form Fe(III) bearing amorphous SiO_2 (Cismasu et al., 2014). Sorption experiments with Zn(II) show that

aluminous ferrihydrite has similar sorption characteristics to pure ferrihydrite, while siliceous ferrihydrite results in increased outer sphere complexation of Zn(II) due to silicate ions blocking surface sites (Cismasu et al., 2013). Ultimately, aluminous ferrihydrite has increased stability (reduced solubility) relative to pure ferrihydrite (Jambor and Dutrizac, 1998). The characteristics of impure ferrihydrites are of interest due to their altered behaviour with respect to contaminant control. It is possible that Al is present as an impurity in ferrihydrite in the DTMF (and other TMFs) due to the elevated concentrations of both elements in the raffinate.

3.0 MODELING THE KEY LAKE URANIUM MILL'S BULK NEUTRALIZATION PROCESS USING A PILOT-SCALE MODEL

PREFACE

This chapter is reproduced with permission (license number 4106060704303) from Robertson, J., Shacklock, K., Frey, R., Gomez, M.A., Essilfie-Dughan, J., Hendry, M.J., 2014. Modeling the Key Lake uranium mill's bulk neutralization process using a pilot-scale model. *Hydrometallurgy* 149, 210–219. doi: 10.1016/j.hydromet.2014.08.010**.** Minor editorial and formatting changes are made for presentation purposes in this thesis.

The purpose of this chapter is to establish the methods used in subsequent chapters, namely through the validation of the SRNS as a geochemical model of the KLBN. The aqueous and solid phase geochemistry of SRNS products are compared to the geochemistry of the same products from the KLBN.Abstract

A pilot-scale model of the Key Lake bulk neutralization process (KLBN), termed the synthetic raffinate neutralization system (SRNS), was constructed to study the geochemical controls and the secondary mineralogy of uranium mine tailings deposited into the Deilmann tailings management facility in northern Saskatchewan, Canada. Comparison of the synthetic raffinate with samples collected from the KLBN indicate the pilot-scale model successfully simulated the full-scale process. Elemental analyses show the precipitation trends of major ions and trace elements in the SRNS are consistent with what occurs in the KLBN. X-ray diffraction patterns, attenuated total reflectance-infrared and Raman spectra show that the bulk mineralogy of SRNS precipitates is consistent with KLBN precipitates, namely 2-line ferrihydrite with adsorbed arsenate, amorphous $Al(OH)_3$, and a Mg-Al hydrotalcite-like layered double hydroxide. The mineral phases precipitated in both systems are supported by thermodynamic modeling. Minor mineralogical differences between the SRNS and KLBN were attributed to low aqueous Fe(II) and SO_4^{2-} concentrations in the synthetic raffinate.

3.1 Introduction

The Key Lake mill, located in northern Saskatchewan, Canada (57°13′N, 105°38′W), is the largest uranium mill in the world, producing 8.85×10^6 kg U_3O_8 per year from an average mill head grade of 4.61% U_3O_8 in 2012 (Cameco, 2013). Since 1999, the mill has been processing ore from the McArthur River mine, located 80 km to the north (Bharadwaj and Moldovan, 2005). The U is extracted from the ore using a sulfuric acid leach followed by solvent extraction and refining. The milling process can be divided into six steps: crushing/grinding, ore receiving and blending, leaching, counter current decantation, solution pre-treatment and solvent extraction, yellowcake (U_3O_8) precipitation, and calcining and packaging (Cameco, 2010). A bulk neutralization process (hereafter termed the Key Lake bulk neutralization process; KLBN) is used to treat the U-barren waste streams (termed raffinate) before their release into the environment. Precipitates formed during raffinate neutralization are mixed with leach residue and have been discharged as tailings to the in-pit Deilmann Tailings Management Facility (DTMF) since 1996 (Bharadwaj and Moldovan, 2005).

A goal of the KLBN is to sequester elements that can cause adverse health effects to biological systems into geochemically stable tailings solids, mitigating their release to the receiving environment. In the case of the Key Lake mill tailings, elements of concern (EOCs) include As, Mo, Ni, and Se dissolved from the ore during the leaching process (Shaw et al., 2011). Due to the potential environmental impacts of EOCs, research efforts have focused on defining the mineralogical controls in the tailings body. The mineralogical controls on tailings deposited in the DTMF, and in other U tailings management facilities in Saskatchewan, are dominated by gypsum ($CaSO_4 \cdot 2H_2O$), 2-line ferrihydrite (FH), Mg-Al hydrotalcite, Al oxides, and poorly crystalline scorodite, among other minor secondary mineral phases that adsorb and/or precipitate EOCs (De Klerk et al., 2012; Essilfie-Dughan et al., 2013; Gomez et al., 2013a; Mahoney et al., 2007; Moldovan et al., 2003; Moldovan and Hendry, 2005; Shaw et al., 2011). While several of these mineralogical controls are well understood, minor changes to the ore and milling process could affect EOC sequestration in the tailings. To improve our understanding of the current mineralogical controls on EOCs in the Key Lake U mill tailings and to characterize the effects of potential changes to the mill process and/or ore bodies on these mineralogical controls, a lab-scale bulk neutralization pilot plant (hereafter termed the synthetic raffinate neutralization system;

SRNS) was constructed to simulate the present-day KLBN and the tailings it generates for storage in the DTMF.

Prior to its use in experiments to define mineralogical controls or the impact of future changes to the mill feed or process, the SRNS must be demonstrated to accurately reproduce the aqueous and solid phases produced during operation of the KLBN. As such, the main objective of this study was to evaluate if the SRNS can replicate the secondary mineralogy and geochemical controls of the present-day KLBN. Synthetic raffinate was tailored to approximate the chemistry observed in the Key Lake raffinate, and the SRNS operated at pH values representative of target and actual concentrations measured in the KLBN. The resulting composition of elemental aqueous and solids was determined by inductively coupled plasma mass spectrometry (ICP-MS). Mineralogical characteristics of SRNS and KLBN solids were determined by X-ray diffraction (XRD), attenuated total reflectance infrared (ATR-IR) and Raman spectroscopy. Thermodynamic modeling was performed to support observations from the characterization techniques.

3.2 Materials and Methods

3.2.1 Key Lake Bulk Neutralization Process

The purpose of the KLBN is to treat contaminated solutions originating from several mill processes including raffinate (i.e., U-barren effluent) from the counter current decantation and solvent extraction processes, reverse osmosis reject water, porewater and seepage from the tailings management facilities, tailings thickener overflow water, waste water used in mill areas, and runoff from operational areas. The scope of this study limited these treatment streams to solely the raffinate because it is the main source of EOCs (Lieu et al., 2010). The raffinate is acidic (nominally pH 1) and oxic (~E_h +600 mV) and contains elevated concentrations of EOCs (Liu and Hendry, 2011). The majority of the EOCs are precipitated as secondary minerals in the KLBN via the addition of slaked lime ($Ca(OH)_2$). These solids are mixed with leach residue and discharged into the DTMF for long-term storage.

In the KLBN process (Figure 3.1), the raffinate flows by gravity through a series of air agitated mixing cells (termed pachucas) and thickeners. The raffinate at pH 1.0 is fed to pachuca 1 (P1) for mixing. From P1, the raffinate flows by gravity to P2 where lime is added to increase the pH to 3.5-4.2. The solution is then pumped to the Se-Mo Thickener and flocculent is added to

enhance solid agglomeration and settling properties. The aqueous overflow from the Se-Mo Thickener is then pumped to P3 where lime is added to increase the pH to 6.5. From P3, the solution is pumped to P4 where more lime is added to increase the pH to 9.2. The resulting slurry is pumped to the Lamella Thickener, which serves to primarily collect the Al oxide mineral phases. The underflow containing the secondary precipitates from both the Se-Mo and Lamella Thickeners are combined and pumped to the DTMF Thickener and raised (via $Ca(OH)_2$) to a terminal pH of 11 prior to discharge into the DTMF. The overflow from the Lamella Thickener reports to the Radium Removal Circuit where H_2SO_4 is used to incrementally decrease the pH to 6.0 via three reactors (pH 7.5, 6.5, and 6.0). This solution flows by gravity to the Radium Removal Thickener where flocculent is added. The overflow from the Radium Removal Thickener is the final effluent and is released to monitoring ponds on site prior to final release to the environment. The underflow from the Radium Removal Thickener is pumped to the DTMF Thickener. Barium chloride ($BaCl_2$) is added at P2, P4, and in the Radium Removal Circuit to reduce ^{226}Ra activity in the final effluent via precipitation (Liu and Hendry, 2011).

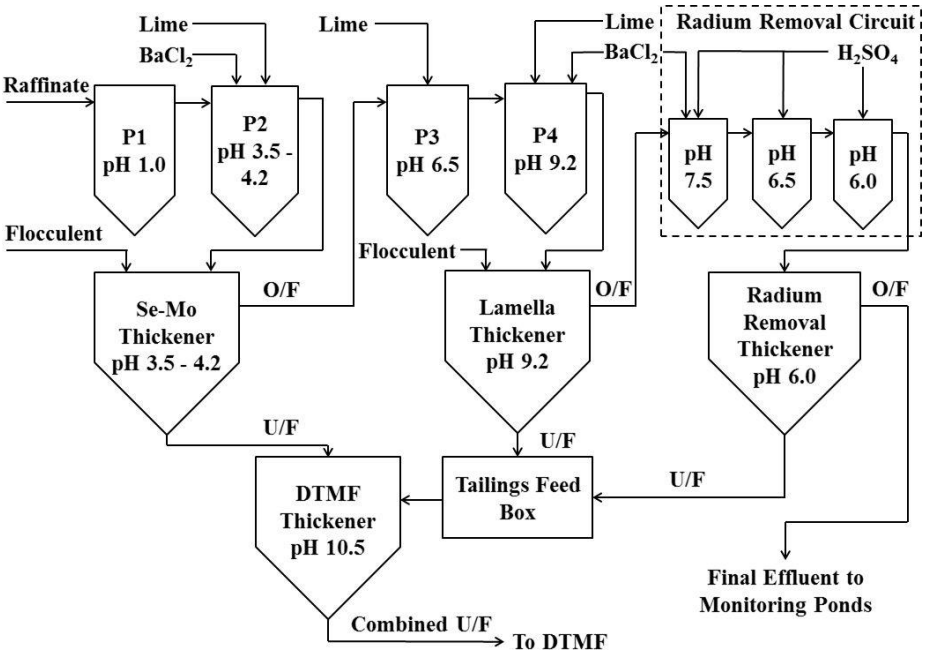

Figure 3.1. Block flow diagram of the Key Lake bulk neutralization process. Only major units of the process are displayed. Overflow and underflow of thickeners are indicated by O/F and U/F, respectively.

3.2.2 Synthetic Raffinate Neutralization System

The SRNS (Figure 3.2) was designed to operate at ambient temperature (approximately 22 °C) and process approximately 200 L of synthetic raffinate solution in 5.5 days at a flow rate of 25 mL/min. The scale of each unit in the SRNS was based on reproducing retention times equal to corresponding units of the KLBN at an overall flow rate of 25 mL/min. To achieve this, the scale of the SRNS to the KLBN ranged between 1:130000 and 1:245000. Tracer tests using deuterium oxide (data not presented) demonstrated that the total retention time of the SRNS (19.8 h) matched that of the KLBN (19.6 h). The SRNS consisted of four reactors (to represent the pachucas) and three thickeners.

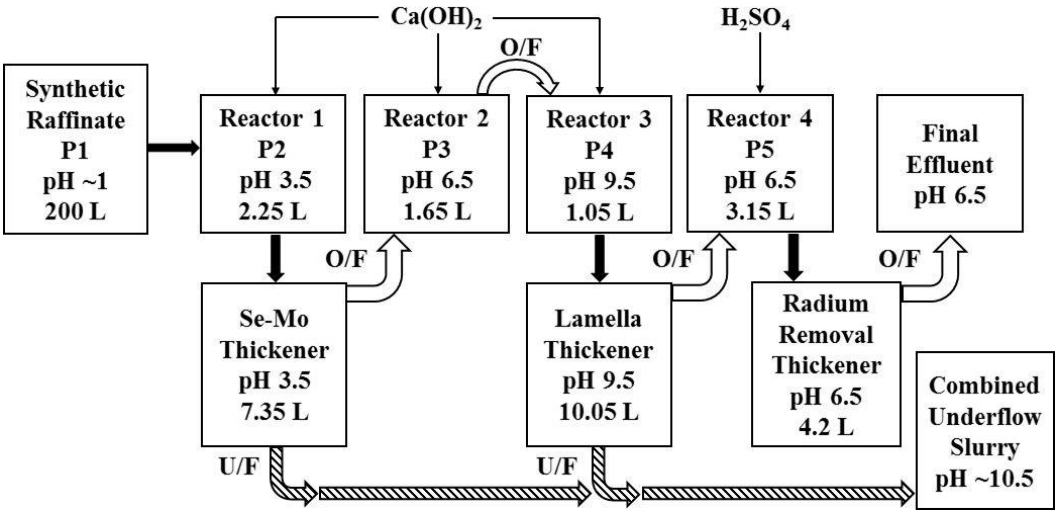

Figure 3.2. Block flow diagram of the synthetic raffinate neutralization system. Solid arrows indicate pumped flow, open arrows indicate gravity flow, line arrows indicate pumped Ca(OH)2, and hatched arrows indicate manual flow by valves. Overflow and underflow of thickeners are indicated by O/F and U/F, respectively.

The reactors were constructed from 127 mm ID opaque PVC pipe, with caps, fittings, and baffles (all PVC; Figure 3.3a,b). The dimensions of the baffles were constructed as specified by Green and Perry (2008). The reactors were agitated at 500-600 rpm using IKA® RW 20 Digital laboratory mixers with 316 SS impellers and ring guards (Figure 3.3b). The thickeners (Figure 3.4a,b) were constructed from 76 and 102 mm internal diameter clear PVC pipe and opaque PVC caps and fittings. A glass wool filter was fitted between two HDPE mesh screens (approximately 9 Mesh) near the top to minimize the carry-over of solids into subsequent reactors. All reactor and thickener components were fitted and sealed using Devcon® Plastic Welder™ II due to its

resistance to extreme acidic and alkaline conditions. The pH of each reactor was controlled using a Cole-Parmer double junction pH electrode (EW-27001-90) connected to an Etatron DLX/DLXB pH-RX/MBB Series Metering Pump, which pumped a $Ca(OH)_2$ solution to increase the pH in reactors P2, P3, and P4 and dilute H_2SO_4 (<5%) to decrease the pH in reactor P5. A Masterflex® peristaltic pump was used to pump synthetic raffinate through Masterflex® Precision FDA Viton® tubing (6.4 mm ID). The neutralized slurry from each reactor was also pumped by Masterflex® peristaltic pumps from the reactors to the thickeners through Masterflex® Tygon® Lab tubing (6.4 mm ID). The slurry flowed from P3 to P4 by gravity through 19 mm ID clear PVC tubing. Clarified thickener overflows flowed by gravity to the appropriate reactor through 19 mm ID diameter clear PVC tubing.

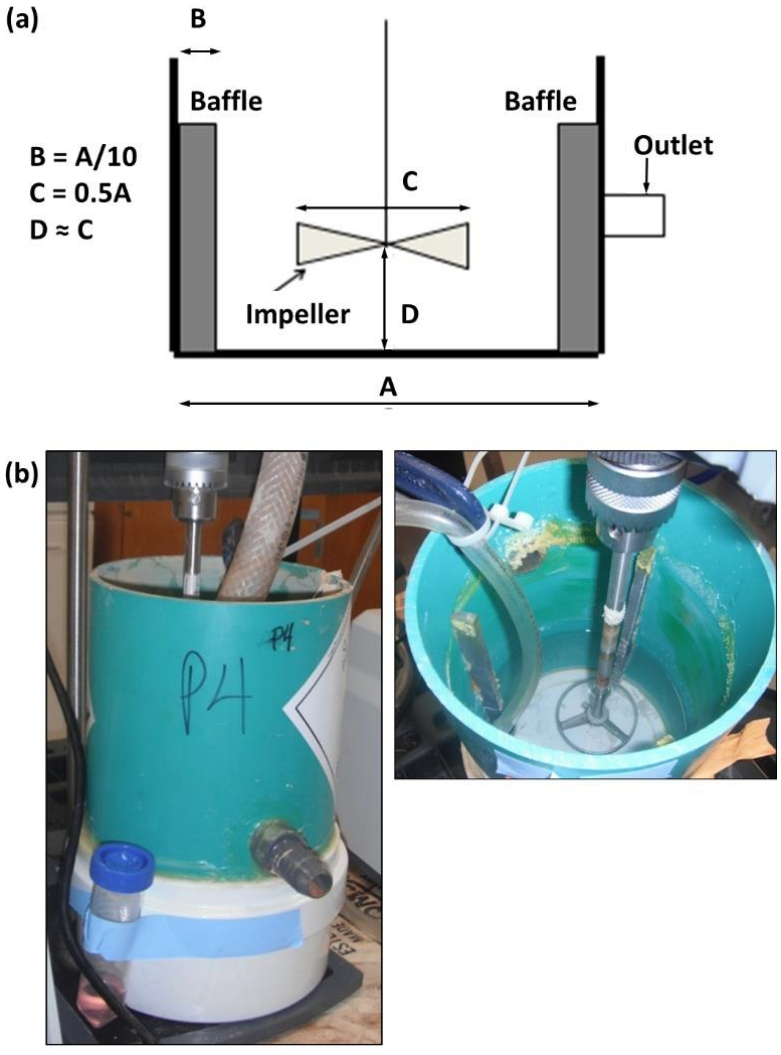

Figure 3.3. (a) General dimensions of the reactors used in the SRNS and (b) photographs of an empty reactor with impeller and inlet tubing attached.

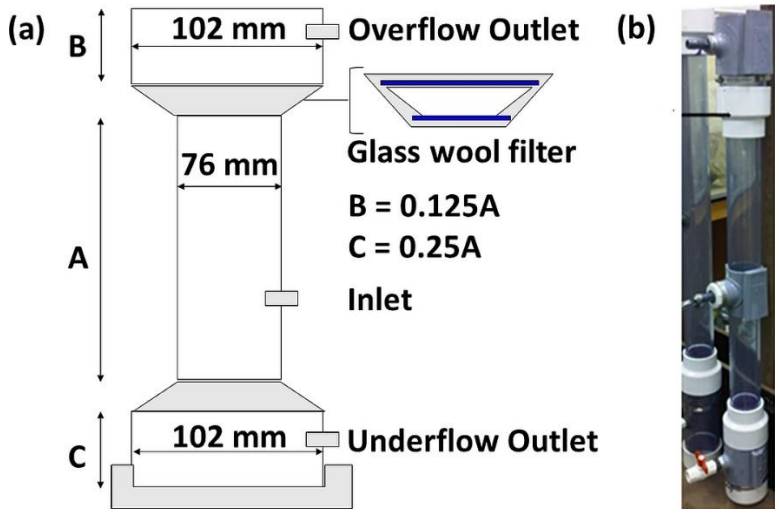

Figure 3.4. (a) General dimension of the thickeners used in the SRNS (not to scale) and (b) photograph of the Se-Mo Thickener showing the inlet, overflow outlet, and underflow outlet.

Prior to neutralization experiments, all reactors were filled with approximately 1 L of municipal tap water and the pH pumps turned on to establish environmental conditions in the SRNS (Figure 3.2). The target pH of the synthetic raffinate (P1) was 1 and was maintained at pH 0.96 ± 0.09. The synthetic raffinate was pumped to P2 where the pH was raised to 3.5 ± 0.5. This solution was subsequently pumped to the Se-Mo Thickener. Overflow from the Se-Mo Thickener flowed via gravity to P3 where the pH was increased to 6.5 ± 0.5. Solution from P3 overflowed to P4 where the pH was increased to 9.5 ± 0.5. The solution from P4 was then pumped to the Lamella Thickener. Overflow from the Lamella Thickener flowed by gravity to P5 where the pH was lowered to 6.5 ± 0.5 with H_2SO_4. The solution was then pumped to the Radium Removal Thickener. Overflow from this thickener represented the final effluent sent to the monitoring ponds at the Key Lake mill.

Neutralization in the KLBN is accomplished using slaked lime at a concentration between 15-20% w/w, but preliminary experiments conducted on the SRNS found this concentration to be too strong for the working volume, resulting in masses of gypsum and lime scale in P2, P3, P4, and the Se-Mo and Lamella Thickeners that limited the identification of important secondary minerals in the SRNS (data not presented). To better control neutralization and minimize gypsum and lime scale formation, a 3% w/w $Ca(OH)_2$ solution was used in the SRNS experiments.

Because a synthetic, non-radioactive raffinate solution (Chapter 3.2.3) was used in the experiments, $BaCl_2$ addition was unnecessary. The addition of flocculent was also deemed

unnecessary because of the relatively small volumes of raffinate used in the SRNS and the potential for the flocculated solutions to plug the connecting tubing.

3.2.3 Raffinate Chemistry

Synthetic raffinate, with concentrations of major elements and EOCs simulating those found in Key Lake mill raffinate (Gomez et al., 2013a) was created from ACS grade reagents (Table 3.1) acquired from Sigma-Aldrich and Fisher Scientific. Concentrations of As, Mo, Ni, and Se were spiked to 10-75 times the measured Key Lake raffinate concentrations to allow for easier quantification and identification of EOC-related mineral phases. Silicon was also added to the synthetic raffinate due to its presence in the Key Lake mill raffinate (Liu and Hendry, 2011); however, the effects of Si on the bulk neutralization system are outside the scope of the current study.

Table 3.1. Chemistry of Key Lake mill raffinate and synthetic raffinate.

Element	Key Lake Raffinate Concentration (mg/L)	Target Synthetic Raffinate Chemistry	
		Concentration (mg/L)	Source Reagent
Al	1635	1635	$AlCl_3$
As	27.8	270	$As_2O_5 \cdot 3H_2O$
Fe	1428	1428	$Fe(NO_3)_3 \cdot 9H_2O$
Mg	1044	1045	$MgCl_2 \cdot 6H_2O$
Mo	3.14	100	$Na_2MoO_4 \cdot 2H_2O$
Ni	23.3	230	$NiCl_2 \cdot 6H_2O$
Se	0.4	30	Na_2SeO_3
Si	-	250	Na_2SiO_3

The reagents were dissolved individually in municipal tap water and combined in a 200 L polyethylene feed tank with a removable top, after which the volume of solution in the tank was increased with tap water to 200 L. Sulfuric acid was added in excess to maintain the pH at approximately 1 (pH 0.96 ± 0.09); a lower pH was favoured to minimize precipitation of solids in the tank during the experiment. The final synthetic raffinate was manually mixed for approximately 1 min after the addition of each reagent and every 12 h thereafter using an impeller.

3.2.4 Experimental Conditions and Sample Collection

KLBN data reported by Gomez et al. (2013a) were measured at five points in the process: raffinate, P2, Se-Mo Thickener overflow, P3, and Lamella Thickener overflow. pH values from this data set deviated from designed pH set points due to the continuous and variable nature of the Key Lake process. Therefore, two experiments were performed with the SRNS to facilitate comparisons with this existing data set: experiment L1 used the designed pH set points (P2 = Se-Mo Thickener = 3.5, P3 = 6.5, P4 = Lamella Thickener = 9.5, P5 = 6.5) and experiment L2 used the pH values measured by Gomez et al. (2013a) (P2 = 4.3, Se-Mo Thickener = 4.4, P3 = 6.4, P4 = Lamella Thickener = 10.1, P5 = 6.5). The Gomez et al. (2013a) data set is hereafter referred to as KL1.

The SRNS ran for at least 24 h prior to sampling to allow the solids-aqueous chemistry to reach steady state. Samples were collected every 12 h for three days from the raffinate feed, all reactors, and all thickener overflows using 50 mL disposable needleless plastic syringes. These samples were immediately transferred to 50 mL polypropylene centrifuge tubes. Solids and supernatants were separated for analysis by centrifugation at 2900 g for 20 min. Supernatants were decanted and filtered using 0.45 μm cellulose filters, then transferred to 30 mL scintillation vials and acidified by adding approximately 0.5 mL of 2% HNO_3 solution. Solids were allowed to dry at room temperature for 3-5 d, then gently ground using an agate mortar and pestle and transferred to 50 mL polypropylene centrifuge tubes and stored prior to analysis.

Precipitated solids (in slurry form) were collected from the base of the Se-Mo and Lamella Thickeners at the end of each experiment using valves located at the base of the thickeners (Figure 3.4). The pH and E_h of the Se-Mo and Lamella slurries were measured immediately after collection using an Orion 250Aplus Portable pH and ISE Meter equipped with a Cole-Parmer double junction pH electrode (EW-27001-90) and a Cole-Parmer single junction ORP electrode (RK-59001-75). Slurry samples were then collected in 50 mL polypropylene centrifuge tubes. After sampling, approximately 2 L of slurry from each of the thickeners was combined in a 4 L polyethylene beaker and mixed using an IKA® RW 20 Digital laboratory mixer for 30 min to form a composite sample to represent the solids reporting to the DTMF thickener prior to deposition into the DTMF. With continued mixing, $Ca(OH)_2$ was added to raise the pH to 10.50 ± 0.25 and a final E_h measurement

was taken. Samples of the combined underflow solids were collected in 50 mL polypropylene centrifuge tubes and prepared for analysis as noted above.

Because gypsum dominates the spectra produced by some analytical techniques (e.g., XRD, ATR-IR spectroscopy, Raman spectroscopy) and makes detection of other secondary mineral phases difficult, subsamples of each solid sample were washed to remove soluble gypsum. Subsamples were mixed with deionized water (18 MΩcm, produced by a Millipore filtration system) at a ratio of 5 g sample per 1 L water for 24 h. The washed samples were separated from the filtrate using pressure filtration with compressed N_2. Each sample was washed three times. Filtrate samples were collected after each wash for analysis to ensure Ca (from gypsum) was the only component leached (Table A.1).

3.2.5 Sample Analysis

Bulk elemental analysis was conducted on the aqueous and solid samples using a Perkin Elmer NexION 300D ICP-MS with a relative standard deviation of ±10% and detection limits less than 6.52×10^{-3} and 1.52×10^{-2} ppm for aqueous and solid samples, respectively. All solids were subjected to an HF-HNO_3 digest (Jenner et al., 1990; Longerich et al., 1990) prior to ICP-MS analysis. Select aqueous samples were analyzed for total S by ICP-optical emission spectrometry (ICP-OES) using a SpectroBLUE ICP-OES with a relative standard deviation of <5%.

Dried solids were analyzed using powder XRD. Samples were mounted on rotating disk transmissions holders and bulk X-ray diffractograms were measured with an Empyrean Pro PANalytical diffractometer equipped with a cobalt target (Co $K_{\alpha1}$ radiation, λ = 1.7902 Å), a crystal graphite monochromator, and a scintillation detector. The diffractometer was operated at 40 kV and 45 mA. Scans were measured from 10 to 80° 2θ with a 0.01° step and a scan step time of 85 s/°.

Infrared spectra were obtained on powdered subsamples using a Bruker Tensor 27 FTIR spectrometer with an ATR attachment and ZnSe crystal. Spectra over the 4000-500 cm^{-1} range were obtained by the co-addition of 64 scans with a resolution of 4 cm^{-1} at the full width at half maximum (FWHM) of the strongest C-H vibration of the internal polystyrene standard.

Raman spectra were collected on subsamples with a Renishaw InVia Raman microscope in both normal and confocal mode. Laser excitation was provided by a solid state diode near-IR

laser operating at 785 nm. The laser beam produced a spot size of approximately ≤5 μm in diameter using a 50× long distance objective. The average of five scans collected from 1400 to 100 cm^{-1} is reported. The energy resolution was 4 cm^{-1} at FWHM of the internal Si reference peak. Scans were collected at 40 s per scan using 10% of the laser output at the microscope exit to minimize radiation damage to the FH particles (Mazzetti and Thistlethwaite, 2002). Some samples were damaged by the 785 nm laser so were instead scanned using a 514 nm laser at the same operating conditions.

3.2.6 Geochemical Modeling

Speciation equilibrium modeling using PHREEQC version 3.1.0-8264 (Parkhurst and Appelo, 2013) was performed to simulate the aqueous and solid environments formed in the SRNS and to validate observations of elemental aqueous removal and solids mineralogy. The MinteqV4 thermodynamic database was employed. Equilibrium constants were slightly adjusted from their database values to optimize the model fit to the measured data (Table 3.2). We considered these adjustments justified because variations of equilibrium constants exist between databases and in the literature. Further, other studies (Dixit and Hering, 2003; Gustafsson, 2003; Stollenwerk, 1994) also adjusted equilibrium constants, generally within an order of magnitude of literature values, to optimize the simulated fit to the measured data. Thermodynamic data for hydrotalcite (Rozov et al., 2010) and surface complexation of Ni to gibbsite (Rajapaksha et al., 2012) were added to the database (Table 3.2). Surface complexation site parameters for ferrihydrite (hydrous ferric oxide; HFO in the model) and $Al(OH)_3$ (alumina) reported by Moldovan and Hendry (2005) were also used.

The modeling procedure used the initial experimental raffinate pH, E_h, and elemental concentrations measured by ICP-MS. Four neutralization process points were modeled: raffinate, Se-Mo Thickener overflow, P3, and Lamella Thickener overflow. To simulate the separation of solids from the aqueous phases in the Se-Mo and Lamella Thickener steps in subsequent calculations, the overflow solution was saved after completion of the equilibrium modeling and a new solution used for subsequent steps. The pH and E_h of the modeled solution was adjusted by adding $Ca(OH)_2$ and O_2. At each point (except the raffinate), the solution was equilibrated with the phases observed in the experimental results by XRD, ATR-IR, and Raman spectroscopy: amorphous $Al(OH)_3$, calcite, poorly crystalline scorodite (i.e., ferric arsenate, or FA), ferrihydrite, gypsum, Mg-Al hydrotalcite, $Mg(OH)_2$, $Ni(OH)_2$, and $NiMoO_4$. The solution was also equilibrated

under atmospheric CO_2 conditions. The output concentrations of the model were compared to the corresponding experimental results, with the concentration values adjusted to account for dilution by $Ca(OH)_2$ addition not accounted for in the model.

Table 3.2. Thermodynamic reactions and equilibrium constants added to and/or adjusted in the MinteqV4 thermodynamic modeling database.

Reaction	Reported logK	Adjusted logK
$Al(OH)_3 + 3H^+ = Al^{3+} + 3H_2O$	10.8	9.6
$Mg(OH)_2 + 2H^+ = Mg^{2+} + 2H_2O$	18.794	18.2
$Mg_4Al(OH)_{10}(CO_3)_{0.5}{:}2.5H_2O + 10H^+ = Al^{3+} + 0.5CO_3^{2-} + 4Mg^{2+} + 12.5H_2O$	68.92 ± 3.50[a]	67.5
$Hfo\_sOH + H_3AsO_4 = Hfo\_sH_2AsO_4 + H_2O$	8.61	9.41
$Hfo\_wOH + H_3AsO_4 = Hfo\_wH_2AsO_4 + H_2O$	8.61	9.41
$Hfo\_sOH + HSeO_3^- = Hfo\_sSeO_3^- + H_2O$	4.29	4.89
$Hfo\_wOH + HSeO_3^- = Hfo\_wSeO_3^- + H_2O$	4.29	4.89
$Alumina\_sOH + 0.5Ni^{+2} = Alumina\_sONi_{0.5} + H^+$	-4.26[b]	-3.3

[a] Added from (Rozov et al., 2010); reaction changed from 3:1 Mg:Al to 4:1 Mg:Al

[b] Added from (Rajapaksha et al., 2012); surface complexation reaction for nickel on gibbsite in lieu of amorphous $Al(OH)_3$

3.3 Results and Discussion

3.3.1 Elemental Concentrations of Aqueous and Solids Phases

Concentrations of aqueous elements of interest were determined at each step of the neutralization process in the SRNS experiments using ICP-MS and compared with the KL1 data set (Figure 3.5, Table A.2). Dissolved Al concentrations reflected a strong dependence on pH on the amount of precipitation of Al between pH 3.5 and 4.4 (Figure 3.5a). Experiment L1, with a pH of 3.5 in P2 and the Se-Mo Thickener, resulted in 30.9% Al removal (with respect to the initial raffinate concentration). Experiment L2 and KL1 were both performed at pH 4.4 in P2 and the Se-Mo Thickener and resulted in nearly complete and identical Al removal (92.9-97.3%). This difference had a major impact on the final characteristics of the solids in the SRNS and KLBN tailings (discussed in Chapter 3.3.3 and Chapter 3.3.4). As a result, more Al was present in the Lamella solids in L1 than in L2 or KL1. By P3 (pH 6.5), all Al had been removed (>99.9%) from the aqueous phase in L1, L2, and KL1.

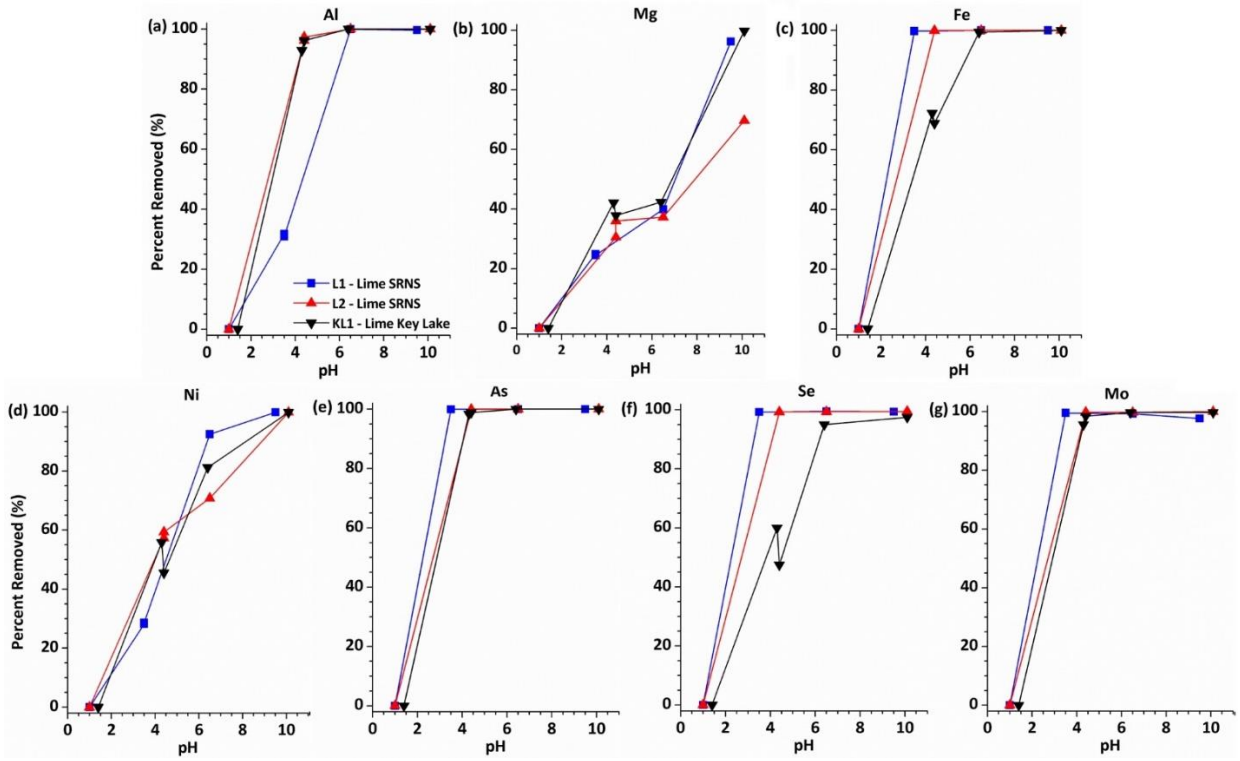

Figure 3.5. Percent removal of (a) Al, (b) Mg, (c) Fe, (d) Ni, (e) As, (f) Se, and (g) Mo from solution with respect to the initial raffinate concentration. L1 = slaked lime neutralization, L2 = slaked lime neutralization at measured Key Lake pH values, KL1 = Key Lake data.

The trend in Mg removal was similar in both SRNS experiments and KL1 data (Figure 3.5b) where an increase in removal occurred with increasing pH, with nearly complete removal (>96.0%) in the Lamella overflow (pH 9.5-10.1) of L1 and KL1 but only 69.7% removal in L2. The limited removal measured in L2 may be the result of the Mg/Al molar ratio being too great for complete precipitation of Mg as Mg-Al hydrotalcite (discussed in Chapter 3.3.3) and/or a pH too low to facilitate complete precipitation of the remaining Mg.

Complete removal (>99.5%) of Fe from the aqueous phase occurred in P2 (pH 3.5-4.4) for both SRNS experiments (Figure 3.5c). In contrast, only 72.3% removal of Fe occurred in the KL1 data by this stage and complete removal of Fe did not occur until P3 (pH 6.5). This difference was attributed to the expected absence of Fe(II) in the synthetic raffinate. Moldovan and Hendry (2005) conducted a study on raffinate neutralization for a similar process but using an Fe(III)/Fe(II) ratio of 9:1. Their results are consistent with the KL1 data, demonstrating 84% removal of the Fe at pH 3.18 and nearly all of the precipitated Fe present as Fe(III); Fe(II) did not begin to precipitate until pH >4.25 and was not completely removed from solution until pH >5.03.

Nickel, As, Se, and Mo behaved consistently in both the SRNS and KLBN. Almost complete removal of these EOCs (>97.6%) was observed in all data sets at pH >9.5 (Figure 3.5d-g). Nickel removal followed a trend similar to Al, with the designed SRNS (L1) operating conditions resulting in poorer Ni removal in P2 and the Se-Mo overflow (pH 3.5) than at the higher pH (4.4) of L2 and KL1 (Figure 3.5d). In contrast to Al, however, the removal of Ni was nearly linear between pH 1.0 and 4.4. While less Ni removal occurred in the early stages of L1 compared to L2 and KL1, the removal of Ni was greater in L1 at pH 6.5. Complete As removal occurred in P2 (pH 3.5 and 4.4) in all data sets (Figure 3.5e). Removal of Se and Mo were difficult to quantify in the KLBN because the raffinate contained low concentrations of Se (0.4 mg/L) and Mo (3.14 mg/L) in contrast to the SRNS (spiked to 27.0 and 100 mg/L, respectively). Although the SRNS experiments removed a greater mass of Se than KL1, KL1 reduced the aqueous Se to lower concentrations. Molybdenum removal was 99.5-99.6% at pH 3.5-4.4 in the SRNS experiments and 95.5% at pH 4.4 in KL1.

Total S was measured in the raffinate, Se-Mo overflow, and Lamella overflow (Figure A.1). All S was assumed to be present as SO_4^{2-} (e.g., HSO_4^- or a complex). Sulfate concentrations were not available in the KL1 data set; however, they were measured at 40,000 mg/L in the Key Lake raffinate (Liu and Hendry, 2011). The synthetic raffinate did not control for SO_4^{2-} and contained concentrations of 4,000-5,000 mg/L. Gypsum formation in the Se-Mo Thickener likely accounts for the large decrease in SO_4^{2-} concentrations in L1 and L2 that resulted in relatively small SO_4^{2-} concentrations in the Lamella Thickener (<358 mg/L).

The composition of solids obtained from the Se-Mo and Lamella Thickener underflows from both SRNS experiments and the KLBN were consistent with the removal of elements from the aqueous phase (i.e., greater removal resulted in a greater solids concentration in the respective thickener underflow). As such, L2 and KL1 Se-Mo solids (precipitated at pH 4.4) were composed of >62.0% Al (on a molar basis) while L1 Se-Mo solids (precipitated at pH 3.5) were composed of 7.58% Al (Table A.3). Iron was a greater component of the Se-Mo solids in the SRNS (75.1% in L1 and 29.8% in L2) than in KL1 (2.76%) due to the lack of Fe(II) in the synthetic raffinate. KL1 Se-Mo solids contained a modest amount of Mg (6.80%) but only very small amounts were present in the SRNS experiments (<0.19%). The discrepancy of Mg in L2 compared to KL1 was attributed to dilution of solids by Fe (which is not present in significant amounts in KL1). The spiked concentrations of As, Se, and Mo in the SRNS experiments resulted in a greater mass of

these elements in the L1 and L2 Se-Mo solids. Aluminum was the major component in the L1 Lamella solids (53.7%) but was less prominent in L2 and KL1 (<18.8%). KL1 had more Fe in the Lamella solids (17.6%), likely due to Fe(II) present in the KLBN raffinate, while minimal Fe was observed in L1 and L2 (<4.63%). All Lamella samples contained significant amounts of Mg (37.5-71.9%). Nickel was more abundant in the Lamella solids than the Se-Mo solids in all data sets; it was also more concentrated in the L1 and L2 (>3.44%) solids versus the KL1 (0.46%) solids due to the spiked concentration of Ni in the synthetic raffinate. Other EOCs were present only in trace amounts in the Lamella solids. The solids compositions in the SRNS and KLBN were consistent after accounting for differences in initial EOC concentrations, dilution, and the presence of Fe(II) in the KLBN.

3.3.2 Comparison and Characterization of Se-Mo Solids

X-ray diffraction patterns of the Se-Mo solids varied with pH (3.5 vs. 4.4; Figure 3.6a). Samples from pH 3.5 (L1) featured an amorphous pattern with two broad peaks that are representative of a mixture of As-adsorbed FH and possibly FA. This is in agreement with the known elemental composition of the L1 solids (Table A.3). At pH 4.4 (L2 and KL1), the XRD pattern featured a weak, broad band between 20° and 30° representative of an amorphous $Al(OH)_3$ phase (Martin et al., 2009). This pattern was in agreement with the Se-Mo solids composition data from L2 and KL1 that show the samples were predominantly Al. The overall shape of the diffraction patterns at pH 4.4 suggests a strong similarity between the SRNS and KLBN Se-Mo samples. The differences in XRD patterns between pH 3.5 and 4.4 can be attributed to additional Al precipitation at pH 4.4 which diluted the amorphous Fe phases.

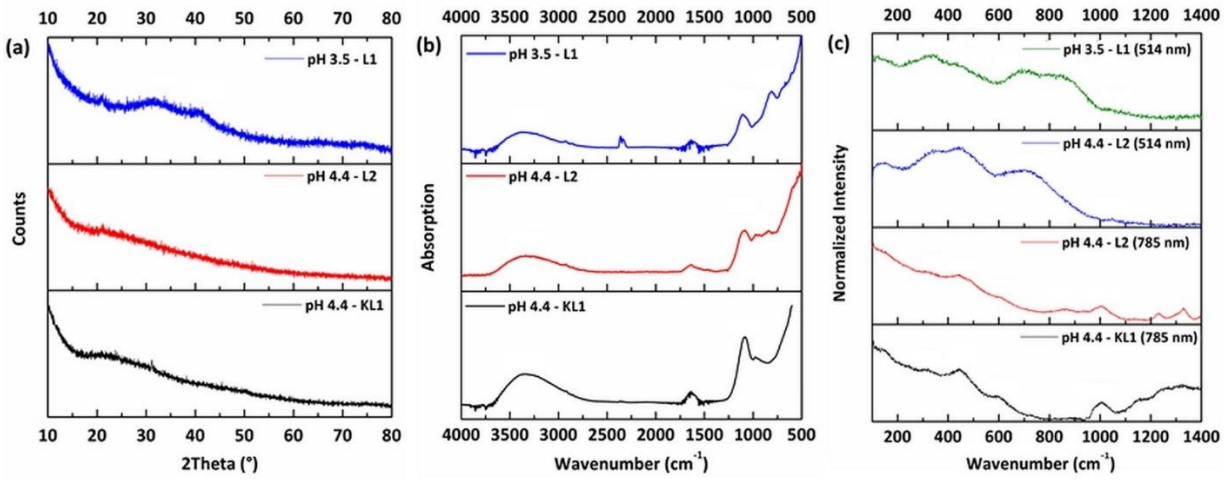

Figure 3.6. (a) XRD patterns, (b) ATR-IR spectra, (c) and Raman spectra for Se-Mo Thickener solids precipitated at pH 3.5 or pH 4.4. Raman spectra for L1 and L2 were obtained with a 514 nm laser, and for L2 and KL1 with a 785 nm laser.

The ATR-IR spectra for the Se-Mo Thickener solids (Figure 3.6b) show the presence of three main molecular groups: OH/H_2O, SO_4^{2-}, and AsO_4^{3-}. The OH/H_2O groups likely result from FH and amorphous $Al(OH)_3$. The presence of SO_4^{2-} vibrations suggests sorption of SO_4^{2-} to FH and possibly $Al(OH)_3$ (Fukushi et al., 2013; Jia et al., 2007; Lane, 2007). The AsO_4^{3-} group indicates the presence of As-adsorbed FH, As-adsorbed $Al(OH)_3$ (L2 only), and possibly FA (Goldberg and Johnston, 2001; Jia et al., 2007; Müller et al., 2010; Park et al., 2011). The AsO_4^{3-} vibrations were only present in the SRNS samples due to spiked As concentrations in the synthetic raffinate. The IR spectra of the SRNS Se-Mo solids were generally in good agreement with the KLBN solids after considering the differences in EOC content.

Raman spectra for the Se-Mo solids (Figure 3.6c) reflect L1 and L2 samples scanned with the 514 nm laser and L2 and KL1 samples scanned with the 785 nm laser. The L1 and L2 Se-Mo spectra from the 514 nm laser shared four broad bands representative of FH, As and SO_4^{2-}-adsorbed FH, and possibly FA (Das et al., 2011b; Das and Hendry, 2011; De Klerk et al., 2012; Jia et al., 2006). The AsO_4^{3-} band in L2 is not observed in this spectrum, possibly because the As concentration was half that observed in L1.

Comparison of the Raman spectra of L2 and KL1 from the 785 nm laser reveals similar spectra. It should be noted that an AsO_4^{3-} band, which was not observed in the L2 514 nm spectrum, is present in the L2 785 nm spectrum. This AsO_4^{3-} band was not present in KL1 due to its relatively

low As content. A series of rounded peaks appeared in the KL1 spectrum at wavenumbers >1000 cm^{-1} and line up with sharper peaks in the L2 spectrum. These peaks are possibly attributable to an amorphous $Al(OH)_3$ phase, the presence of which is supported by the high Al content, XRD, and IR data.

3.3.3 Comparison and Characterization of Lamella Solids

XRD analysis of the Lamella solids shows the presence of calcite (Downs, 2006) and hydrotalcite-like compounds (HTLC) (Evans and Slade, 2006; Frost et al., 2009; Gomez et al., 2013a; Paikaray and Hendry, 2012) as the two major mineral phases formed in the SRNS and KLBN at pH 9.5 and 10.1 (Figure 3.7a). The diffraction patterns from L2 and KL1 were nearly identical. In the case of KL1, a Mg-Al HTLC phase with small amounts of Fe likely formed (Gomez et al., 2013a). Thus, L2 likely consists of a Mg-Al HTLC phase (although with minimal Fe). The diffraction pattern of L1 (pH 9.5) shows evidence of a less crystalline HTLC. This also indicates that HTLC formation is likely more favourable at greater Mg/Al solid phase molar ratios as suggested by Gomez et al. (2013a); the solid phase Mg/Al ratio was >3.36 for L2 and KL1 and 0.70 for L1 (due to less Al precipitation in the Se-Mo Thickener). The remaining sharp peaks in all of the samples are characteristic of calcite (Downs, 2006).

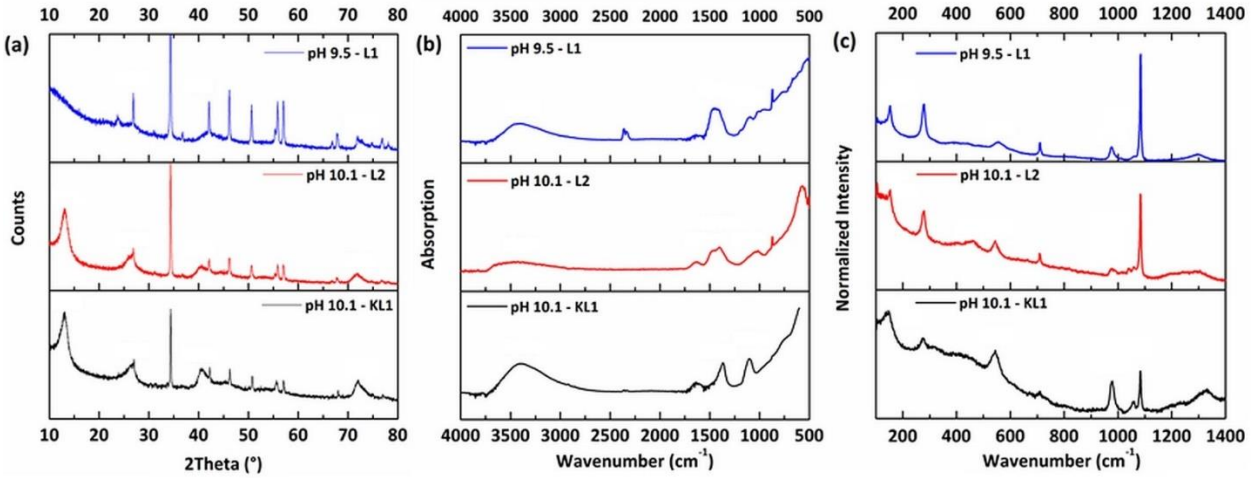

Figure 3.7. (a) XRD patterns, (b) ATR-IR spectra, (c) and Raman spectra for Lamella Thickener solids precipitated at pH 9.5 or pH 10.1.

IR and Raman spectra were used to determine HTLC divalent/trivalent cations and interlayer anions. OH/H_2O vibrations are observed in all samples (Figure 3.7b) and likely result

from HTLCs. The KL1 Lamella underflow displays distinct CO_3^{2-} and SO_4^{2-} bands, indicating the incorporation of these anions in HTLC interlayers (Gomez et al., 2013a; Gunzler and Gremlich, 2002; Paikaray and Hendry, 2012). Comparing L2 to KL1 reveals noticeable differences in the CO_3^{2-} and SO_4^{2-} regions. It is evident that L2 consists of calcite and HTLCs with CO_3^{2-} as the primary interlayer anion (and minimal interlayer SO_4^{2-}). The lack of interlayer SO_4^{2-} in L2 was attributed to low SO_4^{2-} concentrations in the synthetic raffinate (compared to the mill raffinate) and the Se-Mo Thickener overflow (Figure A.1). Differences between L1 and KL1 spectra are likewise accounted for by differences in the HTLC structure.

Raman spectra of the Lamella precipitates (Figure 3.7c) of KL1 and L2 closely match the spectra of $MgAl(CO_3/SO_4)$-type HTLCs synthesized by Paikaray and Hendry (2012). The data indicates, again, that L1 and L2 were low in interlayer SO_4^{2-} when compared to KL1. Calcite bands are also observed in all samples (Downs, 2006). Overall, the Raman spectra support the formation of similar mineral phases in KL1 and L2.

3.3.4 Comparison and Characterization of Combined Solids

XRD patterns, ATR-IR spectra, and Raman spectra of the combined solids from the SRNS and KLBN are representative of the combination of Se-Mo and Lamella Thickener solids (Figure 3.8). In general, the strong features of the Lamella solids (i.e., those resulting from HTLCs and calcite) dominate the spectra but are diluted by the amorphous Fe and Al hydroxides from the Se-Mo solids. This dilution also makes it more difficult to discern details and identify minor phases, such as As-adsorbed FH, present in the original solids. It also appears that no new mineral phases formed due to neutralization with slaked lime to pH 10.5; however, it should also be noted that the KL1 combined solids contain barite (Downs, 2006), which formed in the KL1 solids due to the addition of $BaCl_2$ in the mill (Gomez et al., 2013a). Overall, features present in the SRNS spectra are consistent with those found in the KLBN spectra.

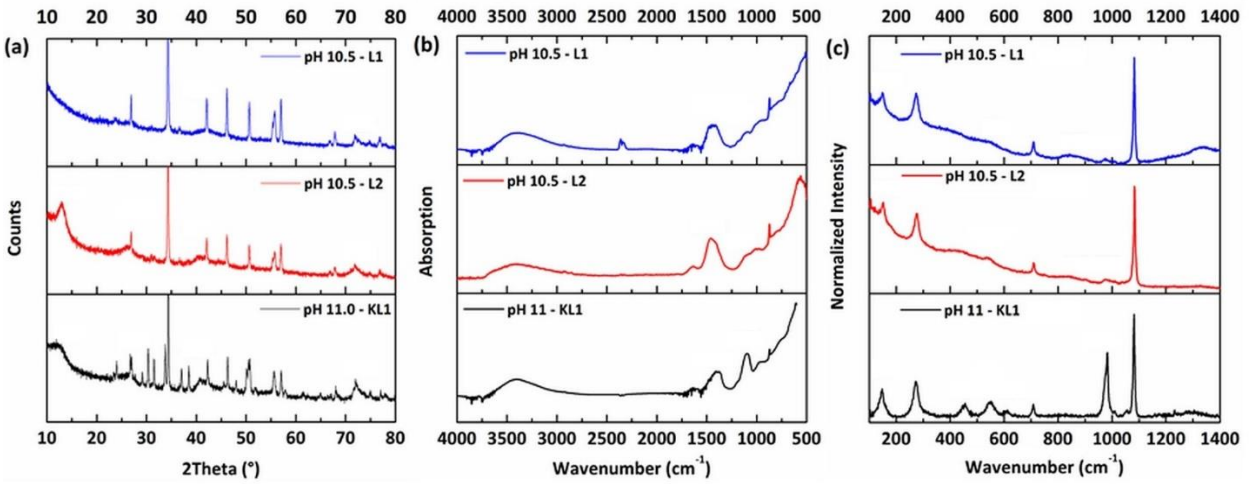

Figure 3.8. (a) XRD patterns, (b) ATR-IR spectra, (c) and Raman spectra for combined Se-Mo and Lamella Thickener solids neutralized to pH 10.5-11.

3.3.5 Geochemical Modeling

The L2 experimental results were modeled because they better represented the aqueous and mineralogical environment of the KLBN than L1. Model results (Figure 3.9a-g) show strong agreement with the experimental aqueous concentrations and mineral phases. Most Al precipitated at pH 4.4 as amorphous $Al(OH)_3$. After the solution was separated from the precipitated phases, the pH increased to pH 6.5 and the remaining Al precipitated as amorphous $Al(OH)_3$. Because the precipitated phases are not separated after this step, data suggest that the amorphous $Al(OH)_3$ re-dissolved and subsequently precipitated with Mg as hydrotalcite at pH 10.1. The equilibrium reaction for hydrotalcite was modeled as a 4:1 Mg/Al reaction instead of a 3:1 Mg/Al reaction to better approximate the Mg/Al ratio in the L2 solids at this pH, thus providing a better model fit. Magnesium precipitation did not begin until pH 10.1, at which point Mg precipitated as hydrotalcite until the Al was exhausted. Iron precipitated completely at pH 4.4 as FH. Surface complexation reactions with FH at pH 4.4 were the dominant control of As and Se, while they controlled <1% of the Mo. Nickel molybdate was modeled as the main control on Mo, which is the case for systems with high Ni concentrations (Essilfie-Dughan et al., 2011b). Nickel molybdate was not observed during mineralogical characterization, possibly because the techniques used were not sufficiently sensitive. Ferric arsenate was not predicted to precipitate in the model. Along with $NiMoO_4$, Ni formed a surface complex with the amorphous $Al(OH)_3$ precipitate at pH 4.4 and pH 6.5 because the model surface complexation of Ni to FH was predicted to be a very weak

control. This mechanism, although not demonstrated experimentally, explains the removal trend of Ni at these lower pH values. Nickel precipitated completely as $Ni(OH)_2$ at pH 10.1, as observed in similar models (Essilfie-Dughan et al., 2012; Mahoney et al., 2007; Shaw et al., 2011). As previously discussed, Ni may form a Ni-Al HTLC at pH 10.1; however, no thermodynamic data was found for modeling purposes. The precipitation of the passive mineral phases gypsum and calcite was predicted to predominantly occur at pH 4.4 and 10.1, respectively, as observed experimentally. Gomez et al. (2013a) predicted that the Al phase at pH 4.4 for KL1 would be in the form of $AlOHSO_4$. When this phase was equilibrated in the model, SO_4^{2-} was precipitated completely $AlOHSO_4$ and no gypsum formed. However, gypsum was observed in large amounts in SRNS experiments. As such, $AlOHSO_4$ was not considered as an equilibrium phase. Instead, the model predicted surface complexation of SO_4^{2-} to FH as hypothesized from the IR spectroscopy results. Overall, the thermodynamic model is in agreement with the bulk mineralogy observed in the L2 experiment conducted with the SRNS.

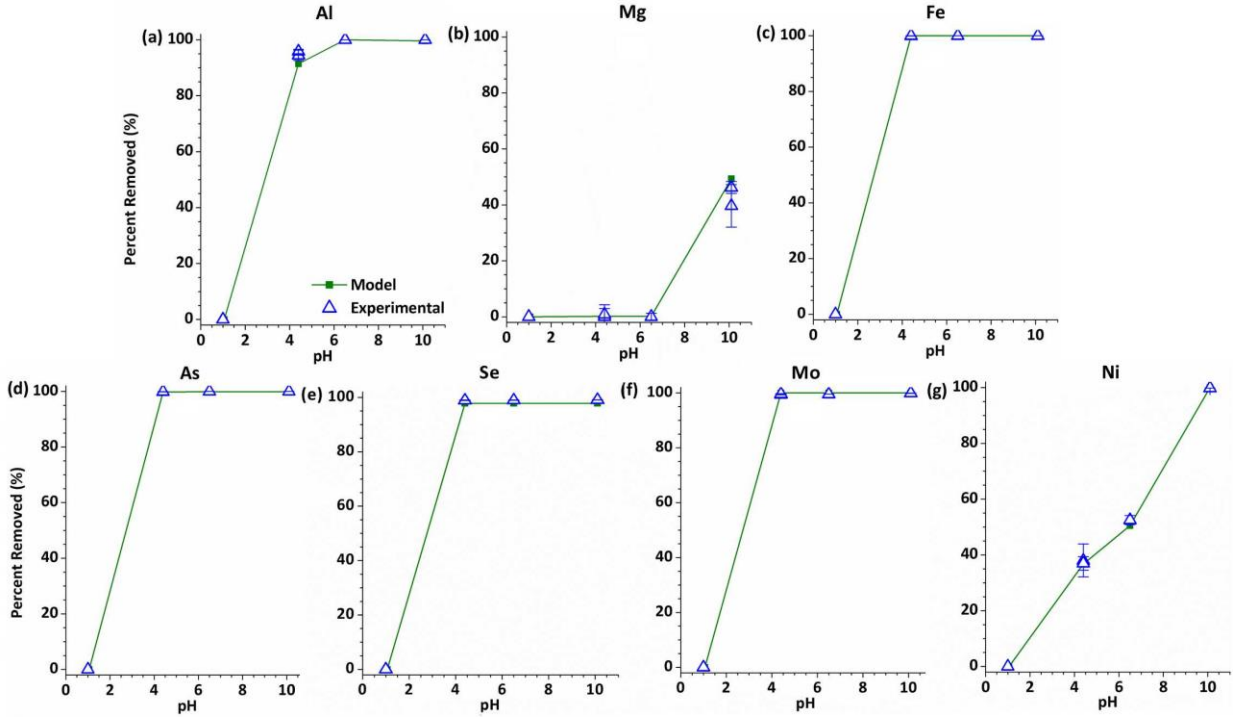

Figure 3.9. PHREEQC model results presented as percent removal of (a) Al, (b) Mg, (c) Fe, (d) As, (e) Se, (f) Mo, and (g) Ni from solution with respect to pH. Model results (solid line and green square) were compared against the experimental results of L2 (blue triangle; error bars represent standard deviations).

3.4 Conclusions

A laboratory-scale bulk neutralization process using a synthetic raffinate based on the bulk neutralization process employed at the Key Lake uranium mill in northern Saskatchewan, Canada was constructed to simulate the secondary mineralogy of the tailings discharged to tailings management facilities. The model allows for the study of the bulk neutralization process and its products in a controlled environment and in the absence of ^{226}Ra that is present in the mill. The overall operation of the laboratory-scale model resulted in aqueous and solid phases that sufficiently reproduced the industrial-scale process.

Differences of the final products of neutralization arose from (i) synthetic raffinate that did not control the Fe(II) and SO_4^{2-} concentrations observed in the raffinate of the Key Lake mill and (ii) differences in pH in the Se-Mo Thickener between the designed process set point (pH 3.5) and that measured during actual mill operation (pH 4.4). In future experiments with the laboratory-scale model, an appropriate amount of Fe(II) should be added to the synthetic raffinate to aid in the accurate reproduction of Fe precipitates downstream of the Se-Mo Thickener. Sulfate concentrations should also be increased to better approximate the mill raffinate chemistry, as the anion plays an important role in the Mg-Al HTLC interlayer composition. Experiments with the model show that relatively small differences in the pH can have significant effects on the aqueous concentrations and solid phases formed throughout the neutralization process. Changing the pH set points in the model to those measured in the mill demonstrated that the model can accurately simulate precipitation trends throughout the process. Future studies could further explore the implications of pH on sequestration of EOCs present in the raffinate.

With the knowledge that the model successfully reproduced the aqueous phase and secondary mineralogy observed in the industrial process, it can now be employed for a wide variety of future experiments. By varying the composition of the synthetic raffinate, the formation of specific secondary mineral phases and their geochemical controls can be studied in a controlled manner, while still simulating the industrial tailings environment. This will allow many different scenarios to be studied in an effort to further understand current geochemical controls in the DTMF and other U tailings facilities as well as to test alternate geochemical controls that could be applied in the mill to improve the geochemical stability of EOCs in the secondary minerals formed in the mill.

3.5 Acknowledgments

Financial support was provided by Cameco Corporation and the Natural Sciences and Engineering Research Council of Canada (NSERC) through a Senior Industrial Research Chair to MJH and NSERC's CGS-M program. The authors acknowledge the technical assistance of Jianzhong Fan, Jing Chen, and Fina Nelson with ICP-MS and -OES analysis, Tom Bonli with XRD analysis, Pia Wennek with ATR-IR spectroscopic analysis, and Jason Maley with Raman spectroscopic analysis.

4.0 PRECIPITATION OF ALUMINUM AND MAGNESIUM SECONDARY MINERALS FROM URANIUM MILL RAFFINATE (PH 1.0-10.5) AND THEIR CONTROLS ON AQUEOUS CONTAMINANTS

PREFACE

This chapter is reproduced with permission (license number 4106051348322) from Robertson, J., Hendry, M.J., Essilfie-Dughan, J., Chen, J., 2016. Precipitation of aluminum and magnesium secondary minerals from uranium mill raffinate (pH 1.0–10.5) and their controls on aqueous contaminants. *Applied Geochemistry* 64, 30–42. doi:10.1016/j.apgeochem.2015.09.002. Minor editorial and formatting changes are made for presentation purposes in this thesis.

This chapter fulfills Objective 1 (to characterize the Al and Mg mineral phases) and Objective 2 (to determine if Al and Mg minerals exert controls on EOCs). The SRNS neutralization system, which was shown reproduce the geochemical conditions of the KLBN in Chapter 3, is used to generate the precipitates studied in this chapter. The operational methods of the SRNS that were developed in the previous chapter are used in this chapter.

4.1 Abstract

Models of geochemical controls on elements of concern (EOCs; e.g., As, Se, Mo, Ni) in U tailings are dominated by ferrihydrite. However, the evolution of aqueous concentrations of Al and Mg through the Key Lake (KL) U mill bulk neutralization process indicates that secondary Al and Mg minerals comprise a large portion of the tailings solids. X-ray diffraction, Al K-edge XAS, and TEM elemental mapping of solid samples collected from a pilot-scale continuous-flow synthetic raffinate neutralization system of the KL mill indicate the secondary Al-Mg minerals present include Mg-Al hydrotalcite, amorphous $Al(OH)_3$, and an amorphous hydrobasaluminite-type phase. The ferrihydrite present contains Al and may be more accurately described as Al-$Fe(OH)_3$. In the final combined tailings sample (pH 10.5) collected from the model experiments

using raffinate with Al, Mg, and Fe, solid phase EOCs were associated with Al-$Fe(OH)_3$ and Mg-Al hydrotalcite. In model experiments using raffinate devoid of Fe, aqueous EOC concentrations decreased greatly at pH 4.0 (i.e., where ferrihydrite would precipitate) and largely remained in the solid phase when increased to the terminal pH of 10.5; this suggests Al-Mg minerals can control aqueous concentrations of EOCs in the raffinate in the absence of Fe. Maximum adsorption capacities for individual and mixtures of adsorbates by Mg-Al hydrotalcite were determined. A revised model of the geochemical controls in U mill tailings is presented in which Al and Mg minerals co-exist with Fe minerals to control EOC concentrations.

4.2 Introduction

The extraction of uranium (U) from host rock in the milling process is most commonly undertaken by acid leaching in the presence of an oxidant (Gupta and Singh, 2003). Due to the mineralogically complex nature of U ores, a range of associated metals and metalloids are also dissolved during the leaching process. After separating the U-complexes from the other dissolved constituents, the raffinate (the U-barren solution) must be treated to meet environmental regulatory standards before the final effluent can be discharged safely to the environment. Raffinate contains elevated concentrations of elements of concern (EOCs), including arsenic (As), selenium (Se), molybdenum (Mo), and nickel (Ni). As such, the acidic (pH ~1.0) raffinate must be treated to sequester the dissolved EOCs in stable minerals prior to discharge. This is often performed through bulk neutralization using slaked lime (hydrated CaO) to increase the pH in a stepwise manner to induce mineral precipitation reactions. This milling and treatment process is used in many U mills in northern Saskatchewan, Canada, all of which process ore mined from the high grade U deposits in the Athabasca basin (Bharadwaj and Moldovan, 2005; Donahue et al., 2000; Langmuir et al., 1999; Mahoney et al., 2007; Moldovan et al., 2003). Many studies have identified various mechanisms of EOC sequestration and the subsequent mineralogy of U tailings generated by similar neutralization processes at numerous sites (Douglas et al., 2010; Essilfie-Dughan et al., 2012; Mahoney et al., 2007; Moldovan et al., 2003; Schindler et al., 2015, 2013; and references therein).

The raffinate neutralization process at the largest producing U mill in the world, the Key Lake (KL) mill, consists of multiple pH steps (Figure 3.1). The first stage of neutralization

increases the pH of the raffinate to 4.0, with the solution and precipitates clarified in the Se-Mo thickener. The next two stages increase the pH to 6.5 and 9.5, respectively, with the resulting precipitates collected in the Lamella thickener. The slurries reporting from the Se-Mo and Lamella thickeners (along with the slurry from the Radium Removal thickener, which is not considered in this study) are combined with residual unleached ore (Hossain, 2014) in the final thickener at pH 10.5 and discharged to the in-pit Deilmann Tailings Management Facility (DTMF) for long-term storage (Bharadwaj and Moldovan, 2005).

The Fe minerals in U mill tailings, specifically ferrihydrite, are a well-studied major geochemical control on the solubility of EOCs through inner and outer-sphere complexation mechanisms (Essilfie-Dughan et al., 2011, 2012, 2013; Moldovan and Hendry, 2005; Moldovan et al. 2003, 2008). Poorly crystalline scorodite also controls As concentrations in tailings generated by bulk neutralization (Chen et al., 2009; Mahoney et al., 2007). In the KL bulk neutralization process, Fe is present in high concentrations in the raffinate (often > 1 g/L) and co-precipitates with oxyanions such as arsenate, selenite/selenate, and molybdate at pH ~4.0 in the Se-Mo thickener (Lieu et al., 2010). Ferrihydrite also adsorbs Ni in tailings samples (Essilfie-Dughan et al., 2012). Given the current oxic conditions of the DTMF, the EOCs sequestered on ferrihydrite could remain stable for > 10,000 years (Das et al., 2011).

Dissolved Al and Mg concentrations in the raffinate can exceed 1 g/L and have been observed at greater concentrations than Fe (Gomez et al., 2013a; Liu and Hendry, 2011). Total dissolved Al and Mg concentrations discharged to the DTMF are on the order of 1 mg/L, indicating large amounts of secondary Al and Mg minerals must be reporting to the DTMF. Few studies have attempted to characterize the Al-Mg system in northern Saskatchewan U mill tailings. Moldovan and Hendry (2005) suggest the formation of amorphous $Al(OH)_3$ and gibbsite using a geochemical model of aqueous solutes in raffinate neutralization from pH 3.2 to 11.0 and propose that more research is needed on the Al system in hydrometallurgical solutions in order to better understand the geochemical controls of these systems. Mahoney et al. (2005) use X-ray diffraction (XRD), scanning electron microscopy, and electron microprobe data to suggest poorly crystalline hydrobasaluminite as a potential secondary Al phase resulting from similar neutralization processes (with a terminal pH of 7-8). Studies from Australian U processing operations identified the precipitation of hydrotalcite-like compounds (hereafter referred to as HTLCs) from barren

lixiviant neutralization as a major secondary Al and Mg mineral capable of sequestering EOCs (Douglas et al., 2012, 2010). Subsequently, Gomez et al. (2013a) identified similar HTLCs (Mg-Al/Fe-CO_3/SO_4-type) as the dominant Al-Mg mineral in the DTMF and show an association of As and Ni with the HTLC phase suggesting HTLCs may play a role in the geochemical control of EOCs in the DTMF in addition to ferrihydrite. To date, secondary Al and Mg minerals and their ability to sequester EOCs in U tailings has not been well characterized.

Because secondary Al and Mg minerals possess excellent adsorbent properties for the uptake of oxyanions, metalloids, and metal cations (e.g., amorphous $Al(OH)_3$ and HTLCs) (Das et al., 2002; Douglas et al., 2012, 2010; Frost et al., 2005; Goh et al., 2008; Goldberg, 2013; Goldberg and Johnston, 2001; Kappen and Webb, 2013; Lazaridis et al., 2002), detailed knowledge on the secondary Al and Mg minerals formed during bulk neutralization and their ability to sequester EOCs in U tailings is needed. Thus, the objectives of this study were to: (1) define the secondary Al and Mg minerals that precipitate during bulk neutralization of U mill raffinate and their mineralogical control(s) on As, Se, Mo, and Ni and (2) quantify the geochemical controls exerted by the Al and Mg minerals with respect to the sequestration of As(V), Se(IV), and Mo(VI). Objective (1) was attained using synthetic raffinate of varying compositions in a validated continuous flow lab-scale model of the KL process (Robertson et al., 2014). The mineralogy of the Se-Mo and Lamella underflow solids and their final mixed form from the lab-model were studied using XRD, Al K-edge X-ray absorption spectroscopy (XAS), and transmission electron microscopy (TEM) elemental mapping. Objective (2) was attained using batch adsorption experiments with samples from the lab-scale model. The results of this study serve to update the geochemical model of the secondary mineralogy in tailings generated at the KL U mill. These results are of value to all U mills that use an acid leaching process coupled with bulk neutralization of effluent as well as other mills that use a neutralized acid leach circuit.

4.3 Materials and Methods

4.3.1 Synthetic Raffinate Neutralization Experiments

Neutralization experiments were performed using a synthetic raffinate neutralization system (SRNS; Figure 4.1) that is a pilot-scale model of the KL bulk neutralization process. The construction, operation, and validity of the SRNS as a model of the KL process is described

elsewhere (Robertson et al., 2014). Minor modifications were made to better approximate the KL process, including: (1) increasing the pH of Pachuca 2 (P2) and the Se-Mo thickener from 3.5 to 4.0 to better reflect recent operating conditions; (2) adding a polyacrylamide flocculant (0.01 % w/w solution pumped continuously into the Se-Mo thickener inlet at 0.2 mL/min) used in the KL mill to minimize the overflow of colloidal nanoparticles to P3 resulting from the increased pH; and (3) before preparing the final combined slurry, raising the pH of the Se-Mo underflow slurry to 7.0 using 2.5 M lime before mixing with the Lamella underflow slurry.

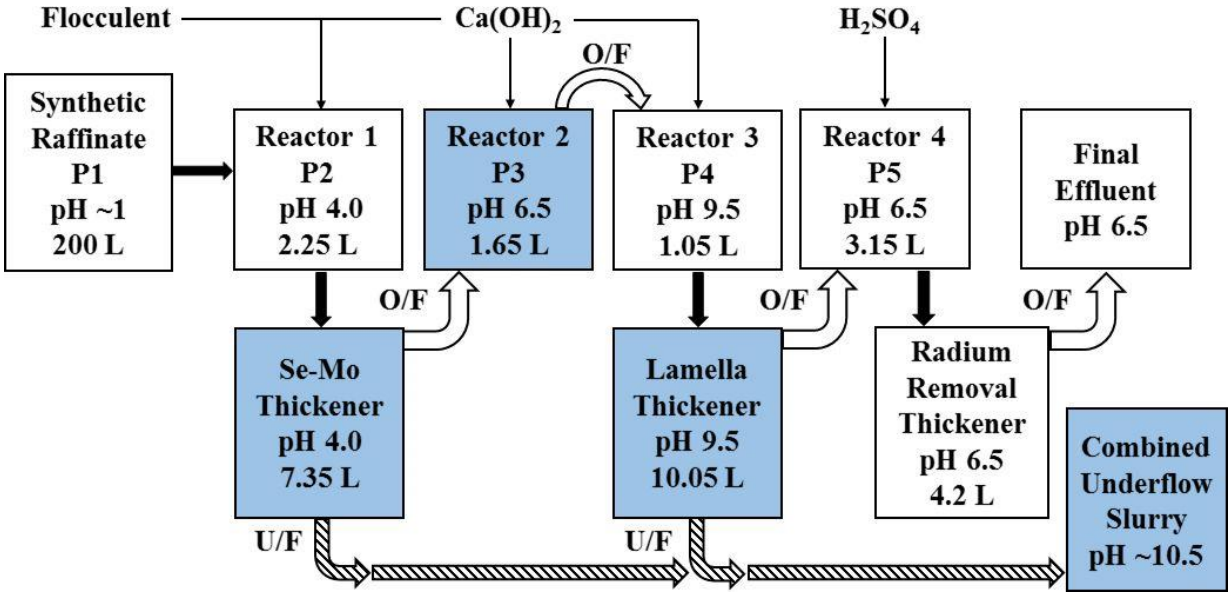

Figure 4.1. Block flow diagram of the synthetic raffinate neutralization system. Solid arrows indicate pumped flow, open arrows indicate gravity flow, line arrows indicate pumped Ca(OH)2, and hatched arrows indicate manual flow by valves. Coloured blocks indicate locations of solid and aqueous sampling points, while white blocks indicate aqueous sampling only. Overflow and underflow of thickeners are indicated by O/F and U/F, respectively.

Four neutralization experiments using synthetic raffinate of varying composition (Table 4.1) were performed using the SRNS. The R1 raffinate was composed of only Al, Mg, and S to determine the Al and Mg minerals that precipitate in an Fe-free system; R2 had Fe added to determine the effect of Fe on Al and Mg minerals. R3 and R4 were the same as R1 and R2, respectively, but with the addition of the EOCs (As, Mo, Se, Ni) to compare their removal in the presence and absence of ferrihydrite (a known EOC control in the KL bulk neutralization process). Elemental concentrations of Al, Mg, S, and Fe were based on measured KL mill raffinate concentrations (Gomez et al., 2013a). EOC concentrations wehre spiked to ~10-75× those reported in the KL raffinate (Gomez et al., 2013a) to aid in EOC mineral phase identification. Each synthetic

raffinate was prepared as outlined by Robertson et al. (2014). The reagents used to create the synthetic raffinate were As_2O_5, $Na_2MoO_4 \cdot 2H_2O$, Na_2SeO_3, $NiSO_4 \cdot 6H_2O$, $Al_2(SO_4)_3 \cdot 16H_2O$, $MgSO_4 \cdot 7H_2O$, and $Fe_2(SO_4)_3 \cdot 5H_2O$ (all ACS grade from commercial suppliers). Sulfate-based reagents were used to simulate the high SO_4^{2-} concentrations observed in U mill raffinates (Liu and Hendry, 2011; Moldovan and Hendry, 2005; Schindler et al., 2013). The pH of the synthetic raffinate was maintained at 1.0±0.1 using H_2SO_4. Each experiment ran continuously for 4-5 d.

Table 4.1. Synthetic raffinate composition (mg/L) for experiments R1-R4 measured by ICP-MS (S by ICP-OES) and the Key Lake raffinate composition from Gomez et al. (2013a) used as a baseline.

Experiment	Mg	Al	S	Fe	Ni	As	Se	Mo
R1	1109	1659	12381	--	--	--	--	--
R2	1068	1609	12932	1267	--	--	--	--
R3	984	1605	13043	--	261	341	45.7	141
R4	1164	1925	13372	1303	217	307	33.6	94.5
Key Lake	1044	1635	13351[a]	1428	23.3	27.8	0.4	3.14

[a]Sulfur concentrations were not measured by Gomez et al. (2013a) but were given as SO_4^{2-} concentrations by Liu and Hendry (2011). Their value has been converted to S and presented in the table for comparison.

4.3.2 Sample Collection and Treatment

Aqueous samples were collected from each process point every 12 h using 50 mL plastic syringes and immediately transferred to 50 mL polypropylene centrifuge tubes and stored at 4 °C. The underflow slurries were collected from the Se-Mo and Lamella thickeners at the end of the neutralization experiment (after 4-5 d). The Se-Mo and Lamella underflow slurries were combined at a 1:1 volumetric ratio and raised to a pH of 10.50±0.25 using 2.5 M lime. This final slurry was designated as the Combined underflow slurry and represented the secondary mineral phases deposited in the DTMF. Samples of the Se-Mo, Lamella, and Combined slurries were collected in 50 mL polypropylene centrifuge tubes. Precipitates from the P3 reactor were also collected for XAS studies. All samples were centrifuged at 2900 g for 20 min. Supernatants were decanted and filtered using 0.45 µm cellulose filters and subsequently acidified using 0.5 mL 2% HNO_3. Solids were dried at room temperature and finely ground using an agate mortar and pestle. Subsets of the solid samples were washed three times with Millipore water (18 MΩ·cm) to remove gypsum prior to XRD and TEM analyses (Robertson et al., 2014).

4.3.3 Batch EOC Adsorption Experiments

Dried solid samples collected from the Lamella thickener (pH 9.5) during the R1 experiment (Al-Mg raffinate) were used as adsorbent materials in batch experiments to determine the AsO_4^{3-}, SeO_3^{2-} , and MoO_4^{2-}adsorption capacity of HTLCs produced in the SRNS. The Lamella samples were chosen for adsorbent testing instead of the final Combined solids because of the increased presence of multiple adsorbent phases in the latter (i.e., ferrihydrite, amorphous $Al(OH)_3$). Separate stock solutions containing 5 mM AsO_4^{3-}, SeO_3^{2-} , and MoO_4^{2-} were prepared to test the adsorption capacity of these individual oxyanions on the HTLCs, while a mixed solution containing 5 mM AsO_4^{3-}, SeO_3^{2-} , and MoO_4^{2-} was prepared to test oxyanion adsorption selectivity. Reagents used for the stock solutions were analytical grade $Na_2HAsO_4 \cdot 7H_2O$, $Na_2MoO_4 \cdot 2H_2O$, and Na_2SeO_3 dissolved in Millipore water. Washed and unwashed adsorbent materials were tested to account for potential EOC uptake by gypsum; all oxyanions were tested with the washed material but only AsO_4^{3-} was tested with the unwashed material due to a shortage of the adsorbent material. The adsorption experiments were conducted in duplicate using 200 mL of stock solution containing 2 g/L of solid sample in HDPE bottles that were continuously shaken at 150 rpm using an orbital shaker for the duration of testing. The pH of each solution was maintained at 9.60 (to reflect the mean pH of the DTMF, 9.62; Shaw et al., 2011) using 0.05 M $Ca(OH)_2$ beginning immediately after dosing the solution with the adsorbent and after collection of each sample. Decreases in pH (up to 0.83 pH units) were observed in some samples between sampling intervals. Approximately 1.5 mL samples were collected and filtered using plastic syringes and 0.2 μm polyethersulfone membrane filters at sample intervals of 20 min for the first 2 h. Samples were then collected 6 h and 1, 7, 14, 21, and 30 d after dosing with the adsorbent.

4.3.4 Sample Analysis

Element analysis was conducted on all aqueous and solids samples using a PerkinElmer NexION 300D inductively coupled plasma mass spectrometry (ICP-MS) instrument with a ±10% relative standard deviation, a 6.52×10^{-3} ppm aqueous phase detection limit, and a 1.52×10^{-2} ppm solid phase detection limit. All solid samples were subjected to a HF-HNO_3 digest prior to analysis (Jenner et al., 1990; Longerich et al., 1990). Total S for aqueous samples was measured using a

SpectroBLUE inductively coupled plasma optimal emission spectrometry (ICP-OES) instrument with a relative standard deviation of <5%.

Powder XRD analysis was performed on the washed solid samples using an Empyrean Pro PANalytical diffractometer equipped with a Co target (Co $K_{\alpha 1}$ wavelength = 1.7902 Å), a crystal graphite monochromator, and a scintillation detector. Powdered samples were mounted on rotating disk transmission holders and were scanned through a range of 10-80° 2θ with a 0.01° step and a scan speed of 0.02°/s. The diffractometer was operated at 40 kV and 45 mA.

Samples washed free of gypsum were analyzed at the National Institute for Nanotechnology using a JEM 2200FS transmission electron microscope at 200 kV. Element mapping was performed under scanning (STEM) mode. The solid samples were transferred in an ethanol solution onto a 300-mesh carbon-coated copper grid and were allowed to air-dry prior to being loaded into the sample chamber.

Aluminum K-edge X-ray absorption near edge spectroscopy (XANES) was performed on unwashed solid samples at the spherical grating monochromator (SGM) beamline (Regier et al., 2007) at the Canadian Light Source synchrotron (Saskatoon, Canada). Aluminum reference compounds were either synthesized or commercially produced. Basaluminite and amorphous $Al(OH)_3$ were synthesized via methods from literature (Adams and Rawajfih, 1977; Kabengi et al., 2005) and MgAlFe-hydrotalcite synthesized by Paikaray et al. (2013) was acquired by the authors. Commercial gibbsite and $Al_2(SO_4)_3$ were purchased from Sigma Aldrich. Solid samples were finely powdered using an agate mortar and pestle and pressed onto double-sided carbon tape mounted on a conductive sample holder. X-ray fluorescence (XRF) spectra were measured under high vacuum for each incident X-ray energy using a four element array of Amptek silicon drift detectors. Partial fluorescence yield (PFY) was obtained by windowing only the Al fluorescence events in each XRF spectrum. The I_o spectrum was measured simultaneously using a gold mesh on the SGM I_o ladder. The PFY spectra of Al were calibrated to the maximum of the most intense peak in the first derivative spectrum of gibbsite (1567.6 eV; Ildefonse et al., 1998). ATHENA software (Ravel and Newville, 2005) was used for normalization, principal component analysis (PCA), target transformations, and linear combination fitting (LCF) of the spectra. The PCA was undertaken to identify a minimum amount of components that could be used to accurately

reconstruct the set of samples, while target transformations were used to identify which standard compounds were potential candidates for components in the sample set.

4.4 Results and Discussion

4.4.1 Precipitation of Al and Mg Secondary Minerals

Substantial amounts of Al precipitation occurred at pH 4.0. Between 54.0-71.0% of the initial mass of Al precipitated at this stage after accounting for dilution by lime addition (Figure 4.2a; raw data in Table B.1). The Al precipitate removed from the Se-Mo thickener was a white colloidal phase with poor settling characteristics. In all experiments, more than 98.8 and 99.6% of the initial Al in the raffinate had precipitated by pH 6.5 and 9.5, respectively. All Al that precipitated at pH 6.5 and 9.5 was collected in the underflow of the Lamella thickener. In contrast to Al precipitation, minimal precipitation of Mg-bearing phases occurred at pH 4.0 (0.4-8.6%) in the Se-Mo thickener (Figure 4.2b). The majority (>95.3%) of the initial Mg precipitated in the Lamella thickener (pH 9.5). Up to 67.9-74.8% of the S (assumed to be SO_4^{2-}) precipitated in the Se-Mo solids (Figure 4.2c) as gypsum and potentially basic aluminum sulfate (see Chapter 4.4.2). Once the solution reached the Lamella thickener, the total S precipitated was between 89.0-92.3% of the initial concentration. For the two experiments containing Fe, 98.0-98.2% of the Fe in the raffinate precipitated at pH 4.0, and complete precipitation of Fe occurred at pH 6.5 (Figure 4.2d). In general, the precipitation trends of Al, Mg, S, and Fe were not constrained by the composition of the synthetic raffinate as shown by the minimal variation in precipitation trends for these elements across all experiments.

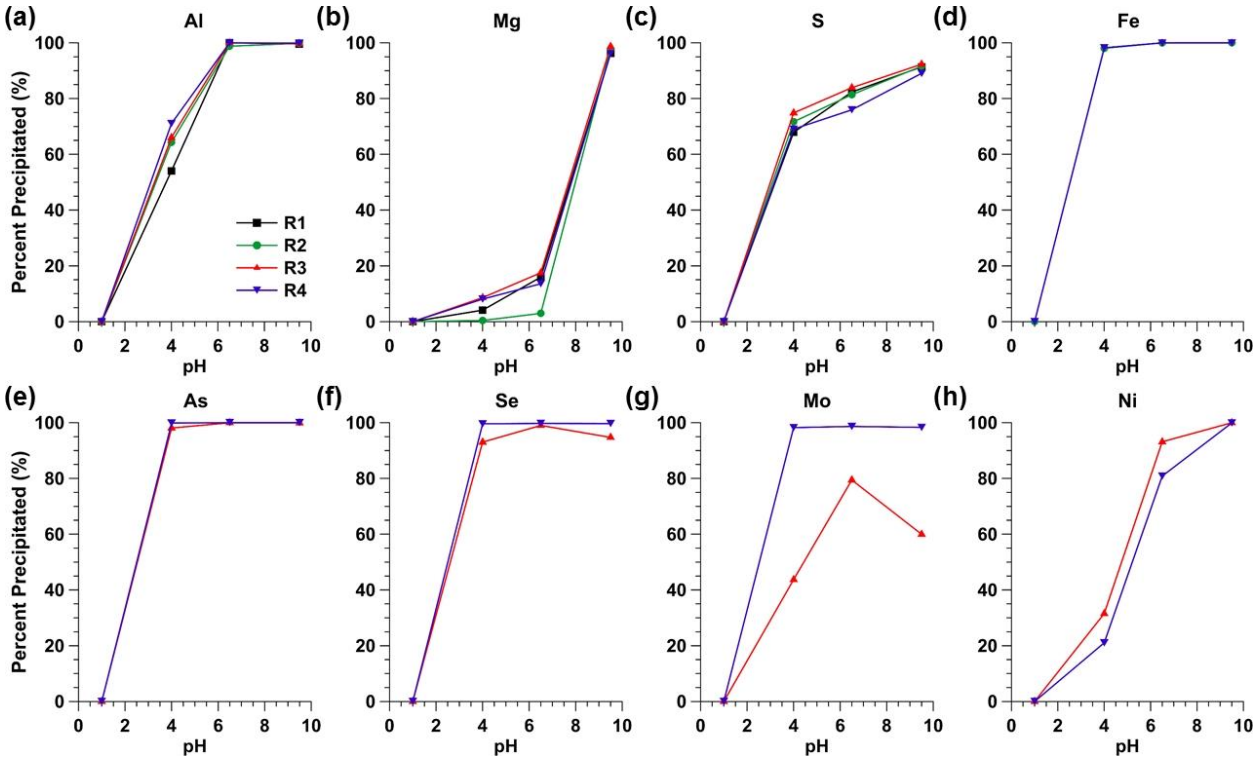

Figure 4.2. Precipitation trends of Al, Mg, S, Fe, As, Se, Mo, and Ni as a function of pH for each experiment. The percent of each element precipitated is based on the initial concentration of each element in the synthetic raffinate after being corrected for dilution by lime addition.

Calcium in the form of gypsum (XRD analyses not presented) dominated the composition of the mass of the solids in the Se-Mo thickener (pH 4.0) for all experiments (>78.1% Ca by mass; Table 4.2). The presence of gypsum indicated that S (not measured in solids) is also a dominant element in the Se-Mo thickener solids. In addition to Ca and S, Al and Fe (in R2 and R4) were dominant elements in non-gypsum minerals of the Se-Mo solids, ranging between 7.99-8.70% and 10.3-11.5% by mass, respectively.

The continued addition of lime contributed to high Ca concentrations in the Lamella solids (pH 9.5), ranging between 33.9-48.8% of the total solids mass. Magnesium was a dominant element in the Lamella solids, ranging between 26.5-37.4% of the total solids mass. Aqueous Al that did not precipitate in the Se-Mo solids precipitated in the Lamella solids, forming between 17.4-25.7% of the total solids mass. The small concentration of Fe that did not precipitate in the Se-Mo thickener was present in the Lamella solids (<1.07% in R2 and R4).

Table 4.2. Solid-phase composition of the Se-Mo, Lamella, and Combined samples (w/w%). The total elemental mass is the sum of Mg, Al, Ca, Fe, Ni, As, Se, and Mo concentrations used to calculate the weight percentages of each element relative to the other elements measured.

R1	pH	Mg	Al	Ca	Fe	Ni	As	Se	Mo	Total Elemental Mass (µg/g)
Se-Mo	4.0	0.54%	8.70%	90.7%	0.06%	0.00%	0.00%	0.00%	0.00%	238546
Lamella	9.5	31.4%	25.7%	42.7%	0.10%	0.01%	0.00%	0.00%	0.00%	250266
Combined	10.5	9.52%	9.70%	80.7%	0.06%	0.00%	0.00%	0.00%	0.00%	228753
R2										
Se-Mo	4.0	0.42%	8.25%	79.8%	11.5%	0.01%	0.00%	0.00%	0.00%	237170
Lamella	9.5	32.7%	17.4%	48.8%	1.07%	0.03%	0.00%	0.00%	0.00%	265194
Combined	10.5	13.4%	10.6%	70.4%	5.67%	0.01%	0.00%	0.00%	0.00%	265039
R3										
Se-Mo	4.0	0.42%	7.99%	89.4%	0.06%	0.12%	1.71%	0.16%	0.16%	240793
Lamella	9.5	26.5%	20.9%	45.9%	0.09%	4.89%	1.21%	0.15%	0.37%	275952
Combined	10.5	12.5%	12.6%	70.9%	0.07%	2.32%	1.26%	0.13%	0.21%	252856
R4										
Se-Mo	4.0	0.39%	8.47%	78.1%	10.3%	0.20%	1.62%	0.20%	0.78%	234347
Lamella	9.5	37.4%	21.0%	33.9%	0.98%	6.59%	0.04%	0.00%	0.02%	259959
Combined	10.5	8.32%	9.29%	73.3%	6.30%	1.49%	0.99%	0.11%	0.26%	256385

The elemental composition of the Combined underflow reflected the elemental mass distribution expected in the final tailings. In the experiments without Fe (R1 and R3), Al and Mg were similar in mass in the Combined solids (Table 4.2). With Fe present (R2 and R4), Al and Mg were also similar in mass in the Combined solids, with Fe contributing a smaller relative % mass to the overall composition. These findings suggest that Al and Mg phases are more prevalent secondary phases than Fe in the final tailings.

4.4.2 Mineralogical Characterization of the Al and Mg Precipitates

The precipitation trends (Table 4.2) indicate Al contributed most to the composition of the Se-Mo solids. X-ray diffraction of the Se-Mo solids from all experiments showed an amorphous pattern (Figure B.1). Previous XRD and geochemical modeling work (Robertson et al., 2014) points to the presence of an amorphous $Al(OH)_3$ phase in the pH 4.0 Se-Mo solids. However, amorphous $Al(OH)_3$ is not expected to precipitate until approximately pH > 5 (Nordstrom, 2011), suggesting that a different (albeit similar) mineral phase is precipitating in the Se-Mo solids. TEM and elemental mapping of the R3 Se-Mo solids (Figure 4.3) show that Al and S are positively

correlated in the amorphous solids, suggesting that the S in the Se-Mo solids played a role in Al precipitation in the form of an amorphous $AlOHSO_4$ phase. The presence of SO_4^{2-} in high concentrations has been suggested to lower the precipitation pH of Al (Bertsch and Parker, 1996); this could explain the precipitation trends of Al and S-bearing phases observed in the SRNS and KL bulk neutralization systems where SO_4^{2-} concentrations are extremely high (39 and 40 g/L in the synthetic and KL raffinates, respectively; Liu and Hendry, 2011). In SO_4^{2-}-rich systems such as these, a class of minerals called basic aluminum sulfates (hereafter referred to as $AlOHSO_4$ as a general non-stoichiometric formula) can control the activity of Al during neutralization of acid mine waters with circumneutral water (Jones et al., 2011). Nordstrom (1982) suggests that these $AlOHSO_4$ phases can exist at pH < 4.5, meaning they could precipitate at the pH range in the Se-Mo thickener. The initial mineral that typically precipitates in acidic Al-SO_4^{2-}-rich waters is hydrobasaluminite ($Al_4(SO_4)(OH)_{10}\cdot 15H_2O$), which can dehydrate to basaluminite ($Al_4(SO_4)(OH)_{10}\cdot 5H_2O$) in low humidity environments (Bigham and Nordstrom, 2000; Sánchez-España et al., 2011); however, the $AlOHSO_4$ phase is amorphous upon rapid precipitation (Adams and Rawajfih, 1977). A geochemical model of the neutralization of acidic sediments shows that basaluminite becomes saturated when the pH is increased above pH ~3.6 to 4.1 and amorphous $Al(OH)_3$ becomes saturated above pH ~4.7 (Tang et al., 2013). Along with the TEM images and amorphous XRD patterns, these studies support the conclusion that amorphous $AlOHSO_4$ (perhaps as a precursor of basaluminite), rather than pure amorphous $Al(OH)_3$, precipitates in the Se-Mo thickener that operates at ~pH 4.0 under rapid precipitation conditions.

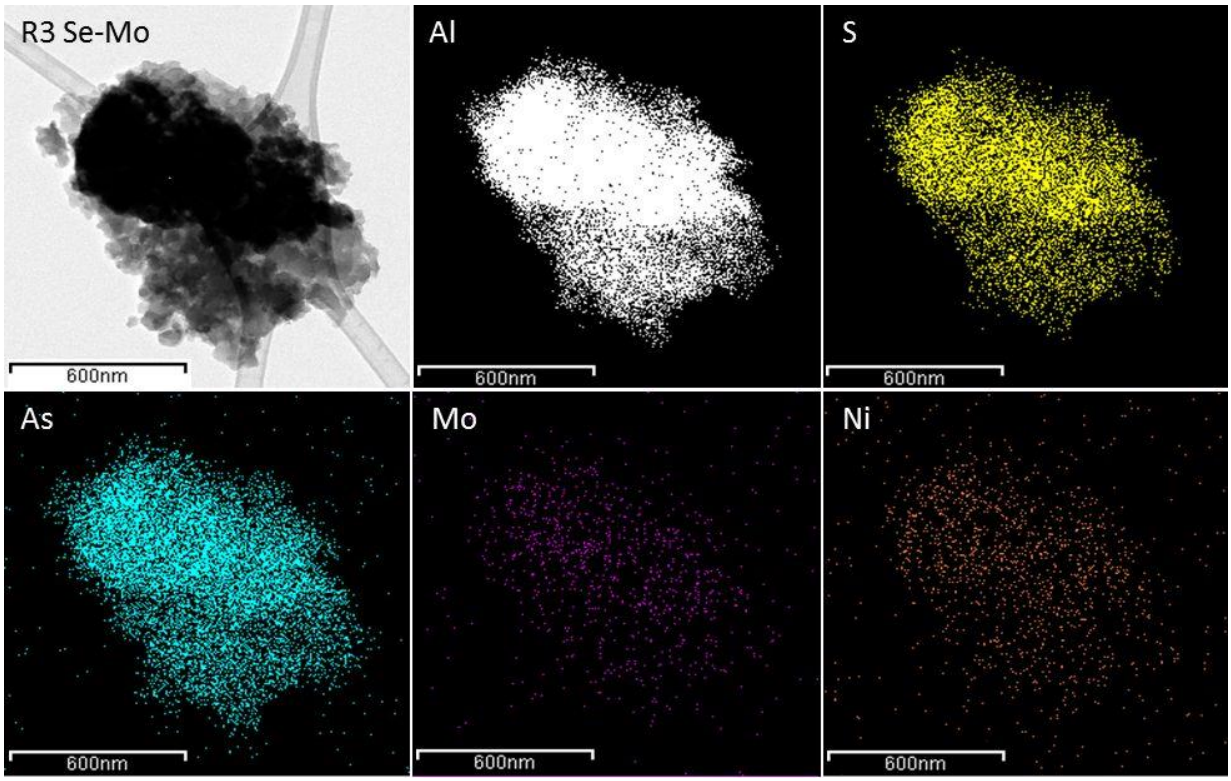

Figure 4.3. Transmission electron microscope image (top left) of a sample collected from the Se-Mo underflow solids (pH 4.0) from experiment R3 and the corresponding X-ray maps.

When Fe was introduced into the raffinate (R4), ferrihydrite was expected to precipitate because it has been identified using XAS and XRD in samples from U mill tailings in northern Saskatchewan sites (Essilfie-Dughan et al., 2013; Pichler et al., 2001). Element mapping demonstrated that a pure ferrihydrite did not precipitate. Rather, an amorphous phase containing Fe, Al, and S was observed (Figure 4.4). The aforementioned studies show ferrihydrite to exist via XAS, and the precipitate could be described as ferrihydrite-like with substituted Al and SO_4. Unfortunately the characteristic 2-line ferrihydrite diffraction pattern used to confirm the crystal structure of the precipitate could not be identified with the powder XRD technique, likely due to the substitution of Al and SO_4 distorting any short-range crystallinity. Because the presence of ferrihydrite cannot be confirmed in this study, this precipitate is referred to as an amorphous Al-$Fe(OH)_3$ phase. The presence of SO_4^{2-} in the amorphous Al-$Fe(OH)_3$ should also be noted; however, it is not clear whether SO_4^{2-} is present with multiple bonds or adsorbed. The substitution of Al^{3+} with Fe^{3+} in natural ferrihydrite during coprecipitation has been documented in multiple studies (Adra et al., 2013; Cismasu et al., 2011; Violante et al., 2009). Cismasu et al. (2012) demonstrate that the upper limit of Al substitution into ferrihydrite is approximately 20-30 mol%

Al/(Al+Fe). Using the compositions presented in Table 4.2 for R2 and R4, the Se-Mo solids contain 59.8-63.1 mol% Al/(Al+Fe). These values suggest an Al concentration in excess of Al solubility/substitution in ferrihydrite. The remaining Al that did not precipitate as Al-$Fe(OH)_3$ likely precipitated as amorphous $AlOHSO_4$ as observed in R3. However, the element maps in Figure 4.4 show that these precipitates likely do not exist as discrete phases, but rather as an intimate mixture of amorphous Al-$Fe(OH)_3$/$AlOHSO_4$ at the nanoscale.

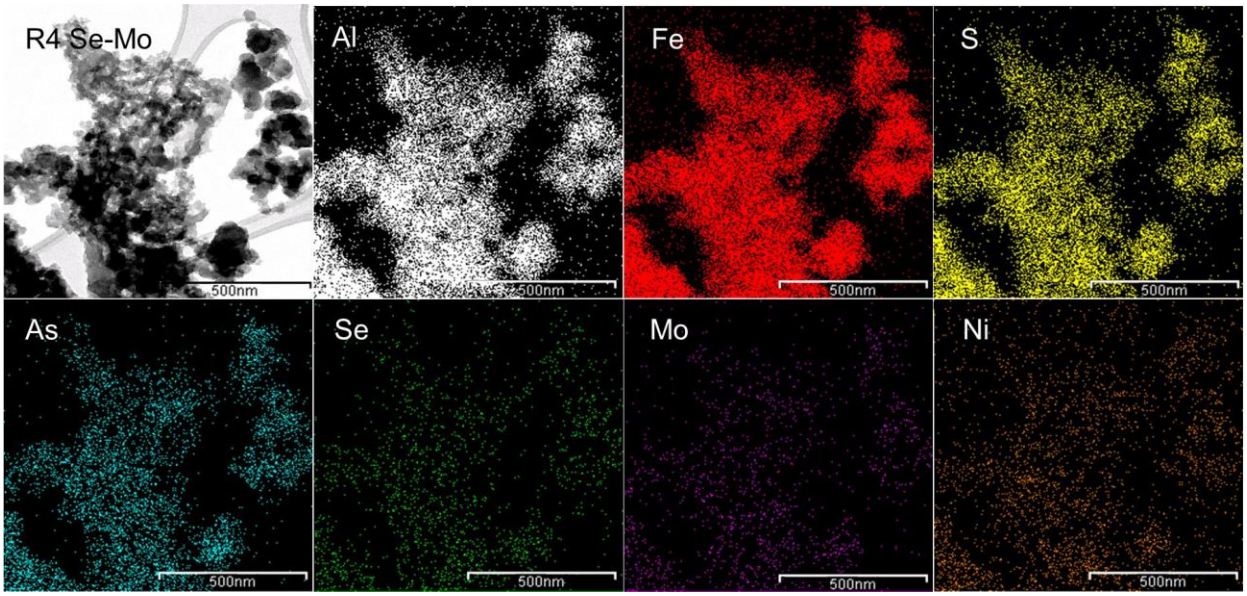

Figure 4.4. Transmission electron microscope image (top left) of a sample collected from the Se-Mo underflow solids (pH 4.0) from experiment R4 and the corresponding X-ray maps.

The Lamella solids (precipitated at pH 9.5) were composed mostly of Ca, Mg, and the remaining Al that did not precipitate in the Se-Mo thickener. There was minimal deviation in the solids composition and mineralogical characteristics between all four experiments, as the majority of the Fe in R2 and R4 precipitated in the Se-Mo thickener. X-ray diffraction data suggest the presence of a semi-crystalline HTLC (Figure B.1). The lack of crystallinity may be attributed to the rapid precipitation of the phase and lack of aging in the solids. Selected TEM images of the R3 and R4 Lamella solids (Figure 4.5 and Figure 4.6) show a porous and semi-crystalline phase similar to that observed by Gomez et al. (2013a). The elemental maps demonstrate a positive correlation between Al, Mg, and S that further supports the presence of Al-Mg-SO_4-type HTLCs observed by Gomez et al. (2013a) and Robertson et al. (2014) in the Lamella thickener and in other similar neutralization processes (Douglas et al., 2014, 2010). The aqueous Mg/Al ratio at pH 4.0

(i.e., the solution prior to neutralization to pH 9.5) ranged from 1.55 to 2.13 and the Mg/Al molar ratio of the Lamella solids ranged from 1.36 to 2.09 indicating excess Al. The generally accepted lower bound of the Mg/Al ratio in HTLCs is 2 (Evans and Slade, 2006); this indicates the Mg-Al hydrotalcite was not the only Al phase in the Lamella solids. Due to the low Mg concentration relative to Al, the general formula can be approximated with the minimum Mg/Al ratio predicted to be thermodynamically favourable for HTLCs ($Mg_2Al(SO_4)(CO_3)(OH)\cdot xH2O$). The remaining balance of Al may have precipitated as amorphous $Al(OH)_3$. Previous geochemical models support the presence of both hydrotalcite and amorphous $Al(OH)_3$ at pH 9.5 (Gomez et al., 2013a).

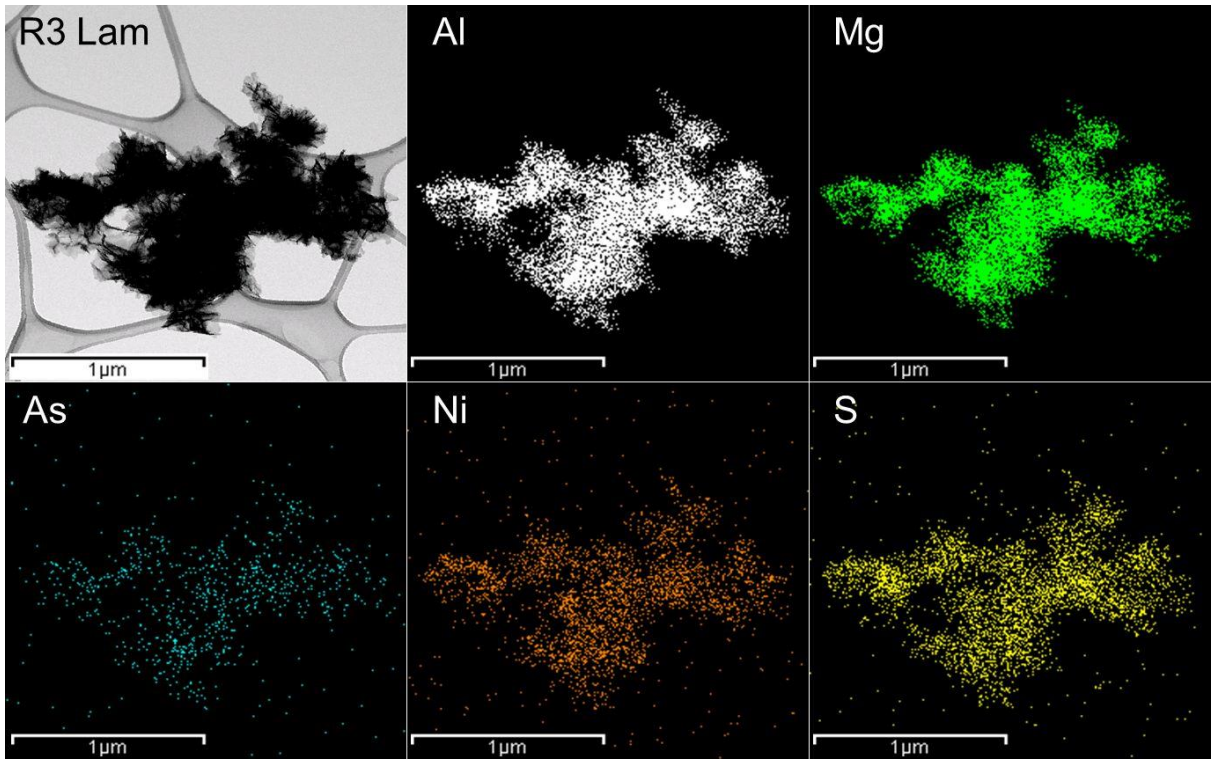

Figure 4.5. Transmission electron microscope image (top left) of a sample collected from the Lamella underflow solids (pH 9.5) from experiment R3 and the corresponding X-ray maps.

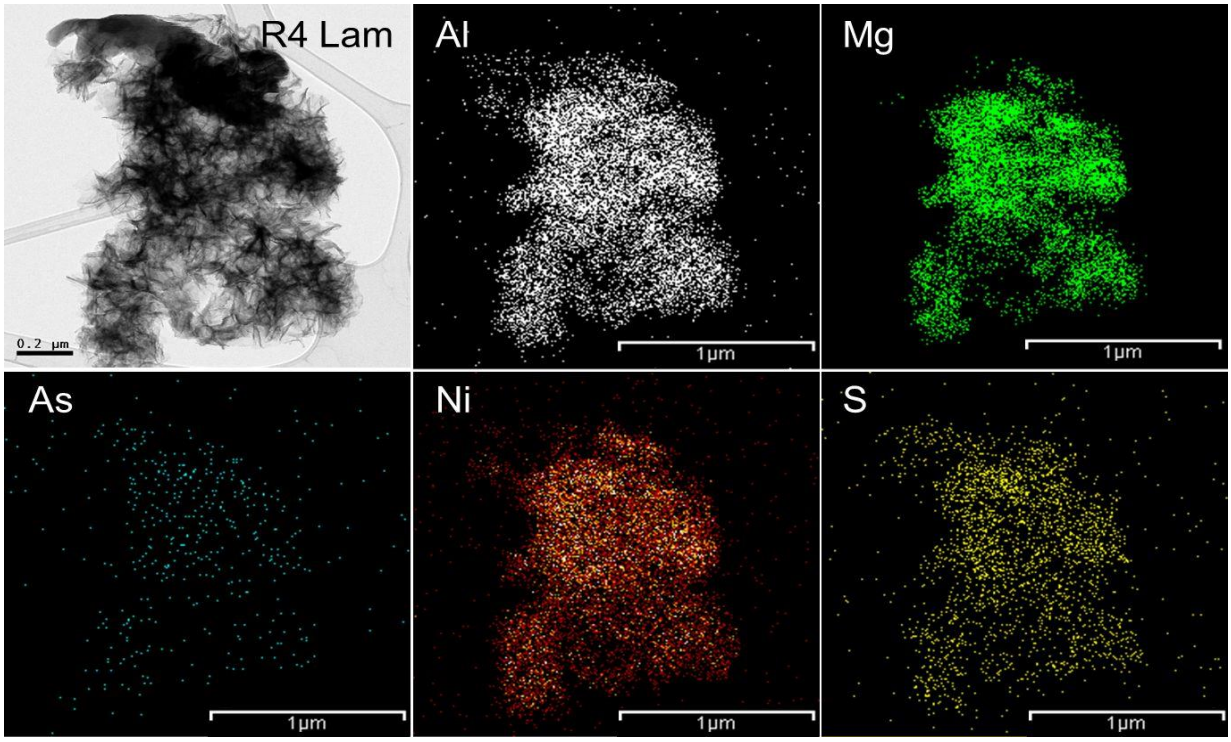

Figure 4.6. Transmission electron microscope image (top left) of a sample collected from the Lamella underflow solids (pH 9.5) from experiment R4 and the corresponding X-ray maps.

The Combined solid samples (pH 10.5), which represent the secondary minerals discharged into the DTMF, possess characteristics of the constituent Se-Mo and Lamella solids. X-ray diffractograms show a hydrotalcite pattern that is lower in intensity with respect to the Lamella solids (Figure B.1), which is attributed to dilution resulting from the addition of the amorphous phases contained in the Se-Mo solids. The sharp peaks in the XRD patterns of the Combined solids are attributed to calcite precipitation as a result of lime addition (to increase the pH to 10.5) and dissolution of atmospheric CO_2. The TEM images of the R3 and R4 Combined samples (Figure 4.7 and Figure 4.8) clearly show the presence of the porous hydrotalcite phase observed in the Lamella solids. Element maps of R3 show a strong association between Al, Mg, and S, as was the case for the Lamella solids. While the hydrotalcite phase is evident, there was no evidence of a discrete amorphous $AlOHSO_4$ phase as would be expected to carryover from the Se-Mo solids. Geochemical modeling of basaluminite and jurbanite ($AlOHSO_4$) indicated that $AlOHSO_4$-type phases are undersaturated above pH 7.5 (Douglas et al., 2012), suggesting that the amorphous $AlOHSO_4$ from the Se-Mo solids transforms or dissolves and re-precipitates as amorphous $Al(OH)_3$ and/or hydrotalcite when the pH is raised to 10.5.Conversely, the images of the R4 solids

clearly show the presence of an amorphous Al-Fe(OH)$_3$ phase amongst the hydrotalcite, indicating Mg-Al hydrotalcite and Al-Fe(OH)$_3$ co-exist in the final tailings.

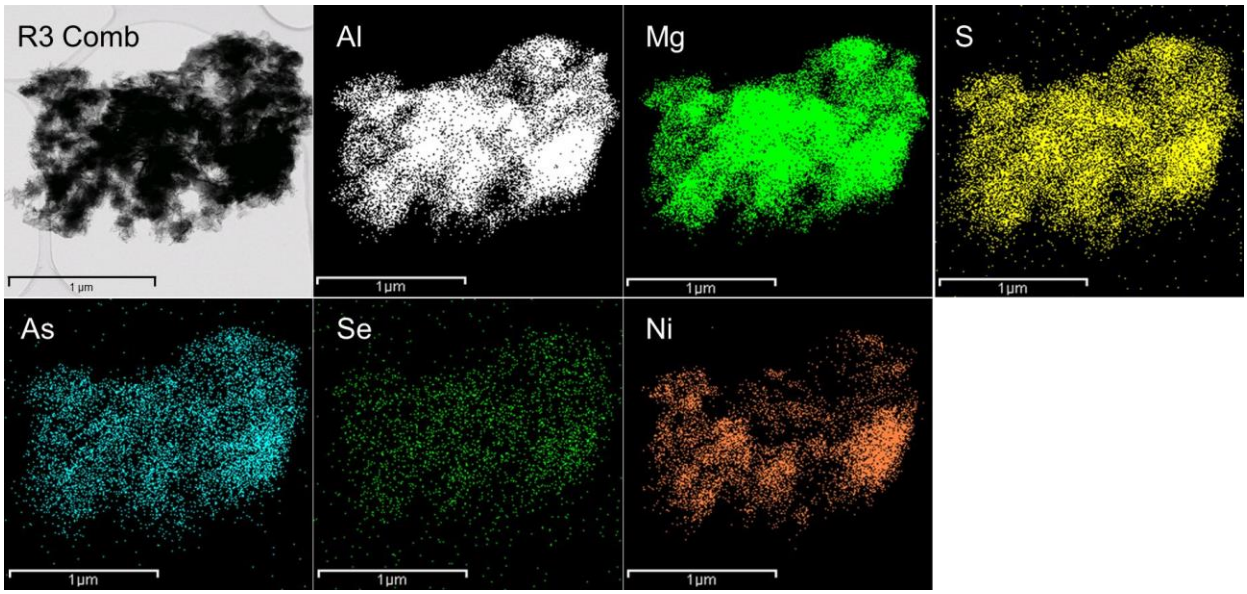

Figure 4.7. Transmission electron microscope image (top left) of a sample collected from the Combined underflow solids (pH 10.5) from experiment R3 and the corresponding X-ray maps.

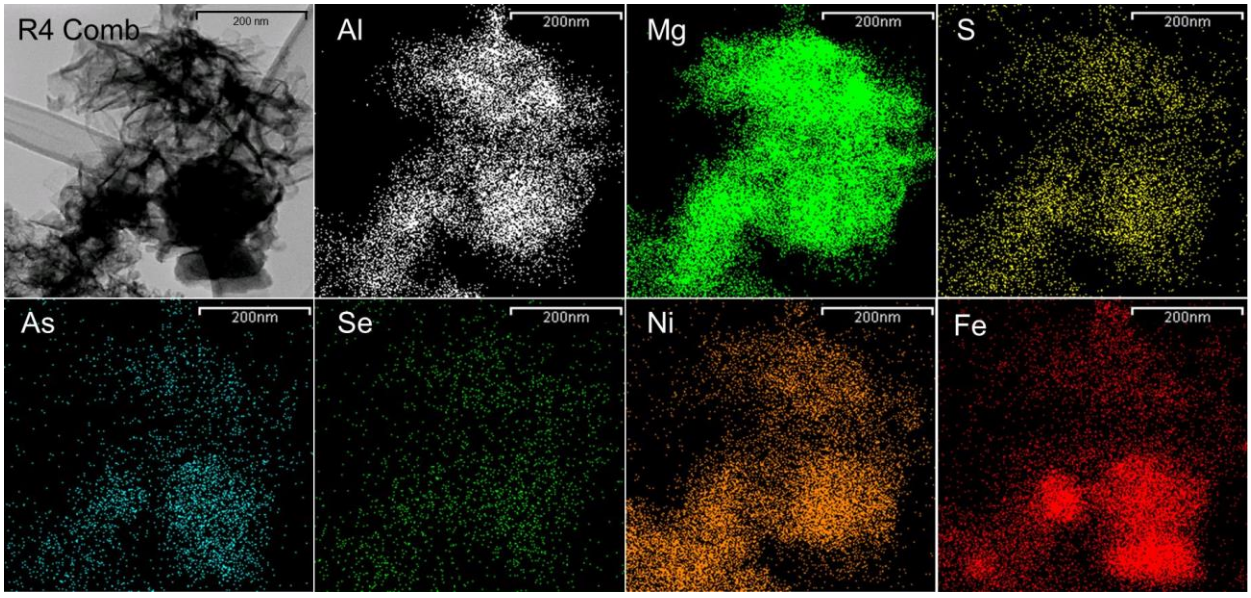

Figure 4.8. Transmission electron microscope image (top left) of a sample collected from the Combined underflow solids (pH 10.5) from experiment R4 and the corresponding X-ray maps.

4.4.3 X-Ray Absorption Spectroscopy

Aluminum K-edge XAS experiments were performed on all solid samples. Overall, the progression in the spectra for the Se-Mo, P3, Lamella, and Combined solids were consistent for each experiment (R1-R4). Representative spectra (R3) and relevant standard compounds are presented in Figure 4.9 (R1, R2, and R4 in Figure B.2). In all spectra, Al exhibits a six-fold coordination geometry, identified by the two main peaks at approximately 1567 and 1572 eV, as opposed to four-fold coordination geometry, identified by lower edge energies (Doyle et al., 1999; Ildefonse et al., 1998). Linear combination fitting (LCF) was performed with model compounds identified as components of the sample by PCA and target transformations (Figure B.3 and Figure B.4). Principal component analysis showed all samples could be reconstructed using three major components. Target transformations were performed to identify which standard compounds were most likely in the set of the three major components (Table B.2). Based on the statistics calculated by the target transformation and prior knowledge of the mineralogical characteristics of the sample determined by XRD, basaluminite, amorphous $Al(OH)_3$, and MgAlFe-type hydrotalcite standards were chosen as the three major components to use for LCF. A summary of LCF results of the Al K-edge XANES data is presented in Table 4.3. Basaluminite was used as the analogue for the $AlOHSO_4$ mineral phase due to their similar stoichiometry. Notably, the residuals for samples containing elevated fractions of basaluminite were larger than desired. This may be attributed to basaluminite not being a perfect analogue for the $AlOHSO_4$ and/or the $AlOHSO_4$ being too complex to precisely model with one standard compound. Nonetheless, the fits show a consistent trend with respect to the evolution of Al minerals throughout neutralization. In the Se-Mo solids (pH 4.0), Al was primarily in the form of $AlOHSO_4$ (>98% in all experiments). The balance of the Se-Mo solids was comprised of amorphous $Al(OH)_3$. The Al that did not precipitate in the Se-Mo thickener precipitated in the P3 reactor (pH 6.5). Spectra of samples taken from P3 exhibit a shift towards increased amorphous $Al(OH)_3$ precipitation, although $AlOHSO_4$ remained the major mineral (with the exception of R3 which contained elevated hydrotalcite, although the reason for this is unclear beyond a small sample size). In the neutralization process, the P3 solids were not removed from the circuit but instead overflowed into P4 (pH 9.5) before overflowing to the Lamella thickener. The LCF results for the Lamella solids indicate a dominant hydrotalcite mineral phase (compositional fraction of 0.63-0.70) in all experiments. Amorphous $Al(OH)_3$ and $AlOHSO_4$ were present in the Lamella solids but in lesser proportions than hydrotalcite (between

0.19-0.33 and 0-0.11, respectively). Nearly all Al precipitated at P3, suggesting that upon the pH adjustment in P4, most of the $Al(OH)_3$/$AlOHSO_4$ that precipitated at P3 either re-dissolved and precipitated as hydrotalcite or transformed in solution to hydrotalcite as Mg precipitated (Susanta Paikaray et al., 2014). In the Combined solids, the fraction of $AlOHSO_4$ decreased disproportionally with the amount of Se-Mo solids mixed with Lamella solids, while the fraction of amorphous $Al(OH)_3$ increased. If no phase transformations with respect to the increasing pH occurred, the proportions of phases calculated by LCF of a 1:1 mixture of Se-Mo:Lamella solids should not change. The Combined solids did not reflect these proportions, which suggests that the majority of the $AlOHSO_4$ re-dissolved and/or transformed to hydrotalcite and amorphous $Al(OH)_3$ upon mixing and treating the tailings to the terminal pH of 10.5; this is supported by a previous geochemical model at pH 10.5 (Douglas et al., 2010; Gomez et al., 2013a). These data suggest that the secondary Al in the final tailings was dominated by Mg-Al hydrotalcite (0.57-0.61), with amorphous $Al(OH)_3$ making up the balance (0.26-0.43).

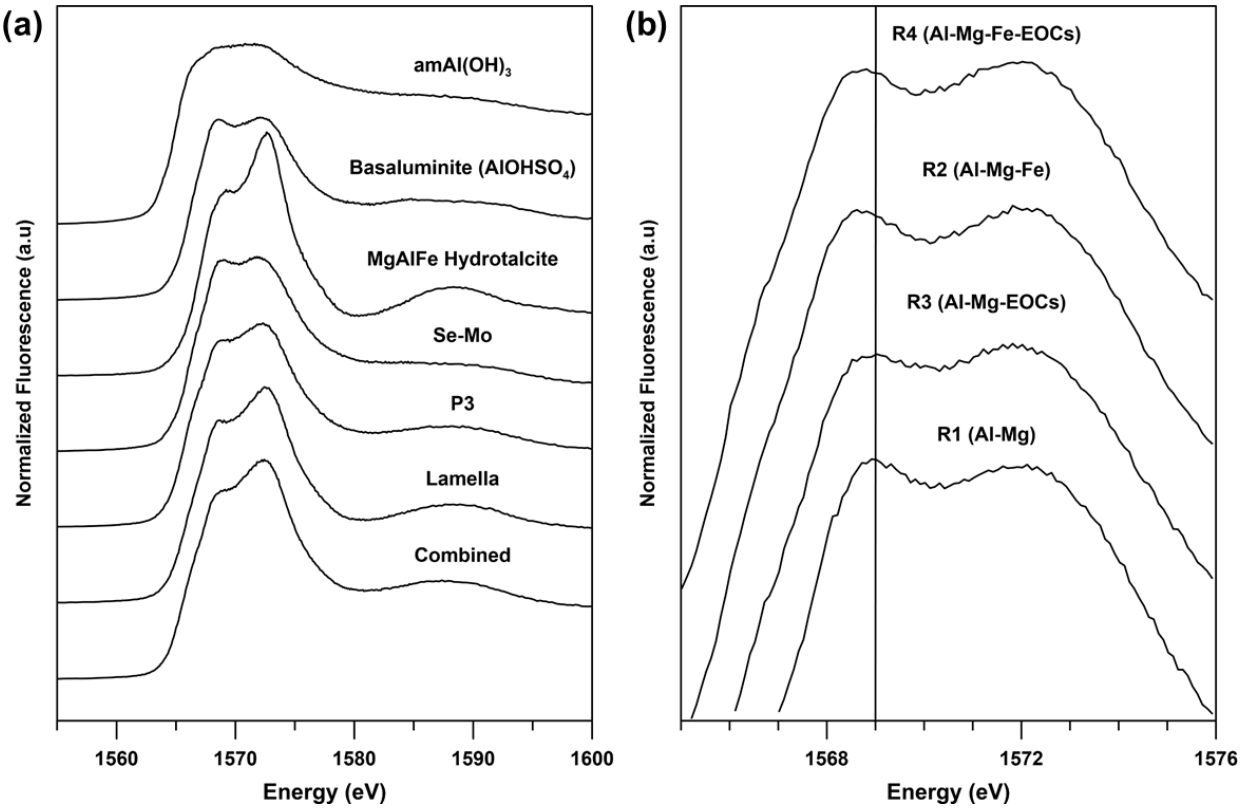

Figure 4.9. X-ray absorption near-edge structure of (a) the R3 solids samples and select standard samples and (b) the Se-Mo solids (pH 4.0) for all experiments to show the shift in energy of the first peak between Fe and non-Fe containing samples.

Table 4.3. Summary of linear combination fitting of Al XANES spectra for all experiments, expressed as a fractional amount ± the estimated standard deviation as calculated by ATHENA.

Sample		Basaluminite	amAl(OH)3	Hydrotalcite	Residual[a] (×10^3)
R1	**SeMo**	1.00 (± 0.00)	0	0	505
	P3	0.60 (± 0.09)	0.40 (± 0.01)	0	1.64
	Lamella	0.02 (± 0.02)	0.33 (± 0.01)	0.65 (± 0.03)	43.5
	Combined	0.13 (± 0.02)	0.26 (± 0.01)	0.61 (± 0.02)	18.9
R2	**SeMo**	0.99 (± 0.01)	0.01 (± 0.01)	0	150
	P3	0.56 (± 0.03)	0.44 (± 0.01)	0	87.6
	Lamella	0	0.31 (± 0.01)	0.69 (± 0.02)	3.63
	Combined	0.09 (±0.02)	0.32 (± 0.01)	0.59 (± 0.02)	1.52
R3	**SeMo**	0.99 (± 0.02)	0.01 (± 0.02)	0	226
	P3	0.18 (± 0.02)	0.40 (± 0.01)	0.42 (± 0.03)	52.0
	Lamella	0.08 (± 0.02)	0.29 (± 0.01)	0.63 (± 0.02)	2.05
	Combined	0	0.43 (± 0.02)	0.57 (± 0.04)	167
R4	**SeMo**	0.98 (± 0.01)	0.02 (± 0.01)	0	52.6
	P3	0.70 (± 0.01)	0.30 (± 0.01)	0	8.99
	Lamella	0.11 (± 0.01)	0.19 (± 0.01)	0.70 (± 0.02)	4.50
	Combined	0.04 (± 0.02)	0.35 (± 0.01)	0.61 (± 0.03)	10.0

[a]Residual calculated as Σ(Iobs - Icalc)2/N, where Iobs = observed normalized intensity, Icalc = calculated normalized intensity, and N = number of data points.

A minor difference was observed in the spectra of the Se-Mo solids for samples containing Fe versus not containing Fe, as shown in Figure 4.9b. The first peak of the Fe-containing Se-Mo solids (R2 and R4) was shifted down to 1568.8 eV compared to the first peak of the Fe-free Se-Mo solids located at 1569.0 eV. This same effect was observed by Cismasu et al. (2012), where the increased presence of Al-ferrihydrite shifted the first peak progressively downwards to 1568.8 eV for a 30% substituted Al-ferrihydrite. This further supports the hypothesis of the presence of Al-Fe(OH)$_3$ in the samples, as a shift to lower energy was only observed for the Fe-containing samples.

4.4.4 Al and Mg Geochemical Controls on Elements of Concern

The majority of As, Se, and Mo precipitation occurred in the Se-Mo thickener (pH 4.0), where greater than 98.5% of As, Se, and Mo precipitated in experiment R4 (Figure 4.2e-g). Similar observations are reported for the KL bulk neutralization process by Gomez et al. (2013a). Although ferrihydrite controls the aqueous concentrations of these elements around pH 4.0 (Essilfie-Dughan

et al., 2013, 2011b; Moldovan et al., 2003), the ferrihydrite that precipitated in the SRNS and, by analogy, in the KL process, was Al-ferrihydrite. Element maps of Al, Fe, S and EOCs (Figure 4.4) show consistent spatial correlations between EOCs and Al-$Fe(OH)_3$; this suggests that Al-$Fe(OH)_3$, rather than pure ferrihydrite, is the major geochemical control on aqueous As, Se, and Mo. This observation is emphasized by the fact that concentrations of As, Se, and Mo decreased by >98.5% at pH 4.0 compared to the initial raffinate; this is despite EOC concentrations in the SRNS raffinate being spiked well above those measured in the KL raffinate.

Element maps of the solid samples collected from the Se-Mo thickener (pH 4.0) in experiment R3 (Figure 4.3) show a strong correlation between the $AlOHSO_4$ phase and As, Mo, and Ni (Se data not collected). The density of As on $AlOHSO_4$ was especially high, which suggests this phase could also be an As control at low pH in the absence of Al-$Fe(OH)_3$. Although a considerable mass of As and Se precipitated in the Se-Mo thickener (pH 4.0) (98.5% As and 94.4% Se) in experiment R3 (i.e., in the absence of Al-$Fe(OH)_3$), the sequestering ability of the $AlOHSO_4$ is slightly less than that of the Al-$Fe(OH)_3$. The sequestration of Mo by $AlOHSO_4$ in the Se-Mo thickener (pH 4.0) (54.5%) was considerably less than for Al-$Fe(OH)_3$.

The precipitation trends of Ni-bearing phases in experiments R3 and R4 (Figure 4.2h) show that the removal of Ni increases in the absence of Fe (31.5% and 21.0% Ni removed at pH 4.0 for R3 and R4, respectively). Previous studies suggest that Ni sequestration in lime neutralized U tailings is controlled by $Ni(OH)_2$ and $NiMoO_4$ precipitation and adsorption to ferrihydrite (Donahue et al., 2000; Essilfie-Dughan et al., 2012, 2011b; Mahoney et al., 2007). The previous mineralogical characterization suggests Ni adsorption by amorphous $AlOHSO_4$ (R3) and Al-$Fe(OH)_3$ (R4). This observation is supported by element maps for Ni (Figure 4.3 and Figure 4.4). Once neutralized to pH 6.5, Ni precipitation increased from 31.5 to 93.1% in R3 and from 21.0 to 80.8% in R4. Complete precipitation of Ni (> 99.9%) occurred in both experiments once the pH was raised to 9.5. These data show that the majority of Ni precipitated in the Lamella solids (pH 9.5) regardless of Fe content. The observation that Ni sequestration is greater in R3 for all sampling points than in R4 indicates that the amorphous $Al(OH)_3$/$AlOHSO_4$ could be a stronger Ni control than the Al-$Fe(OH)_3$. The elemental maps of the R3 Lamella solids (pH 9.5) (Figure 4.5) show a strong spatial correlation between Ni and Mg-Al hydrotalcite. Mixed metal layered double hydroxides (such as Ni-Al hydrotalcite) are more thermodynamically favourable and stable

compared to their corresponding metal hydroxide phases (d'Espinose de la Caillerie et al., 1995; Peltier et al., 2006; Scheidegger et al., 1997), suggesting Ni is more likely to exist in a hydrotalcite phase rather than a pure $Ni(OH)_2$ in the tailings. The mechanism of Ni uptake (either through Mg-Al hydrotalcite adsorption or a mixed-phase Ni/Mg-Al hydrotalcite) is the focus of an ongoing study.

Element maps of As, Se, and Ni (Mo data was not collected) in the Combined sample for experiment R3 (pH 10.5) (Figure 4.6) show that these elements are associated with the Al-Mg phases identified as a mixture of amorphous $Al(OH)_3$ and Mg-Al hydrotalcite (via XAS). Arsenic and Se are homogeneously distributed throughout the Al-Mg phase in the sample, while Ni appears to be localized to certain areas. This observation could be explained by selective association of Ni to Mg-Al hydrotalcite as observed in the Lamella solids, rather than adsorption to amorphous $Al(OH)_3$; further spectroscopic data are needed to support this conclusion. The element maps of As, Se, and Ni (Mo not scanned) in the Combined sample for experiment R4 (pH 10.5) show that As and Se appears to be primarily associated with the Al-$Fe(OH)_3$ (see the bottom right corner of Figure 4.8) and secondarily with the hydrotalcite. As was the case in experiment R3, Ni is primarily associated with Mg-Al hydrotalcite; a less pronounced association is observed with respect to Al-$Fe(OH)_3$.

4.4.5 Sequestration of EOCs by SRNS-Generated Hydrotalcite

Hydrotalcite-like compounds have been studied extensively due to their ability to sequester trace metals, metalloids, and oxyanions through both surface adsorption and interlayer substitution (Li and Duan, 2006). As such, quantifying the ability of the SRNS-generated hydrotalcite to sequester EOCs was of interest to those studying hydrometallurgical waste solution neutralization. Results of batch AsO_4^{3-}, SeO_3^{2-} , and MoO_4^{2-} adsorption experiments performed on hydrotalcite from the Lamella thickener (pH 9.5) at a target pH of 9.6 show that the hydrotalcite sequesters EOCs to varying degrees. Amorphous $Al(OH)_3$, which was also determined to be present in these solids using LCF, was not considered. Results of experiments conducted to determine the maximum adsorption capacities of AsO_4^{3-}, SeO_3^{2-} , and MoO_4^{2-} on hydrotalcite are presented in Figure 4.10a. In all three cases, the EOCs attained a pseudo-equilibrium concentration after approximately 6 h, yielding adsorption capacities of AsO_4^{3-} (0.79 mmol/g) > SeO_3^{2-} (0.56 mmol/g)

> MoO_4^{2-} (0.35 mmol/g) at 24 h. Beyond the 7 d sampling point, the measured adsorption capacity for AsO_4^{3-} and SeO_3^{2-} increased slightly from that measured at 24 h to values of 0.91 and 0.62 mmol/g, respectively, after which concentrations remained constant for the remainder of the 30 d test period. The adsorption capacity of MoO_4^{2-} beyond 7 d was nearly double that at 24 h, attaining a final value of 0.67 mmol/g at 30 d. This resulted in a final equilibrium adsorption trend of AsO_4^{3-} > MoO_4^{2-} > SeO_3^{2-}. No apparent desorption of the EOCs was observed under the conditions and time frame tested.

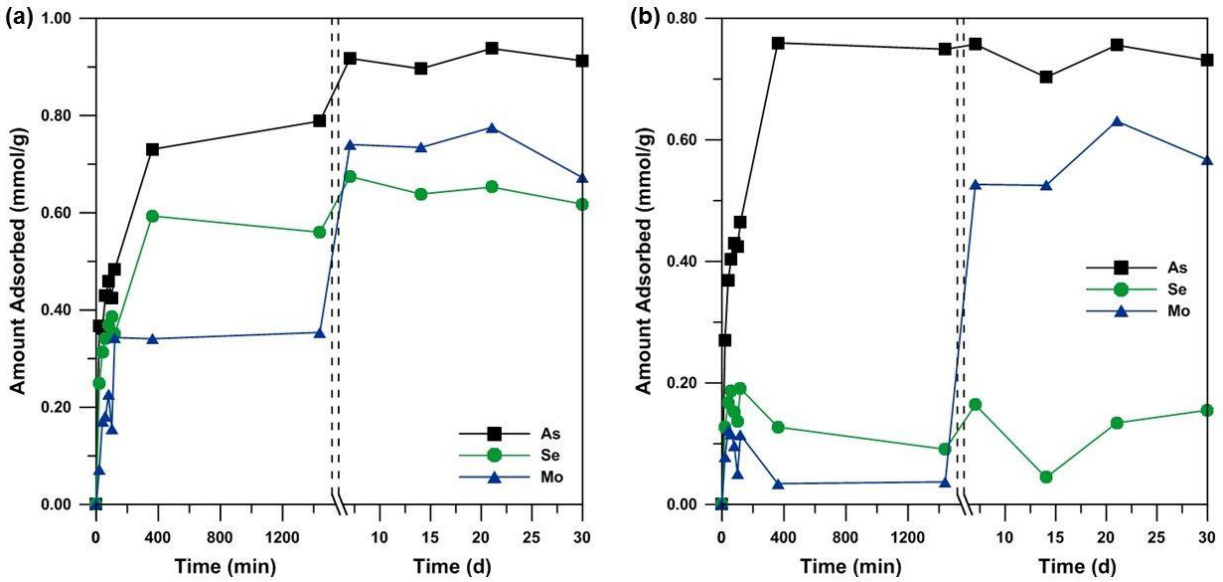

Figure 4.10. Adsorption experiments over 30 d at pH ≈ 9.60 of 5 mM As(V), Se(IV), and Mo(VI) with 2 g/L SRNS-generated hydrotalcite collected from the Lamella thickener. Note the break in time units between 1440 min and 7 d.

Comparisons of the adsorption capacities for hydrotalcite produced in the SRNS were compared to literature values for ferrihydrite (Table 4.4). These comparisons show that the hydrotalcite possesses an adsorption capacity for AsO_4^{3-} on the same order of magnitude as ferrihydrite, and adsorption capacities for SeO_3^{2-} and MoO_4^{2-} at least 10× greater than ferrihydrite. The increased adsorption capacity for SeO_3^{2-} and MoO_4^{2-} with hydrotalcite could be a result of the initial EOC concentrations being 10-12.5× greater than the studies referenced in Table 4.4; such high values were purposefully used to determine the maximum loading capacity.

Table 4.4. Comparison of element of concern (EOC) adsorption capacities of Mg-Al hydrotalcite (present study) versus ferrihydrite (literature).

Adsorbate	Adsorbent	pH	Initial Concentration (mmol EOC/g)	Adsorption Capacity (mmol EOC/g)	Reference
As(V)	**Hydrotalcite**	**9.37**	**2.5**	**0.91**	**Present Study**
	Ferrihydrite	9.2	13.3	1.10	(Raven et al., 1998)
	Ferrihydrite	9.2	0.267	0.265	(Raven et al., 1998)
	Ferrihydrite	8	1.48	1.48	(Jia and Demopoulos, 2005)
	Ferrihydrite	8	5.93	3.60	(Jia and Demopoulos, 2005)
Se(IV)	**Hydrotalcite**	**9.37**	**2.5**	**0.62**	**Present Study**
	Ferrihydrite	9.5	0.25	0.03	(Su and Suarez, 2000)
	Ferrihydrite	9.5	0.25	0.22	(Su and Suarez, 2000)
Mo(VI)	**Hydrotalcite**	**9.07**	**2.5**	**0.67**	**Present Study**
	Ferrihydrite	8.81	0.20	0.029	(Gustafsson, 2003)
	Ferrihydrite	9.76	0.20	0.010	(Gustafsson, 2003)

A second experiment was performed to test competitive adsorption of AsO_4^{3-}, SeO_3^{2-}, and MoO_4^{2-} with hydrotalcite. The general trends observed in the individual EOC tests (Figure 4.10a) were also observed in the competitive system (Figure 4.10b). Adsorption equilibrium was reached after approximately 6 h for AsO_4^{3-} and SeO_3^{2-} and, unlike the individual EOC tests, did not vary much over the 30 d test period; adsorption capacities at 30 d were 0.73 mmol/g AsO_4^{3-} and 0.16 mmol/g SeO_3^{2-}. Consistent with the individual EOC tests, MoO_4^{2-} reached a pseudo-equilibrium adsorption capacity of 0.03 mmol/g after 6 h, but dramatically increased between the 24 h and 7 d sampling interval to a final equilibrium adsorption capacity of 0.57 mmol/g. The mechanism responsible for this sudden increase in adsorption of MoO_4^{2-} after 24 h in both the individual and mixed adsorption experiments is unclear. The final adsorption trend for the competitive system showed preferential uptake in the order $AsO_4^{3-} > MoO_4^{2-} > SeO_3^{2-}$, as also observed by Paikaray et al. (2013). The adsorption capacities for each EOC in the competitive environment were lower than in the individual environments due to competition between the adsorbates in the hydrotalcite interlayer and on the surface sites and saturation of the these sites.

4.5 Conclusions

To date, minimal research has been conducted on the secondary Al and Mg mineralogy precipitated during bulk neutralization of raffinate in U milling in spite of Al and Mg being major raffinate constituents. Based on elemental mass balances of the KL U mill process, Al and Mg

minerals appear to constitute a major fraction of the minerals precipitated during the neutralization of the raffinate as identified in recent studies (Douglas et al., 2012, 2010; Gomez et al., 2013a). Prior to the current study, the geochemical model defining controls on EOCs in lime neutralized U mill tailings was dominated by ferrihydrite adsorption and poorly crystalline scorodite (Chen et al., 2009; Essilfie-Dughan et al., 2013, 2011b; Mahoney et al., 2007; Moldovan and Hendry, 2005). Based on the KL bulk neutralization process using the SRNS, an updated model is presented that includes Al and Mg minerals as complementary geochemical controls to Fe minerals from pH 1.0 to 10.5. XRD, TEM, and XAS analyses suggest four Al and Mg phases make up the bulk of the Al-Mg mineralogy in the precipitates formed during neutralization of raffinate in the KL mill: an amorphous $AlOHSO_4$ phase (with stoichiometry approaching that of hydrobasaluminite), Al-$Fe(OH)_3$, Mg-Al hydrotalcite, and amorphous $Al(OH)_3$. The amorphous $AlOHSO_4$ and Al-$Fe(OH)_3$ precipitate at pH 4.0 and form a non-discrete phase. Mg-Al hydrotalcite begins precipitating at pH $\geq$6.5 and continues to precipitate until pH 9.5. Semi-crystalline Mg-Al hydrotalcite, amorphous $Al(OH)_3$, and Al-$Fe(OH)_3$ are present in the final Combined tailings (pH 10.5).

TEM elemental mapping and analysis of the evolution of the solution chemistry show that Al-$Fe(OH)_3$ and amorphous $AlOHSO_4$ sequester As, Se, and Mo at pH 4.0. The sequestration of As and Se by amorphous $AlOHSO_4$ alone are only 1.8 and 6.6% less than in an Al-$Fe(OH)_3$/amorphous $AlOHSO_4$ system, suggesting Al minerals can also play an important role in As and Se sequestration in the absence of Al-$Fe(OH)_3$. In contrast to As and Se, sequestration of Mo at pH 4.0 is influenced by the presence of Al-$Fe(OH)_3$; 98.2% of the Mo was removed when Al-$Fe(OH)_3$ was present vs. only 43.7% when Al-$Fe(OH)_3$ was not present. Precipitation of Ni is greatest at pH 9.5; Ni is completely removed from the aqueous phase and strongly associated with Mg-Al hydrotalcite, suggesting that Ni sequestration is controlled by either adsorption or structural incorporation in Mg-Al hydrotalcite. In the final combined tailings (pH 10.5), EOCs are associated not only with Al-$Fe(OH)_3$, but also Mg-Al hydrotalcite and amorphous $Al(OH)_3$. Batch adsorption experiments of the SRNS-produced Mg-Al hydrotalcite show it can sequester AsO_4^{3-}, SeO_3^{2-}, and MoO_4^{2-}, with adsorption capacities comparable to ferrihydrite. These results show that, in addition to Al-$Fe(OH)_3$, secondary Al and Mg minerals discharged to the DTMF could play a role in EOC sequestration as the tailings geochemistry evolve in the future.

While this study defined the mineralogy for this updated model, additional testing is required. This includes, for example, defining the exact bonding nature of Al-Mg phases with As, Se, Mo, and Ni. This specifically includes quantifying the importance of EOC sequestration by Al-Mg phases in relation to the well-established controls exerted by ferrihydrite. Gaining a more thorough understanding of the secondary mineralogy of the tailings is necessary not only during the active operation of the DTMF but also long after the site has been decommissioned.

4.6 Acknowledgments

Financial support was provided by Cameco Corporation and the Natural Sciences and Engineering Research Council of Canada (NSERC) through a Senior Industrial Research Chair to MJH and NSERC's CGS-M program. The authors acknowledge the technical assistance of Jianzhong Fan, Jing Chen, and Fina Nelson with ICP-MS and -OES analysis, Tom Bonli with XRD analysis, and Mario Gomez at the University of Saskatchewan. Finally, the use of the SGM beamline at the Canadian Light Source and the support received by the SGM beamline staff (T. Regier, J. Dynes, and D. Chevrier) is gratefully acknowledged.

5.0 COORDINATION OF ARSENIC AND NICKEL TO ALUMINUM AND MAGNESIUM PHASES IN URANIUM MILL RAFFINATE PRECIPITATES

PREFACE

This chapter is reproduced with permission (license number 4106060616692) from Robertson, J., Essilfie-Dughan, J., Lin, J., Hendry, M.J., 2017. Coordination of arsenic and nickel to aluminum and magnesium phases in uranium mill raffinate precipitates. *Applied Geochemistry* 81, 12-22. doi:10.1016/j.apgeochem.2017.03.015. Minor editorial and formatting changes are made for presentation purposes in this thesis.

This chapter fulfills Objectives 2 (to determine the Al and Mg mineralogical controls of EOCs) and 3 (quantify the mineralogical control exerted by Al and Mg mineral phases on As and Ni concentrations with and without Fe mineral phases). Samples generated from SRNS experiments discussed in Chapter 4 were used for As and Ni XAS experiments. The bulk Al and Mg mineralogy that was identified in Chapter 4 provided a framework for the proposed models of As and Ni mineralogical controls discussed in the current chapter.

5.1 Abstract

The Key Lake U mill uses a stepwise neutralization process (pH 4.0, 6.5, 9.5, and 10.5) to treat raffinate (acidic, metal-rich wastewater) prior to safely releasing effluent to the environment. This process generates a complex mixture of precipitates that are deposited to a tailings facility. In this study, the coordination environments of As and Ni with respect to Al-Mg phases precipitated in the presence and absence of Fe in mill-generated and synthetic precipitates were defined using bulk X-ray absorption spectroscopy complemented with bulk X-ray diffraction. In low pH (pH 4.0-4.6) samples, As(V) precipitates as ferric arsenate and adsorbs to $AlOHSO_4$ (an amorphous hydrobasaluminite-like phase) and ferrihydrite via bidentate-binuclear complexes. Nickel(II) predominantly adsorbs to amorphous $Al(OH)_3$ via edge-sharing bidentate-mononuclear

complexes. In high pH (pH 9.5-9.9) samples, As(V) adsorbs to amorphous $Al(OH)_3$, ferrihydrite, and MgAlFe-hydrotalcite (bidentate complex). Nickel(II) octahedra adsorb to amorphous $Al(OH)_3$ and likely form a Ni-Al layered double hydroxide (LDH) surface precipitate on MgAlFe-hydrotalcite via Al dissolution-precipitation. In the final solids (blended low and high pH precipitates) discharged at ~pH 10.5, As(V) adsorbs to amorphous $Al(OH)_3$, ferrihydrite, and MgAlFe-hydrotalcite. Nickel(II) adsorbs to amorphous $Al(OH)_3$ and forms Ni-Al LDH surface precipitates on hydrotalcite. This study demonstrates that neutralization of chemically complex wastewater precipitates multiple phases capable of controlling dissolved As and Ni concentrations. Knowledge gained from this study will aid investigations in understanding the long-term fate of these potential contaminants in the environment and can be applied to other industries and environmental systems with similar conditions.

5.2 Introduction

The milling of metallic ores often results in the generation of acidic wastewater (raffinate) rich in metal(loid)s that are liberated from minerals in the host rock during processing. Raffinate must be treated before releasing the final effluent to the environment. The most common neutralization process used in the metal processing industry is hydroxide precipitation, in which metal hydroxides precipitate from the raffinate due to the addition of a base such as $Ca(OH)_2$ (Blais et al., 2008; Djedidi et al., 2009; Langmuir et al., 1999). Neutralization of acidic waters and soils are common processes observed in the environment and include the neutralization of acid mine drainage by natural sources (e.g., circumneutral pH river water or limestones) and the liming of acidic, metal(loid) rich soils affected by smelters (Adra et al., 2013; Nkongolo et al., 2013). Due to the ubiquitous occurrence of these neutralization processes, it is critical to characterize the mineralogical and chemical composition of the resulting precipitates. Understanding mineral/chemical compositions of these precipitates will aid studies in understanding the long-term fate of uranium tailings.

The milling of uranium (U) at Key Lake (KL) in northern Saskatchewan, Canada is one example of an industrial activity that acid-leaches primary minerals (such as kaolinite, chlorite, arsenopyrite, and gersdorffite) associated with U ore and uses a neutralization process to precipitate the dissolved metals (e.g., Al, Mg, Fe) and elements of concern (EOCs; e.g., As, Ni,

Se, and Mo) from raffinate prior to discharging the effluent to the environment (Shaw et al., 2011). The KL neutralization process uses slaked lime (hydrated CaO) to raise the pH in a stepwise manner. The resultant precipitates are collected in low pH (~4.0) and high pH (~9.5) thickeners, termed the Se-Mo and Lamella thickeners, respectively. The two sets of precipitates are mixed in a separate tank and the pH of the mixture is increased to 10.5 using slaked lime. This final slurry is sent to the in-pit Deilmann Tailings Management Facility (DTMF) as a portion of the overall tailings (details of the process are given in Figure C.1; Robertson et al., 2014). The mineralogy and geochemistry of these and other similar tailings (e.g., Au and other U tailings facilities) have been actively studied to gain an understanding of any potential risk EOCs may pose to the surrounding groundwater (Corriveau, 2006; Craigen, 2006; Douglas et al., 2010; Essilfie-Dughan et al., 2013; Gomez et al., 2013a; Mahoney et al., 2007; Moldovan et al., 2003; Pichler et al., 2001; Robertson et al., 2016). These studies show that secondary metal-oxyhydroxide phases with adsorptive properties are the dominant controls on aqueous concentrations of EOCs. Based on high concentrations of Fe in the raffinate and resulting tailings, previous studies focus on Fe-oxyhydroxides and their adsorption of EOCs through inner- and outer-sphere surface complexation in the neutralized precipitates (Essilfie-Dughan et al., 2013, 2011b; Mahoney et al., 2007; Moldovan et al., 2003). Calcium arsenate precipitates have also been a focus in previous studies due to the addition of excess $Ca(OH)_2$ (Donahue et al., 2000; Donahue and Hendry, 2003; Pichler et al., 2001). These studies, however, were not able to directly quantify the presence of Ca-arsenates, and it was suggested that Ca-arsenates will not precipitate when the Fe/As molar ratio is elevated (>4). At ratios as high as Fe/As = 4, batch synthesis experiments show Ca-arsenates begin to form from Ca-Fe-As slurries at 75-85°C after 336 h (Paktunc et al., 2015). Given that Fe/As ratios are frequently elevated beyond 4 at the KL mill and the tailings temperature is ≈ 4°C, Ca-arsenates were not considered for this study.

Because Al and Mg are also prevalent in raffinate, recent studies characterized the Al and Mg solids in the neutralization process and resulting tailings (Gomez et al., 2013a; Robertson et al., 2016). An amorphous phase bearing similar stoichiometry to hydrobasaluminite ($Al_4(SO_4)(OH)_{10}\cdot 15H_2O$) was identified in pH 4.0 precipitates and is simply referred to as $AlOHSO_4$. Aluminum-bearing amorphous $Fe(OH)_3$ also precipitates at pH 4.0. Precipitates formed at pH 9.5 consist of MgAlFe-type hydrotalcite and amorphous $Al(OH)_3$. The final precipitates discharged to the DTMF (pH 10.5) are a complex mixture of amorphous $(Al,Fe)(OH)_3$, MgAlFe-

type hydrotalcite, and amorphous $Al(OH)_3$. The non-Fe phases also appear to control the aqueous concentration of EOCs; however, the bonding characteristics of these Al and Mg minerals could not be determined using the methods applied by Robertson et al. (2016). The presence of these non-Fe sequestration mechanisms of EOCs is of interest because they could represent a secondary, long-term sequestration mechanism in metal (e.g., U and Au) tailings storage facilities as well as remediated acid mine drainage and acidic soil sites. Studies of Al-oxyhydroxides and mixed-metal layered double hydroxides (LDH), such as hydrotalcite, in other applications have identified EOC controls similar to Fe-oxyhydroxides (Douglas et al., 2010; Jobbágy and Regazzoni, 2013; Kappen and Webb, 2013). Few studies, however, have investigated the sequestration mechanisms exerted by Al-Mg phases on EOCs in the presence of Fe phases (Foster et al., 1998; Gomez et al., 2013a; Moldovan and Hendry, 2005).

The objective of this study is to characterize the coordination environments of As and Ni in Al-Mg phases as an additional control to the well-known ferrihydrite controls present during raffinate neutralization. This is achieved using X-ray absorption spectroscopy (XAS) measured at the As and Ni K-edges on synthetic and field (mill process) precipitates in the absence and presence of Fe minerals by analyzing their extended X-ray absorption fine structure (EXAFS) regions. The samples are collected from three stages of neutralization: low pH (4.0-4.6), high pH (9.5-9.9), and mill discharge pH (10.5-10.9). The complexation mechanisms of Al-Mg phases that control concentrations of As and Ni are determined through EXAFS analysis of reference compounds. These results are applied to the synthetic and mill samples using linear combination fitting (LCF) to determine the local coordination environment of As and Ni to Al, Mg, and Fe phases in the precipitates during and after neutralization. The relative distribution of As and Ni to these phases is also determined. The results of this study improve upon the current model of EOC sequestration in metallurgical tailings by describing the contributions of Al-Mg phases in these complex mineralogical systems. Because of the common occurrence of hydroxide neutralization of wastewaters and soils in industrial and environmental settings, this improved geochemical understanding of the precipitates in the KL system can be applied to other systems where acidic, metal(loid)-laden waters, tailings, and soils are neutralized to precipitate mixtures of metal-hydroxides to better predict the environmental impact of these processes and to better design remediation strategies.

5.3 Materials and Methods

5.3.1 Preparation of Samples and Standards

Three sets of samples were used in this study. Two sets of samples were produced in a synthetic raffinate neutralization system (SRNS). The SRNS is a continuous-mode physical model (Figure C.2) of the neutralization process used at the KL mill that has been verified to reproduce the aqueous and solids geochemistry of the mill process (Robertson et al., 2014). The first SRNS experiment (termed R3) used synthetic raffinate devoid of Fe, while the second SRNS experiment (termed R4) used raffinate containing Fe. The composition of the two synthetic raffinates is shown in Table 5.1 and is based on a raffinate sample collected from the KL mill by in 2011 (Gomez et al., 2013a). Concentrations of As, Ni, Se, and Mo were increased relative to the mill sample (approximately 10x for As and Ni, 75x for Mo, and 100x for Se) to aid in characterizing EOC-bearing phases. The detailed procedure and conditions used to synthesize the raffinate is presented by Robertson et al. (2014). Neutralized precipitates were collected from the Se-Mo (pH 4.0) and Lamella (pH 9.5) thickeners and equal volumes were mixed at pH 10.5 to simulate the treatment of the final tailings discharged from the KL mill to the DTMF (termed Combined samples). The third set of samples were field samples collected directly from the KL neutralization process in 2015 at pH 4.6 (Se-Mo), 9.9 (Lamella), and 10.9 (Combined) and are prefixed with “KL”. A difference in synthetic and field raffinate compositions exists and is attributed to multiple process variables including variability in the composition of the current ore, upstream reagent addition, and operational parameters of the process. Field samples were collected every day for 3 days from the Se-Mo and Lamella thickeners. A composite sample was created by mixing equal volumes of each sample. The Combined sample was created from the composite Se-Mo and Lamella samples using the same method as for the synthetic samples. All samples were collected in 50 mL polypropylene centrifuge tubes and centrifuged at 2900 g for 20 min. The supernatants were decanted and the solids allowed to air dry for 3 d. The chemical composition of the solid samples as determined by inductively coupled plasma mass spectrometry (ICP-MS) is presented in Table 5.2 (the corresponding solution compositions are presented in Table C.1).

Table 5.1. Raffinate composition (mg/L) for the synthetic R3 and R4 experiments and the field raffinate sample collected from the Key Lake bulk neutralization process.

Experiment[a]	Mg	Al	S	Fe	Ni	As	Se	Mo
R3	984	1610	13000	-	261	341	45.7	141
R4	1160	1930	13400	1300	217	307	33.6	94.5
KL	2330	1380	20700	4460	129	127	0.28	1.91
Detection Limit	1E-3	2E-4	2E-2	2E-3	2E-5	1E-4	5E-4	5E-5
RSD[b]	1%	1%	1%	6%	3%	2%	0.90%	2%

[a] Sample prefix definitions: R3 - No Fe added to the raffinate; R4 - All elements present in the raffinate; KL - samples collected directly from the Key Lake mill.

[b] The relative standard deviation (RSD) was calculated from replicate samples of the raffinate.

Table 5.2. Composition of each solid phase sample (μg/g) as determined by ICP-MS. The pH indicates the pH of the solution that the solid sample was precipitated in.

Experiment[a]	pH	Mg	Al	Ca	Fe	Ni	As	Se	Mo
R3Se-Mo	4.0	1020	19300	215000	135	280	4110	396	397
R3Lam	9.5	73000	57700	127000	241	13500	3330	414	1010
R3Combined	10.5	31600	31900	179000	170	5860	3180	325	521
R4Se-Mo	4.0	923	19800	183000	24000	461	3800	469	1830
R4Lam	9.5	97200	54600	88000	2540	17100	103	8.70	57.4
R4Combined	10.5	21300	23800	188000	16200	3810	2530	288	662
KLSe-Mo	4.6	2200	40800	126000	24700	349	1180	7.84	90.0
KLLam	9.9	58300	5350	126000	73500	2040	28.0	10.1	5.57
KLCombined	10.9	29400	25300	138000	34600	1120	739	9.57	44.0
DL[b]		5E-3	1E-3	2.5E-2	1E-2	1E-4	5E-4	2.5E-3	1E-4
RSD[c]		2%	1%	0.20%	0.30%	2%	2%	1%	0.40%

[a] Sample prefix definitions: R3 - No Fe added to the raffinate; R4 - All elements present in the raffinate; KL - samples collected directly from the Key Lake mill.
[b] DL: detection limit.
[c] The relative standard deviation (RSD) was calculated from replicate solid samples.

Reference standards were synthesized, purchased, or obtained from collaborators to aid in characterizing the As- and Ni-bearing phases in the neutralized precipitates using XAS. These reference standards were chosen based on mineralogical characterization from previous studies using multiple techniques (e.g., XAS, X-ray diffraction (XRD), and scanning transmission electron microscopy (STEM)) (Gomez et al., 2013a; Robertson et al., 2016, 2014). X-ray diffraction data for all synthetic samples and select standards are presented in Figure C.3. The following precipitates were equilibrated with solutions of As or Ni to form adsorption standard compounds:

ferrihydrite (As-Fh and Ni-Fh), amorphous $Al(OH)_3$ (As-am$Al(OH)_3$ and Ni-am$Al(OH)_3$), amorphous $AlOHSO_4$ (As-$AlOHSO_4$), and $MgAlFeSO_4$-type hydrotalcite (As-HT and Ni-HT). The $MgAlFeSO_4$-type hydrotalcite standard was used because it was identified as the dominant hydrotalcite in the KL tailings (Gomez et al., 2013a). The As-HT and Ni-HT adsorption standards were synthesized using the methods described by Paikaray et al. (2013) by adding 5 g/L $MgAlFeSO_4$-type hydrotalcite to solutions containing 0.66 mM $Na_2HAsO_4 \cdot 7H_2O$ or 0.85 mM $NiSO_4 \cdot 6H_2O$ as described by the procedure from. Ferric arsenate and scorodite standards were provided by Essilfie-Dughan et al. (2013). β-$Ni(OH)_2$ was purchased from Alfa Aesar (CAS #12054-48-7). Amorphous $Al(OH)_3$ was synthesized according to the method described by Kabengi et al. (2006). Amorphous $AlOHSO_4$ was synthesized by rapid co-precipitation of an equimolar (55 mM) $AlCl_3/H_2SO_4$ solution by adding 0.5 M NaOH to pH 4.0. The elevated Al^{3+} and SO_4^{2-} concentrations were designed to represent the high concentrations of these elements in the raffinate. Ferrihydrite was synthesized as described by Das et al. (2011). Amorphous $Ni(OH)_2$ was prepared as a standard compound and synthesized by rapidly precipitating 55 mM $NiCl_2 \cdot 6H_2O$ with 5 M NaOH to pH 9.5. For adsorbed standards, 10 g/L of sorbate (amorphous $Al(OH)_3$, amorphous $AlOHSO_4$, or ferrihydrite) was added to a 2 mM solution of $Na_2HAsO_4 \cdot 7H_2O$ or $NiSO_4 \cdot 6H_2O$ and equilibrated for 24 h. The equilibrium pH for each standard was 5.3 for As-am$Al(OH)_3$, 4.2 for As-$AlOHSO_4$, 8.7 for As-Fh, 4.8 for Ni-am$Al(OH)_3$, and 5.8 for Ni-Fh. All precipitates were filtered, rinsed three times with DI water to remove excess salts, and air dried. The dried samples and standards were finely powdered using an agate mortar and pestle, mounted on 0.5 mm path length Teflon sample holders, and sealed on both sides with Kapton tape for the XAS experiments.

5.3.2 Aqueous and Solid Elemental Analysis

Elemental analyses of the aqueous and solid samples were performed using a PerkinElmer NexION 300D ICP-MS. The solid samples were subjected to an HF-HNO_3 digest prior to analysis (Jenner et al., 1990; Longerich et al., 1990). The method detection limit and relative standard deviation for each element (aqueous and solid) is provided in Table 5.1 and Table 5.2. A SpectroBLUE inductively coupled optical emission spectrometer was used to measure the total S concentration of aqueous samples.

5.3.3 X-ray Absorption Spectroscopy Experiments

Arsenic and Ni K-edge XAS experiments were conducted at the HXMA beamline (06ID-1) at the Canadian Light Source (University of Saskatchewan, Saskatoon, Canada), a third generation synchrotron facility with an operating energy of 2.9 GeV and a beam current of 250 mA. The energy resolution of the beamline optics are E (eV)/10^4. For both As and Ni K-edge experiments, Rh-coated upstream collimating and downstream focusing mirrors were used. Two types of double crystal monochromators were used: Si(111) for As K-edge and Si(220) for Ni K-edge. Higher harmonics were rejected by detuning the second crystal monochromator to 50% of the beam intensity. XAS data for the samples and the adsorbed standards were collected under ambient conditions in fluorescence mode using a 32-element solid state Ge detector. To reduce scattering and fluorescence from other elements in the samples and enhance the As and Ni fluorescence signals reaching the detector, eight layers of Al foil, Soller slits, and Ge and Co filters for As and Ni K-edges, respectively, were placed between the sample and the detector. During collection of all XAS data, Au (for As K-edge) or Ni (for Ni K-edge) foil was placed between the second and third ionization chambers for energy calibration. Helium gas was used in the ionization chambers for all the experiments. Data in the near-edge region were collected at 0.4 eV steps while data in the EXAFS region were collected at 0.05 $Å^{-1}$ steps. An average of three XAS scans were collected for all samples whereas two scans were collected per reference standard.

The XAS analysis software packages ATHENA and ARTEMIS (Demeter v. 0.9.24) were used for data reduction and analyses of X-ray absorption near-edge spectroscopy (XANES) and EXAFS (Ravel and Newville, 2005). Non-linear least squares fitting of EXAFS data were performed with ARTEMIS to characterize the structure of the As and Ni reference compounds. Amplitude and phase functions for EXAFS fitting were generated by FEFF 6.0 for scorodite ($FeAsO_4 \cdot 2H_2O$) for As paths, a modified hercynite ($FeAl_2O_4$) crystal structure with Ni(II) substituted for Fe(II) for Ni-Al paths, and the same modified hercynite structure with Fe(III) substituted for Al(III) for Ni-Fe paths in Ni fits. Radial structure functions (RSFs) were obtained through Fourier transforms of the $\chi(k) \cdot k^3$ functions using a Hanning window over varying k-ranges depending on the quality of the data. The amplitude reduction factor (S_0^2) was fixed at 0.9 for all fits.

Principal component analysis (PCA) and target transforms were performed using the SIXPACK interface (v. 1.1; Webb, 2005). SIXPACK calculates the IND function of Malinowski, which indicates the minimum number of components of the dataset when the function is minimized (Malinowski, 1991), and the SPOIL value of the target transforms, which is a quantity used to determine whether a target transformed reference compound is a likely component in a sample set. Linear combination fitting was performed with ATHENA on sample data to determine the relative proportions of the reference compounds within the samples. All combinations of reference compounds were considered; however, the LCF result that was deemed to be the most likely combination of reference compounds was based on the following criteria: (1) the compound was identified as a potential component by PCA and target transformation, (2) the presence of the compound was supported by other data (e.g., XRD, TEM, or the chemical composition of the sample), and (3) a low residual was obtained in the fit relative to other fitting combinations. Components fit to <5% of the total LCF result were considered insignificant.

5.4 Results and Discussion

5.4.1 Arsenic K-edge XAS

The oxidation state of As in all samples was primarily As(V) as indicated by the edge position located at approximately 11,874 eV (Figure 5.1). The edge energy for As(III) species occurs at approximately 11,870 eV and was not observed in the samples (Manning, 2005). Scorodite was used as the As(V) reference compound to demonstrate the pentavalent oxidation state of the samples. The results show that the oxidation state of As does not change during neutralization of both the synthetic (R3 and R4) and field (KL) samples. The dominance of As(V) species in U mill tailings has also been noted in previous studies (Donahue and Hendry, 2003; Langmuir et al., 1999; Shaw et al., 2011).

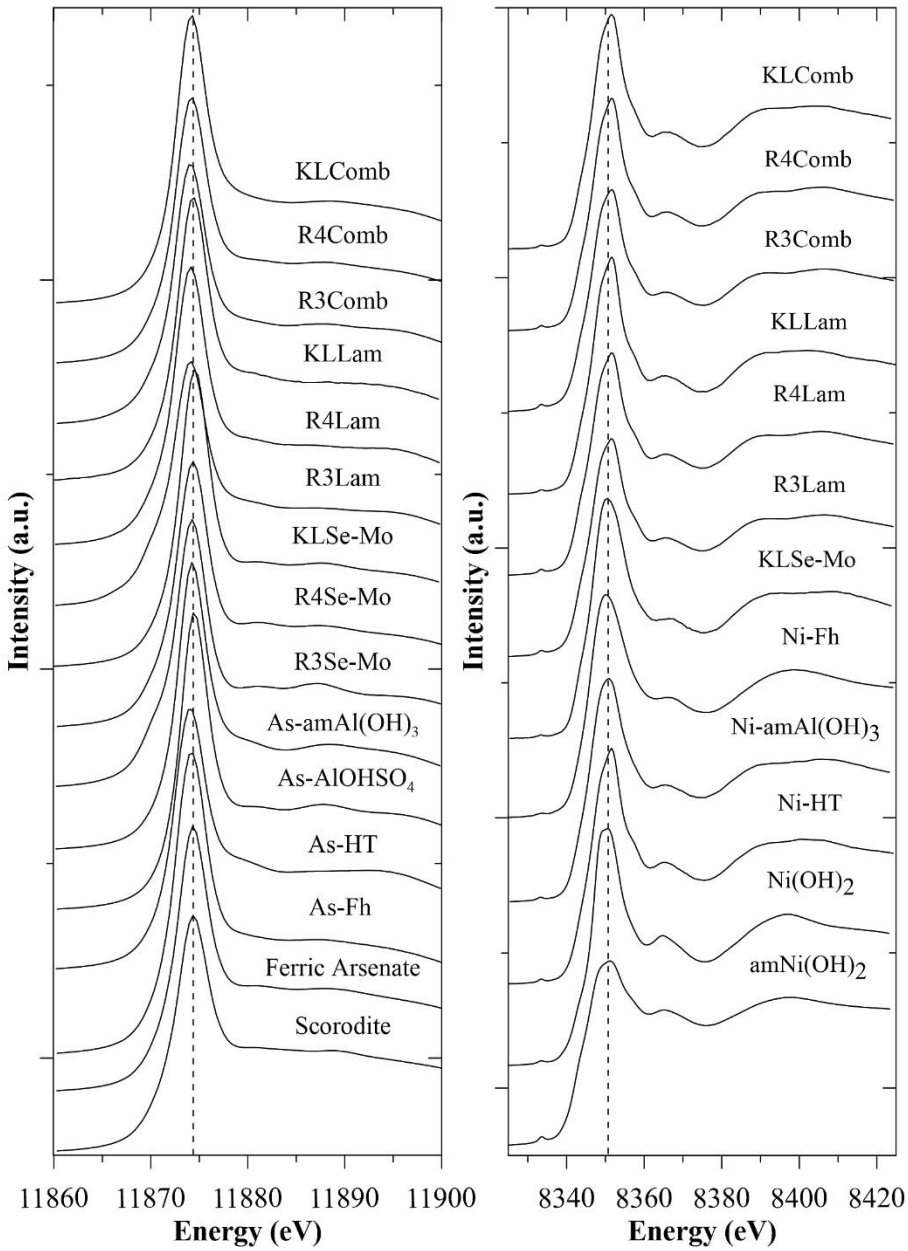

Figure 5.1. Arsenic K-edge (left) and Ni K-edge (right) X-ray absorption near-edge spectra of each sample and standard compound. The vertical dashed line represents the approximate white line peak position of the As(V) or Ni(II) oxidation state.

Non-linear least squares fitting analysis was performed on the As K-edge spectra of the As-Al and As-Fe standard compounds. The $\chi(k)\cdot k^3$ spectra and Fourier transformed data and fits are shown in Figure 5.2. All As standards were fit with three components: the first shell As-O path represents the AsO_4^{3-} tetrahedron, the As-O-O multiple scattering (MS) path represents triangular backscattering of the photoelectron around the AsO_4^{3-} tetrahedron, and the second shell As-Fe or

As-Al path (Table 5.3; Figure C.4). The As-O paths are represented by the first major peak in the RSF. The coordination number (CN) of the As-O shell for all standards was fixed at 4.0 and the resulting interatomic distances (R) were fit to 1.68-1.69 Å. The MS path is represented by the second peak at 2.2-2.4 Å (all references to RSF peaks are uncorrected for phase shift) in the RSF. It was constrained with a CN_{MS} = 12 during the fit analyses. This MS path was deemed the largest contributing MS path in AsO_4^{3-} EXAFS (Manceau et al., 2007). Fitting other MS paths did not improve the results.

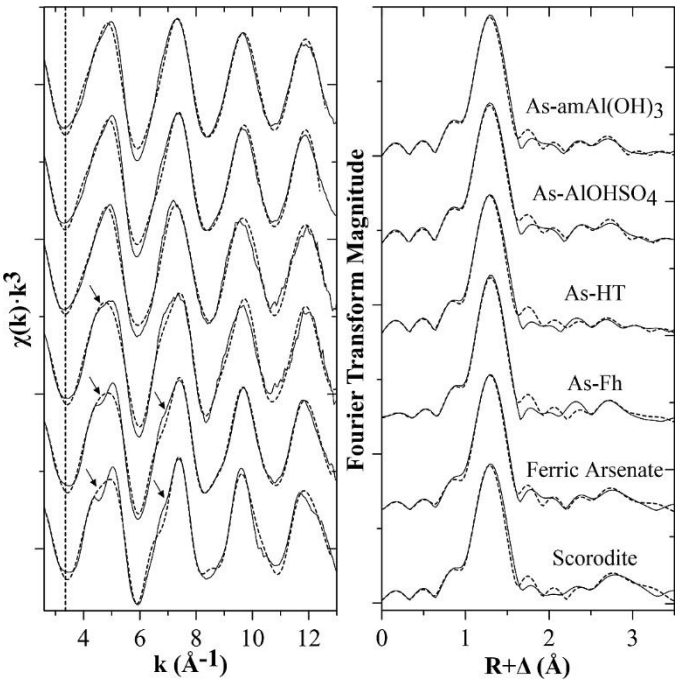

Figure 5.2. Arsenic K-edge k^3-weighted $\chi(k)$ spectra of the As standard compounds and the corresponding RSFs. Whole lines represent data and dashed lines represent fits. The vertical dashed line at 3.3 $Å^{-1}$ is a visual aide for the slight peak shift observed between As-Al and As-Fe standards. Arrows denote important features of the As-Fe phase discussed in the text.

The third peak in the RSFs at 2.6-2.8 Å corresponds to the As-Al or As-Fe paths. The fit parameters for the As-Al path in each standard show that AsO_4^{3-} forms bidentate-binuclear coordination complexes with the $Al(OH)_3$ and $AlOHSO_4$ standards. The As-Al coordination numbers for As-am$Al(OH)_3$ and As-$AlOHSO_4$ are ~2 (see Table 5.3), and agree with previous studies on the adsorption of As on similar Al phases (Douglas et al., 2010; Foster, 1999). The interatomic distances of the As-Al shells for As-am$Al(OH)_3$ and As-$AlOHSO_4$ are 3.19 and 3.17 Å, respectively, which agree with other studies involving As bonded to a range of Al oxides (Arai et al., 2001; Arai and Sparks, 2002; Beaulieu and Savage, 2005; Foster et al., 1998; Kappen and

Webb, 2013; Ladeira et al., 2001; Luo et al., 2006). These results indicate there is no structural difference between As adsorbed to amorphous $Al(OH)_3$ or $AlOHSO_4$.

Table 5.3. Summary of As K-edge EXAFS fitting parameters of the standard compounds.

	E_o (eV)	CN	R (Å)	σ^2 (Å^2)	R-Factor	χ_v^2
As-Al(OH)$_3$						
As-O	6(1)	4.0[a]	1.69(1)	0.0014(4)	0.016	9714
As-O-O MS	6(1)	12.0[a]	3.17(2)	0.0028[b]		
As-Al	6(1)	1.9(7)	3.19(8)	0.01(1)		
As-AlOHSO$_4$						
As-O	6(1)	4.0[a]	1.68(1)	0.0014(5)	0.016	7617
As-O-O MS	6(1)	12.0[a]	3.18(4)	0.0027[b]		
As-Al	6(1)	2.0(6)	3.17(5)	0.006(6)		
As-HT						
As-O	5(1)	4.0[a]	1.69(1)	0.0014(5)	0.017	1615
As-O-O MS	5(1)	12.0[a]	3.15(4)	0.0028[b]		
As-Al	5(1)	2.1(8)	3.31(7)	0.01(1)		
As-Fh						
As-O	7(1)	4.0[a]	1.69(1)	0.0012(6)	0.022	2084
As-O-O MS	7(1)	12.0[a]	3.17(5)	0.0024[b]		
As-Fe	7(1)	2.1(6)	3.29(4)	0.009(5)		
Ferric Arsenate						
As-O	6(1)	4.0[a]	1.69(1)	0.0017(4)	0.011	7747
As-O-O MS	6(1)	12.0[a]	3.16(4)	0.0033[b]		
As-Fe	6(1)	2.6(6)	3.33(2)	0.009(3)		
Scorodite						
As-O	6(1)	4.0[a]	1.69(1)	0.0016(4)	0.014	9295
As-O-O MS	6(1)	12.0[a]	3.17(4)	0.0032[b]		
As-Fe	6(1)	4.1(6)	3.37(2)	0.010(3)		

Fitting was performed over a range from k_{min} = 2.6-2.8 Å^{-1} to k_{max} = 13.6-13.7 Å^{-1}. The amplitude reduction factor, S_0^2, was fixed at 0.9. MS = multiple scattering. E_o = energy shift. R = interatomic distance. σ^2 = Debye-Waller factor. χ_v^2 = reduced chi square. The numbers in parentheses are the Artemis provided errors calculated from the diagonal of the covariance matrix and scaled by the square-root of χ_v^2.

[a]Parameter held constant in the fitting procedure
[b]Parameter correlated to the Debye-Waller factor of the As-O path ($2\sigma^2$)

The parameters for As-HT indicate a slightly different coordination environment for AsO_4^{3-} adsorbed to hydrotalcite. The As-Al coordination number for As-HT is 2.1 and the corresponding interatomic distance is 3.31 Å which indicates bidentate surface complexation. The As-Al interatomic distance of As-HT is greater than the other Al standards and agrees with previous

studies (Burke et al., 2013; Opiso et al., 2010). The reason for this increased distance is unclear; however, AsO_4^{3-} has been observed to be adsorbed at both the interlayers and edges of LDHs, which may affect the fitted As-Al CN and R (Jobbágy and Regazzoni, 2013; Li and Duan, 2006). It is possible that both adsorption types are present in the As-HT standard. Another study suggests outer-sphere complexation of AsO_4^{3-} to LDHs (Wang et al., 2009). This scenario was tested in the analysis but yielded a poor fit. The second shell peak at ~2.7 Å (Figure 5.2) is also evidence for inner-sphere complexation. Based on the presence of Fe in the As-HT standard, fitting an As-Fe shell was attempted but did not yield good results. An As-Mg path was not included in the fit because it would exhibit little difference from an As-Al path due to its similar atomic number.

The Fe standards were fit with a slightly greater R for the As-Fe shell versus the As-Al shell (Table 5.3). A bidentate-binuclear surface complex was fit for As-Fh and has been well documented in other studies (Foster et al., 1998; Moldovan et al., 2003; Waychunas et al., 1993). The fit results for ferric arsenate and scorodite (Table 5.3) are consistent with other studies (Paktunc, 2015; Paktunc et al., 2008). In general, the As-Fe interatomic distance increases as the coordination number of the As-Fe shell increases.

Non-linear least squares fitting of the EXAFS spectra of the samples for CN and R proved to be difficult due to the complexity of the samples that potentially contained multiple As-Fe and As-Al backscattering paths with similar R. As such, PCA, target transformations, and LCF analyses were performed to quantify the partitioning of As in the synthetic and field samples using the Al and Fe standard compounds characterized by EXAFS. Principal component analysis of the As $\chi(k)\cdot k^3$ sample spectra was performed over the range k = 1-13 $Å^{-1}$. The resulting eigenvectors of the components are plotted in Figure 5.3 and the component variance is summarized in Table C.2. These data suggest that three to five As components comprise the sample data set as the variance decreases sharply after the third component, although visually there appears to be contribution from the fifth component (Figure 5.3). Conversely, the IND function was minimized at the first component and indicates only one component is required to reconstruct the data. There must be at least two As components in the sample set, however, because (1) it is well known that As adsorbs to ferrihydrite in this system and (2) our data shows that an Al-phase is likely associated with As in the R3 experiment. Additionally, the value of IND showed sensitivity to the chosen k-range and could be minimized at the third component when k = 1-8.2 $Å^{-1}$. This sensitivity

emphasizes that the IND function should be used as a guideline rather than a definitive indicator on the number of components in a sample set.

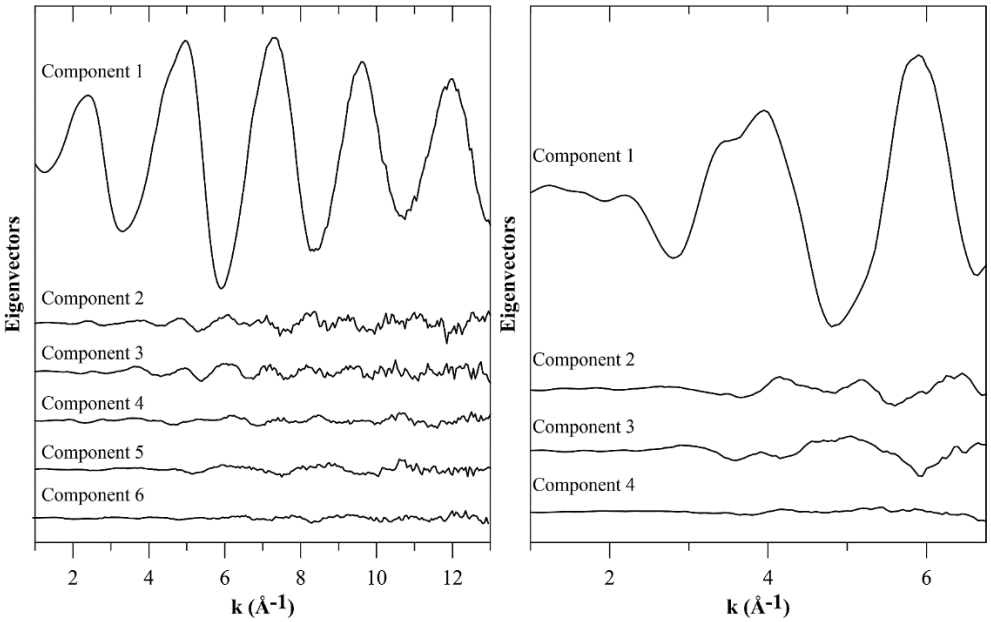

Figure 5.3. Principal component analysis of the As (left) and Ni (right) samples in k^3-space. Arsenic PCA was performed over k = 1 - 13 $Å^{-1}$ and Ni PCA was performed over k = 1 - 6.8 $Å^{-1}$ (a shorter range for Ni was used due to the interference of the absorption edges of other elements in the sample). Components with a variance <0.02 were omitted from the plot.

The target transforms of all standards are plotted in Figure 5.4 and their corresponding residuals and SPOIL values are summarized in Table C.3. SPOIL values <1.5 indicate excellent matches, 1.5-3 are good, 3-4.5 are fair, 4.5-6 are poor, and >6 are unacceptable (Manceau et al., 2002) and excluded as a potential candidate. All reference compounds returned SPOIL values in the excellent to good range. Scorodite possessed the greatest SPOIL and residual and previous XRD data exclude it from being a potential phase in the samples. After considering the components in Figure 5.3 and the uncertain statistical information given in Table C.2, five candidates (As-am$Al(OH)_3$, As-HT, As-Fh, As-$AlOHSO_4$, and ferric arsenate) were chosen as potential phases to be further considered for LCF. These are in keeping with the phases characterized for the KL system in previous studies by geochemical modeling, XRD, XAS, and STEM (Gomez et al., 2013a; Robertson et al., 2016, 2014).

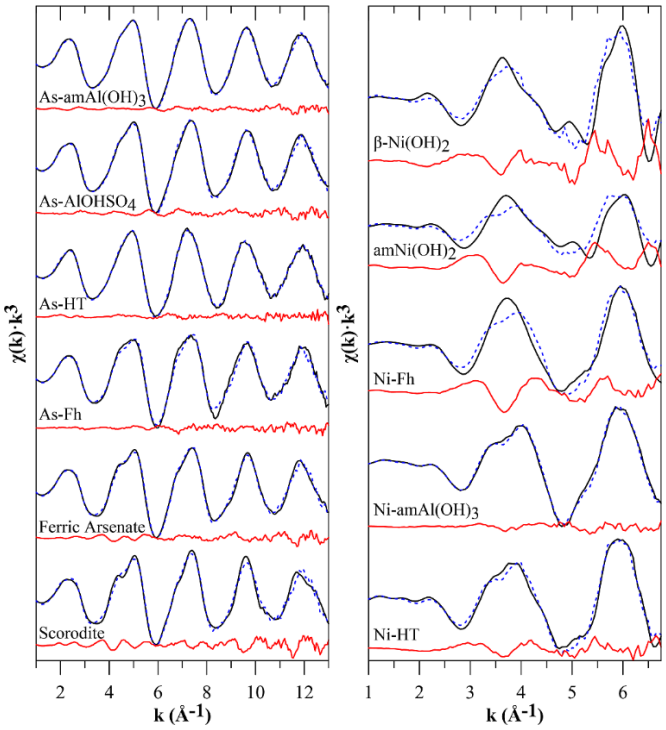

Figure 5.4. Target transformations of the As (left) and Ni (right) standard compounds using the PCA results (solid black = standard compound spectra, dashed blue = target transformation, solid red = residual).

The $\chi(k)\cdot k^3$ spectra and RSFs of the samples and the resulting LCF fits are presented in Figure 5.5 and Figure 5.6. All reference compounds were used for LCF, but the results of the PCA and target transforms were considered when inspecting the fits. The R3Se-Mo sample (Fe-free) fits best to As-AlOHSO$_4$ (88%) with no other components fitting well in combination. This could indicate that an additional undefined Al phase may be exerting control on AsO_4^{3-} at low pH in the absence of Fe. The results for the R4Se-Mo sample (containing Fe) indicate that 61(±3)% of As occurs as As-Fh, 26(±6)% as ferric arsenate, and 15(±5)% as As-AlOHSO$_4$. The predominance of As-Fe phases is evident by inspecting the peaks at 5.0 and 7.4 Å^{-1}, which display pronounced shoulders characteristic of the Fe standards. A similar result is observed for KLSe-Mo, although slightly more As (26(±5)%) is bound to AlOHSO$_4$. This may be due to the elevated Al/Fe molar ratio in KLSe-Mo versus R4Se-Mo (Table 5.2) as a result of the pH differences (i.e., pH 4.6 vs. 4.0, respectively). The mass of ferric arsenate present in KLSe-Mo is lower than in R4Se-Mo (13(±5)% versus 26(±6)%, respectively), likely as a result of the lower As concentration in the raffinate of KLSe-Mo (Table 5.1). These results indicate As is sequestered primarily by Fe phases and secondarily by Al phases at pH 4.0. In the absence of Fe, however, As is sequestered by Al

phases at pH 4.0. Also, the occurrence of As adsorbed to Al-substituted ferrihydrite is a possibility in the Se-Mo samples. Aluminous ferrihydrite is evident in the Se-Mo samples based on Al K-edge XAS (Robertson et al., 2016), although an As-adsorbed standard was not prepared for this study.

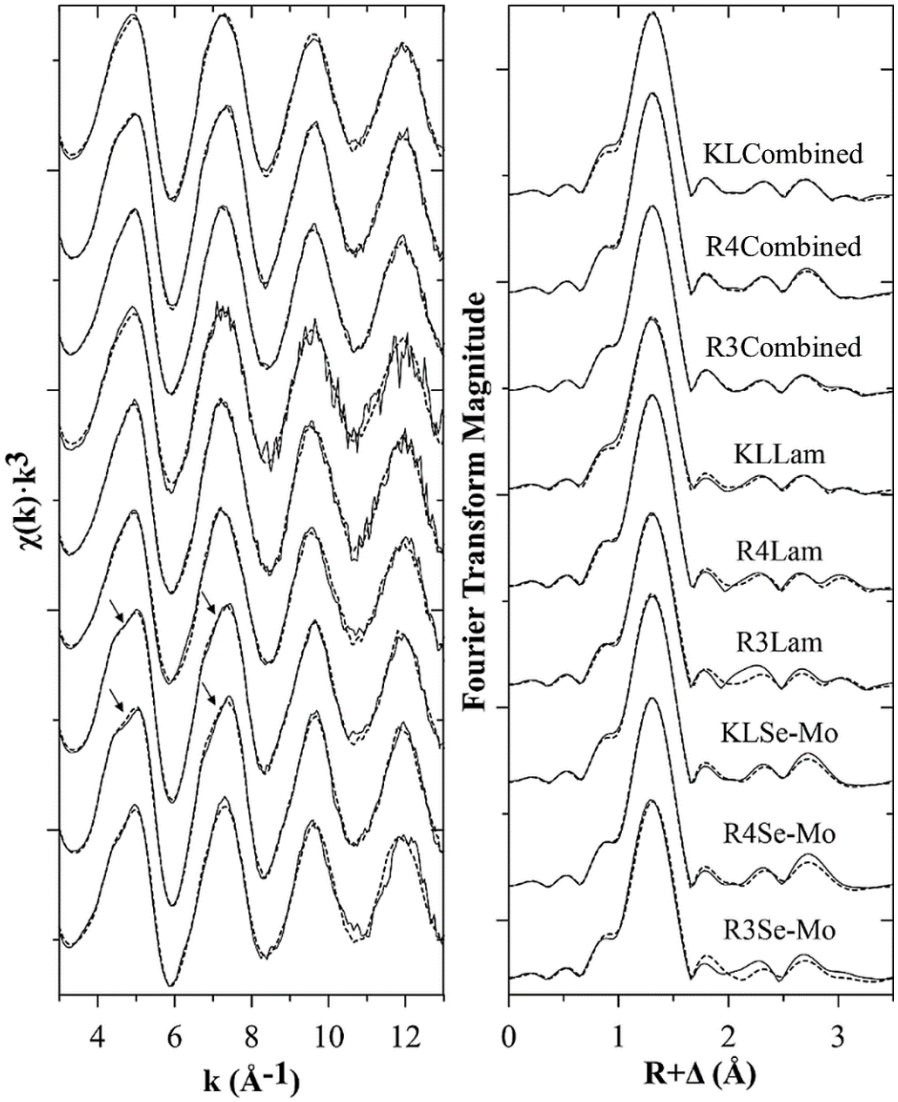

Figure 5.5. Arsenic K-edge k^3-weighted $\chi(k)$ spectra of the synthetic and field samples and their corresponding RSFs. Whole lines represent data and dashed lines represent results from LCF. Arrows denote important features of the As-Fe phase discussed in the text.

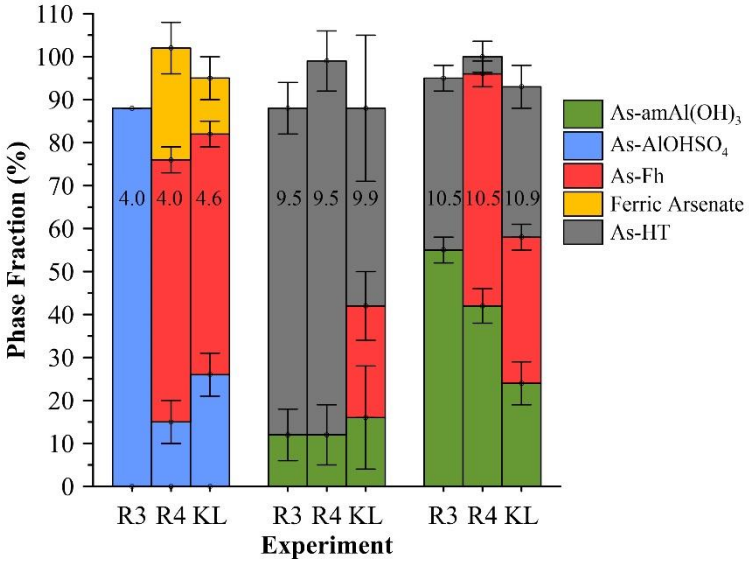

Figure 5.6. Linear combination fitting results of As K-edge XAS spectra for all samples. Error bars are the estimated standard deviation of the fits. Numbers plotted on the bars are measured pH of the solution during precipitation of the solids. Fitting was performed in k-space from 1.0-13.0 Å and components were not required to sum to 100%. Components fit to <5% are not considered significant but were included as they contribute to the total sum. See Table C.4 for complete summary of values.

Arsenic precipitation is not a primary objective of the Lamella stage as >99% of the As has precipitated out by pH 4.0, although settling issues in the Se-Mo thickener during the R3 experiment caused EOC-rich solids to overflow to the high pH neutralization stage, resulting in elevated concentrations of EOCs in the R3Lam sample (Robertson et al., 2016). Nonetheless, the RSFs of all Lamella samples contain a low amplitude second shell peak at ~2.7 Å characteristic of the As-Al shell in the As-HT standard. Hydrotalcite is a major phase in the Lamella samples due to the presence of dissolved Mg^{2+}, Al^{3+}, and SO_4^{2-} precipitating between pH 6.5 and pH 9.5. The LCF results indicate that As in R3Lam and R4Lam occurs as a mixture of As-HT (76(±6)% and 87(±7)%, respectively) and As-amAl(OH)$_3$ (12(±6)% and 12(±7)%, respectively). For KLLam, 26(±8)% of As is bound as As-Fh in addition to As-HT and As-amAl(OH)$_3$. Ferrihydrite precipitates in KLLam due to the presence of Fe^{2+} in the KL raffinate (but not present in the SRNS), which does not precipitate at the pH 4.0 stage. In the KL mill, Fe^{2+} is oxidized to Fe^{3+} by H_2O_2 after the Se-Mo stage, causing ferrihydrite to precipitate in the Lamella thickener.

Inspection of the $\chi(k)\cdot k^3$ spectra of the Combined samples shows the first two peaks that contain the characteristic shoulders of Fe-phases in the Se-Mo samples are supressed once combined with the Lamella solids at pH 10.5, suggesting a greater abundance of As bound to Al-

phases. Figure 5.6 shows partitioning of As to amAl(OH)$_3$, ferrihydrite, and hydrotalcite. As-AlOHSO$_4$ and ferric arsenate are not observed as they are predicted to dissolve at pH 10.5 (De Klerk et al., 2012; Robertson et al., 2016). In R4Combined, the LCF results indicate that 54(±3)% of As occurs as As-Fh and 42(±4)% as As-amAl(OH)$_3$. There is an overall increase in the amount of As associated with Al-phases in the Combined solids compared to the Se-Mo and Lamella solids. For instance, the LCF results indicate that 59% of As in KLCombined is associated with Al-phases (24(±5)% with As-amAl(OH)$_3$ and 35(±5)% with As-HT) while only 26(±5)% of As in KLSe-Mo is associated with Al-phases. This could indicate that upon mixing the Se-Mo and Lamella solids and raising the pH to 10.5, As released from the dissolution of ferric arsenate is adsorbed by amAl(OH)$_3$ and hydrotalcite. These results suggest that both Fe- and Al-phases play important roles in controlling the As concentrations in hydroxide-neutralized precipitates.

A small peak shift in the low-k region is identified in the standards as an indicator of either As-O-Fe or As-O-Al bonding in the samples (shown by the vertical line in Figure 5.2 and emphasized in Figure C.5). All three Al standards contain a shifted asymmetric peak with minima occurring at 3.3 Å^{-1}. All three Fe standards contain a symmetric peak with minima occurring around 3.5 Å^{-1}. These variations in position and shape are attributed to destructive/constructive interference between As-O and As-Al/As-Fe backscattering functions that are dependent on the type of backscatterer (i.e., Al or Fe). Constructive interference of the As-Al path with the As-O path results in the peak shifting asymmetrically to lower k with respect to Fe standards. Conversely, destructive interference of the As-Fe path with the As-O path results in a symmetric peak shape. This peak difference can be used to qualitatively fingerprint the predominant ligand-metal complex (Al or Fe) in the samples. Applying this indicator to the samples provides additional evidence of the type of ligand-metal complexation present (see Figure C.6). In the Al-only samples (R3), the peak position is shifted to lower energies. In the Al-Fe samples (R4 and KL), the peak position is located between the two types of peaks, suggesting As bonding to both Al and Fe phases. This is in agreement with LCF results. The feature became more symmetric as the minima shifted to higher k with increasing As-Fe content of the sample (as determined by LCF results). However, even samples with the greatest Fe content (KLSe-Mo and R4Se-Mo) show evidence of As-O-Al coordination, supporting a mixed Al/Fe control model of As adsorption on Al and Fe-hydroxides.

5.4.2 Nickel K-edge XAS

The Ni K-edge near edge spectra for the samples and standards are presented in Figure 5.1. All spectra line up with the Ni(II) oxidation state at ~8,350 eV as demonstrated by the positioning with respect to β-$Ni(OH)_2$. The spectra of the Lamella and Combined samples have the same near edge features as the Ni-HT standard whereas the KLSe-Mo sample has characteristic features of Ni-$amAl(OH)_3$. Ni-Fh displays a broad peak at ~8,398 eV that is not present in any of the samples.

The fitted $\chi(k)\cdot k^3$ spectra and RSFs of the Ni standard compounds are shown in Figure 5.7. Fit results of β-$Ni(OH)_2$ and $amNi(OH)_2$ are given in Table C.5 and Figure C.7 because the sample spectra were ultimately fitted without these phases. Due to lower quality data at higher k-ranges, fits are limited to two shells and R < 3.2. The RSFs of the Ni standards show a large peak around 1.6-1.7 Å, representing a component for an octahedral Ni-O first shell (Table 5.4). Second shell peaks are located between 2.6-2.7 Å (Figure 5.7) and are fit with either Fe, Al, or Ni backscatterers (Table 5.4).

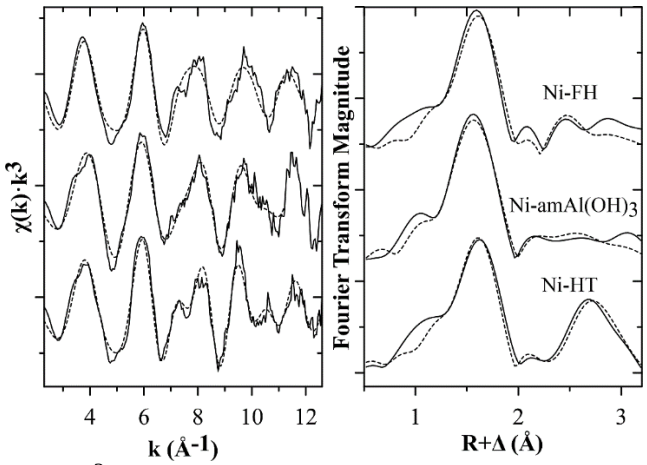

Figure 5.7. Nickel K-edge k^3-weighted χ(k) spectra of the Ni standard compounds and the corresponding RSFs. Whole lines represent data and dashed lines represent fits.

Ni-Fh was modeled with two Ni-Fe shells representing two modes of edge-sharing bidentate-mononuclear adsorption (described as chain and row bonding) of Ni octahedra to ferrihydrite (Arai, 2008). Nickel is coordinated to 1.9 Fe octahedra in the chain configuration at 3.00 Å and 2.1 Fe octahedra in the row configuration at 3.17 Å, consistent with results by Arai (2008). A single mode of Ni adsorption for $amAl(OH)_3$ resulted in poor fit results. Thus, a model similar to Ni-Fh with two modes of Ni coordination was used to fit Ni-$amAl(OH)_3$. This model

improved the fit, and chain and row edge-sharing bidentate-mononuclear arrangements of Ni octahedra coordinated with amAl(OH)$_3$ can be inferred from the bond distances (Table 5.4).

Table 5.4. Summary of Ni K-edge EXAFS fitting parameters of the standard compounds**.**

	E_o (eV)	CN	R (Å)	σ^2 (Å^2)	R-Factor	χ_v^2
Ni-Fh						
Ni-O	-3(1)	6.0[a]	2.06(2)	0.006(1)	0.027	1569
Ni-Fe$_1$	-3(1)	1.9(4)	3.00(4)	0.006(6)[b]		
Ni-Fe$_2$	-3(1)	2.1(4)	3.17(5)	0.006(6)[b]		
Ni-amAl(OH)$_3$						
Ni-O	-6(2)	6.0[a]	2.04(2)	0.005(1)	0.021	839
Ni-Al$_1$	-6 (2)	2.4(5)	2.97(3)	0.006(5)[b]		
Ni-Al$_2$	-6(2)	1.1(5)	3.26(9)	0.006(5)[b]		
Ni-HT						
Ni-O	-5(1)	6.0[a]	2.05(1)	0.0059(9)	0.017	455
Ni-Al	-5(1)	1.8(5)	3.09(2)[b]	0.008(2)[b]		
Ni-Ni	-5(1)	4.1(6)	3.09(2)[b]	0.008(2)[b]		

Fitting was performed over a range from k_{min} = 2.3 Å^{-1} to k_{max} = 11.8-12.6 Å^{-1}. The amplitude reduction factor, S_0^2, was fixed at 0.9. E_o = energy shift. R = interatomic distance. σ^2 = Debye-Waller factor. χ_v^2 = reduced chi square. The numbers in parentheses are the Artemis provided errors calculated from the diagonal of the covariance matrix and scaled by the square-root of χ_v^2.

[a]Parameter held constant in the fitting procedure

[b]These Debye-Waller factors were set to be equal in their fits to constrain the number of variables.

The EXAFS data of the Ni-HT standard suggests that a Ni-Al LDH surface precipitate formed on the hydrotalcite surface during synthesis instead of a Ni surface complex as expected. The fitting parameters fit well to a mixed second shell containing Ni-Ni and Ni-Al interactions where the central Ni octahedron is coordinated to 4.1 Ni atoms and 1.8 Al atoms at 3.09 Å. Such a large coordination of Ni to other Ni atoms is not expected in an adsorption complex. This result suggests that a Ni-Al LDH surface precipitate may have formed on the hydrotalcite surface. Octahedral units in an ideal hydrotalcite structure are surrounded by six neighbouring octahedra; in this case, one Ni octahedron is surrounded by an average of 5.9 Ni and Al octahedra (d'Espinose de la Caillerie et al., 1995; Scheinost and Sparks, 2000). Surface precipitation is demonstrated by Scheidegger et al. (1998) through a mechanism of Al dissolution from the hydrotalcite phase followed by Ni-Al LDH precipitation. This would also explain the lack of Fe backscatterers in the fit (which was attempted) despite the presence of Fe in the hydrotalcite substrate.

The plot of eigenvectors for Ni PCA (Figure 5.3) indicates there are two or three components in the sample set. Likewise, the IND function is minimized for the second component (Table C.2). Target transformations of the Ni reference compounds revealed Ni-amAl$(OH)_3$ and Ni-HT as the most likely phases present in the samples. The SPOIL values for Ni-amAl$(OH)_3$ and Ni-HT border the "good" to "fair" range, while large residuals and SPOIL values (ranging from "fair" to "unacceptable") were observed for β-Ni$(OH)_2$, amNi$(OH)_2$, and Ni-Fh, suggesting that these components were likely not present in the samples (Figure 5.4 and Table C.3). The PCA results were considered when performing the linear combination fitting presented in the main text and were self-consistent.

Linear combination fitting of the field samples could only be performed up to 6.8 A^{-1} due to interference from the Dy L_2- and Cu K-edges which were present in trace amounts in the KL samples. It should be noted that Al in the Se-Mo phase is primarily in the form of amorphous $AlOHSO_4$; however, a Ni-adsorbed $AlOHSO_4$ standard was not prepared and therefore amorphous $Al(OH)_3$ was used as an analogue during fitting. Despite the presence of ferrihydrite, Ni-amAl$(OH)_3$ is the only possible phase in KLSe-Mo through LCF (Figure 5.8) and is evident from the double-peaked feature at ~4.0 $Å^{-1}$ (Figure 5.9). These LCF results do not exclude the possibility of Ni-adsorbed ferrihydrite in KLSe-Mo considering the assumed relative detection limit of the technique (~5%); however, Ni-amAl$(OH)_3$ appears to be the dominant Ni control at the low pH stage.

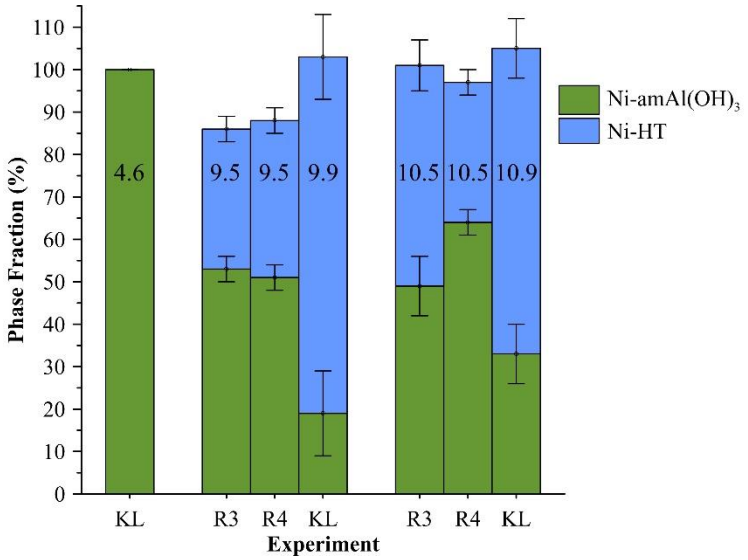

Figure 5.8. Linear combination fitting results of Ni K-edge XAS spectra for all samples. Error bars are the estimated standard deviation of the fits. Numbers plotted on the bars are measured pH of the solution during precipitation of the solids. Fitting was performed in k-space from 1.0-10.9 Å and components were not required to sum to 100%. See Table C.6 for complete summary of values.

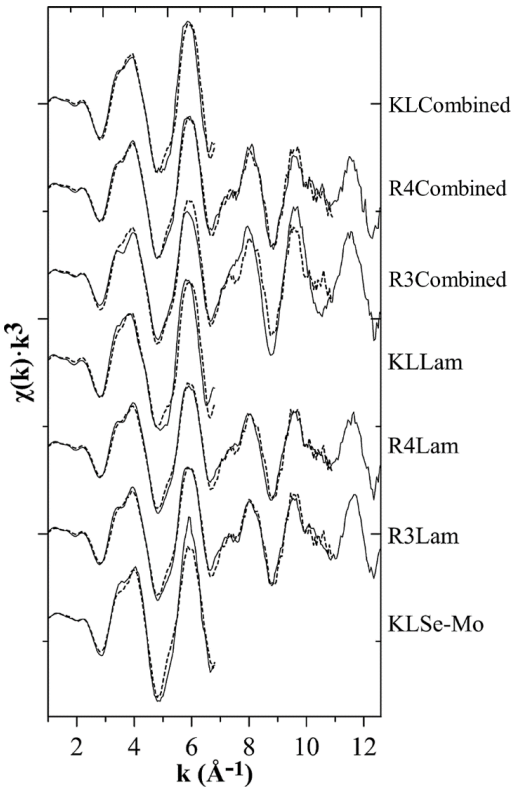

Figure 5.9. Nickel K-edge k^3-weighted $\chi(k)$ spectra of the synthetic and field samples. Whole lines represent data and dashed lines represent results from LCF. RSFs of the R3 and R4 samples are presented in Figure C.5.

The Ni RSFs of the synthetic Lamella and Combined samples are shown in Figure C.8. Most of the Ni was present in the Lamella samples, which consisted of hydrotalcite and amorphous $Al(OH)_3$ as shown by LCF. R3Lam and R4Lam contained similar amounts of Ni-HT (33(±3)% and 37(±3)%, respectively) and Ni-am$Al(OH)_3$ (53(±3)% and 51(±3)%, respectively). KLLam contained 84(±10)% Ni-HT and 19(±10)% Ni-am$Al(OH)_3$. The synthetic samples likely contained higher proportions of Ni-am$Al(OH)_3$ compared to the KL sample because the Ni concentrations in the raffinate are approximately double that in the synthetic samples. Because LDHs are limited to $2 < M(II)/M(III) < 4$, elevated concentrations of M(II) should cause the formation of other phases (Li and Duan, 2006). In this case, Ni-am$Al(OH)_3$ could precipitate in greater proportions when the hydrotalcite surfaces become saturated with Ni. The presence of Ni-am$Al(OH)_3$ (rather than solely Ni-HT as observed in many other systems) is explained by the stepwise neutralization of the process that increases the solution pH to 6.5 which causes am$Al(OH)_3$ to precipitate first (with lesser amounts of hydrotalcite), followed by neutralization to pH 9.5 (Figure C.1) where hydrotalcite precipitation is more favourable (Livi et al., 2009; Robertson et al., 2016; Scheidegger et al., 1998; Scheinost and Sparks, 2000). The greatest amount of Ni precipitation occurs at pH 6.5 where amorphous $Al(OH)_3$ is the dominant Al phase; thus, the presence of Ni-am$Al(OH)_3$ is reasonable (Robertson et al., 2016). At pH 9.5, it is possible that multiple mechanisms of Ni sequestration exist. The first mechanism is through surface precipitation of Ni-Al LDH as suggested by EXAFS analysis of the reference Ni-HT compound and the subsequent LCF results. A co-precipitation mechanism cannot be ruled out though, as hydrotalcite precipitates simultaneously at pH 6.5 and 9.5 with Ni as evidenced by the change in elemental composition during neutralization (Table C.1). This could result in a mixed layered double hydroxide of the general form $(Mg,Ni)(Al)(SO_4,CO_3)\cdot nH_2O$ in addition to the Ni-Al LDH surface precipitate.

The composition of the Combined samples is a mixture of Ni-am$Al(OH)_3$ and Ni-HT (Figure 5.8) and closely resembles the Lamella samples, although LCF results indicate that the percentage of Ni-am$Al(OH)_3$ is greater in R4Combined and KLCombined likely due to the contribution of am$Al(OH)_3$ in the Se-Mo solids. The R3Combined data appear to contain an unknown component; the feature at 10.5 $Å^{-1}$ present in the other samples and Al-based standards is absent, resulting in a poor fit. The $\chi(k)\cdot k^3$ spectra of the KL samples (Figure 5.9) contain a first peak feature at 3.8 $Å^{-1}$ that is similar to the double-peaked feature of Ni-am$Al(OH)_3$ and Ni-HT rather than the symmetric feature in Ni-FH; this is despite the KL samples containing a greater

amount of Fe precipitates (resulting from greater concentrations of Fe in the raffinate). As such, Fe is abundant in R4 and KL samples but Al-phases appear to be a more dominant Ni control.

5.5 Environmental Significance

This study improves upon the understanding of concentration controls of EOCs such as As and Ni in hydroxide-neutralized precipitates of raffinate and provides evidence of layered double hydroxides and amorphous Al/Fe-hydroxides coordinating with As(V) tetrahedra and Ni(II) octahedra. With the identification of As and Ni sequestration mechanisms exerted by Al/Mg-bearing phases, it would be prudent to investigate the effects of changing pH, ionic strength, and time on these mechanisms and their influence on other EOCs such as Se(IV)/(VI) and Mo(VI). While these variables were out of the scope of this study, past studies investigated the stability of several of the components identified in this work. Aging studies showed strong chemical bonding of As(V) to Mg(Al/Fe)-LDH precipitates results in minimal As(V) desorption at pH ≈ 9.5 (Paikaray et al., 2013; Robertson et al., 2016). A rate-based study showed ferrihydrite to be a stable, long-term sorbent (>10,000 a) for As(V) (Das et al., 2011a). Although in systems where Fe/As ≈ 3-4, 99.8% of the As(V) is fixed in the solid phase as a mixture of ferric arsenate and ferrihydrite adsorption complexes (Mahoney et al., 2005). Multiple studies indicate that ferric arsenate is unstable at neutral to alkaline pH (as encountered in lime-neutralized tailings) and dissolves incongruently over time, releasing As and precipitating ferrihydrite (Paktunc et al., 2008; Paktunc and Bruggeman, 2010). It is unclear if the resulting ferrihydrite would re-adsorb the dissolved As under these geochemical conditions. The aging of NiAl-LDH precipitates (which are more stable than pure-phase Ni-hydroxides) is demonstrated to increase the stability of these phases (Scheckel et al., 2000). While not all of the EOC control phases identified in the current study have been thoroughly characterized, a study of tailings from the DTMF shows near constant tailings porewater concentrations of As and Ni over fifteen years residence time suggesting a degree of in-situ stability (Shaw et al., 2011). Under the assumption that the controls identified in the present study prevail in the tailings studied by Shaw et al. (2011), these controls can be expected to be stable for multiple years. However, further investigations, including aging studies, will be required to confirm the geochemical stability of the identified phases and the extent of their roles as concentrations controls of EOCs in the tailings.

The results of the present study can be transferred to other industries and environments with similar processes where precipitation of metal-hydroxides and EOCs occurs and stable sequestration of As and Ni is desired. Understanding the complete system of concentration controls of EOCs in this neutralization process will allow for tailings facilities to be better designed for geochemical stability and could be useful for environmental remediation efforts of acid mine drainage, acidic soil sites with elevated Al and Ni concentrations, and As contaminated drinking waters.

5.6 Acknowledgments

Financial support was provided by Cameco Corporation and the Natural Sciences and Engineering Research Council of Canada (NSERC) through a Senior Industrial Research Chair to MJH (grant 184573) and an NSERC CGS-M (JR). Research described in this paper was performed at the Canadian Light Source, which is supported by the Canada Foundation for Innovation, NSERC, the University of Saskatchewan, the Government of Saskatchewan, Western Economic Diversification Canada, the National Research Council Canada, and the Canadian Institutes of Health Research. The use of the HXMA beamline at the Canadian Light Source and the support received by the HXMA beamline staff (Dr. Ning Chen and Dr. Weifeng Chen) is gratefully acknowledged. The authors also appreciate the input from Dr. Dogan Paktunc and two anonymous reviewers which greatly improved the manuscript.

6.0 GEOCHEMISTRY OF URANIUM MILL TAILINGS IN THE ATHABASCA BASIN, SASKATCHEWAN, CANADA - A REVIEW

PREFACE

This chapter is intended for submission as a journal article. This chapter fulfills Objective 4 (compile a review of the literature on the U in-pit tailings management facilities of the Athabasca Basin). The results from Chapter 3, 4, and 5 were included in the complete review of published literature on the subject and fill in gaps in the literature pertaining to Al and Mg mineralogy and the geochemical controls exerted by these minerals on EOCs.

6.1 Abstract

The Athabasca Basin, located in northern Saskatchewan, Canada, is a major source of global uranium (U) and an important economic driver for the province and country. The Athabasca Basin U deposits consist of uraninite and pitchblende dominated with clay, silicate, arsenide, and sulfide minerals, all of which are associated with varying concentrations of As, Se, Mo, Ni, and ^{226}Ra (elements of concern; EOCs). Uranium production generates tailings that are often enriched in these EOCs. Athabasca Basin U tailings are the subject of many studies with the objective of defining the short- and long-term geochemical evolution of tailings and the potential impact of these tailings to the surrounding hydrosphere and biosphere. These studies are the focus of the review.

Three U mills are operational in the Athabasca Basin (Rabbit Lake, Key Lake, and McClean Lake). These mills use an oxidative acid leach process (to dissolve U) that dissolves many of the arsenide and sulfide minerals in the U ore. Metal(loid)s that dissolve in the leaching process are precipitated as low solubility secondary minerals and surface complexes in neutralization processes to minimize their aqueous concentrations within mill discharge waters and tailings porewater. The precipitates of the neutralization process are combined with the

residual leached solids (leach residue) and discharged to sub-aqueous in-pit tailings management facilities (TMF). The tailings consist of unleached primary minerals (such as quartz, clay, silicates, and minor sulfides and arsenides) and fine grained, amorphous secondary minerals from the neutralization process (such as $Fe(OH)_3$, $Al(OH)_3$, and mixed-metal layered double hydroxide). The secondary minerals control the aqueous concentrations of EOCs during the neutralization process and in the tailings body. The in-pit TMFs are engineered to maintain hydrogeological conditions that limit transport of EOCs from the tailings mass to the surrounding groundwater regime.

Many studies have contributed to the understanding of the geochemical behaviour of these tailings. Using nearly two decades of data from tailings and neutralization process sampling campaigns and controlled laboratory experiments, the goal of this review is to provide a comprehensive analysis of the geochemistry and long-term behaviour of U tailings in the Athabasca Basin and develop a geochemical model of the tailings system. Results of this review are applicable to tailings generated from other milling operations with comparable hydrometallurgical processes, ores, and gangue mineral assemblages. The holistic review presented here also allows for commentary on the weaknesses and limitations to the current understanding of the tailings geochemistry.

6.2 Introduction

6.2.1 Development of the Uranium Industry in the Athabasca Basin

The Athabasca Basin covers 85,000 km^2 of northern Saskatchewan (and a small part of Alberta), Canada (Figure 6.1), and is a major source of global uranium (U) supplies. The basin hosts unconformity-type U ores that are comprised of uraninite (UO_{2+x}) and coffinite ($U(SiO_4)_{1-x}(OH)_{4x}$) intergrown with silicate and clay gangue minerals (Hossain, 2014; Jefferson et al., 2007). Uranium mined from the Basin comprised 22% (or 13,325 tons U) of the world's supply in 2015, and there are 235,000 tons of known economically mineable U in reserve in the Basin as of 2014 (Saskatchewan Mining Association, 2014; World Nuclear Association, 2016a). As of 2016, over 11% of the world's electricity is generated by nuclear power plants (World Nuclear Association, 2016b). As such, the region is an important source of U for nuclear power plants and global efforts to reduce carbon-based fuel consumption (World Nuclear Association, 2016b). The U mined and

milled in the Basin is also economically important to Canada and the province of Saskatchewan. Canada exported 85% of U mined in the basin, valued at CAD 1 billion, in 2013. The remaining U supplied 15% of Canada's electricity (Natural Resources Canada, 2014).

The Athabasca Basin contains some of the richest U deposits in the world, with grades ranging 0.5-25% U_3O_8 by mass (Bharadwaj and Moldovan, 2005; World Nuclear Association, 2016c). Uranium production in the basin began at Rabbit Lake in 1975 (grades of 0.8% to 2.1% U_3O_8). Mining and milling activities increased with the commissioning of the Cluff Lake (decommissioned in 2002) and Key Lake operations in 1980 and 1983, respectively (World Nuclear Association, 2016c). The McClean Lake mill began operation in 1999, mining and milling ore from the JEB, Sue A, Sue B, Sue C, and Sue E deposits (averaging 2.4% U_3O_8; World Nuclear Association, 2016c). In 2014, McClean Lake began milling ore (averaging 20.7% U_3O_8) from the Cigar Lake deposit (World Nuclear Association, 2016c). The Key Lake mill processes ore from the McArthur River deposit (averaging 25% U_3O_8) and production is expected to continue until 2034 (Bharadwaj and Moldovan, 2005; Cameco Corporation, 2012). The locations of current and historic U mills and mines in the basin are shown in Figure 6.1. Earlier U mining operations (1950's) on the northern shore of Lake Athabasca near Uranium City (Figure 6.1) are not considered part of Athabasca Basin mining operations because they are not part of the same geological group and are often rich in carbonate minerals (Merritt, 1971).

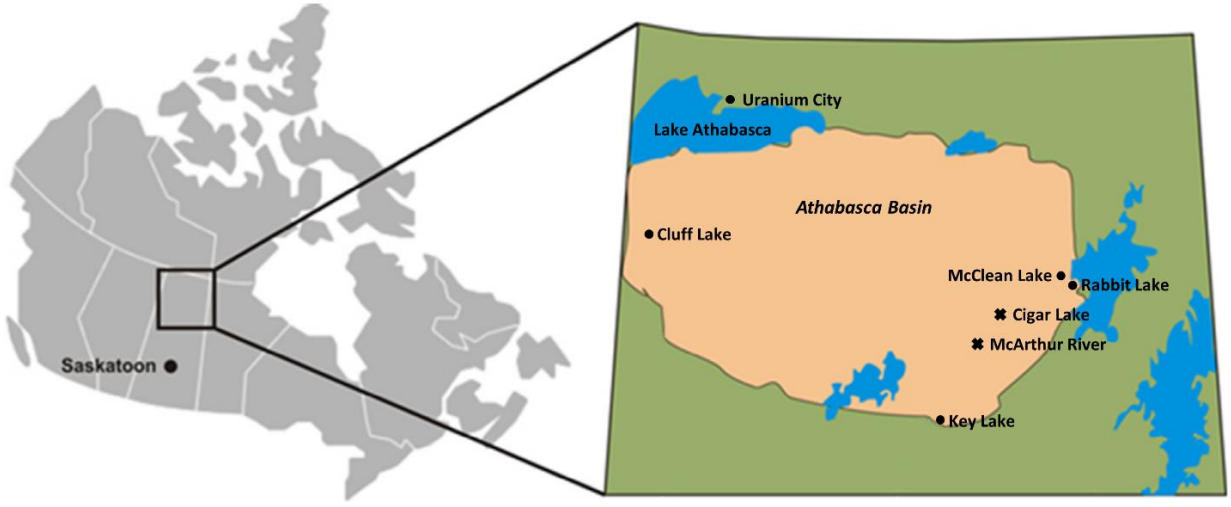

Figure 6.1. Location of the Athabasca Basin and the positions of past and present U mills and major ore deposits in the region (adapted from Liu et al. (2011)). Circles denote locations of mills and mines, 'X's denote mines only. The mines at Rabbit Lake are Collins Bay A, B, and D-zones; mines at Key Lake are Deilmann, Gaertner and Key Lake; mines at McClean Lake are JEB, Sue A, B, C, and E.

With the ongoing expansion of U mining in the basin, the environmental impact of mine and mill tailings generated from U production must be understood. The tailings slurries (a mixture of liquid and solid waste from the mill process) can be rich in elements of concern (EOC) including As, Ni, Se, Mo, and ^{226}Ra. Above ground tailings management facilities (TMF) were the first method of tailings storage when U mining and milling in the basin began in the 1970's (Donahue, 2000). These TMFs were constructed with engineered berms and long-term dedicated collection systems for recycling tailings seepage and surficial supernatants back to mill neutralization circuits. These facilities confined the tailings above the water table to minimize transport of contaminants present in the tailings porewater and were constructed at the Cluff Lake, Rabbit Lake, and Key Lake mine sites. Above ground TMFs were replaced a decade later with in-pit TMFs that use the pits of mined-out deposits for tailings storage. In-pit TMFs are engineered to optimize tailings consolidation, minimize groundwater flow through the tailings, and ensure EOC transport is controlled by diffusion processes. The first in-pit TMF was constructed at Rabbit Lake in 1984 and is called the Rabbit Lake In-Pit Tailings Management Facility (RLITMF; Donahue et al., 2000). The second in-pit TMF in the basin was the Deilmann Tailings Management Facility (DTMF) constructed at Key Lake in 1996 in the mined out Deilmann pit (a cross-section of the DTMF is shown in Figure 6.2; Shaw et al., 2011). The third and most recent TMF was constructed at McClean Lake in 1999 and is called the JEB TMF (Figure 6.3; Mahoney et al., 2005). All three mills discharge tailings sub-aqueously to the TMFs to prevent transportation of contaminated dust and to spread the tailings more evenly around the TMF (IAEA, 2004).

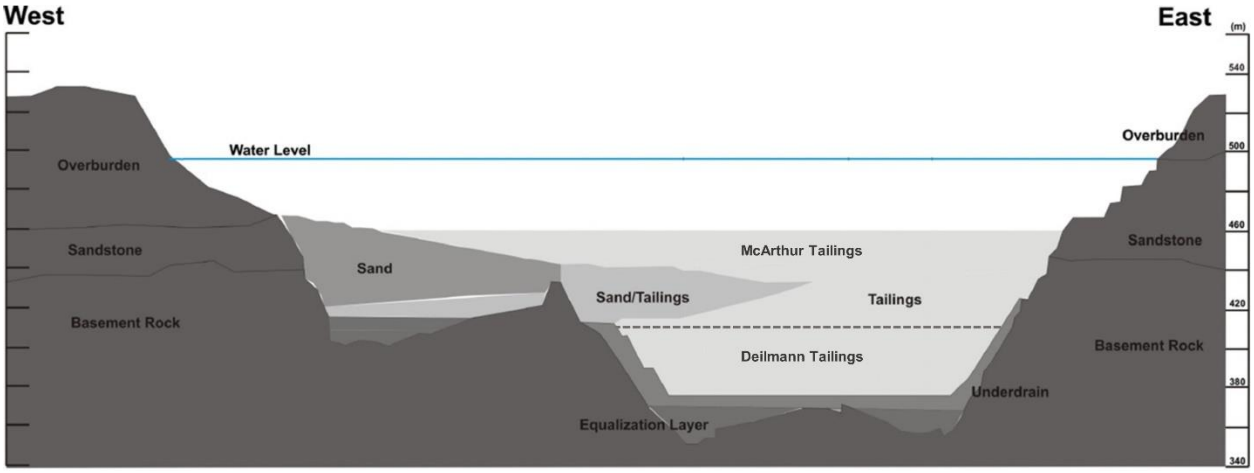

Figure 6.2. Cross-section of the DTMF at Key Lake ca. 2009. The horizontal dashed line represents the boundary at 410 masl where the tailings origin transitions from the Deilmann ore deposit to the McArthur River ore deposit (adapted from Shaw et al. 2011).

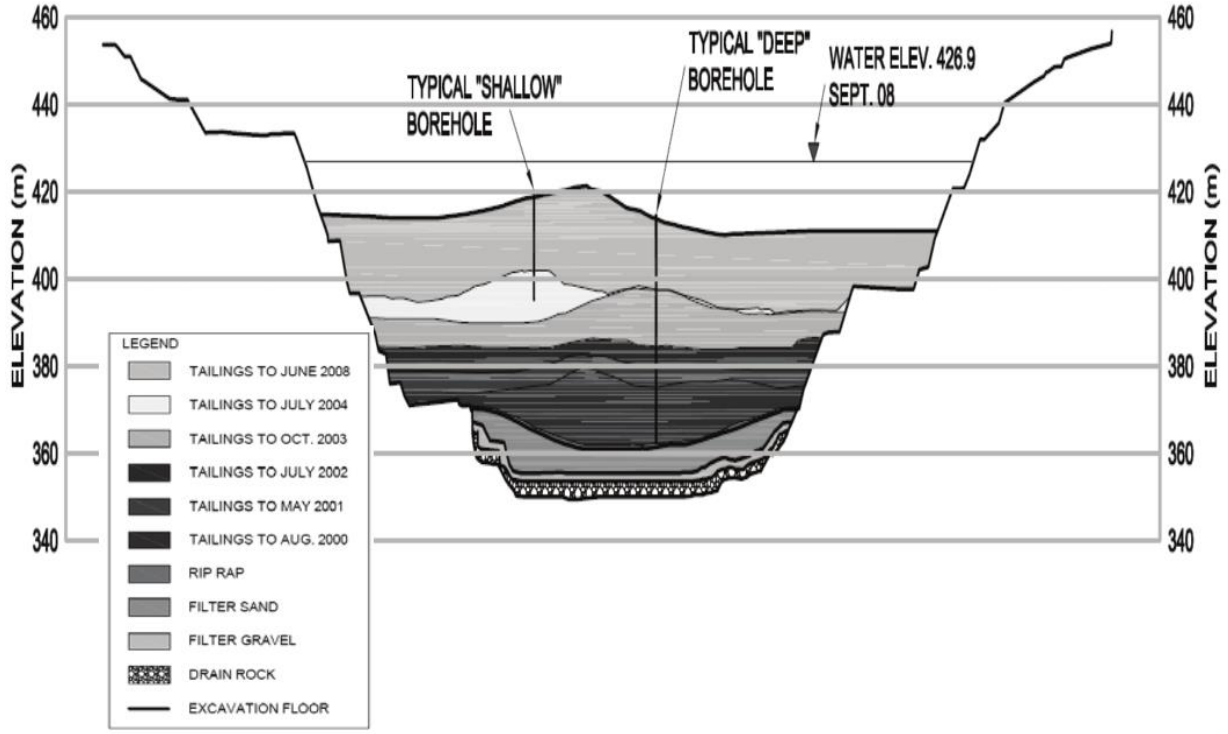

Figure 6.3. Cross-section of the JEB TMF at McClean Lake ca. 2008 (from Frey et al. 2010).

6.2.2 The Uranium Milling Process

The U milling process (which is dependent on the ore mineralogy) defines the geochemistry of U tailings. The major characteristics of the Rabbit Lake, Key Lake, and McClean Lake mills are summarized in Table 6.1. The conventional U milling process (Figure 6.4) follows the pathway of: comminution, leaching, solid-liquid separation, purification, precipitation, and packaging. The first four steps of this process impact the tailings geochemistry, although the precipitation step also impacts the geochemistry in some mills.

Table 6.1. Major characteristics of each mill in the scope of the review that affect tailings geochemistry.

	Rabbit Lake Mill	Key Lake Mill	McClean Lake Mill
Host Rock Characteristics	Monometallic and polymetallic	Monometallic (current) and polymetallic (past)	Polymetallic
Ore Mineralogy	Uraninite, pitchblende	Uraninite, pitchblende, coffinite	Uraninite, pitchblende, coffinite
Leach Process Reagents	H_2SO_4, $NaClO_4$	H_2SO_4, O_2	H_2SO_4, H_2O_2, $Fe_2(SO_4)_3$, O_2
Initial Raffinate Fe/As[a]	1-4	15-70	1-4
Neutralization Reagents	CaO, $BaCl_2$, $Fe_2(SO_4)_3$	CaO, $BaCl_2$, H_2O_2	CaO, $BaCl_2$, $Fe_2(SO_4)_3$
Leach Residue	Mixed with neutralized raffinate slurry	Mixed with neutralized raffinate slurry	Mixed with raffinate before neutralization
Neutralization Steps	3	3	2
Tailings Discharge pH	10 – 11	10 - 11	7 - 8
Tailings Discharge Control	Injection, subaerial, or submerged discharge	Submerged discharge	Placement by tremie pipe

[a] Ranges estimated based on published raffinate compositions

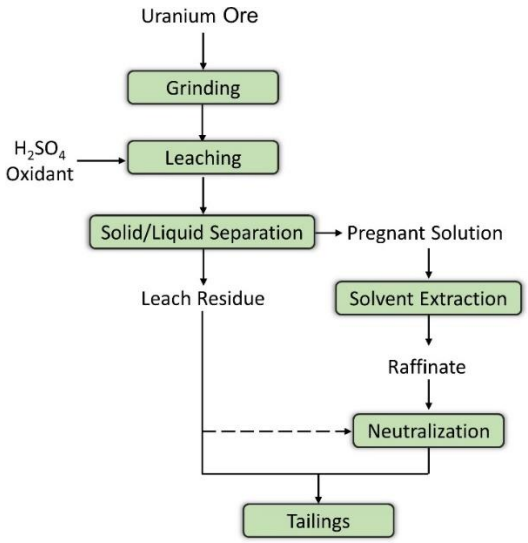

Figure 6.4. Generalized process flow diagram of the tailings stream of the U milling processes used in the Athabasca Basin.

The U ore brought to the mill from the mine is sized through crushing and grinding (comminution; particle size distribution of 30-40% < 75 µm) to optimize the exposure of U minerals for the downstream leaching process (Merritt, 1971). Next, the ore is fed to the leaching

process as a slurry (ore mixed with water). The lixiviant used during leaching is dependent on the host rock mineralization. Athabasca Basin U mills use a strong acid leach process to dissolve U minerals because the ores occur with clay and silicate minerals. Sulfuric acid is used in combination with O_2, $HClO_4$, or H_2O_2 to convert insoluble U(IV) to soluble U(VI) at temperatures between 50-60°C and Eh ≥ 600 mV. The leaching of U is described by the dissolution-redox series (Eq. 6.1-6.2):

$$2Fe^{2+} + \frac{1}{2}O_2 + 2H^+ \rightarrow 2Fe^{3+} + H_2O \quad (6.1)$$

$$UO_{2(uraninite)} + 2Fe^{3+} \rightarrow UO_2^{2+} + 2Fe^{2+} \quad (6.2)$$

Iron(II) is generated by the dissolution of Fe-containing minerals and from oxidation of elemental Fe resulting from mechanical abrasion of equipment in the grinding circuits (Merritt, 1971). At McClean Lake, $Fe_2(SO_4)_3$ is added (if there is not enough Fe in the ore) to ensure U(IV) is oxidized to maximize U recovery. The acidic and oxic conditions of the process dissolve and oxidize other minerals present in the host rock, resulting in a solution rich in Fe, Al, Mg, Si, As, Ni, Se, Mo, SO_4, and U (among other elements). These reactions are enhanced due to the increased surface area after comminution. The oxidation of gersdorffite (NiAsS) is an example of the concomitant dissolution of As and Ni with U (Eq. 6.3).

$$2NiAsS + 3H_2O + \frac{13}{2}O_2 \rightarrow 2SO_4^{2-} + 2AsO_4^{3-} + 2Ni^{2+} + 6H^+ \quad (6.3)$$

Uranium recoveries during leaching are > 95%; however, the majority of host rock (refractory silicates and clay minerals) and minor amounts of sulfide and arsenide minerals survive the leaching process. These minerals are separated from the U-rich leachate (pregnant leach solution) using clarifiers forming a thickened slurry called the leach residue.

The purification step separates the U from the other dissolved metals and metalloids. Solvent extraction is used in milling processes, although ion-exchange techniques are also used as an alternate purification step. An organic solvent selectively extracts U from the pregnant leach solution. The resulting aqueous solution is termed raffinate and is acidic (~pH 1-2) and rich in major elements (Mg, Si), metal(loid)s (Al, As, Co, Cu, Fe, Mo, Ni, Se) and sulfate. The U-rich stream continues through the mill to produce a final "U ore concentrate". The remainder of the process (U precipitation and packaging) is beyond the scope of this review.

The raffinate is the primary carrier of EOCs in the milling process and is treated by a neutralization process to remove the EOCs. The neutralization process used by the mills in the basin all follow the same general principles. Raffinate is neutralized to neutral to alkaline pH with slaked lime (hydrated CaO) resulting in precipitation of the dissolved metal(loid)s as secondary minerals. The precipitates are separated from the aqueous solution using thickeners or clarifiers. The neutralized aqueous solution is analyzed, and, if the concentrations of metal(loids) meets regulatory requirements, the solution is discharged to the environment. The thickened precipitates are pumped as a slurry to a TMF for final disposal. Depending on the mill, the leach residue from the leaching circuit is either neutralized with the raffinate or with the neutralized raffinate slurry prior to disposal to the TMF. The environmental conditions of the TMFs are discussed in Chapter 6.6.2.

6.2.3 Objectives

Elements of concern originally present in primary minerals in the ore were solubilized during oxidative leaching and subsequently adsorbed or precipitated in secondary minerals before being discharged into TMFs. The stability of these newly formed secondary minerals and the unreacted primary minerals is the subject of numerous studies of U tailings in the basin. A key driver for these studies is the extensive federal and provincial regulatory oversight of the tailings bodies. These regulatory agencies require containment of mine and mill tailings for 10,000 years for facilities licensed by the Canadian Nuclear Safety Commission (Mahoney et al., 2007; Moldovan et al., 2008). These requirements include minimizing EOC transport to the regional groundwater regime and meeting water quality objectives. Geochemical studies of the tailings bodies define the potential short- and long-term environmental impacts of EOCs on the hydrosphere and biosphere to determine if regulatory requirements can be met with current practices.

The objectives of this review are to: (1) integrate the existing literature into a single document and critically review the current understanding of mineralogical controls on EOCs in tailings; (2) define the long-term environmental impacts of EOCs in tailings generated in the basin; and (3) identify potential limitations in our scientific understanding.

This review article is arranged into eight sections. The sampling and experimental methods used to study tailings geochemistry are presented to outline the data collected over the past two decades. The mineralogy of the U ore deposits are characterized followed by discussion on the fate of the non-U minerals during the milling process and how they affect the final tailings. Next, the effluent treatment systems of the three mills are outlined followed by detailed analysis on the secondary minerals that form during effluent treatment and the mineralogical controls exerted on EOCs in these processes. The geochemistry of the tailings bodies are evaluated to provide a summary of the current and future states of the U tailings in the basin. The results of the review are integrated into a geochemical model of the neutralization and tailings systems to predict long-term geochemical conditions. Because the extent of mineralogical and EOC characterization undertaken at U mills and tailings bodies is far greater than any other acid-leaching milling processes of metals and resultant tailings bodies, we relate our findings to understand the mineralogical controls on EOCs in other tailings bodies.

6.3 Sampling and Experimental Methods

Several methods are used to study the Athabasca Basin tailings system, ranging from in situ analysis of decades-old tailings to studies of laboratory generated precipitates of synthetic raffinate solutions. Table D.1 summarizes the published geochemical literature relating to the in-pit TMFs and neutralization circuits of the Athabasca Basin mills. This section outlines the methods that are used, with the objective being to introduce the main methods used in the Athabasca Basin literature and to inform future studies of the most appropriate techniques to collect geochemical data.

6.3.1 *In Situ* Sampling Campaigns

Studying the precipitates directly from each mill's raffinate neutralization process and the *in situ* tailings present in the TMFs is the most valuable tool in understanding the long-term geochemistry of the tailings. A mixture of leach residue, waste rock, and neutralized raffinate precipitates have been deposited at the RLITMF since 1984, DTMF since 1996, and JEB TMF since 1999 (Donahue et al., 2000; Mahoney et al., 2005; Shaw et al., 2011). This provides researchers with over three decades of *in situ* aging tests to study. Because tailings are continually layered on top of each other and stratigraphically separated (Figure 6.5), the geochemical evolution

of the tailings can be studied by sampling material at various depths and time intervals. Porewater and solid phase chemical compositions are measured and can be used for modeling calculations and to study spatial and temporal trends of the tailings. Solid samples are subjected to a suite of complementary characterization techniques such as sequential extractions, X-ray diffraction (XRD), X-ray absorption spectroscopy (XAS), and electron microscopy (EM). Critical information about the geochemistry and ultimate reaction pathways can be determined from these data with an authenticity that cannot be replicated in the laboratory.

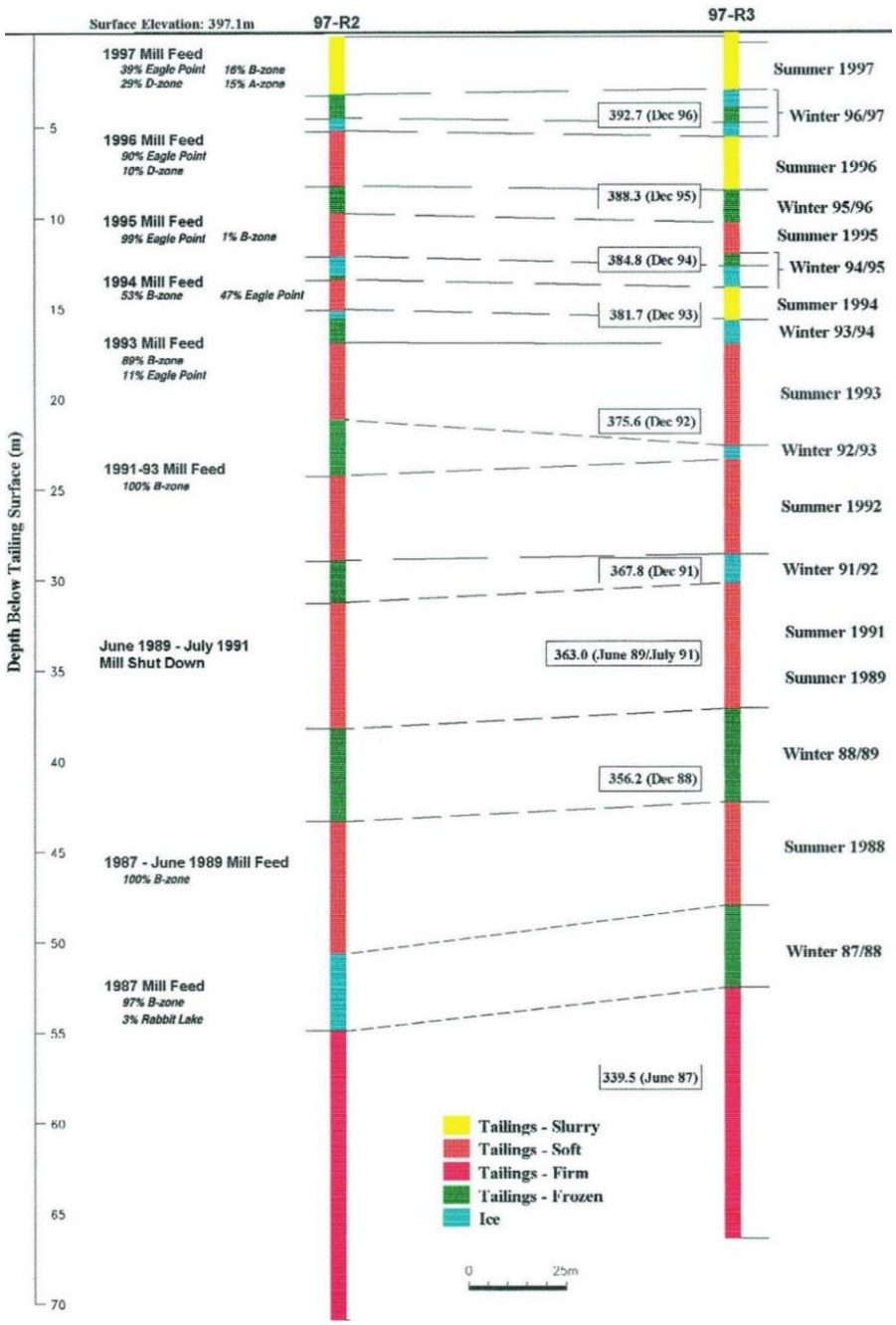

Figure 6.5. Stratigraphic diagram of core samples collected from the RLITMF in 1997 showing the corresponding ore being fed to the mill at the time of deposition (from Donahue et al. 2000).

In situ sampling campaigns are commonplace for the Athabasca Basin mills (although not all of the data is published in peer-reviewed journals). The majority of these studies collect tailings cores from boreholes that span the entire depth of the tailings, enabling chronological characterization of the tailings. McClean Lake personnel conduct sampling campaigns of the JEB TMF as part of their tailings optimization and validation program with the objectives of

understanding the reactions controlling EOC solubility during neutralization, optimizing the tailings neutralization process, and evaluating the long-term behaviour of EOCs in the TMF (Blanchard et al., 2015; Hayes et al., 2014; Mahoney et al., 2005). At the Key Lake DTMF, Shaw et al. (2011) sampled tailings cores in 2004, 2005, 2008, and 2009 from the same four locations in order to characterize the spatial and temporal evolution of the porewater chemistry and the tailings mineralogy (the results will be discussed in Chapter 6.6.2). In addition, geochemical data from as-discharged tailings (i.e., tailings at the time of deposition) were compared to the aged tailings to further understand the geochemical evolution. Similar sampling campaigns completed at the RLITMF allowed for robust geochemical modeling of As controls in the tailings (Donahue et al., 2000; Donahue and Hendry, 2003; Pichler et al., 2001). The solid phases of samples from all TMFs are characterized to varying degrees using X-ray absorption near edge spectroscopy (XANES) and extended X-ray absorption fine structure (EXAFS) techniques which allow oxidation states, speciation, and relative proportions of mineralogical phases to be determined (Essilfie-Dughan et al., 2013, 2012, 2011b; Frey et al., 2010; Hayes et al., 2014; Moldovan et al., 2003).

Sampling campaigns are also conducted directly in the neutralization processes of the mills to study the secondary precipitates prior to being mixed with leach residue as tailings. The precipitation profiles as a function of pH of each major element was reported for the Rabbit Lake and Key Lake mills through *in situ* sampling (Bharadwaj and Moldovan, 2005; Gomez et al., 2013a). These profiles allow the mineralogy of the precipitates to be inferred as a result of the decreasing concentrations and show which stages are responsible for precipitation of specific EOCs. These campaigns bypass the inherent hurdle of primary minerals from the leach residue masking or convoluting signals in characterization methods of secondary minerals (although this still occurs at the McClean Lake mill, as the leach residue is mixed with the raffinate prior to neutralization). However, the precipitates in the raffinate neutralization samples are newly formed and likely not at equilibrium but they give researchers the initial conditions of the tailings which are required to trace the geochemical evolution.

In situ sampling campaigns are the best way to study the geochemistry of these systems; however, there are difficulties in collecting these samples that limit the feasibility of these campaigns. Drilling for tailings samples is costly and requires diligence to properly preserve the samples. Logistically, sending radioactive samples off-site for the appropriate analytical tests can be prohibitive due to regulatory restrictions and shipping costs. In addition, the sampling

environment in the mill is uncontrolled and many variables can affect the sample. Process upsets make it difficult to collect representative, steady state samples. The best way to eliminate these variables is to collect as many samples as possible. These difficulties can be balanced with well-designed laboratory experiments.

6.3.2 Laboratory Experiments

While *in situ* sampling is the best method for studying the tailings geochemistry, the complexity of the samples makes it difficult to completely describe the geochemistry. Laboratory experiments provide a controlled environment to minimize uncertainties and test only specific hypotheses. These studies should strive to replicate the *in situ* conditions as closely as possible, although the limitations of laboratory experiments should be acknowledged in the context of these studies' conclusions. Studies that utilize laboratory experiments should work cooperatively with field studies; conclusions from the field should be tested rigorously in the laboratory, while observations in the laboratory should be confirmed in the field.

6.3.2.1 Batch Mode Experiments

The batch mode experiments in Table D.1 are typically performed for two reasons: (1) initial tests or feasibility studies are required prior to starting larger scale experiments (such as continuous-mode experiments or mill trials) or (2) a specific aspect of the tailings neutralization process needs to be studied under controlled conditions (e.g., aging tests, new reagents, pH setpoints, or other altered process conditions). Langmuir et al. (1999) performed batch experiments at McClean Lake prior to commissioning of the JEB TMF in order to demonstrate that porewater concentrations of As and Ni in the final tailings would meet the design criteria and remain stable. The test results provided a baseline for the McClean Lake operation once tailings deposition to the JEB TMF began. At Key Lake, batch experiments were used to determine a method to decrease Se and Mo concentrations in the mill's final effluent (Lieu et al., 2010). These experiments led to the implementation of a vessel called the Se-Mo thickener to the neutralization process and resulted in improved final effluent quality. These examples demonstrate the utility of batch-mode laboratory tests for initial testing of process performance and improvement.

Small scale laboratory experiments are also important for characterizing geochemical reactions in Athabasca Basin tailings. Many of these experiments are not limited to U mill tailings but are directly motivated by the industry. Examples of these experiments include characterizing As(V)-Fe(III) precipitates (Jia et al., 2006), stability tests of Ca-Fe-arsenates (Becze et al., 2010), rates of ferrihydrite transformation as a function of adsorbed As (Das et al., 2011a), adsorption of Se on Fe-oxyhydroxides (Das et al., 2013), and the effect of abiotic reduction of ferrihydrite on adsorbed As, Mo, and Ni (Mario A. Gomez et al., 2013b).

6.3.2.2 Continuous Mode Experiments

Continuous-mode laboratory experiments provide replication of the steady state conditions of the mill and are favourable over batch-mode experiments. However, the cost, time, and difficulty in performing continuous-mode experiments in these experiments can be prohibitive. Their size and cost also limits the sample size of the experiment when compared to batch-mode. As such, high quality statistics for continuous experiments are difficult to obtain.

De Klerk et al. (2012) constructed a general continuous co-precipitation circuit with three neutralization reactors and a final clarification stage to separate the precipitates from the aqueous phase. Their model allowed them to test the effect of the number of neutralization stages on the neutralization of acidic sulfate solutions concentrated with Fe(III) and As(V) and the effect of Ni and Al on the precipitates. Their primary focus was the characterization of the Fe-As precipitates and their morphology. They demonstrated a clear difference in the density and crystallinity of the precipitates between batch- and continuous-mode experiments, suggesting batch mode experiments may not be appropriate for secondary mineral characterization in these neutralization systems. Robertson et al. (2014) constructed a model of the Key Lake bulk neutralization process to simulate the aqueous and solid chemistry in a controlled environment. A validation study of the model showed the neutralization process chemistry was accurately replicated by the model (Robertson et al., 2014). Their model was used to characterize the Al and Mg secondary mineralogy of the Key Lake neutralization process and to determine the local coordination environment of As and Ni in the secondary minerals (Robertson et al., 2017, 2016). Bissonnette et al. (2016) built a model of the Key Lake neutralization process to test the influence of various ore blends on the secondary mineralogy generated by the neutralization process. These models allowed

controlled studies to characterize a complex mineralogical system and could be used for additional tailings characterization of different mills, raffinates, process conditions, etc.

6.4 Primary Mineralizations

6.4.1 Characterization of Uranium Ore

It is important to understand the type of deposits being milled as they have a strong influence on the mineralogy and composition of the resulting tailings. A broad range of mineralizations occur in the U deposits of the basin. The bulk mineralogy generally contains quartz (SiO_4) and phyllosilicates such as illite ($(K,H_3O)(Al,Mg,Fe)_2(Si,Al)_4O_{10}((OH)_2,(H_2O))$), Mg-chlorite ($Mg_5Al(Si_3Al)O_{10}(OH,F)_2$), kaolinite ($Al_2Si_2O_5(OH)_4$), muscovite ($KAl_2(Si_3Al)O_{10}(OH,F)_2$), and clinochlore ($(Mg,Fe)_5Al(Si_3Al)O_{10}(OH)_8$; Carl et al., 1992; Delaney et al., 1998). A summary of the mineralogy of the major deposits in the basin is presented in Table 6.2. These deposits can be divided into two types, monometallic and polymetallic. Monometallic U ores contain trace amounts of other metals (with the exception of Cu). The Eagle Point deposit milled at Rabbit Lake and the McArthur River deposit milled at Key Lake are examples of monometallic ores. Polymetallic U ores are associated with sulfide and arsenide minerals rich in Ni, Co, Cu, Pb, Zn, Mo, and Se. McClean Lake primarily mills polymetallic ores from the JEB, Sue A, Sue B, Sue C, Sue E, and (more recently) Cigar Lake deposits. The Collins Bay A, B, and D-zone polymetallic deposits are milled at Rabbit Lake. The Deilmann, Gaertner, and Key Lake deposits were all polymetallic deposits milled at Key Lake, but these deposits are mined out (although waste rock from these deposits is blended into the McArthur River ore feed for dilution; Jefferson et al., 2007).

The U ores in the basin are mostly in the form of uraninite and pitchblende, although there are occurrences of coffinite and uranophane (Jefferson et al., 2007). Of more relevance to this review, however, is the association of the U minerals with sulfide- and arsenide-rich mineralizations. The Key Lake, Deilmann, and Gaertner ore bodies contained elevated amounts of Ni- and Co-bearing arsenide/sulfide minerals (e.g., gersdorffite, niccolite (NiAs), and cobaltite (CoAsS); von Pechmann, 1981). Likewise, the ore milled at McClean Lake and Rabbit Lake is concentrated with up to 10% As and 5% Ni as arsenide/sulfide minerals (rammelsbergite ($NiAs_2$), niccolite, and gersdorffite; Donahue et al., 2000; Langmuir et al., 1999; Rinas et al., 2010). The

McArthur River ore currently milled at Key Lake contains lower concentrations of sulfide and arsenide minerals compared to the other deposits. Trace metals in the McArthur River ore are associated with pyrite, chalcopyrite ($CuFeS_2$), covellite (CuS), and arsenopyrite (FeAsS; Delaney et al., 1998; Jamieson and Frost, 1997). Analyses of the McArthur River ore by Heinrich et al. (2010) show Se and Mo are present in phyllosilicates, uraninite, and, to a lesser extent, sulfides (Heinrich et al., 2010). A characterization study of the McArthur River ore by Hossain (2014), showed As and Ni to be most frequently associated with cobaltite, gersdorffite, molybdenite, galena (PbS), pyrite, and chalcopyrite.

Table 6.2. Summary of the typical mineralogy of each major uranium deposit mined and milled at the reviewed sites.

Rabbit Lake	Key Lake	McClean Lake
Rabbit Lake - Niccolite, carollite, pyrite, chalcopyrite, bornite *B-zone* - Niccolite, gersdorffite, rammelsbergite, maucherite, bravoite, violarite, polydimite, safflorite, millerite, tennantite, pyrite, chalcopyrite, bornite, hematite *A-zone & D-zone* - Niccolite, gersdorffite, rammelsbergite, pararammelsbergite, hematite *Eagle Point* - Bravoite, chalcopyrite, bornite, marcasite	*Key Lake, Deilmann, Gaertner* - Gersdorffite, niccolite, cobaltite *McArthur River* - Pyrite, chalcopyrite, covellite, arsenopyrite, gersdorffite, cobaltite, molybdenite, galena	*JEB, Sue A, Sue B, Sue C, Sue E, Cigar Lake* - Gersdorffite, niccolite, rammelsbergite, galena, chalcopyrite, jarosite, pyrite, rutile

* All deposits contain major amounts of quartz, illite, chlorite, and kaolinite.

6.4.2 The Fate of Primary Gangue Minerals During Uranium Milling

The oxic-acid leaching of U ores dissolves the U minerals and many other host rock minerals; however, a fraction of the ore does not dissolve (leach residue) and is ultimately discharged as part of the tailings. The constituent elements of the dissolved minerals are precipitated downstream as secondary minerals during raffinate neutralization.

Hossain (2014) quantified the minerals that dissolve during acid leaching using mineral liberation analysis (Table 6.3). Leaching tests of McArthur River ore showed that kaolinite, quartz,

and illite are the most resistant constituents in the ore with only 2%, 6%, and 7% of these phases dissolving, respectively. Unlike kaolinite and illite, the other phyllosilicates (mica and chlorite) were less resistant to acid leaching. The mica content (presumably muscovite due to previous characterization of this ore) decreased 26% and chlorite decreased 84% after leaching; these minerals are a major source of soluble Al and Mg (and potentially Fe(II)) that is precipitated downstream during raffinate neutralization. Phyllosilicate dissolution, especially chlorite (Eq. 6.4; Lowson et al., 2005) contributes a large number of major cations (i.e., Al, Mg, and Fe) to the eventual raffinate on a mass basis.

$$(Mg, Fe, Al)_6(AlSi_3O_{10})(OH)_8 + 16H^+ \rightarrow 6(Mg, Fe, Al)^{13+} + Al^{3+} + 3H_4SiO_4 + 6H_2O \quad (6.4)$$

Table 6.3. Adapted mineralogical analysis of McArthur River ore blended with waste rock and subjected to an acidic, oxic leaching process. Proportions of mineral phases were determined by mineral liberation analysis (from Hossain 2014).

	Percent Mineral Abundance		
	Leach Feed Ore	**Leach Residue**	**Unleached**
Quartz	60.15	72.40	94
Mica	6.2	5.85	74
Pyroxene	3.84	2.13	---
Chlorite	3.4	0.69	16
K-feldspar	2.37	2.80	---
Illite	1.75	2.10	93
Kaolinite	0.52	0.65	98
Pyrite	0.3	0.21	55
Hematite	0.19	0.19	---
Chalcopyrite	0.15	0.07	36
Galena	0.09	0.02	52
Barite	0.08	0.19	---

Sulfides are slightly resistant to the oxic leaching process, as 45% of the pyrite, 48% of the galena, and 64% of the chalcopyrite leached into solution (suggesting kinetic limitations). A major portion of the dissolved Fe that is precipitated downstream likely originates from the oxidative dissolution of pyrite and chalcopyrite, although uncharacterized Fe-oxides also contribute to the total soluble Fe. Pyrite is oxidatively dissolved as shown in Eq. 6.5, in addition to a cascading oxidation couple for pyrite as shown in Eq. 6.6-6.7:

$$2FeS_2 + 7O_2 + 2H_2O \rightarrow 2Fe^{2+} + 4SO_4^{2-} + 4H^+ \quad (6.5)$$

$$2Fe^{2+} + 1/2\,O_2 + 2H^+ \rightarrow 2Fe^{3+} + H_2O \quad (6.6)$$

$$FeS_2 + 14Fe^{3+} + 8H_2O \rightarrow 15Fe^{2+} + 2\,SO_4^{2-} + 16H^+ \quad (6.7)$$

Other sulfides such as gersdorffite dissolve by a similar mechanism. The release of As and Ni is demonstrated through Eq. 6.8:

$$4NiAsS + 6H_2O + 13O_2 \rightarrow 4SO_4^{2-} + 4AsO_4^{3-} + 4Ni^{2+} + 12H^+ \quad (6.8)$$

The remaining sulfides should be considered in long-term environmental assessments of the tailings due to their oxidation potential, thus releasing any associated EOCs and generating acid (discussed further in Chapter 6.6.3). These minerals were likely able to survive the leaching process for two reasons. First, sub-optimal grinding results in large grains of sulfide minerals entering the leaching process. The decreased surface area to volume ratio inhibits oxidative dissolution rates. Given enough time in the leaching circuit, these minerals would likely dissolve completely. Second, sulfide grains can be locked up in acid-resistant minerals such as quartz and phyllosilicates (observed by Hossain (2014) in BSE and EM images).

Similar (but less detailed) results were observed at Rabbit Lake where a sample of the leach residue contained primarily quartz and minor amounts of clays (Pichler et al., 2001). Kaolinite is a likely residual clay mineral due to the high concentration of Al_2O_3 measured (13.58%) compared to other oxide fractions in the leach residue. Minor amounts of total S remained in the leach residue, indicating the persistence of sulfide minerals in the Rabbit Lake process. Pichler et al. (2001) measured low concentrations of As and Ni in the leach residue compared to the neutralized secondary precipitates, indicating that these elements are solubilized during the leaching process. Leach residue data was not obtained for McClean Lake ores. Unlike the leach residues from Key Lake and Rabbit Lake, the leach residue stream from McClean Lake is mixed with the raffinate prior to neutralization (Mahoney et al., 2007). This should have the effect of increasing the dissolution of sulfide and arsenide minerals from the leach residue in the mill rather than dissolving in the tailings. The dissolution products can then be neutralized. Still, not all reactive minerals dissolve through this method as evidence of arsenide oxidation within the tailings is observed, and is discussed further in Chapter 6.6.3.

6.4.3 Primary Gangue Minerals in Tailings

The leach residue is disposed of in the tailings after a washing process that recovers as residual soluble U. Understanding the mineralogy of the leach residue will help define reaction pathways that could occur in the tailings over time. In the JEB TMF, RLITMF, and DTMF, the most common gangue minerals in the tailings are quartz, illite, and smaller amounts of kaolinite and chlorite (Hossain, 2014; Langmuir et al., 1999; Mahoney et al., 2005; Shaw et al., 2011). The leaching test in Table 6.3 reflects this observation. A study of laboratory generated tailings from the McClean Lake process quantified the amount of primary minerals remaining in the final tailings (including the neutralized precipitates) to be 26% illite, 25% quartz, 3.4% kaolinite, and 3.1% Mg-chlorite (Langmuir et al., 1999). Sulfide minerals are present in minor concentrations (<1%) and include galena, chalcopyrite, and pyrite. These results are consistent with Key Lake and Rabbit Lake leach residue samples discussed in Chapter 6.4.2.

Primary minerals associated with EOCs are important as they represent both a stable sequestration mechanism and a potential reactive pathway for the release of these elements in the tailings. Hossain (2014) shows As and Ni in the leach residue are mostly present in the clay size fraction (<2 μm), although associations to sulfide minerals also exist. Supporting these results, Essilfie-Dughan et al. (2013, 2012) characterized Fe and As in the tailings and observed chalcopyrite, pyrite and gersdorffite as the major primary Fe, As, and Ni minerals in the DTMF tailings. About 10-30% of the total Fe in the DTMF is in pyrite and chalcopyrite regardless of ore type, while 12% of the total As in the McArthur River ore section of the DTMF is in gersdorffite (Essilfie-Dughan et al., 2013). Pichler et al. (2001) made a similar measurement for As at Rabbit Lake where about 20% of the total As is associated with sulfide minerals. Molybdenum and Se were observed to be evenly distributed in the bulk and clay size fractions in McArthur River leach residue (Hossain, 2014). Molybdenite exists as a discrete Mo phase in both the JEB TMF and DTMF (Blanchard et al., 2015; Hossain, 2014). The presence of primary sulfide minerals in the tailings presents a potential risk of EOC mobilization through oxidation (discussed in Chapter 6.6.3).

6.5 Uranium Mill Raffinate Neutralization and Secondary Mineral Precipitation

6.5.1 Neutralization Processes

For U mills, all water that is brought into the mill (e.g., water added to the ore to produce a slurry, acid added to the leaching circuit, etc.) is discharged as clean effluent or tailings slurry. The water stream that needs the most treatment is the raffinate because it contains the greatest concentrations of EOCs and acidity (pH ≈ 1) compared to the other streams. Accordingly, the majority of literature (including this review) addresses raffinate neutralization because it is the only stream that majorly affects the tailings composition. Each mill in the basin neutralizes raffinate differently, however these neutralization processes all operate under the same principles: add a neutralizing agent (i.e., slaked lime) to the raffinate to precipitate the dissolved constituents, separate the precipitates from the water, discharge the water to the environment, and discharge the precipitates to the TMF.

The neutralization process at the Rabbit Lake mill evolved over the years since the first geochemical study on this system was published. Improvements to the process were made based on conclusions from these studies. All Rabbit Lake studies, however, were conducted before these improvements were made. As such, all discussion of Rabbit Lake geochemistry is in the context of the proceeding process flow (Figure 6.6a). The first iteration of the Rabbit Lake neutralization process neutralized raffinate in steps from pH 1 to 3.5, 6.5, and 8.5-11.0 in Pachucas (tall, cylindrical, air-agitated tanks). The residence time of each Pachuca ranges between 1 to 3 hours (in all discussed mills) depending on mill flow rates (Moldovan et al., 2003). A single clarifier was used to separate the final neutralized precipitates from the treated effluent. Clarifiers (or thickeners) used in the neutralization processes thicken the neutralized precipitate slurry from <5% solids to >15% solids with 35% solids being targeted for the final tailings. These precipitates were mixed with the leach residue that was neutralized upstream to pH 10-11. This final mixture was discharged to the RLITMF at pH 10-11. In 2008, the configuration of the Rabbit Lake solution neutralization process was changed (Figure 6.6a). Since then, raffinate is neutralized to pH 4.5-5.5 and flows to the low pH clarifier that separates low pH precipitates from solution. A second stage of neutralization raises the pH of the clarified solution to pH 10.5-11.2. The precipitates are separated from solution again in the high pH clarifier. The clarified solution is sent to an additional Ra removal and pH adjustment stage prior discharging as clean effluent. The low pH and high pH

precipitates are pumped to the residue neutralization circuit where the leach residue from the leaching and solid/liquid separation stages is mixed in. The target slurry pH is 8.5 prior to discharging the tailings to the RLITMF (Cameco, 2011). The upgrade to the solution neutralization process likely affects the precipitates that form at high pH, because the low pH precipitates are removed from the process early. If the low pH precipitates remain in solution during high pH neutralization, the following may occur: (1) there are more nucleation sites for high pH precipitates which may change crystal growth rates and alter the final mineralogy, (2) certain low pH precipitates (e.g., ferric arsenate) may re-dissolve and alter the solution chemistry, thereby affecting the saturation states of mineral phases, and (3) low pH surface complexes may be altered, resulting in adsorbed species transferring from low pH to high pH precipitates while also affecting final effluent quality. While not an exhaustive list, these reasons show that the conditions under which the precipitates are formed under will have an impact on their tailings geochemistry.

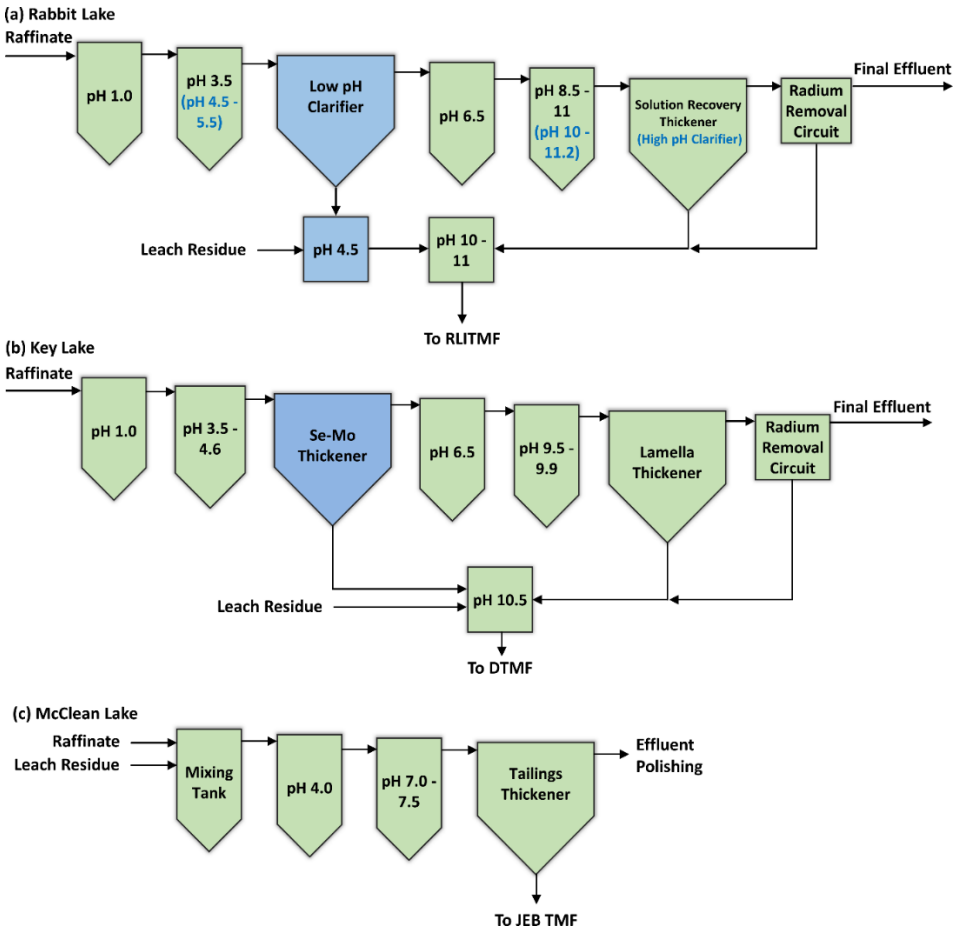

Figure 6.6. Process flow diagrams of the (a) Rabbit Lake, (b) Key Lake, and (c) McClean Lake raffinate neutralization processes. Additions to both the Rabbit Lake and Key Lake processes were made in 2008 and are denoted in blue. Changes to the pH setpoints are denoted in blue text.

The Key Lake neutralization process, like Rabbit Lake, was upgraded from its original design in 2008. Geochemical studies of Key Lake tailings were conducted on samples generated before and after these changes were made, a factor that must be taken into account when examining the geochemistry of a given sample. The original and upgraded process flow of the Key Lake bulk neutralization process is presented in Figure 6.6b. Raffinate (~pH 1-1.5) from the solvent extraction process is fed to Pachuca 2 where lime is added to a setpoint of ~pH 4. Barium chloride is added at Pachuca 2, Pachuca 3, and the Lamella thickener overflow to precipitate Ra (Liu and Hendry, 2011). Other contaminated water streams are also added to Pachuca 2; however, raffinate is the major source of EOCs. Prior to 2008, the neutralized slurry continued to Pachuca 3. Since 2008, a new thickener (called the Se-Mo thickener) was added to the process to separate the low pH precipitates before Pachuca 3. The Se-Mo thickener underflow slurry is pumped to the tails tank and the clarified aqueous overflow is pumped to Pachuca 3. In Pachuca 3 and 4, the pH is increased to pH 6.5 and pH 9.5. The pH 9.5 precipitates settle in the Lamella thickener where the underflow slurry is pumped to the tails tank and the clarified aqueous overflow continues to the Ra removal circuit. Sulfuric acid is added to three reactors to decrease the pH to 7.5, 6.5, and finally 6.0. Radium precipitates are settled in the Ra removal thickener and the solution flows to monitoring ponds prior to being discharged as clean effluent. In the tails tank, the leach residue from the CCD circuit is mixed with the Se-Mo, Lamella, and Ra removal thickener underflows and the pH is increased to 10.5. This mixture is the final tailings slurry and is discharged to the DTMF (Bharadwaj and Moldovan, 2005; Bissonnette et al., 2016; Gomez et al., 2013a; Robertson et al., 2016). As discussed for the Rabbit Lake process above, studies that analyzed neutralized precipitates and tailings deposited prior to 2008 are likely geochemically different from those generated after the implementation of the Se-Mo thickener.

The flow sheet of the McLean Lake neutralization process is shown in Figure 6.6c. Unlike Key Lake and Rabbit Lake, McClean Lake mixes the leach residue with the raffinate in a pre-treatment stage (i.e., prior to neutralization) with the goal of dissolving residual sulfides and arsenides that survived the leaching process. Ferric sulfate is added to this tank to maintain a molar $Fe(III)/As_{Total}$ ratio ≥ 3. Barium chloride is added to precipitate ^{226}Ra. Two neutralization stages are used in the process; lime is added to raise the pH 4 and 7.5 in each Pachuca. Each Pachuca has a residence time of 90 min. The neutralized slurry is transferred to a thickener from which the

underflow slurry is pumped to the JEB TMF, and the aqueous overflow is discharged as clean effluent (Hughes et al., 2010; Mahoney et al., 2007; Rinas et al., 2010).

There is no solid-separation stage of the low pH precipitates at McClean Lake like there is at the current Rabbit Lake and Key Lake neutralization processes (Figure 6.6a-c). This mode of mill operation is advantageous for seeding new precipitates, increasing the crystallinity of the precipitates, and increasing the slurry density which is desirable from an operational viewpoint (Demopoulos, 2009). Separating the precipitates at low pH prevents re-dissolution of pH-sensitive elements at higher pH stages. McClean Lake circumvents this issue by operating at a terminal pH (~7-8) slightly below the pH where re-dissolution of As, Se, and Mo occurs. This is in contrast to the Rabbit Lake and Key Lake processes that have terminal pH values of 10-11. The differences in terminal pH from mill to mill affects the major secondary mineralogy of the tailings as discussed in Chapter 6.5.2.

6.5.2 Secondary Mineral Precipitation

Secondary minerals constitute 10-20% of the total tailings mass, with the remaining being leach residues. With the exception of gypsum, these precipitates are generally amorphous (i.e., no long-range order) or nanocrystalline because of the rapid neutralization at high saturation conditions and ambient temperature and pressure inhibiting crystallization (Demopoulos, 2009). Here we describe the precipitation mechanisms and characteristics of the major secondary precipitates and the controls of these precipitation processes. This discussion will establish the basis for the mineralogical controls of EOCs described in Chapter 6.5.3.

The addition of slaked lime to the raffinate causes supersaturation and precipitation of metal-hydroxide minerals at multiple pH steps. The most important factor influencing the mineralogy of the resulting secondary precipitates is the concentrations of metal(loid)s in the raffinate (which is dependent on the mineralogy of the ore feed). A summary of the elemental compositions of raffinates from the three U mills in the basin is presented in Table 6.4. The origin of the raffinate composition is discussed in Chapter 6.4.1 and Chapter 6.4.2. There are differences in raffinate compositions between mills and also between different samples collected from the same mill at different times. These variations reflect the different ore deposits and the heterogeneity of ores from the same deposit. The variations in raffinate compositions makes it

difficult to generalize what secondary minerals will precipitate from neutralization processes, although general trends exist (discussed further in Chapters 6.5.2.1-6.5.2.3). As such, mill samples represent a snapshot in time rather than a representative sample of steady state operations. This emphasizes the need to sample over a long time span to characterize the wide range of possible secondary precipitates.

As discussed above, McArthur River ore is from a monometallic deposit while ores processed at McClean Lake and Rabbit Lake are dominated by ore from polymetallic deposits. The effect of monometallic ores on raffinate composition is shown by the elevated concentrations of Al and Mg (Table 6.4) in raffinates from McArthur River ore because of a large clay content (Table 6.3). In contrast, Al and Mg concentrations are generally lower in raffinates from polymetallic ores (milled at Rabbit Lake and McClean Lake). These data indicate that tailings resulting from McArthur River ore will be enriched in secondary Al/Mg precipitates and may possess a different set of EOC mineralogical controls compared tailings from polymetallic deposits. Concentrations of Fe are also elevated in McArthur River raffinates, although the difference in concentrations between mills is not as drastic as for Al and Mg. The McClean Lake samples of Mahoney et al. (2007) contained concentrations of Fe in the same range as McArthur River; however, these samples were spiked with Fe to maintain a molar Fe/As ratio > 4. The concentration of Fe is controlled at McClean Lake and Rabbit Lake with the addition of $Fe_2(SO_4)_3$ to maintain this ratio (discussed in Chapter 6.5.3.1). Key Lake has not required the addition of Fe to its raffinate because the McArthur ore contains elevated Fe and decreased As concentrations. In the mill samples, Fe(III) is the dominant Fe species; however, McClean Lake laboratory leaching experiments resulted in raffinates dominated by Fe(II). The reason for this discrepancy is unclear; however, it is possible that the redox conditions during the laboratory leaching tests were less oxic than in the mill, resulting in increased Fe(II). While McArthur River ore is a monometallic deposit associated with lower concentrations of As and Ni compared to the polymetallic deposits of the basin, it is blended with legacy Deilmann and Gaertner waste rock (polymetallic) in the grinding circuit, resulting in raffinate concentrations of As and Ni similar to those observed in McClean Lake and Rabbit Lake raffinates. The measured Eh for the samples range from 400-750 mV, representing oxic conditions at the beginning of raffinate neutralization. These initial conditions dictate the final secondary precipitate mineralogy.

Table 6.4. Compositional data of uranium mill raffinates from the Athabasca Basin. KL = Key Lake; ML = McClean Lake; RL = Rabbit Lake.

Mill Samples					**Analyte Concentration (mg/L)**										
Study	**Site**	**Ore**	**pH**	**Eh (mV)**	**Al**	**As**	**As(III)**	**As(V)**	**Fe**	**Fe(II)**	**Mg**	**Mo**	**Ni**	**^{226}Ra**	**Se**
Bissonnette 2016	KL	McArthur	1.6	596	3277	210			2429		2270	2.23	154		0.257
Gomez 2013	KL	McArthur	1.4		1635	27.8			1428		1044	3.14	23.3		0.4
Liu 2011	KL	McArthur	1.2		3510				2555		3020	1.264	99.2	150	
Mahoney 2007	ML	Unknown	1.5		420	732[b]			2400[b]		260		560[b]		
Mahoney 2007	ML	Unknown	0.97	670	200	690[b]	450	220	1850[b]	685	230		515[b]		
Moldovan 2005	RL	Unknown	1	750	498	526			862	86	502		265		
Laboratory Generated Samples[a]															
Bissonnette 2016	KL	McArthur	1.59	635	3167	195			4062		2792	3.08	295		0.376
Bissonnette 2016	KL	McArthur/ Millenium	1.16	610	5076	223			5628		4438	6.1	222		0.45
Bissonnette 2016	KL	Millenium	1.46	629	1108	47.7			1311		553	1.34	63.6		0.127
Langmuir 1999	ML	JEB	0.77	400	434	366	72	294	430	310	341		201	56.84	
Langmuir 1999	ML	JEB	0.85	576	503	271	52.9	218	517	413	303		144	43	
Langmuir 1999	ML	Sue C	0.3	632	708	141	29	112	811	633	455		145	27.3	
Langmuir 1999	ML	ML	0.75	623	393	275	52.5	222	950	419	61.7		164	1.18	
Langmuir 1999	ML	Sue A + B	0.3	491	1690	2430	493	1937	1080	821	716		2740	26.7	
Langmuir 1999	ML	Cigar	0.4	588	4280	580	126	454	3260	2670	2330		453	82.7	
Langmuir 1999	ML	Sue C + Cigar	0.34		1601	251	53	198	1423	1142	924		222	41	
Langmuir 1999	ML	Midwest/Sue A/ Sue B/Cigar	0.99		2491	6807	1080	5727	1492	1240	1207		5165	27	
Langmuir 1999	ML	Midwest/Sue A/ Sue B	0.99	538	2940	9100	2620	6480	2870	2680	752		6990	5.86	

[a] Laboratory generated samples are raffinates generated from laboratory-scale leaching experiments of the corresponding ore.
[b] The concentration of these analytes were spiked to enable easier characterization of subsequent precipitates.

Finally, the differences in the neutralization processes between the three mills studied (Chapter 6.5.1) as the resulting precipitates are highly dependent on the process pathway. Different pH setpoints at each stage affects the saturation state of minerals and influences the final mineralogy of the precipitates. The presence of a thickening/clarification step that separates precipitates at different neutralization stages also influences the final mineralogy.

6.5.2.1 Iron Precipitation

Iron comprises 1-4% of the secondary precipitates by mass (Robertson et al., 2016, 2014). The precipitation trend of Fe through the neutralization process is shown in Figure 6.7a. The type of Fe precipitate strongly depends on the molar ratio of Fe/As in the raffinate. The Fe/As ratio in raffinates from polymetallic deposits (McClean Lake and Rabbit Lake) are frequently low (~1-4), while the ratio in raffinates from monometallic deposits (Key Lake) are frequently high (~15-70; Bissonnette et al., 2016; Gomez et al., 2013a; Langmuir et al., 1999; Mahoney et al., 2007; Moldovan and Hendry, 2005). At low Fe/As ratios, the ferric arsenate mineral system controls Fe concentrations beginning at ~pH 2 (De Klerk et al., 2012; Mahoney et al., 2007). It should be noted that the nomenclature of the ferric arsenate system is frequently ambiguous and poorly-defined in the literature that identified it. Clarification of this system is required. Elemental analyses of low pH precipitates of raffinate often show a solid phase with a low degree of crystallinity and a 1:1 Fe/As molar ratio corresponding to the stoichiometry of the mineral scorodite ($FeAsO_4 \cdot 2H_2O$). This has led to the use of multiple names for this phase including scorodite, poorly crystalline scorodite, and amorphous ferric arsenate. Crystalline scorodite is not observed as a secondary precipitate in these tailings systems. Similarly, we consider the term poorly crystalline scorodite a misnomer, adding confusion to the literature with multiple names referring to the same precipitate. In this review, we use the term ferric arsenate to describe these initial precipitates with approximate 1:1 Fe/As molar ratios and poor crystallinity whereas we use scorodite to describe the crystalline mineral. As the Fe/As ratio approaches 8, the dominant Fe phase shifts towards ferrihydrite (more detailed discussion on the Fe-As system is presented in Chapter 6.5.3.1; Chen et al., 2009; Jia et al., 2006). Geochemical modeling shows 2-line ferrihydrite (effectively amorphous $Fe(OH)_3$) starts to rapidly precipitate between pH 3.1 and 3.4 (Essilfie-Dughan et al., 2012; Moldovan and Hendry, 2005). XAS analyses confirmed the presence of ferrihydrite in samples of collected from neutralization processes (pH 3.2-4.2; Bissonnette et al., 2016; Moldovan et al., 2003; Robertson et

al., 2017). Microscale "structures" of ferrihydrite were also observed as ferrihydrite coatings on gypsum particles (possibly providing a nucleating surface for ferrihydrite; Essilfie-Dughan et al., 2012). These structures are discussed in detail in the context of EOC control in Chapter 6.5.3.1. Iron(III) is the main Fe species precipitating at low pH; however, Mahoney et al. (2007) identified fougerite ($(Fe(II), Mg)_6Fe(III)_2(OH)_{18}\cdot 4H_2O$) as a potential Fe(II) mineral phase at pH 3.2 in batch neutralizations of McClean Lake raffinate. Their study also posited that Fe(II) substitutes for Fe(III) in ferric arsenate in a sample collected at pH 2.2, although it is unclear how this was determined. The neutralization range from pH 1-4 marks the end point of the low pH stage of the three processes, although as previously stated, the precipitates at McClean Lake are not separated from the solution being treated at this stage.

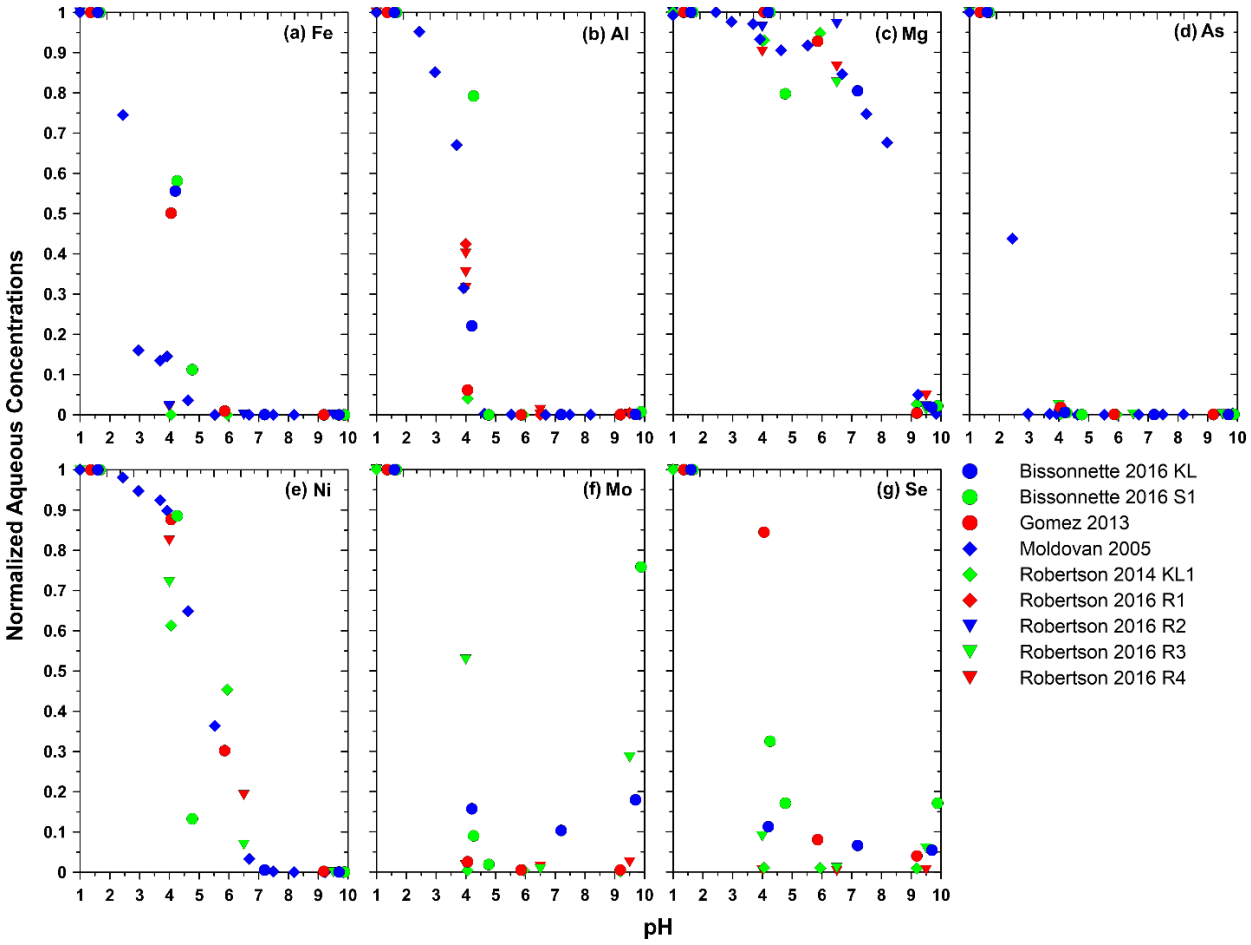

Figure 6.7. Aqueous precipitation trends of elements during the neutralization process. Data points were collected from multiple publications. When multiple datasets were available, the dataset name used in the publication is used in the legend. Due to the range in concentrations, values were normalized relative to the raffinate concentration (i.e., C/Co).

At ~pH 5, <1 mg/L Fe(III) remains in solution but Fe(II) begins precipitating (although data for Fe(II) precipitation during mill raffinate neutralization is limited). At Key Lake, H_2O_2 is added to the overflow solution of the Se-Mo thickener at ~pH 4 causing dissolved Fe(II) to oxidize to Fe(III) and precipitate as ferrihydrite in Pachuca 3 (pH 6.5). In the absence of an oxidant, Fe(II) may precipitate as an amorphous $Fe(OH)_2$ phase although its presence is only supported by thermodynamic modeling (Robertson et al., 2014). X-ray diffraction data of McClean Lake laboratory precipitates suggest that a green rust phase initially precipitates at neutral pH (7.34), but then transforms to a "true ferrihydrite" phase (Mahoney et al., 2007). In the same study, multiple solid samples between pH 6.09 and 7.4 that were initially olive green in colour (representing Fe(II)) transitioned to an orange brown colour due to oxidation to Fe(III), although Fe(II) persisted in subsequent measurements (Mahoney et al., 2007). It is not clear how long the green rust-containing samples were exposed to oxidizing conditions before the XRD measurements were made, although it can be inferred from their observations that Fe(II) will oxidize over time in the oxic conditions of the JEB TMF (and in other oxic TMFs). In Key Lake samples, pH 9.5 precipitates contained greater concentrations of Fe than the precipitates formed at pH 4 (Bissonnette et al., 2016; Gomez et al., 2013a). Gomez et al. (2013a) identified Fe in the high pH phase to be mostly ferrihydrite. This could result from the pathway discussed above where Fe(II) is oxidized by H_2O_2 after the Se-Mo thickener, resulting in rapid precipitation of Fe(III) as ferrihydrite. Minor amounts of Fe were also identified in Mg-Al hydrotalcite particles in the same samples. Analysis by Paikaray et al. (2014) support the presence of Mg-Al-Fe hydrotalcite precipitates in these samples. Conversely, Essilfie-Dughan et al. (2013) identified (1) ferrihydrite as the only secondary Fe precipitate and (2) pyrite as the only appreciable Fe(II) phase in Key Lake tailings (Essilfie-Dughan et al., 2013). At Rabbit Lake, Pichler et al. (2001) identified ferrihydrite as the dominant phase at pH 10.5 (after washing gypsum and calcite from the sample), while Moldovan et al. (2003) identified ferrihydrite in pH 8.5 precipitates. Although these results do not exclude the possibility of solid phase Fe(II) secondary precipitates in the TMFs, Fe(II) is not a major species in the final neutralized precipitates.

The major Fe mineralogy of the final precipitates is dominated by ferrihydrite in all three neutralization processes. The lower terminal pH at McClean Lake is, however, favourable for increased concentrations of ferric arsenate (see Chapter 6.5.3.1 for additional details). Processes with elevated Al and Mg may increase the mass of Fe precipitated in the form of a layered double

hydroxide as observed at Key Lake. Layered double hydroxide-type precipitates were not explicitly observed in processes with low Al and Mg, suggesting Fe is predominantly present as ferrihydrite in Rabbit Lake precipitates.

6.5.2.2 Aluminum and Magnesium Precipitation

Aluminum and Mg comprise 1-5% of the secondary precipitates by mass in Key Lake tailings (Robertson et al., 2016, 2014). Raffinates processed at Key Lake contain much greater concentrations of Al compared to raffinates processed at McClean Lake and Rabbit Lake due to the ores used. As shown in Table 6.4, measured Al concentrations in mill samples ranged from 1,635-3,510 mg/L at Key Lake and from 200-498 mg/L at McClean Lake and Rabbit Lake samples (although laboratory raffinates generated from hypothetical ore blends resulted in higher Al concentrations in the latter). This large discrepancy likely results in differences in the Al mineralogy in the secondary precipitates.

The majority of Al precipitation occurs between pH 3.5 and 5.0 (Figure 6.7b). Robertson et al. (2016) characterized the evolution of Al secondary mineral precipitates at Key Lake. Scanning transmission electron microscopy and Al K-edge XANES identified an amorphous Al phase in pH 4.0 precipitates. The Al and SO_4 stoichiometry was consistent with hydrobasaluminite ($Al_4SO_4(OH)_{10}\cdot 12\text{-}36H_2O$) but referred to as $AlOHSO_4$. Some debate exists in the acid mine drainage literature over the characterization of $AlOHSO_4$-type phases because many models predict Al to remain soluble below pH 5, above which $Al(OH)_3$ precipitates (Nordstrom and Ball, 1986). However, it is suggested that SO_4^{2-}-rich media (such as raffinate) lowers the solubility of Al, causing $AlOHSO_4$ phases to precipitate before $Al(OH)_3$/gibbsite (Bertsch and Parker, 1996). In addition to $AlOHSO_4$, substitution of Al into the structure of co-precipitated ferrihydrite was observed at pH 4.0 (Robertson et al., 2016). Aluminum that did not precipitate at the low pH stage precipitated at the pH 6.5 stage as a mixture of amorphous $Al(OH)_3$ and $AlOHSO_4$. The solubility of $AlOHSO_4$ increases with pH and could transform to amorphous $Al(OH)_3$ by Eq. 6.9 (Adams and Rawajfih, 1977).

$$Al_4(OH)_{10}SO_4 + 2OH^- \rightarrow 4Al(OH)_3 + SO_4^{2-} \quad (6.9)$$

At pH 9.5, hydrotalcite (a layered double hydroxide mineral) was identified as the dominant Al-phase (61-70%) and amorphous $Al(OH)_3$ made up the remainder of the Al. Paikaray

et al. (2014) examined the mechanism of hydrotalcite precipitation. They suggested Mg^{2+} substitutes into the existing $Al(OH)_3$ phase as the pH increases to pH > 8 and transforms $Al(OH)_3$ to hydrotalcite by the reaction described by Eq. 6.10 (Paikaray et al., 2014).

$$Al(OH)_3 + 2Mg^{2+} + 3OH^- + A^{n-} + xH_2O \rightarrow Mg_2Al(OH)_6A \cdot xH_2O;\ A^{n-} = anion \quad (6.10)$$

Magnesium precipitation is greatest at pH 8 during neutralization (Figure 6.7c) and is evidence for hydrotalcite precipitation. Robertson et al. (2016) suggests that residual $AlOHSO_4$ at high pH transforms to hydrotalcite by a similar mechanism, with SO_4^{2-} being incorporated into the hydrotalcite interlayer. This is consistent with the final mineralogy of the secondary mineral precipitates that yielded minimal to no detectable hydrobasaluminite at pH 10.5 and was predominantly hydrotalcite and amorphous $Al(OH)_3$.

Mineralogical investigations at McClean Lake identified $AlOHSO_4$ (referred to as a poorly crystalline hydrobasaluminite) in laboratory neutralization experiments conducted at pH values ranging from pH 3.2 to 7.3 (Langmuir et al., 1999; Mahoney et al., 2007, 2005). Although it is difficult to determine how much Al and Mg is present in the initial raffinates in McClean Lake studies, data suggest the concentrations of both elements range between 200 and 420 mg/L (an order of magnitude lower than concentrations measured at Key Lake). Because the McClean Lake neutralization process only increases the pH of the tailings to pH 7-8 and the raffinate concentrations of Al and Mg are lower than Key Lake, it is unlikely that hydrotalcite is as abundant in the JEB TMF as in the DTMF. While hydrotalcite can precipitate at neutral pH, the transformation mechanism of Mg^{2+} substituting into $Al(OH)_3$ precipitates is not observed until pH > 8. Rather, amorphous $AlOHSO_4$ likely persists in the tailings as a stoichiometric variation of hydrated $Al_4SO_4(OH)_{10}$ along with amorphous $Al(OH)_3$. Mahoney et al. (2005) also observed Al to substitute into ferric arsenate at low pH, consistent with the Al substitution into ferrihydrite at Key Lake (Mahoney et al., 2005).

Aluminum precipitation at Rabbit Lake is not well-documented. Geochemical modeling by Moldovan and Hendry (2005) suggests amorphous $Al(OH)_3$ and gibbsite are the major Al precipitates, but they state these may not be the only phases controlling Al solubility based on modeling data. Pichler et al. (2001) identified a Ni-Al hydroxide phase low in S content in neutralized precipitates (pH 10.5) at Rabbit Lake, suggesting $AlOHSO_4$ may not be present in the final tailings at Rabbit Lake (although only one TEM-EDX observation was made). It is also

possible that the Ni-Al hydroxide phase was a layered double hydroxide given the Ni(II)/Al(III) ratio was ~1 and the pH is comparable to the Key Lake neutralization process. Although Mg was not measured in this sample, it is likely present and may associate with this Ni-Al hydroxide phase to form a layered double hydroxide, thereby increasing the M(II)/M(III) ratio of the phase to values required for layered double hydroxide formation. X-ray diffraction of these samples did not indicate any gibbsite precipitation, suggesting that any $Al(OH)_3$ present is amorphous.

6.5.2.3 Calcium Precipitation

Calcium comprises 10-20% of the final neutralized precipitates and is mostly in the form of gypsum ($CaSO_4 \cdot 2H_2O$; Bissonnette et al., 2016; Robertson et al., 2014). Mixing SO_4^{2-}-rich raffinate with slaked lime results in gypsum supersaturation in the neutralization process (Langmuir et al., 1999). The majority of gypsum precipitates between pH 1.0-4.0 and lesser masses continue to precipitate as lime is added to the terminal pH (Essilfie-Dughan et al., 2012). Calcite ($CaCO_3$) precipitates at higher pH stages and is a minor Ca phase (Pichler et al., 2001; Robertson et al., 2014). The major Ca mineralogy (gypsum and calcite) is relatively simple in these processes and is consistent across the three mills. Excess aqueous Ca leads to the possibility of As and Mo controls exerted by other Ca minerals and is discussed in Chapter 6.5.3.3.

6.5.3 Mineralogical Controls on Elements of Concern

The initial concentrations of the major raffinate elements (which determines the mass of the minerals that precipitates) and the pH setpoints of the neutralization steps determine the solubility controls of EOCs driven by surface complexation or co-precipitation. Understanding these controls is important to evaluate the short-term performance of water treatment and the long-term fate of EOCs in the tailings. A summary of mineralogical controls known to exert solubility controls on As, Se, Mo, Ni, and ^{226}Ra during the neutralization process is presented in Table 6.5. Research conducted over the past few decades show Fe and Al secondary minerals are the major mineralogical controls of EOCs in the precipitates from Athabasca Basin raffinates (Essilfie-Dughan et al., 2013, 2012, 2011b; Langmuir et al., 1999; Mahoney et al., 2007, 2005; Moldovan et al., 2003; Moldovan and Hendry, 2005). There are many studies of Ca mineralogical controls on As and Mo (Blanchard et al., 2015; Donahue et al., 2000; Donahue and Hendry, 2003; Essilfie-Dughan et al., 2011b; Hayes et al., 2014; Pichler et al., 2001). However, most of these studies

conclude Ca minerals are minor or secondary to the controls exerted by Fe and Al minerals. Finally, co-precipitation with barite is a simple but important mineralogical control on ^{226}Ra (Goulden, 1997; Liu and Hendry, 2011). This section defines the geochemistry of the EOC controls.

Table 6.5 Known mineralogical controls of elements of concern in raffinate neutralization processes at the reviewed sites.

Element	Rabbit Lake	Key Lake	McClean Lake
As	Ferrihydrite (ads) Amorphous $Al(OH)_3$ (ads) $Ca_4(OH)_2(AsO_4)_2 \cdot 4H_2O$	Ferrihydrite (ads) Amorphous $Al(OH)_3$ (ads) Hydrotalcite (ads) $Ca_4(OH)_2(AsO_4)_2 \cdot 4H_2O$	$FeAsO_4 \cdot 2H_2O$ Ferrihydrite (ads) Annabergite Cabrerite
Se		Ferrihydrite (ads) Amorphous $Al(OH)_3$ (ads) Hydrotalcite (ads)	
Mo		Ferrihydrite (ads) $Fe_2(MoO_4)_3$ $CaMoO_4$ $NiMoO_4$ Hydrotalcite (ads)	$Fe_2(MoO_4)_3$ $CaMoO_4$
Ni	$Ni(OH)_2$ Ni-Al hydroxide	Ferrihydrite (ads) Amorphous $Al(OH)_3$ (ads) NiAl layered double hydroxide $NiMoO_4$ $Ni(OH)_2$	Annabergite Cabrerite $Ni(OH)_2$ $NiMoO_4$
^{226}Ra	Barite	Barite Ferrihydrite	Barite

* (ads) denotes the element is controlled by adsorption

An important aspect to consider before discussing EOC mineralogical controls is the speciation and oxidation state of EOCs in the raffinate. Minimal *in situ* oxidation state data is available, although laboratory generated raffinates at McClean Lake contained As(V)/As(III) ratios between 2.5-5.3 (Langmuir et al., 1999). In lieu of *in situ* data, stability field diagrams are used to predict speciation and oxidation states at equilibrium for As, Mo, Se, and Ni during the neutralization process (Figure 6.8a-d). The stability field diagrams show the EOCs generally remain in the same oxidation state (As(V), Mo(VI), Se(IV), and Ni(II)) and the dominant aqueous species is dependent on pH.

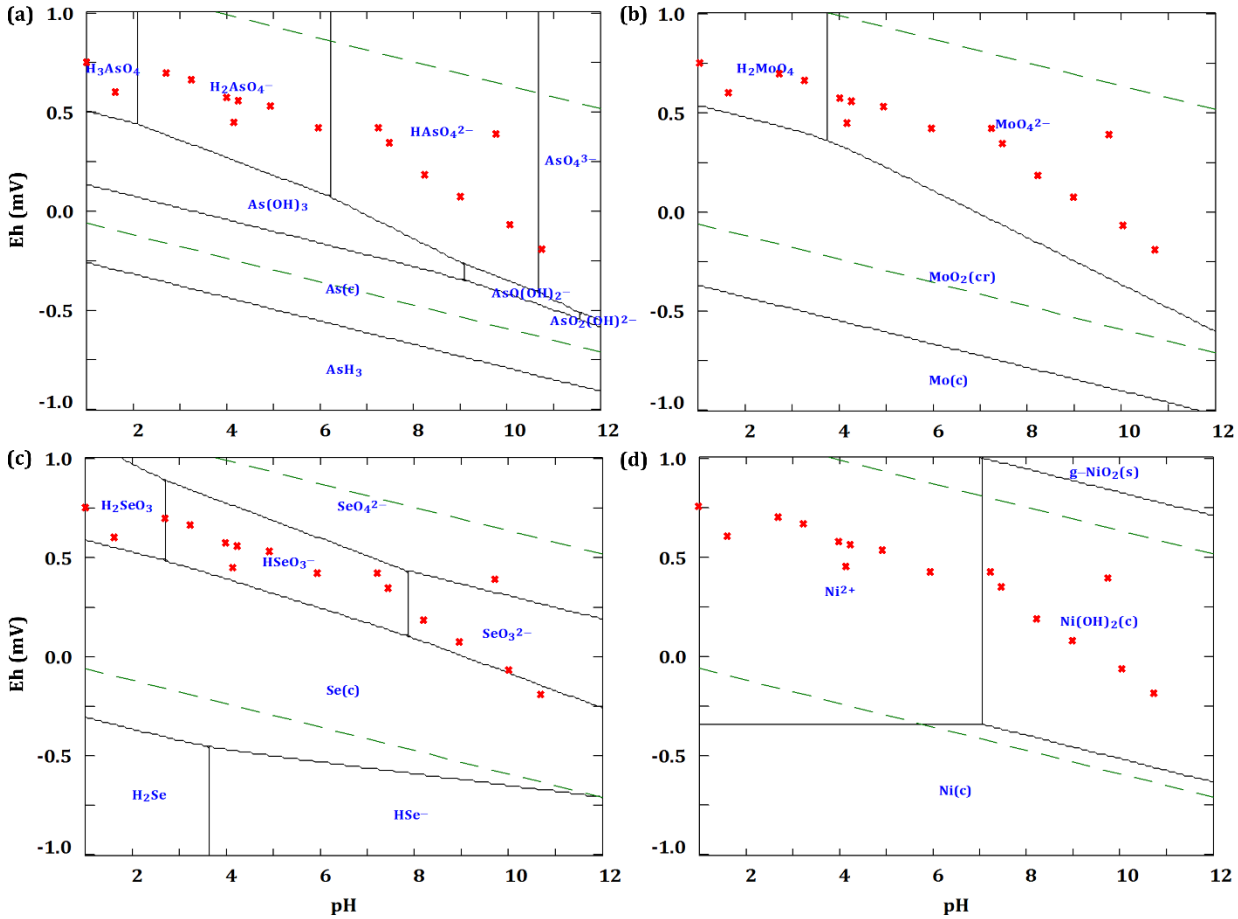

Figure 6.8. Stability field diagrams of (a) As, (b) Mo, (c) Se, and (d) Ni. Red "x's" denote Eh-pH measurements from Moldovan and Hendry (2005) and Bissonnette et al. (2016) in the Rabbit Lake and Key Lake neutralization processes, respectively. The elemental concentration used for each diagram are on the same order of magnitude typically observed in raffinates. Ionic strength is set at I = 0.05 and temperature at 25°C. Diagrams generated from the programs Hydra and Medusa (Puigdomenech, 2010).

6.5.3.1 Controls Exerted by Iron

Co-precipitation of ferric arsenate and the adsorption of arsenate to ferrihydrite are major mechanisms of As sequestration (Essilfie-Dughan et al., 2013; Langmuir et al., 1999; Mahoney et al., 2007; Moldovan et al., 2003). Distinguishing between the two phases can be difficult because ferric arsenate precipitation and ferrihydrite adsorptions occurs as a continuum dependent on multiple variables (e.g., pH and initial Fe/As molar ratio; Paktunc et al., 2008). A study by Paktunc et al. (2008), who examined the Fe(III)-As(V) co-precipitation and adsorption system, is relevant to precipitates resulting from raffinate neutralization. Acidic solutions with Fe/As between 1 and 4 neutralized to pH 4.5 result in a mixed precipitate of ferric arsenate and As-adsorbed ferrihydrite

rather than a single phase. Increasing the pH of ferric arsenate precipitates (Fe/As = 2) to pH 4.5 results in incongruent dissolution of 85% of the ferric arsenate and polymerization of ferrihydrite, providing additional surface sites for arsenate. Ferric arsenate is absent from precipitates with Fe/As $\geq$ 5 at pH 4.5 (Paktunc et al., 2008). Chen et al. (2009) synthesized ferric arsenate compounds (Fe/As = 4) that showed a distinct change in the coordination environment as the pH increased from pH 4 to 8 whereby the As-Fe coordination number decreased from 3.9 to 1.6. This suggests ferric arsenate transforms to As-adsorbed ferrihydrite as observed by Paktunc et al. (2008). A two-stage (pH 4 and pH 8) laboratory neutralization of a solution with Fe/As = 4 measured that 57% of solid phase As was associated with ferric arsenate and the remainder adsorbed to ferrihydrite at pH 8 (De Klerk et al., 2012).

Greater than 99% of As in the raffinate is precipitated by pH 3 (Figure 6.7d). The McClean Lake literature shows that As concentrations are dominated by co-precipitation of Fe(III) and As(V) as ferric arsenate, followed by precipitation of ferrihydrite and subsequent adsorption of As(V) as the pH increases (Chen et al., 2009; Frey et al., 2010; Langmuir et al., 1999; Mahoney et al., 2007, 2005). The molar Fe/As ratio in the raffinate plays a major role in the final As concentrations in the tailings porewater and is a primary focus during operation at McClean Lake. An Fe/As ratio $\geq$ 3-4 generally results in As concentrations of 1-2 mg/L and is controlled by adding $Fe_2(SO_4)_3$ to the raffinate solution (Langmuir et al., 1999). A study of batch neutralizations of McClean Lake raffinate estimated the mineralogy of the precipitates at different pH steps (Mahoney et al., 2007). Ferric arsenate comprised 6.5% of the precipitates at pH 2.2 and 4.4% of the precipitates once the slurry reached pH 7.3. In the same samples, ferrihydrite was not detected until pH 5.3 where it comprised 2.4% of the precipitates. At pH 7.3, the precipitates were 3.7% ferrihydrite (Mahoney et al., 2007). This shows a decrease in ferric arsenate with pH and an increase in ferrihydrite with pH. In the EXAFS study by Chen et al. (2009), the As-Fe CN in McClean Lake raffinate precipitates decreased from 3.3 to 2.7 as the pH increased from ~2 to 6 (solid phase Fe/As = 1.1 to 2.9), indicating that an increasing fraction of As adsorbs to ferrihydrite rather than co-precipitating as ferric arsenate. Observing this transformation at low Fe/As ratios that are believed to be favourable for ferric arsenate formation indicates that As-adsorbed ferrihydrite is more favourable at Fe/As ratios typical of mill raffinates (> 4) above neutral pH. These results can be linked to the batch experiments of Mahoney et al. (2007) where the

ferrihydrite concentration increased with pH and suggest at least two Fe phases control As concentrations in the JEB TMF.

At Key Lake, the As distribution to Fe-phases in two samples collected from the Se-Mo thickener (~pH 4) was approximately 75% adsorbed to ferrihydrite and 25% co-precipitated as ferric arsenate (Bissonnette, 2015; Robertson et al., 2017). The raffinate Fe/As ratios for these samples were 15.1 and 47.1, while the solid phase Fe/As ratios were 13.1 and 28.2, respectively. Synthetic and field samples from Robertson et al. (2017) that contained ferric arsenate at ~pH 4 were devoid of ferric arsenate once neutralized to pH 10.5. *In situ* tailings samples from the DTMF showed As-adsorbed ferrihydrite is the dominant Fe sequestration mechanism, even in samples where Fe/As < 4 (Essilfie-Dughan et al., 2013). The lack of ferric arsenate in a system where the Fe/As ratio is ideal for its precipitation indicates that above a certain pH, ferric arsenate is no longer stable and the Fe-As system is controlled by ferrihydrite. This agrees with the conclusions by Paktunc et al. (2008) discussed earlier.

Pichler et al. (2001) analyzed a solid-phase sample from the Rabbit Lake neutralization process at pH 10.5 and suggested As associates with amorphous Fe-oxyhydroxides, with only minor evidence for a ferric arsenate phase. They also characterized three Fe-containing particles: As-Fe rich, Al-Ni-As-Fe rich, and Ni-As-Fe rich (Pichler et al., 2001). Subsequent Rabbit Lake samples collected by Moldovan et al. (2003) at pH 3.5 and 8.5 confirmed As adsorbed to ferrihydrite. EXAFS analyses of these samples precipitated from a raffinate with Fe/As = 7.4 showed As(V) was coordinated to two Fe atoms at both pH 3.5 and 8.5. Subsequent geochemical modeling of the same system, however, indicated that the precipitation trend of Fe at low pH is described by precipitation of both ferrihydrite and ferric arsenate (Moldovan and Hendry, 2005). The lack of ferric arsenate in the EXAFS results could be explained by the transformation mechanism of ferric arsenate to As-adsorbed ferrihydrite with increasing pH as discussed above.

Using the information generated on the Fe-As geochemistry from the three mills, we developed a pathway of Fe-As control during raffinate neutralization that explains differences between the Fe-As system at McClean Lake and that at Key/Rabbit Lake. A large range of Fe/As ratios (Fe/As = 0.3-68.9) are reported for raffinates (Gomez et al., 2013a; Langmuir et al., 1999). The mass of ferric arsenate that precipitates during the first neutralization step is dependent on the Fe/As ratio of the initial solution. In other words, a low Fe/As ratio will result in more ferric

arsenate relative to As-adsorbed ferrihydrite (as observed at McClean Lake), and vice versa for solutions with high Fe/As ratios (as observed at Key Lake). Raffinate is rapidly neutralized to pH ~4 in the first neutralization Pachuca. Laboratory and modeling studies of raffinate neutralization show that ferric arsenate precipitation begins at pH 2-3 (Mahoney et al., 2007; Moldovan and Hendry, 2005). Given an arbitrary volume of raffinate that begins mixing with slaked lime, rapid ferric arsenate co-precipitation occurs during the transient period where the pH of the volume sweeps through pH 2-3. As that volume of solution in the Pachuca reaches the target pH of 4, ferrihydrite begins precipitating and simultaneously adsorbs As (if aqueous Fe and As are still available). The ferric arsenate that precipitated during the transient pH period remains stable. This specific volume of solution remains at pH 4 for the residence time of the Pachuca (on the order of 1-3 hr depending on flow rates). The presence of ferric arsenate in solutions with high Fe/As ratios is potentially caused by this brief period of disequilibrium as the incoming solution is raised to its target pH. As the low pH slurry (pH 4) is pumped to the next neutralization step (pH 6.5-7.5), ferric arsenate begins to transform to As-adsorbed ferrihydrite. At McClean Lake, this transformation is arrested at the terminal pH of 7-8, resulting in a mixture of ferric arsenate and As-adsorbed ferrihydrite. At Key Lake and Rabbit Lake, the transformation continues in the next neutralization step (before 2008) or in the tailings mix box as the pH increases to 10.5, resulting in ferrihydrite being the primary Fe control on As in the tailings regardless of Fe/As ratio.

The nucleation and growth of ferrihydrite coatings on gypsum particles was observed by Essilfie-Dughan et al. (2012) in Key Lake tailings deposited before the installation of the Se-Mo thickener. Their results show EOC controls evolving as the precipitates move through the neutralization process. Gypsum particles rapidly precipitate at the beginning of the process. The surface of these particles provides a nucleation site for ferrihydrite, which provides adsorption sites for As (and presumably Se and Mo). These ferrihydrite-coated gypsum particles contained elevated concentrations of adsorbed As on the inner section of the particle, representing precipitation at low pH. The ferrihydrite coating continued to grow as the pH increased and the As concentrations decreased in the outer sections of the coating. This mechanism, however, will only be present in neutralization processes that do not have an intermediate separation step (e.g., Key Lake/Rabbit Lake prior to 2008 and McClean Lake). Coated gypsum particles are likely not the dominant mechanism of EOC controls; however, these structures are an example of mineralogical controls evolving with pH.

As previously mentioned, Al substitution into the structure of ferrihydrite and ferric arsenate is observed in neutralized precipitates (Mahoney et al., 2005; Robertson et al., 2016). Impurities within ferrihydrite are also common in natural systems, and studies of acid mine drainage sites (which are mechanistically similar to these neutralization processes) observed As adsorption on Al-ferrihydrite and examined the change in the reactivity of impure ferrihydrite (Adra et al., 2016, 2013). When the Al/Fe ratio of ferrihydrite increases, the As(V) adsorption density increases. It was observed that inner-sphere corner sharing As surface complexes form on Al-ferrihydrite in addition to an increased number of outer-sphere surface complexes relative to pure ferrihydrite (Adra et al., 2016). The sorption experiments in this study were conducted at pH 6.5, so it is uncertain if the additional As outer-sphere complexes will remain stable in alkaline TMFs. It is also unclear if the number of inner-sphere surface complexes in Al-ferrihydrite decreases, although the specific surface area of the sorbent decreased, suggesting decreased inner-sphere adsorption capacity (Adra et al., 2016). The adsorption capacity and stability of Al-ferrihydrite in the neutralized raffinate precipitates with respect to EOCs could be an area of future study for the tailings.

Studies of mineralogical controls of dissolved Ni are less prominent than As and much of the data is only qualitative or semi-quantitative (Donahue et al., 2000; Essilfie-Dughan et al., 2012; Gomez et al., 2013a; Langmuir et al., 1999; Mahoney et al., 2007; Pichler et al., 2001; Robertson et al., 2017; Shaw et al., 2011). Nickel precipitation occurs primarily in the second pH neutralization stages beginning at ~pH 5 with complete precipitation occurring at pH > 8 (Figure 6.7e; Essilfie-Dughan et al., 2012; Moldovan and Hendry, 2005). Adsorption of Ni to ferrihydrite was shown on ferrihydrite-coated gypsum particles above pH 5 (Essilfie-Dughan et al., 2012). However, batch neutralizations of McClean Lake raffinate showed the concentration of Ni was independent of the Fe/Ni ratio, suggesting other elements are more important as mineralogical controls for Ni (although Ni was observed as an impurity in ferric arsenate pH 2; Mahoney et al., 2007). A distinct Ni-Fe mineralogical control was not evident in Rabbit Lake precipitates; rather, minor associations of Ni and Fe were overshadowed by Ni-Al associations (Pichler et al., 2001). Similarly, an EXAFS study of Key Lake samples (synthetic and *in situ*) could not identify Fe controls on Ni. Instead, Al was the dominant mineralogical control of Ni (discussed further in Chapter 6.5.3.2; Robertson et al., 2017).

Molybdenum is primarily removed from raffinate by outer-sphere complexation with ferrihydrite at low pH neutralization stages (pH 3.5-4, Figure 6.7f; (Bissonnette, 2015; Blanchard et al., 2015; Essilfie-Dughan et al., 2011b; Gomez et al., 2013b; Hayes et al., 2014). Only one XAS study addressed the distribution of Mo in mill samples at a low pH stage; Bissonnette et al. (2016) determined (from a set of three samples collected from pH 3.9 to 4.2) that 84% to 100% of the solid phase Mo was adsorbed to ferrihydrite, with the remainder as ferrimolybdite ($Fe_2(MoO_4)_3$). In the current configuration of the Key Lake process, the Se-Mo thickener is the primary point where Mo-bearing precipitates are removed from the neutralization process. Removing the precipitates in the Se-Mo thickener ensures Mo does not re-dissolve in the treated water as the pH increases. Residual aqueous Mo that persists after the Se-Mo thickener precipitates as $NiMoO_4$ and adsorbs to ferrihydrite, although the actual concentration of Mo at this stage is negligible (< 0.003% in the solid phase) as most Mo precipitates at pH 3.5-4 (Bissonnette et al., 2016). At McClean Lake, the mineralogical controls of Mo were studied in tailings but not directly in the neutralization process (Blanchard et al., 2015; Hayes et al., 2014). McClean Lake tailings samples showed a larger variability in the distribution of solid phase Mo compared to Key Lake; 17-55% was adsorbed to ferrihydrite and 25-60% precipitated as ferrimolybdite at a final pH of 7-8. The increase in ferrimolybdite at McClean Lake compared to Key Lake may be attributed to differences in the terminal pH at the two mills, much like the transformation of ferric arsenate to As-adsorbed ferrihydrite as the terminal pH increases above 8. There are not known studies of Mo at Rabbit Lake.

There is a lack of literature on the removal of Se during the neutralization processes. Selenium precipitates at low pH (Figure 6.7g), most likely through inner-sphere adsorption to ferrihydrite (Bissonnette et al., 2016; Gomez et al., 2013a; Lieu et al., 2010; Robertson et al., 2016, 2014). This is supported by elemental maps from synthetic Key Lake precipitates that show an association of Se to an amorphous Al-$Fe(OH)_3$ phase (Robertson et al., 2016). The effectiveness of Se adsorption with ferrihydrite depends on the oxidation state of Se; Se(IV) has a stronger affinity to ferrihydrite than Se(VI), although both form inner-sphere surface complexes (Das et al., 2013; Su and Suarez, 2000). Selenium speciation at low pH neutralization steps is not reported; however, a stability field diagram suggests Se(IV) is the dominant species at pH 4 (Figure 6.8c). This agrees with the observation of Se(IV) as the primary Se species in the DTMF, although Se(VI) is observed as well (Essilfie-Dughan et al., 2010).

Barium chloride is added to the neutralization processes to precipitate ^{226}Ra (discussed in Chapter 6.5.3.4); however, adsorption of ^{226}Ra to ferrihydrite is the dominant sequestration mechanism (Liu and Hendry, 2011). Sequential extractions showed that 73% of solid-phase ^{226}Ra in neutralized precipitates is associated with amorphous $Fe(OH)_3$ (Liu and Hendry, 2011). In the absence of $BaCl_2$, ^{226}Ra activities decreased from 150 Bq/L (pH 1.2) to 1 Bq/L (pH 11) with the majority of precipitation occurring after pH 6 in laboratory neutralizations (Liu and Hendry, 2011). This shows the relative importance of Fe in the removal of ^{226}Ra. However, ferrihydrite adsorption is not enough to decrease ^{226}Ra activities below environmental release limits. Barium chloride addition is required to decrease ^{226}Ra to acceptable activities.

A final point to consider is the pH dependence of surface complexes with ferrihydrite. Ferrihydrite adsorption of oxyanions and cations is controlled by the point of zero charge of ferrihydrite (pH 7.9-8.2; Dzombak and Morel, 1990). At low pH, oxyanions are attracted to the positively charged surface; AsO_4^{3-} adsorbs strongly at low pH until pH 9 where adsorption is minimized at pH 13, and SeO_4^{2-} adsorbs strongly at low pH until pH 4 where adsorption decreases to zero after pH 7.5. Conversely, Ni adsorbs to ferrihydrite at pH 6 and reaches a maximum at pH 8 (Dzombak and Morel, 1990).

6.5.3.2 Controls Exerted by Aluminum and Magnesium

Prior to 2013, the influence of Al and Mg minerals on the sequestration of EOCs in Athabasca Basin tailings was not investigated. However, the adsorption properties of amorphous $Al(OH)_3$ are well-defined in other fields (Arai et al., 2001; Foster and Kim, 2014; Goldberg and Johnston, 2001; Kappen and Webb, 2013). Amorphous $Al(OH)_3$ possesses similar adsorptive characteristics to ferrihydrite, although amorphous $Al(OH)_3$ is a weaker adsorbent (Goldberg, 2002). Arsenic(V) adsorption with amorphous $Al(OH)_3$ occurs through bidentate-binuclear corner-sharing linkages with As-Al interatomic distances ranging from 3.11-3.22 Å (Foster and Kim, 2014). This complex is strongly resistant to phosphate exchange, demonstrating a degree of stability (Burke et al., 2013). Hydrotalcite, and layered double hydroxides in general, adsorbs oxyanions both at its surface and interlayer (Das et al., 2002; Frost et al., 2005; Goh et al., 2008). Unlike the Al-oxyhydroxide surface complex, As adsorbed on hydrotalcite is moderately phosphate-exchangeable which may suggest a degree of instability if chemical conditions change (Burke et al., 2013).

Most studies of EOC controls by Al and Mg minerals originate from Key Lake (Bissonnette et al., 2016; Gomez et al., 2013a; Robertson et al., 2017, 2016). Aluminum is measured to control 5-25% of As at low pH stages (pH 4) through adsorption with amorphous $AlOHSO_4$ (bidentate-binuclear bonds; Bissonnette et al., 2016; Robertson et al., 2017). Arsenic remaining in solution after the low pH stage forms bidentate adsorption complexes with amorphous $Al(OH)_3$ and hydrotalcite at pH 9.5. Between 41% and 71% of adsorbed As in pH 9.5 precipitates is associated with these Al phases (Bissonnette et al., 2016; Robertson et al., 2017). In a final tailings slurry sample collected at pH 10.9, 59% of solid phase As was associated to Al phases (amorphous $Al(OH)_3$ and hydrotalcite) and the remainder was associated to Fe phases (Robertson et al., 2017). A possible explanation for this distribution is the higher point of zero charge of Al-hydroxides relative to Fe-hydroxides, resulting in As desorbing from the ferrihydrite surface and re-adsorbing to the Al phases during the pH adjustment (Adra et al., 2016). The dissolution of ferric arsenate could also be a source of As adsorption to Al phases.

Robertson et al. (2017) also observed Ni to be controlled by amorphous $Al(OH)_3$ and Ni-Al layered double hydroxide surface precipitates on the surface of hydrotalcite. This conflicts with results from other studies of laboratory and *in situ* tailings that suggest Ni is predominantly controlled by adsorption to ferrihydrite or precipitation of $Ni(OH)_2$ (theophrastite), annabergite ($Ni_3(AsO_4)_2 \cdot 8H_2O$), or cabrerite ($(Ni,Mg)_3(AsO_4)_2$; Essilfie-Dughan et al., 2012; Langmuir et al., 1999; Mahoney et al., 2007). A primary difference from systems where annabergite or cabrerite are identified is elevated As concentrations in the raffinate that results in saturation of these minerals (Langmuir et al., 1999; Mahoney et al., 2007). The concentration of Al in the raffinate of these studies were less than those measured at Key Lake which may promote Al controls of Ni.

To study the adsorption characteristics of hydrotalcite, Robertson et al. (2016) adsorbed As(V), Mo(VI), and Se(IV) with hydrotalcite-rich precipitates from a laboratory model of the Key Lake neutralization process at pH 9.6 (mean pH of the DTMF) for 30 d. With each element isolated, equilibrium was reached after 7 d and the adsorption capacities of the hydrotalcite-rich precipitate were 0.91 mmol/g (As(V)), 0.67 mmol/g (Mo(VI)), and 0.62 mmol/g (Se(IV)). These adsorption capacities were the same order of magnitude as those for ferrihydrite. In a competitive system where As, Se, and Mo were adsorbed in the same beaker, the adsorption capacities of these elements decreased relative to the isolated experiments due to competition for adsorption sites. After 30 d, the hydrotalcite-rich precipitate adsorbed 0.73 mmol/g (As(V)), 0.57 mmol/g (Mo(VI)),

and 0.16 mmol/g (Se(IV)). These experiments demonstrate the type of layered double hydroxide precipitated at Key Lake can adsorb residual EOCs at high pH and potentially "buffer" any release of EOCs in the DTMF (e.g., in the event of Fe reduction or sulfide mineral oxidation). However, stability tests of these adsorption controls were not performed and the mechanism of EOC uptake is unclear.

Pichler et al. (2001) analyzed neutralized precipitates (~pH 10.5) at Rabbit Lake and observed an ambiguously named Ni-Al hydroxide that was most often associated with As-rich ferrihydrite. A particle with equimolar concentrations of Ni and Al was identified, suggesting the presence of a mixed-metal layered double hydroxide consistent with that observed in Key Lake samples (Pichler et al., 2001). No evidence of Al controls on As was presented in their study. Geochemical modeling of Rabbit Lake neutralization by Moldovan and Hendry (2005) included amorphous $Al(OH)_3$ adsorption of As, but As was determined controlled ferrihydrite adsorption. Amorphous $Al(OH)_3$ only adsorbed 0.2% of the As in the model.

Laboratory neutralization tests of McClean Lake raffinate by Langmuir et al. (1999) did not explicitly identify Al EOC controls, rather they observed Al associations with ferric arsenate. Amorphous $AlOHSO_4$ phases were also characterized, although EOC controls were not reported. Hydrotalcite is not identified in McClean Lake tailings, probably due to the terminal pH (~7.5) in the mill being below the pH that hydrotalcite precipitation occurs (generally pH > 8; Paikaray et al., 2014). As previously mentioned, Ni and Mg in the form of cabrerite was identified in several samples by XRD during batch neutralization of potential McClean Lake raffinates (Langmuir et al., 1999). The four major peaks of crystalline cabrerite were identified in all tailings samples of this study. Cabrerite peaks are not observed in any other XRD analyses of *in situ* tailings in the basin. The formation of cabrerite in these samples may be a product of laboratory conditions. Langmuir et al. (1999) suggested cabrerite only precipitates around pH 5 to 6 when concentrations of Fe is low and Ni is abundant. When Fe concentrations are high, more ferric arsenate precipitates, resulting in lower concentrations of AsO_4^{3-} and undersaturated conditions for cabrerite. A subsequent study of laboratory neutralized tailings identified a highly disordered Ni-Mg hydroxide phase at higher pH values – no reference to cabrerite was made in this study (Mahoney et al., 2007). No further characterization of the Ni-Mg hydroxide phase was provided in this study.

6.5.3.3 Calcium Controls

The precipitation of excess Ca (added as $Ca(OH)_2$ added during raffinate neutralization) as calcium minerals is often proposed as a mineralogical control for arsenate and molybdate anions. Geochemical models predict supersaturation of Ca-arsenates and Ca-molybdates in these neutralization processes; however, physical evidence of Ca mineral phases is limited. Donahue et al. (2000) showed samples from the RLITMF to contain associations between Ca, As, Ni, and S (Donahue et al., 2000). A follow-up study of the same tailings body by Donahue and Hendry (2003) showed an association of As to an amorphous Ca-arsenate phase in tailings samples where the Fe/As ratio was < 2. This phase also contained the greatest mass of water soluble As, which indicates a lack of stability. Saturation calculations of pore fluids in the RLITMF and DTMF show Ca-arsenate phases are either over- or under-saturated depending on the thermodynamic data used; however, $Ca_4(OH)_2(AsO_4)_2 \cdot 4H_2O$ is the most likely phase on the basis of the alkaline pH (~10) and the Ca/As molar ratio of the samples (Donahue and Hendry, 2003; Shaw et al., 2011). A parallel study of RLITMF samples by Pichler et al. (2001) supports the theoretical result that Ca-arsenates are saturated in the tailings via indirect evidence from sequential extractions; however, Ca-arsenates were not observed with SEM, TEM, EDX, or XRD. The Fe/As ratios of these samples were ~2.2. Additionally, XANES studies of fresh precipitates or aged tailings samples from all three TMFs do not indicate the presence of Ca-arsenate phases (Bissonnette et al., 2016; Chen et al., 2009; Essilfie-Dughan et al., 2013, 2012; Moldovan et al., 2003; Robertson et al., 2017; Warner and Rowson, 2007). Calcium arsenate precipitation cannot be ruled out on these data alone; however, Ca-arsenates are not a major mineral phase in the tailings.

Like Ca-arsenates, powellite ($CaMoO_4$) is predicted to precipitate in the TMFs based on thermodynamic calculations (Blanchard et al., 2015; Shaw et al., 2011). A combination of geochemical and Mo K-edge XANES data from the JEB TMF confirm the presence of powellite (Blanchard et al., 2015; Hayes et al., 2014). Blanchard et al. (2015) identified powellite precipitation increasing over the course of five years after core samples from the same location and depth showed an increase in powellite content from 10% to 25% and a corresponding decrease in the aqueous Mo concentration from relatively young tailings. Beyond five years, the rate of powellite precipitation slows. The proportion of powellite in the JEB TMF ranges from 10% to 40% of Mo-bearing phases. Blanchard et al. (2015) suggest that Mo sequestered as ferrimolybdite

and outer-sphere surface complexes with ferrihydrite dissolves and re-precipitates as powellite. Samples from the bottom of the JEB TMF collected at the same position five years apart show minimal change in powellite concentrations, suggesting powellite is stable under the current TMF conditions. Powellite precipitation is rate limited and attributed to the low hydraulic conductivity and low temperature of the TMF (Hayes et al., 2014).

Powellite is also observed in the DTMF, although at lower concentrations compared to the JEB TMF. An increasing trend of powellite precipitation with time was not observed in the DTMF; rather, powellite concentrations tend to increase when the molar Fe/Mo and Ni/Mo ratios decrease and Ca and Mo concentrations are high (Essilfie-Dughan et al., 2011b). The Mo concentration profile with depth in the DTMF is relatively constant between sampling campaigns in 2005 and 2009 (Shaw et al., 2011). Young tailings do not show the same major deviations in Mo porewater concentrations observed in the JEB TMF. The mass of Mo in the tailings could explain the difference in powellite concentrations between the JEB TMF and DTMF. There is significantly more Mo in the JEB TMF samples (mean concentrations of 164 µg/g and median concentration of 118 µg/g from Blanchard et al. (2015)) versus DTMF samples (mean concentrations of 68 µg/g and median concentrations of 77 µg/g from Essilfie-Dughan et al. (2011b)). Powellite concentrations show an increase correlation with the Fe/Mo ratio of tailings samples in both the JEB TMF and DTMF (Blanchard et al., 2015; Essilfie-Dughan et al., 2011b). The combined results of these studies suggest that both sufficient time and low Fe/Mo ratios are required for powellite to precipitate.

6.5.3.4 Other Mineralogical Controls

Annabergite precipitation was observed in low pH precipitates during laboratory neutralization of McClean Lake raffinates containing high concentrations of Ni and As (Mahoney et al., 2007). Annabergite supersaturation is not calculated at any point during the neutralization process. Grains of CaO coated with a Ni-As type precipitate were identified, suggesting annabergite precipitates around high pH gradients surrounding CaO (Langmuir et al., 1999). Bulk XAS studies of all neutralization precipitates and tailings samples do not support the presence of annabergite (in As and Ni K-edge experiments). In addition, concentrations of Ni in mill neutralization samples at Rabbit Lake indicated that Ni precipitates independently from As and

does not precipitate until pH > 5, suggesting annabergite precipitation is not a dominant process during neutralization (Moldovan and Hendry, 2005).

Theophrastite precipitation at pH 7 to pH 8 is a suggested mineralogical control of Ni in multiple studies (Bissonnette, 2015; Essilfie-Dughan et al., 2012; Mahoney et al., 2007; Shaw et al., 2011). Like scorodite, however, the lack of crystalline phases in XRD data of laboratory and field samples precludes the presence theophrastite despite the relative abundance of Ni in the raffinate (De Klerk et al., 2012). It is possible that amorphous $Ni(OH)_2$ precipitates in these samples as McClean Lake laboratory samples contain a Ni-phase not associated with other metals (Mahoney et al., 2007). However, Ni removal is greater in the presence of other precipitates, suggesting adsorption or surface precipitation of Ni is favourable (Mahoney et al., 2007). Mahoney et al. (2007) determined that $Ni(OH)_2$ precipitation alone cannot explain the decrease in Ni concentrations during raffinate neutralization. Samples from Rabbit Lake precipitates showed evidence of Ni associating with Al and Fe hydroxides (Donahue et al., 2000; Pichler et al., 2001). Nickel K-edge analysis on high pH (~10) samples did not identify pure phase $Ni(OH)_2$; Ni was only associated with Al (Robertson et al., 2017). The physical evidence from these studies suggest Ni is only present with other co-ions and not as a pure $Ni(OH)_2$.

$NiMoO_4$ is observed in DTMF tailings and its abundance is dependent on the ore composition (Essilfie-Dughan et al., 2011b). Tailings derived from the Deilmann deposit are elevated in Ni and Mo concentrations and contain higher concentrations of $NiMoO_4$ (~45-95% of the total Mo) versus Mo-adsorbed ferrihydrite; tailings derived from McArthur River contain low concentrations of Ni and Mo relative to Fe and contain higher proportions of Mo-adsorbed ferrihydrite versus $NiMoO_4$ (~26-29% of the total Mo; Essilfie-Dughan et al., 2011b). Bissonnette et al. (2016) identified 20% of Mo precipitated as $NiMoO_4$ in high pH samples from the Key Lake neutralization process. A similar study was unable to identify α-$NiMoO_4$ in JEB TMF samples, although they suggest β-$NiMoO_4$ (which was not synthesized) could exist in the samples (Hayes et al., 2014). The same study reported intimate associations of Ni and Mo in μXRF data although it was not determined if the phase was a primary or secondary mineral.

Barium chloride is added in all three neutralization processes to co-precipitate ^{226}Ra with barite (Eq. 6.11).

$$Ba^{2+} + Ra^{2+} + SO_4^{2-} \rightarrow (Ba, Ra)SO_4 \quad (6.11)$$

Radium and Ba possess similar chemical properties. Both elements are divalent cations in solution with nearly identical hydrated ionic radii (Liu and Hendry, 2011). Excess SO_4^{2-} in the raffinate ensures Eq. 6.11 is strongly favoured. Storing ^{226}Ra as a solid solution in barite is desirable because barite is sparingly soluble ($\log K_{sp}$ = -9.97) and should be stable on a long-term basis under the conditions of the tailings (Langmuir and Melchior, 1985). Goulden (1997) analyzed tailings from the decommissioned Cluff Lake mill and concluded that barite is the major solubility control of ^{226}Ra. Liu and Hendry (2011) titrated raffinate from the Key Lake process (with and without $BaCl_2$) to systematically determine the fate of ^{226}Ra during raffinate neutralization. The activity of ^{226}Ra in the raffinate sample was 150 Bq/L; activities of ^{226}Ra in the Key Lake treated effluent range from 0.02-0.07 Bq/L, demonstrating the effectiveness of the mineralogical controls of ^{226}Ra during neutralization. However, Liu and Hendry (2011) determined that only 17% of ^{226}Ra was associated with barite, while 73% was associated to Fe-oxides (e.g., ferrihydrite), 3.7% was associated to soluble phases (likely gypsum), and the remainder associated with minor phases. Conversely, Goulden (1997) concluded that adsorption and ion exchange mechanisms only exert minor controls on ^{226}Ra activities. The reason for this discrepancy is unclear. However, both studies show that barite is important in regulating the long-term geochemical stability of ^{226}Ra.

6.6 The Geochemistry of the Tailings Bodies

6.6.1 Hydrogeology of In-Pit Tailings Management Facilities

The three active U TMFs in the basin are mined-out pits repurposed to control the hydrogeology around the tailings body. The RLITMF uses a pervious surround design whereby permeable coarse grained rock and sand-filter walls line the boundary of the TMF, allowing the surrounding groundwater to preferentially flow around the tailings through the section of high hydraulic conductivity (Figure 6.9; Donahue et al., 2000). Water is drawn through the pervious surround using raise wells connected to a drainage system to dewater the tailings body. This method decreases the hydraulic conductivity of the tailings and creates a "plug" in the hydrogeological system to ensure long-term transportation of EOCs in the tailings is controlled by diffusion (Langmuir et al., 1999; Moldovan et al., 2008). Diffusion cell testing and reactive transport modeling of the RLITMF suggests the source term of As is controlled by diffusion and adsorption processes, resulting in a 40-70% decrease of aqueous As relative to the initial tailings

over a 10,000 year period. The same model demonstrates that As concentrations in groundwater 50 m downstream from the tailings should remain at background levels (0.001 mg/L; Moldovan et al., 2008). The DTMF uses a similar concept with the exception that the pervious surround is a natural formation of outwash sand rather than a man-made construction (Bharadwaj and Moldovan, 2005). Tailings porewater is recycled to the mill through underdrains located at the bottom of the DTMF (Figure 6.2), further dewatering the tailings. The JEB TMF uses a similar tailings management method with water drawn through drainage rock from below the tailings (Figure 6.3) and recirculated back to the mill (Rinas et al., 2010).

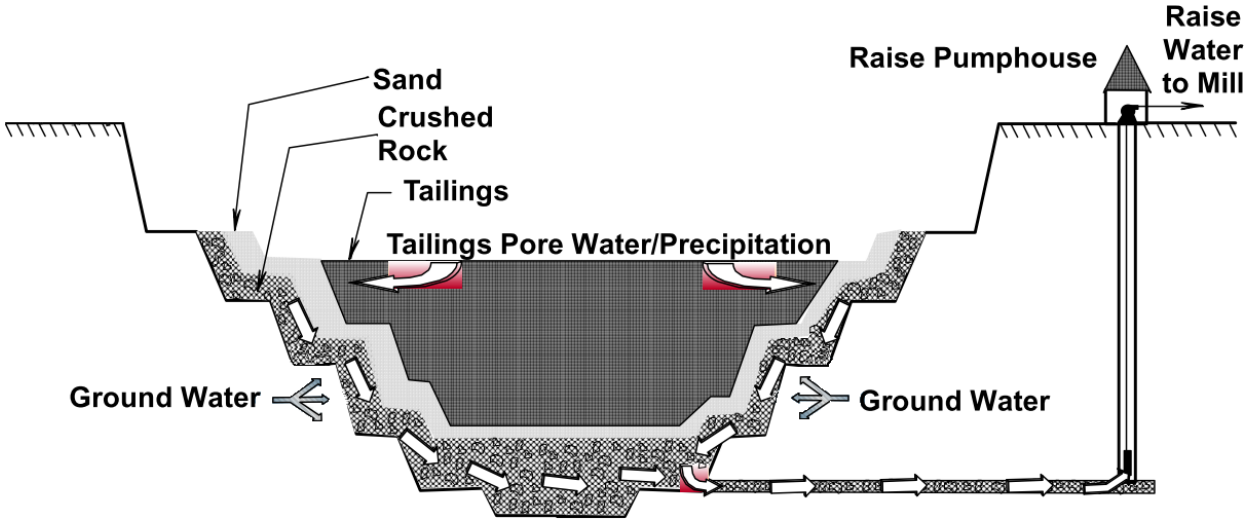

Figure 6.9. Schematic of the pervious surround method used for controlling groundwater flow around the tailings by creating an area of high hydraulic conductivity around the tailings (after Moldovan 2006).

6.6.2 Aqueous and Solid Geochemistry of the Tailings

The geochemical conditions in the three TMFs are neutral to alkaline in pH, oxic, and are at low temperatures (0-12°C; Donahue and Hendry, 2003; Langmuir et al., 2006; Shaw et al., 2011). Donahue and Hendry (2003) analyzed pore fluids from in-pit monitoring wells at the RLITMF. They measured a mean pH of 9.9, ranging from pH 6.6-13.0 (n = 580). The mean Eh of the pore fluid was 174 mV but ranged from -400 mV to 400 mV, indicating reduced zones are present in the RLITMF. A similar study that spanned the depth of the DTMF and sampled tailings from two orebodies (Deilmann and McArthur River) was performed by Shaw et al. (2011). The mean porewater pH was pH 9.6 (n = 159) in both tailings types with a minimum and maximum pH of 7.6 and 10.7. The mean Eh was 189 mV (Deilmann orebody) and 220 mV (McArthur

orebody) with a minimum and maximum Eh of -64 mV and 472 mV. The range in Eh shows a primarily oxic geochemical system. Comprehensive geochemical literature of the JEB TMF is limited; however, three porewater samples from depths spanning 33 m ranged in pH from 7.5-7.7 and in Eh from 370-450 mV (Langmuir et al., 2006).

The equilibrium geochemistry of EOC surface complexes in each TMF will be dependent on the terminal pH (discussed in Chapter 6.5.3.1). The terminal pH of tailings is historically set at pH > 10 to ensure Ni remains precipitated. However, increased re-dissolution of As occurs at this pH. This was a contributing factor for the JEB TMF terminal pH being set to 7-8 because McClean Lake was anticipating to process As-rich ore (Langmuir et al., 1999). The pH dependence of EOC solubility influenced Key Lake and Rabbit Lake to re-design their neutralization processes, adding thickeners at low pH neutralization stages to prevent Se and Mo from desorbing at high pH neutralization stages and contaminating the final effluent. This does not, however, prevent Mo from desorbing in the tailings. At the low pH neutralization stage, Mo concentrations decrease from 2-3 mg/L to 0.1 mg/L (Bissonnette et al., 2016; Gomez et al., 2013a). The Mo-containing precipitates are removed from the neutralization process and are neutralized to pH 10.5 during tailings preparation, causing Mo concentrations to increase to 4-5 mg/L (the aqueous concentration is greater than the initial raffinate concentration because there is less water content in the tailings slurry). Desorption occurs because of the increased negative charge on the surface of ferrihydrite and agrees with the Mo adsorption capacity of ferrihydrite as a function of pH (Dzombak and Morel, 1990; Shaw et al., 2011).

It is important to define the speciation of EOCs in the tailings because the mobility, reactivity, and toxicity of an element is dependent on speciation. In the RLITMF, As(V) comprises 88% of the total aqueous As, with the remainder in the form of As(III) (Moldovan et al., 2008). Up to 18% of solid phase As in the RLITMF tailings was associated with sulfide minerals (Pichler et al., 2001). In the DTMF, the bulk oxidation state of solid phase As is As(V) (~96%) with the residual associated with gersdorffite and other sulfide minerals (Essilfie-Dughan et al., 2013). Minor amounts of solid phase As(III) was measured in ferrihydrite adsorption complexes (Essilfie-Dughan et al., 2012). Conversely, Shaw et al. (2011) did not observe aqueous As(III) in the DTMF; arsenic was either As(V) (86%) or in the form of a monomethyl/monothio As(V). The presence of monomethyl-As(V) is explained by abiotic methylation of As with entrained organic compounds from the solvent extraction process, while monothioarsenate potentially forms through an abiotic

reaction of As(III) with sulfide minerals (Shaw et al., 2011). Monothioarsenates are only observed at depths corresponding to Deilmann ore tailings (i.e., polymetallic ore with elevated sulfide and As concentrations). The lack of aqueous As(III) in the DTMF is confounding considering it is younger and possesses geochemical conditions similar to the RLITMF. In the JEB TMF, a mixture of aqueous As(V) and As(III) is observed. A trend of increasing As(V) and variable As(III) with time is observed and is attributed to oxidation reactions of arsenide minerals (discussed in Chapter 6.6.3; Rinas et al., 2010; Warner and Rowson, 2007).

Speciation of Se and Mo in the tailings is not well defined. Shaw et al. (2011) generated stability field diagrams for Se and Mo in the DTMF. Measurements of tailings porewater pH and Eh indicate SeO_3^{2-} (Se(IV)) and MoO_4^{2-} (Mo(VI)) are the dominant aqueous species at equilibrium. Quantitative speciation measurements of aqueous Se showed ~65% was in the Se(VI) oxidation state, suggesting that the aqueous geochemistry is not at equilibrium with respect to Se (Shaw et al., 2011). From the raffinate neutralization data in Chapter 6.5.3, solid phase Se and Mo in the tailings is potentially in the form of Se(IV) and Mo(VI) surface complexes with ferrihydrite, $Al(OH)_3$, and hydrotalcite. Surface complexation with ferrihydrite is likely more dominant in the RLITMF and JEB TMF due to lower concentrations of Al in the raffinate.

The effect of the ore minerology on tailings geochemistry is observed in geochemical depth profiles from tailings cores (Figure 6.10-12; COGEMA, 2003; Donahue and Hendry, 2003; Moldovan, 2006; Shaw et al., 2011). In the DTMF, there is a geochemical boundary separating Deilmann orebody tailings and McArthur River orebody tailings (Figure 6.10). Deilmann derived tailings contain elevated concentrations of solid phase As, Fe, Mo, Ni, and Se and possess a low Fe/As ratio (~4). McArthur River tailings contain lower concentrations of the same elements and possess a greater Fe/As ratio (~30; Shaw et al., 2011). The concentrations of As, Mo, and Fe in the solid phase correlate to porewater concentrations of As and Mo. For example, the mean As concentration in Deilmann tailings porewater (3.780 mg/L) is 6.7 times greater than McArthur River tailings porewater (0.567 mg/L). The greater Fe/As ratio in the McArthur River tailings favours the formation of As surface complexes on ferrihydrite during neutralization (rather than ferric arsenate precipitation) without oversaturating ferrihydrite surface sites, resulting in lower As porewater concentrations. Similarly, the Mo porewater concentration is 3.7 times greater in the Deilmann tailings (15.1 mg/L) relative to the McArthur tailings (4.13 mg/L). The difference in Fe/Mo ratio is likely the major control in the different porewater concentrations. A decrease of the

mean fresh and *in situ* Deilmann porewater concentrations of Mo (23.2 mg/L and 15.1 mg/L, respectively) suggests that powellite precipitates after tailings deposition in the DTMF as discussed in Chapter 6.5.3.3. Selenium and Ni porewater concentrations are not significantly different between the two tailings types. The boundary between tailings from different orebodies in the RLITMF is not well defined because multiple deposits were often processed in a single year (Figure 6.5). However, As porewater concentrations are < 1 mg/L in tailings from raffinates with Fe/As > 10, while concentrations can exceed 40 mg/L in tailings from raffinates with Fe/As < 4 (Figure 6.11; Donahue and Hendry, 2003; Moldovan, 2006). This correlation agrees with the relationship of the Fe/As ratio and As porewater concentrations in the DTMF. Aqueous and solid phase As and Ni concentrations are strongly correlated in the RLITMF because the polymetallic ores milled at Rabbit Lake contain large amounts of gersdorffite and niccolite (Figure 6.11; Donahue, 2000). The same correlation between As and Ni occurs in the JEB TMF (Figure 6.12). Evidence of *in situ* oxidation of sulfide minerals (discussed in Chapter 6.6.3) from the polymetallic ores at McClean Lake is observed from the increasing As porewater concentration, which is independent of Fe/As ratio (Figure 6.12).

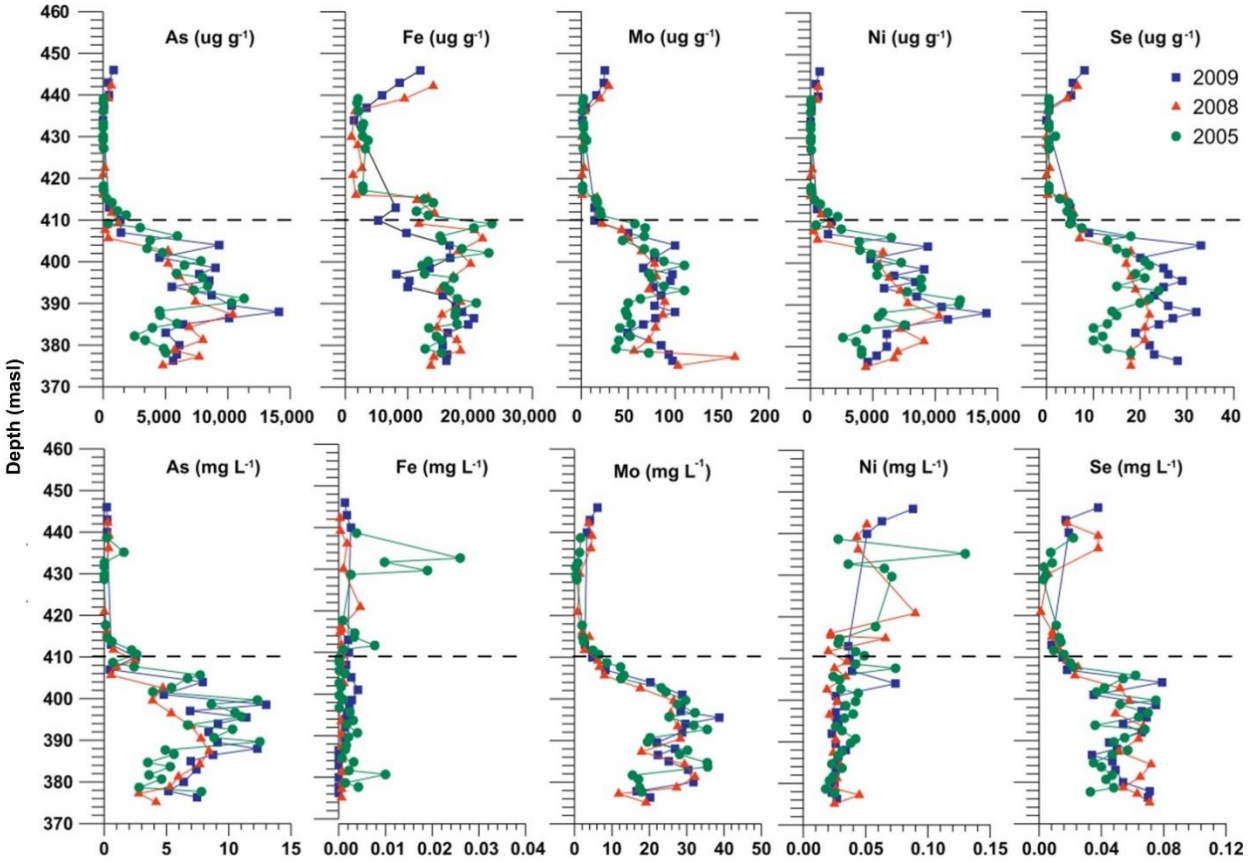

Figure 6.10. Solid phase (top) and porewater (bottom) concentrations of three sets of tailings samples drilled from a single location in 2005, 2008, and 2008 at the DTMF. The dashed line denotes the boundary between tailings derived from McArthur River ore (above the line) and Deilmann ore (below the line; after Shaw et al. 2011).

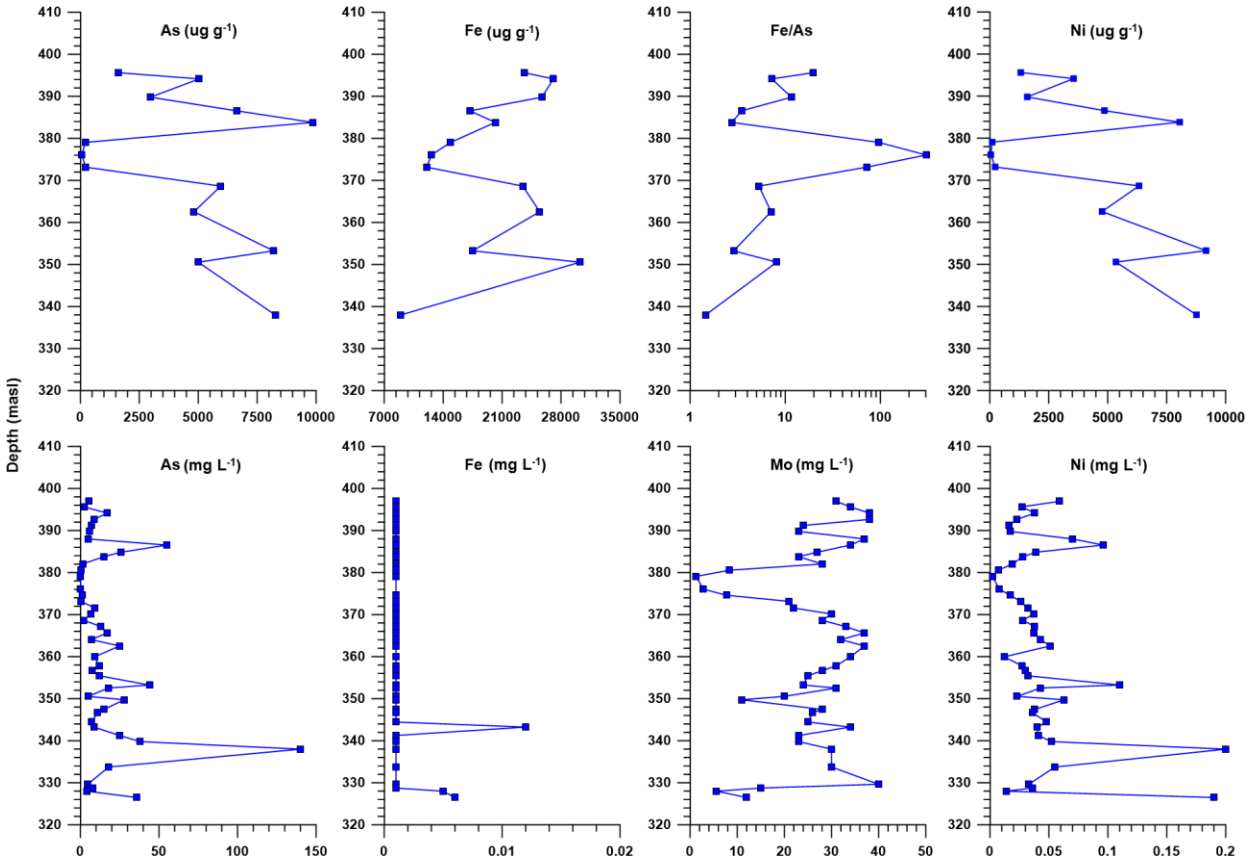

Figure 6.11. Solid phase (top) and porewater (bottom) concentrations from one core profile from the RLITMF in 1999 (data from Moldovan 2006).

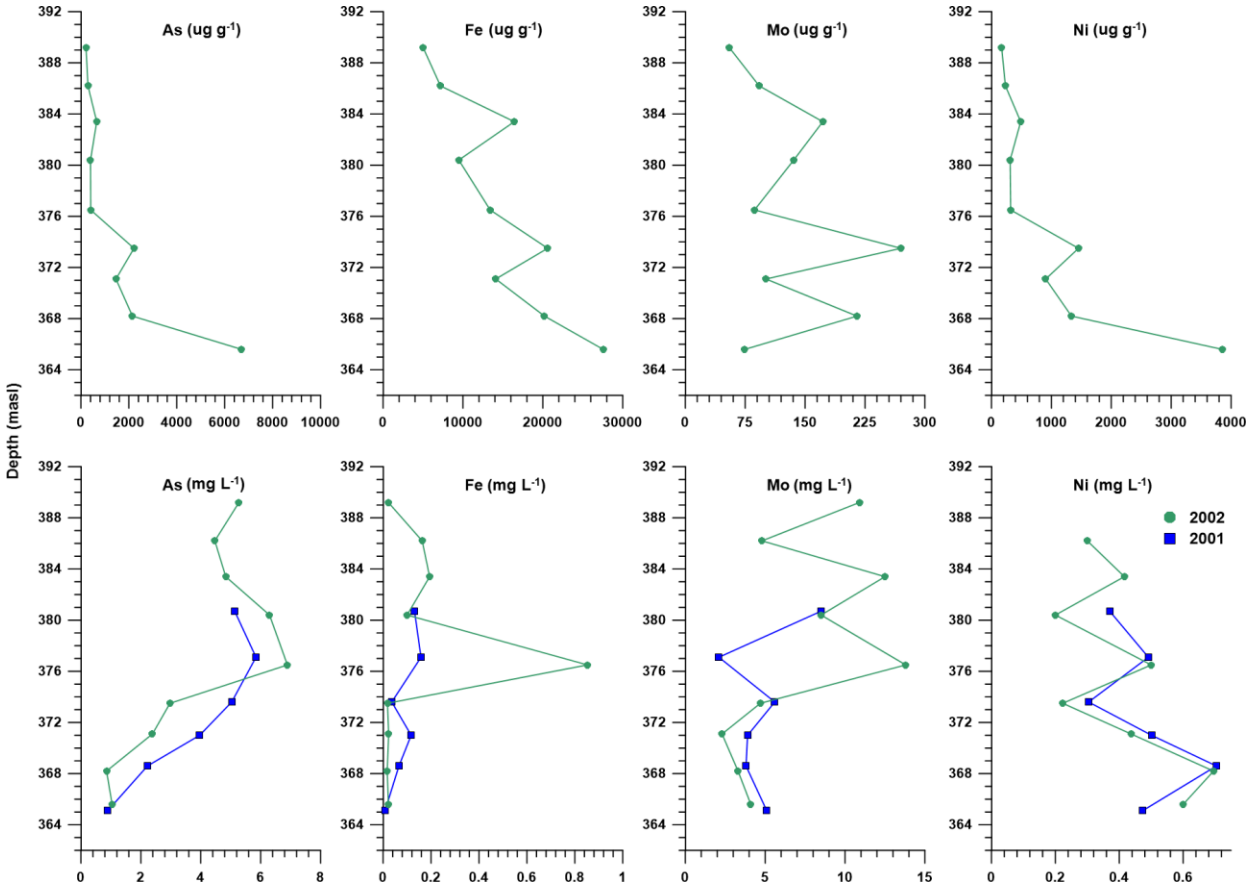

Figure 6.12. Solid phase (top) and porewater (bottom) depth averaged concentrations of tailings core samples from five locations collected one year apart at the JEB TMF in 2001 and 2002 (data from COGEMA 2003).

Mineral saturation indices in tailings porewater can be used to infer the presence and stability of specific mineral phases at equilibrium. Shaw et al. (2011) calculates ferrihydrite to be slightly undersaturated in the DTMF porewater, while hematite and goethite are supersaturated, suggesting ferrihydrite will crystallize to these phases over time. However, surface complexes (e.g., adsorbed AsO_4^{3-}) stabilize ferrihydrite should inhibit or prevent ferrihydrite crystallization (Das et al., 2011a). Scorodite and ferric arsenate are undersaturated in the DTMF and RLITMF because of the alkaline pH (Donahue and Hendry, 2003; Shaw et al., 2011). Experiments with theoretical tailings in the JEB TMF predict scorodite saturation and ferric arsenate undersaturation; however, ferric arsenate is observed in the JEB TMF, and not scorodite (Chen et al., 2009; Mahoney et al., 2007). It is unclear if ferric arsenate will crystallize to scorodite in the JEB TMF over time as suggested by thermodynamic calculations. Powellite is saturated in the each TMF and is physically observed in the DTMF and JEB TMF (Blanchard et al., 2015; Essilfie-Dughan et al.,

2011b). The increasing powellite concentration in the JEB TMF over time (Chapter 6.5.3.4) is evidence of tailings disequilibrium. As was discussed in Chapter 6.5.3.3, tailings porewater is saturated with respect to Ca-arsenate minerals yet physical evidence for Ca-arsenates is minimal. It is possible that Ca-arsenate precipitation is rate-limited like powellite and will precipitate as equilibrium is reached.

6.6.3 Geochemical Stability

When tailings are discharged to the TMF they are not at geochemical equilibrium (Hayes et al., 2014). Fresh tailings are a mixture of newly precipitated solids and primary minerals from the leach residue that were ground up and exposed to acid. Chemical reactions will occur in this mixture as the tailings move towards equilibrium. Changes in tailings porewater chemistry are observed in studies that sample tailings over multiple years. Temporal studies of As speciation in JEB TMF porewater observed total As concentrations increasing after deposition due to As(III) accumulating in the porewater. Over time, As concentrations from the same depth began decreasing to an equilibrium concentration of < 2 mg/L. Warner and Rowson (2007) and Rinas et al. (2010) determined that arsenide minerals are oxidizing, releasing As(III) to solution, and oxidizing to As(V) (Rinas et al., 2010; Warner and Rowson, 2007). Oxidation of As(III) to As(V) is the rate limiting step and causes temporary accumulation of As(III) in the porewater (Rinas et al., 2010; Warner and Rowson, 2007). This mechanism is not explicitly observed in the RLITMF or DTMF. In the RLITMF, the distribution of As speciation remains constant with depth (Moldovan et al., 2008). Although as mentioned in Chapter 6.4.3, As is present as sulfides in the RLITMF, suggesting As could be mobilized through sulfide oxidation (Pichler et al., 2001). In the DTMF, Essilfie-Dughan et al. (2012) observed As(III) adsorbed to ferrihydrite and hypothesized the origin of As(III) to be a result of primary mineral oxidation (Essilfie-Dughan et al., 2012). However, the bulk oxidation state of As in the DTMF solids is ~96% As(V) and has not changed over a 16 year period (as of 2013; Essilfie-Dughan et al., 2013). Arsenide oxidation suggests that other sulfide minerals (e.g., pyrite, chalcopyrite, and molybdenite) are being oxidized in the tailings causing acid generation and releasing associated metal(loid)s. Ultimately, the presence of sulfides in any tailings system must be considered as a potential long-term source of As and other EOCs.

A kinetic study of As concentrations in tailings porewater was performed by Langmuir et al. (1999) using simulated McClean Lake tailings at pH 8. Ferric arsenate dissolution occurs at 25°C and causes As concentrations to increase with time. The dissolution rate is proportional to increasing pH and decreases exponentially with increasing Fe/As. The equilibrium As concentration is calculated to be 1 mg/L at pH 8 and Fe/As = 3.0 (Langmuir et al., 1999). Similarly, the stability of As-adsorbed ferrihydrite at pH 10 was tested by Das et al. (2011a) to determine if ferrihydrite crystallizes to hematite or goethite. It was concluded that adsorbed As stabilizes ferrihydrite within the tailings and should remain stable for several tens of thousands of years under the geochemical conditions of the DTMF.

The stability of layered double hydroxides and their controls on EOC concentrations were not explicitly studied in the TMFs. However, hydrotalcite is present in 15 year-old DTMF samples, suggesting it is stable, at least over a short time period (Gomez et al., 2013a). Structural metals of layered double hydroxides (e.g., Mg^{2+}) dissolve as the pH decreases and approaches circumneutral conditions (Goh et al., 2008). In a laboratory study, As(V)-adsorbed hydrotalcite equilibrated at pH 10 released < 1.0% of the total As (Palmer and Frost, 2011). Additionally, adsorbed oxyanions are shown to stabilize hydrotalcite (Morimoto et al., 2012). These data suggest the alkaline conditions of the DTMF and RLITMF are favourable for the stability of layered double hydroxides and their EOC controls. Aging of Ni-Al layered double hydroxides decreases the solubility of Ni due to silicate replacing interlayer anions and resulting in transformation to a Ni-Al phyllosilicate precursor (Scheckel et al., 2000). This could suggest that layered double hydroxides are only metastable and phyllosilicates are the long-term stable mineral phase.

The low temperature and hydraulic conductivity of the TMFs promote mineralogical stability of the tailings. The local climate results in mean tailings temperatures on the order of 0-12°C, which inhibit reaction rates of mineral dissolution or transformation (Donahue and Hendry, 2003; Hayes et al., 2014; Shaw et al., 2011). The low hydraulic conductivity of the tailings limits solute transport to diffusion rather than advective processes, further inhibiting reactions and transport (Moldovan et al., 2008). The combination of these characteristics suggest that U tailings in the basin should be more geochemically stable relative to other mine tailings impoundments in warmer climates or those that use other means of tailings disposal that are not as controlled as the in-pit method.

6.7 Geochemical Modeling

Multiple studies construct equilibrium models of the neutralization processes and tailings systems using the hydrogeochemical modeling code PHREEQC (Parkhurst and Appelo, 2013). These models are narrow in scope and focus on the chemistry of elements that are relevant to the subject of the study (Essilfie-Dughan et al., 2012; Gomez et al., 2013a; Mahoney et al., 2007; Moldovan, 2006; Moldovan and Hendry, 2005; Robertson et al., 2014). Using the comprehensive knowledge presented in this review, we develop an integrated geochemical model of raffinate neutralization and tailings bodies that predicts the equilibrium mineralogy and long-term aqueous chemistry of the tailings in the TMFs.

The model was built with PHREEQC v.3.3.10.12220 (Parkhurst and Appelo, 2013). The LLNL(D2) thermodynamic database was used because it represents the metal-arsenate aqueous complexes well (Langmuir et al., 2006; Mahoney et al., 2007). A number of solubility products constants (K_{sp}) and surface complexation constants were modified or added to match those used in other geochemical models (Table 6.6). Due to a lack of thermodynamic data in the literature, hydrobasaluminite and hydrotalcite surface complexation constants for As and Ni were assumed to be the same as $Al(OH)_3$. Surface complexation of Se and Mo to Al phases was ignored because there is minimal direct evidence of these elements associating with Al in the tailings. Ferric arsenate was adjusted based on the results of Mahoney et al. (2007); the high pH value ($\log K_{sp}$ = -25.55 between pH 6.24-7.32) was selected to better model ferric arsenate in the neutral to alkaline tailings bodies (Mahoney et al., 2007). Arsenic surface complexation constants for ferrihydrite were adjusted to match values used by Moldovan and Hendry (2005).

Table 6.6. Equilibrium phase and surface complexation solubility product constants added to and/or adjusted in the LLNL(D2) thermodynamic database.

Reaction	Original logK	Adjusted logK
Equilibrium Phase		
$Al(OH)_3$ (am) + $3H^+ \rightleftharpoons Al^{3+} + 3H_2O$ (Sánchez-España et al., 2011)	10.2	-
$Mg_{0.72}Al_{0.28}(OH)_2(SO_4)_{0.14}\cdot 0.39H_2O + 2H^+ \rightleftharpoons 0.72Mg^{2+} + 0.28Al^{3+} + 0.14SO_4^{2-} + 2.39H_2O$ (Allada et al., 2006)	9.82	-
$Ni_{0.69}Al_{0.31}(OH)_2(CO_3)_{0.155}{:}0.37H_2O + 2H^+ \rightleftharpoons 0.69Ni^{+2} + 0.31Al^{+3} + 0.155CO_3^{-2} + 2.37H_2O$ (Allada et al., 2006)	2.24	
$Al_4(SO_4)(OH)_{10}\cdot 15H_2O + 10H^+ \rightleftharpoons 4Al^{3+} + SO_4^{2-} + 25H_2O$ (Sánchez-España et al., 2011)	23.0	-
$FeAsO_4\cdot 2H_2O \rightleftharpoons Fe^{3+} + AsO_4^{3-} + 2H_2O$	-21.69	-25.55
Surface Complexation Reaction		
[a]$Hfo\_OH + H_3AsO_4 \rightleftharpoons Hfo\_H_2AsO_4 + H_2O$	8.61	8.81
$Hfo\_OH + H_3AsO_4 \rightleftharpoons Hfo\_HAsO_4^- + H_2O + H^+$	2.81	3.01
$Hfo\_OH + H_3AsO_4 \rightleftharpoons Hfo\_OHAsO_4^{-3} + 3H^+$	-10.12	-11.22
[a]$Alumina\_OH + H^+ \rightleftharpoons Alumina\_OH_2^+$ (Goldberg 2002)	7.38	-
$Alumina\_OH \rightleftharpoons Alumina\_O^- + H^+$ (Goldberg 2002)	-9.09	-
$Alumina\_OH + H_3AsO_4 \rightleftharpoons Alumina\_HAsO_4^- + H^+ + H_2O$ (Goldberg 2002)	2.51	-
$Alumina\_OH + H_3AsO_4 \rightleftharpoons Alumina\_AsO_4^{-2} + 2H^+ + H_2O$ (Goldberg 2002)	-2.45	-
$Alumina\_OH + Ni^{+2} \rightleftharpoons Alumina\_ONi^+ + H^+$ (Rajapaksha et al., 2012)	-12.85	-
$2Alumina\_OH + Ni^{+2} \rightleftharpoons (Alumina\_O)_2Ni + 2H^+$ (Rajapaksha et al., 2012)	-4.78	-

[a] Hfo represents the surface of hydrous ferric oxide (i.e., ferrihydrite) and Alumina represents the surface of an Al oxide (i.e., amorphous $Al(OH)_3$).

The Rabbit Lake, Key Lake, and McClean Lake neutralization processes provide the general framework for the model (Figure 6.13). The model input is provided in the supplementary information. The required inputs are the solution chemistries of streams being neutralized, mineralogical composition of solid streams, reagent addition, and process parameters (e.g., initial and final pH, temperatures, solid/liquid separation steps, etc.). The model is divided into a mill neutralization model and a tailings model. In the neutralization model, raffinate is neutralized with slaked lime to a target pH and equilibrium phases are allowed to precipitate. For the McClean Lake process, the leach residue is also added to the neutralization model. The neutralization model

outputs neutralized solution chemistry (final effluent) and the mass of each precipitated phase. The tailings model uses the raffinate and leach residue compositions to calculate the tailings porewater chemistry and the minerals that precipitate or dissolve in the tailings. Parameters specific to each process were adjusted for each version of the model (e.g., there are multiple solid/liquid separation stages at Key Lake, and only one at McClean Lake).

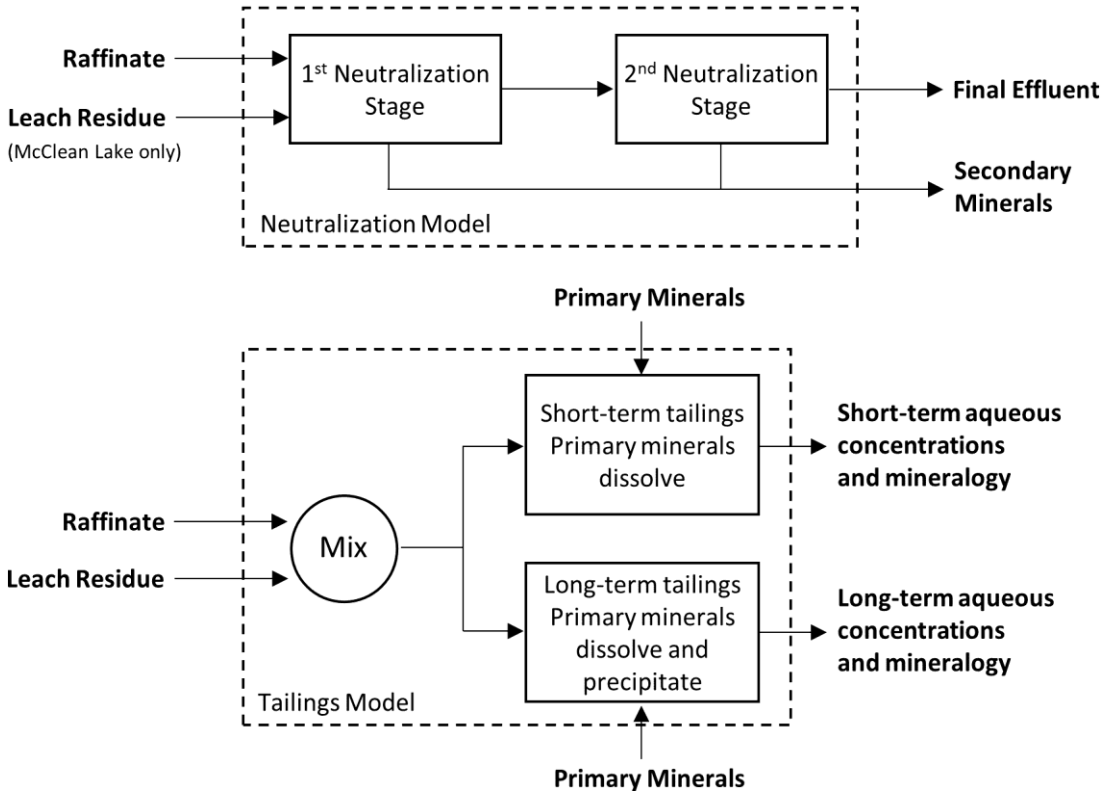

Figure 6.13. Generalized geochemical model flow diagram. Bold text indicates input and output streams. Boxes indicate pH adjustments and equilibrium steps. Boxes with broken lines indicate model boundaries. A two stage neutralization process is shown for demonstration purposes.

A major assumption of the model is the neutralization process is thermodynamically controlled. In practice, the residence time of each neutralization stage is on the order of hours and it is unlikely that thermodynamic equilibrium is reached. However, most of the precipitation reactions in these processes are rapid as evidenced by the substantial decreases of dissolved elements between the raffinate and the final effluent. The rate limiting step is likely transformation of amorphous precipitates to crystalline minerals. For example, gibbsite precipitation is thermodynamically favoured over amorphous $Al(OH)_3$. Data from previous studies, however, show that amorphous $Al(OH)_3$ precipitates and gibbsite is not observed in fresh precipitates. The

amorphous phase should crystallize to gibbsite over time, although these time scales are beyond the scope of the model.

The following mineral phases were allowed to reach equilibrium at each neutralization step: amorphous $Al(OH)_3$, barite, calcite, $CaMoO_4$, ferric arsenate, ferrihydrite, gypsum, hydrobasaluminite, hydrotalcite ($Mg_{0.72}Al_{0.28}(OH)_2(SO_4)_{0.14}\cdot 0.39H_2O$), $Mg(OH)_2$, annabergite, NiAl-hydrotalcite ($Ni_{0.69}Al_{0.31}(OH)_2(CO_3)_{0.155}:0.37H_2O$), $Ni(OH)_2$, $NiMoO_4$, and amorphous SiO_2. Surface complexation was allowed for ferrihydrite, amorphous $Al(OH)_3$, hydrobasaluminite, and hydrotalcite. These phases were allowed to reach equilibrium based on observations of studies presented in this review.

Five independent neutralization datasets from the three sites were selected to test the output of the model (Table 6.7). The datasets were selected based on data availability (i.e., raffinate, intermediate solution, and final effluent chemistry). Aqueous phase data for the leach residue slurry was not available for any dataset; therefore, the solution was assumed to be a four-fold dilution of the raffinate. The leach residue slurry is washed with process water and raffinate in the counter-current decantation process in the mill, which provides the basis for this assumption. The mineralogical composition of the Key Lake leach residue from Hossain (2014) was used for the Key Lake model (Table 6.3). The percentages were normalized and the moles/kg of each mineral was calculated based on the 35% solids target used for the leach residue slurry. Simplified leach residue compositions for Rabbit Lake and McClean Lake were assumed because detailed compositions are not available; quartz, kaolinite, illite, and chlorite (using the same fractions as Key Lake) were used based on observations from previous studies (Langmuir et al., 1999; Pichler et al., 2001).

Table 6.7. Initial raffinate compositions used for each model. Italicized values are assumed values that were not given in the cited study and were included to ensure all major species were accounted for.

Source	Site	pH	Al	As	Ca	Fe (III)	Fe (II)	Mg	Ni	Mo	S[a]	Se	Si
Robertson et al. (2016)	KL	1.0	1924	307	48.7	1303	0	1164	217	94.5	13372	33.6	293
Gomez et al. (2013)[b]	KL	1.4	1016	17.3	*179*	443	445	649	14.5	1.95	*1340*	0.25	*2000*
Bissonnette (2015)[b]	KL	1.6	738	47.3	179	243	304	511	34.7	0.50	1340	*0.25*	*2000*
Moldovan and Hendry (2005)	RL	1	498	526	724	776	86	502	265	*0.50*	6246	*0.25*	*2000*
Mahoney et al. (2007)	ML	0.97	800	690	510	1165	685	1100	515	*0.50*	7148	*0.25*	580

[a] Total S measurements were used as inputs. Equilibrium calculations show SO_4^{2-} is the dominant aqueous S species. Sulfur was used to balance charge.

[b] Concentrations were adjusted for dilution from waste water streams added at the first neutralization stage at Key Lake. The diluted raffinate composition was back-calculated assuming Mg is a conservative element in the low pH neutralization stage.

The Key Lake dataset from Bissonnette (2015) is used to test the model (Bissonnette, 2015). The solution chemistry calculated by the model is compared to mill data from each neutralization step in Figure 6.14. Excluding gypsum, ferric arsenate is the first phase to precipitate at pH 2.3 (Figure 6.15). Ferrihydrite precipitates at pH 2.5, followed by hydrobasaluminite at pH 4.0. Arsenic and Ni adsorption with ferrihydrite and hydrobasaluminite occurs at pH 4.0 in nearly equal amounts (Figure 6.16), while Mo is adsorbed by ferrihydrite. Ferric arsenate precipitation decreases to zero at pH 4.2 because of increased ferrihydrite precipitation and As adsorption. All precipitates are removed from the model after pH 4.2 to mimic the separation of solids in the Se-Mo thickener in the Key Lake neutralization process. After this separation, ferrihydrite continues to precipitate because Fe(II) from the raffinate oxidizes to Fe(III) from H_2O_2 addition at the Se-Mo thickener outlet. Amorphous $Al(OH)_3$ precipitates at pH 6.0 before Al precipitation is dominated by hydrotalcite at pH 8.5. In this scenario, Al is the limiting element for hydrotalcite precipitation and excess Mg remains. In practice, an alternate layered double hydroxide phase likely precipitates as a MgFe-hydrotalcite because of the available Fe(III); however, thermodynamic data for MgFe-hydrotalcite with a sulfate-rich interlayer is not available. As such, the mass of hydrotalcite precipitated is likely underestimated. In lieu of MgFe-hydrotalcite data, the remaining aqueous Mg is precipitated as $Mg(OH)_2$. Nickel concentrations are controlled by

surface complexes with ferrihydrite, amorphous $Al(OH)_3$, and hydrotalcite (Figure 6.16). Minor amounts of NiAl-hydrotalcite and $Ni(OH)_2$ precipitate after pH 9.0. The most abundant minerals in the final neutralization stage (~pH 10) are ferrihydrite, hydrotalcite, and $Mg(OH)_2$. Aqueous concentrations of the model compare well to mill data (Figure 6.14). The greatest discrepancy between the model and measured data is the Mg precipitation trend, but this is explained by MgFe-hydrotalcite precipitation in the mill rather than $Mg(OH)_2$. The type of precipitated mineral phases agree with mineralogical characterization from Bissonnette et al. (2016).

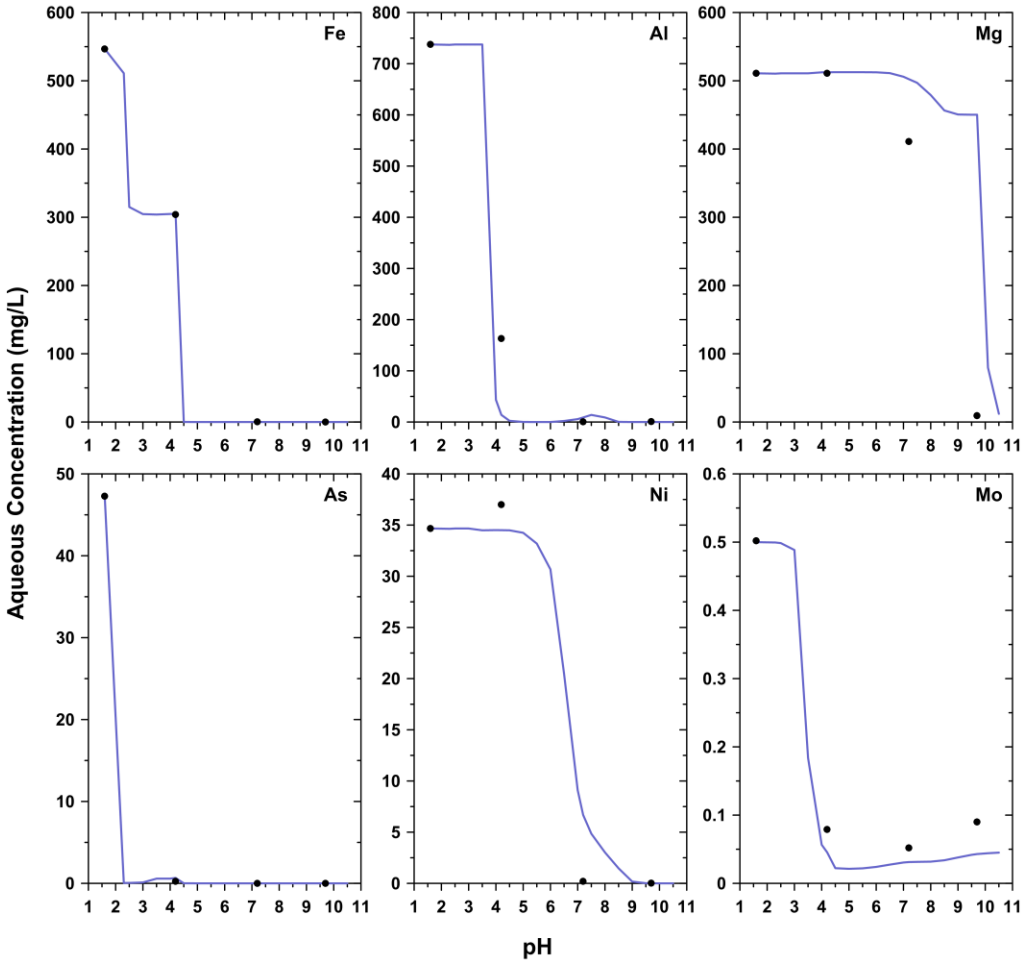

Figure 6.14. Comparison of the neutralization model and mill results from the Key Lake neutralization process (data from Bissonnette (2015)). The blue line represents model results, circles represent actual mill data points.

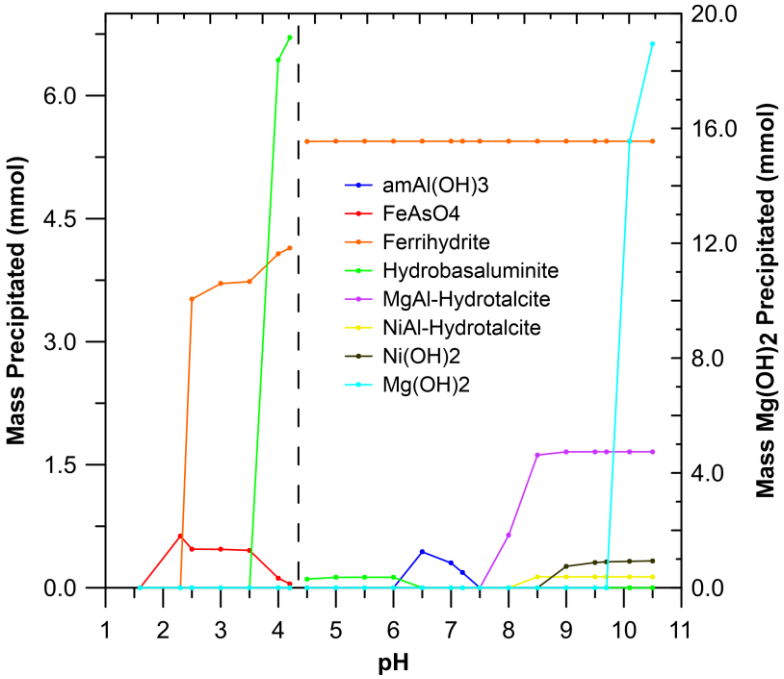

Figure 6.15. Moles precipitated of equilibrium phases of interest in the Bissonnette neutralization model. The first set of solid phases are removed from the model at pH 4.2 (indicated by the dashed vertical line). Gypsum is excluded from the figure. $Mg(OH)_2$ precipitation is plotted on a secondary axis.

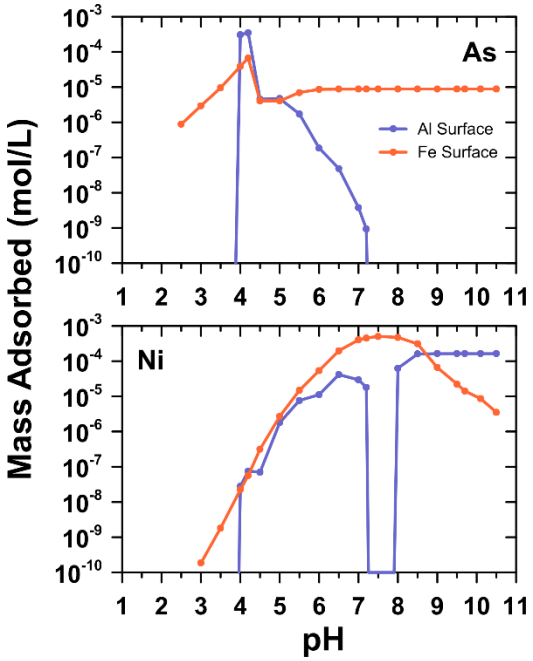

Figure 6.16. Distribution of As and Ni surface complexes in the Bissonnette neutralization model. Aluminum surfaces are hydrobasaluminite (pH 4.0-6.0), amorphous $Al(OH)_3$ (pH 6.5-10.5), and hydrotalcite (pH 6.5-10.5); Iron surfaces are the weak and strong sites of ferrihydrite.

As noted above, accurately modeling layered double hydroxide precipitation in the neutralization processes is difficult; accounting for the variability of the mineral stoichiometry of the layered double hydroxide is difficult because minor changes affect the mineral's K_{sp} value dramatically. A library of thermodynamic data for layered double hydroxides with varying stoichiometries, metal composition, and interlayer anions would benefit models of processes rich with these phases. Studies by Allada et al. (2006) and Rozov et al. (2010) provide a starting point for these data.

The deviation between the model and mill final effluent composition ranges from small to multiple orders of magnitude (Table 6.8). Greater deviations occur when initial concentrations of As, Se, and Mo are high. Surface precipitation, which is difficult to model, could explain the deviations for scenarios with elevated As, Se, and Mo concentrations. To account for surface precipitation of As in the Rabbit Lake and McClean Lake models (Fe/As = 2.2 and 3.6, respectively), ferric arsenate was allowed to precipitate before ferrihydrite. If ferrihydrite and ferric arsenate are allowed to precipitate simultaneously, ferrihydrite precipitation consumes all aqueous Fe. The only mechanism for As sequestration once this occurs is through adsorption with ferrihydrite. This cannot, however, explain As concentrations from Moldovan and Hendry (2005). Precipitating ferric arsenate before ferrihydrite describes As concentrations well up to pH 10 where the pH is too high for ferric arsenate stability. The assumption of surface complexation constants for hydrobasaluminite and layered double hydroxides are also a source of error. Aluminum and Mg were difficult to model at high pH due to the aforementioned variability of the hydrotalcite stoichiometry. In the mills, MgAl-hydrotalcite should precipitate with varying Mg/Al ratios. Improvements to the model are needed before it can be used to reliably calculate final effluent compositions.

Table 6.8. Comparison of neutralization model and field data results for the final effluent (before pH readjustment). Bold values indicate field or laboratory data cited from the corresponding study. Non-bold values indicate results from the model. Dashes indicate no data available.

Model Reference	pH	Al	As	Fe	Mg	Ni	Mo	S	Se	Si	Ca
Key Lake											
Robertson et al. (2016)	**9.5**	**2.29**	**0.01**	**0.11**	**45.2**	**0.19**	**1.58**	**1465**	**0.11**	**0.56**	**1443**
Model	9.5	< 0.01	0.17	< 0.01	1050	0.13	0.02	1828	17.3	50.8	485
Gomez et al. (2013)	**10.1**	**0.49**	**0.01**	**0.06**	**2.38**	**0.03**	**0.01**	**---**	**0.01**	**---**	**---**
Model	10.1	< 0.01	< 0.01	< 0.01	67.9	0.01	0.12	---	0.11	---	---
Bissonnette (2015)	**9.7**	**0.94**	**0.01**	**0.03**	**9.25**	**0.02**	**0.09**	**---**	**---**	**---**	**612**
Model	9.7	< 0.01	< 0.01	< 0.01	450	0.01	0.04	---	---	---	552
Rabbit Lake											
Moldovan and Hendry (2005)	**10.82**	**0.45**	**1.34**	**0.01**	**1.01**	**0.01**	**---**	**1196**	**---**	**---**	**955**
Model	10.82	276.77	259	< 0.01	0.31	< 0.01	---	386	---	---	1532
McClean Lake											
Mahoney et al. (2007)	**7.32**	**0.01**	**0.39**	**33**	**340**	**13**	**---**	**1002**	**---**	**8**	**612**
Model	7.25	0.36	2.49	48.5	1062	0.00	0.32	1864	0.25	50.9	482

The tailings model mixes the raffinate and leach residue solutions (Figure 6.13). The mixing ratio of these streams varies in practice; however, a 1:1 raffinate to leach residue ratio was assumed for model calculations. The variables sensitive to this assumption are the mass of primary minerals dissolved and secondary minerals precipitated (per kg of tailings) at equilibrium. The final pore water concentrations of certain elements could decrease relative to the presented model results if the raffinate to leach residue ratio is decreased such that element concentration are diluted below saturation of their mineralogical controls. This mixture is neutralized to the terminal pH of the TMF being modeled and equilibrated with the primary minerals in the leach residue and the secondary minerals used in the neutralization model. Short-term and long-term scenarios were modeled. In the short-term scenario, primary minerals are allowed to dissolve but not precipitate because of the assumption that precipitation of primary minerals (i.e., the minerals in Table 6.3) are rate-limited due to low-temperatures and mass transfer limitations. This scenario represents fresh tailings deposited in the TMF. The long-term scenario allowed the primary minerals defined in the leach residue assemblage to precipitate if saturation occurred. The model output represents porewater chemistry and the mineral assemblage at the time when equilibrium of the tailings is reached.

The porewater concentrations of the long-term model demonstrated good agreement with tailings data in most cases (Table 6.9). The major species (Al, Ca, Fe, Mg, S, and Si) precipitated as kaolinite, muscovite, chlorite, quartz, and gypsum (which assumes hydrotalcite, amorphous $Al(OH)_3$, and ferrihydrite dissolve or transform over time). However, the modeled porewater concentrations were impacted by similar issues to those of the final effluent chemistry, described above. Accuracy of the short-term Al and Mg concentrations was affected by poorly defined hydrotalcite thermodynamic data. Adsorption of As was overestimated in models with low initial As concentrations (i.e., Key Lake). Conversely, elevated As concentrations were difficult to model accurately at high pH because of the complex interplay of ferric arsenate and ferrihydrite. Like the neutralization model, ferric arsenate was allowed to precipitate first when the Fe/As ratio was low. This method overestimated As sequestration in the McClean Lake model (Fe/As = 3.6), likely because this is an oversimplification of the Fe-As system. However, the As concentration of the Rabbit Lake model (65.7 mg/L) lines up with the depth profile shown in Figure 6.11 for Fe/As = 2.2, where the As porewater concentration is approximately 50 mg/L. Selenium and Mo concentrations were modeled well for Key Lake. Initial concentrations of Se and Mo at Rabbit Lake and McClean Lake were assumed because these concentrations were not known. Nickel sequestration was generally overestimated, although the mechanism (adsorption or precipitation) differed in each model.

Table 6.9. Tailings porewater concentrations from *in situ* samples (bold) and geochemical model calculations. Each model calculation is based on the initial raffinate composition given in the cited study and neutralized under the conditions of the site's neutralization process. Dashes indicate no data available.

Site/Model[a]	Timeframe[b]	pH	Al	As	Ca	Fe	Mg	Ni	Mo	S	Se	Si
Key Lake Porewater		**9.6**	**0.29**	**0.57**	**597**	**0.02**	**2.86**	**0.05**	**4.13**	**507**	**0.02**	**5.74**
Robertson et al. (2016) Model	Short	9.6	153	0.03	759	< 0.01	0.46	< 0.01	0.35	449	2.06	92.6
	Long	9.6	0.13	0.03	627	< 0.01	0.03	< 0.01	0.42	512	2.25	4.99
Gomez et al. (2013) Model	Short	9.6	153	< 0.01	753	< 0.01	0.46	< 0.01	0.35	452	0.01	92.6
	Long	9.6	0.14	< 0.01	625	< 0.01	0.03	< 0.01	0.42	513	0.01	4.99
Bissonnette (2015) Model	Short	9.6	153	< 0.01	751	< 0.01	0.46	< 0.01	0.35	453	0.01	92.6
	Long	9.6	0.14	< 0.01	625	< 0.01	0.03	< 0.01	0.42	513	0.01	4.99
Rabbit Lake Porewater (1)		**10.0**	**0.21**	**16.5**	**591**	**0.02**	**9.88**	**0.04**	**24.8**	**679**	**---**	**5.60**
Rabbit Lake Porewater (2)		**9.7**	**0.25**	**26**	**537**	**0.09**	**---**	**0.14**	**35.8**	**596**	**---**	**2.96**
Moldovan and Hendry (2005) Model	Short	9.7	173	65.7	1652	< 0.01	1.60	0.01	0.19	311	0.22	141
	Long	9.7	0.34	65.8	1476	< 0.01	0.01	0.01	0.20	311	0.22	8.22
McClean Lake Porewater		**7.6**	**0.01**	**1.7**	**504**	**0.09**	**77.7**	**0.59**	**6.12**	**557**	**---**	**6.00**
Mahoney Model	Short	7.6	0.88	< 0.01	515	< 0.01	724	< 0.01	0.54	1386	< 0.01	54.7
	Long	7.6	< 0.01	< 0.01	541	< 0.01	415	< 0.01	0.45	1022	< 0.01	2.96

[a] Key Lake, Rabbit Lake (1) and (2), and McClean Lake porewater tailings concentrations originate from Shaw et al. (2011), Moldovan (2006), Donahue and Hendry (2003), and Mahoney et al. (2007).

[b] Short – the model did not allow any primary minerals to precipitate; Long – primary minerals were allowed to precipitate.

The major precipitates in the short-term tailings model were gypsum, amorphous Al(OH)3, hydrotalcite, ferrihydrite, and amorphous SiO2. The minor precipitates were barite, calcite, CaMoO4, ferric arsenate, NiAl-hydrotalcite, and Ni(OH)2 (Table 6.10). Surface complexation of As, Ni, Se, and Mo was predicted to be a major sequestration mechanism of EOCs (Table 6.11), with the exception of Mo in the Robertson et al. model that was controlled by $CaMoO_4$ due to elevated initial Mo concentrations. Ferrihydrite adsorption was the dominant adsorbent for As, Se, and Mo in all tailings models. Measurements by Robertson et al. (2017) showed 47-59% of As associated with secondary minerals in the tailings (pH 10.5) was partitioned to hydrotalcite and amorphous $Al(OH)_3$, while the model predicted < 4.1% of As adsorbs to these phases (pH 9.6; Table 6.11). This discrepancy could be rationalized by the lack of accurate surface complexation data for hydrotalcite and the state of disequilibrium of the tailings sample. The model also simulates ideal surface site availability of ferrihydrite. Many surface sites could be blocked by other precipitates in the tailings, resulting in more As partitioning to hydrotalcite and amorphous $Al(OH)_3$. Conversely, Ni adsorption was dominated by amorphous $Al(OH)_3$ and hydrotalcite and agrees with the measurements by Robertson et al. (2017). The McClean Lake model showed appreciable Ni adsorption to ferrihydrite (53.8%) because of relatively low initial Al concentrations. NiAl-hydrotalcite was a major Ni sequestration phase in all models. Nickel hydroxide precipitated in the Rabbit Lake model due to initial raffinate conditions (high Ni and low Al concentrations).

Table 6.10 Summary of mineral phases precipitated or dissolved (mmol) in the tailings model. Negative values indicate mineral dissolution. Dashes indicate no precipitation or dissolution occurred. Fh = ferrihydrite, Ht = hydrotalcite.

Model	Time	$Al(OH)_3$	Barite	Calcite	$CaMoO_4$	$FeAsO_4$	Fh	Gypsum	$Al_4(OH)_{10}SO_4$	Ht	NiAl Ht	$Ni(OH)_2$	SiO_2(am)
Robertson et al.	Short	78.7	2.40	1.67	0.37	---	16.2	203	---	41.8	0.15	---	33.1
	Long	---	2.42	1.22	0.36	---	16.2	207	---	---	2.99	---	---
Gomez et al.	Short	73.0	2.40	1.69	0.005	---	16.6	132	---	26.1	---	---	43.8
	Long	---	2.42	1.65	0.004	---	16.6	134	---	---	0.24	---	---
Bissonnette	Short	---	2.40	1.69	---	---	16.6	144	---	30.9	---	---	8.80
	Long	---	2.42	1.55	---	---	16.6	146	---	---	0.90	---	---
Moldovan and Hendry	Short	---	---	2.24	---	2.61	7.04	131	---	18.0	0.14	0.92	---
	Long	---	0.04	---	0.01	2.61	7.04	---	---	18.0	0.14	0.92	---
Mahoney et al.	Short	---	0.04	---	---	5.61	15.4	197	5.40	---	7.96	---	19.5
	Long	---	0.04	---	---	5.61	15.4	214	---	---	7.96	---	---

Model	Time	Chalcopyrite	Chlorite	K-Feldspar	Galena	Illite	Kaolinite	Muscovite	Pyrite	Pyroxene	Quartz
Robertson et al.	Short	-1.30	---	---	-0.30	---	---	---	-6.1	-34.0	---
	Long	-1.30	6.94	-35.0	-0.30	-19.0	9.98	46.4	-6.1	-34.0	0.03
Gomez et al.	Short	-1.30	---	---	-0.30	---	---	---	-6.1	-0.02	---
	Long	-1.30	4.69	-35.0	-0.30	-19.0	7.54	46.4	-6.1	-34.0	49.9
Bissonnette	Short	-1.30	---	---	-0.30	---	---	---	-6.1	-34.0	---
	Long	-1.30	5.39	-35.0	-0.30	-19.0	9.29	46.4	-6.1	-34.0	44.4
Moldovan and Hendry	Short		---			---	---				---
	Long		0.01			-0.01	3.20				26.6
Mahoney et al.	Short		---			---	---				---
	Long		3.30			-2.37	10.2				-0.71

Table 6.11. Summary of surface complexation reactions for the tailings model. The "%Al" column is the fraction of As or Ni adsorbed to Al phases relative to the total amount of adsorption complexes. Fh = ferrihydrite, Ht = hydrotalcite.

Model	Time	pH	Arsenic				Nickel				Se-Fh	Mo-Fh
			$Al(OH)_3$	Ht	Fh	%Al	$Al(OH)_3$	Ht	Fh	%Al		
Robertson et al.	Short	9.6	4.2E-05	2.2E-05	1.5E-03	4.1%	1.3E-03	6.8E-04	---	100%	1.2E-04	1.0E-07
	Long	9.6	---	---	1.5E-03	0.0%	1.3E-03	---	---	0.0%	1.1E-04	9.4E-08
Gomez et al.	Short	9.6	1.1E-07	3.9E-08	1.0E-04	0.1%	1.2E-04	4.4E-05	---	100%	1.7E-06	1.1E-06
	Long	9.6	---	---	1.0E-04	0.0%	---	---	---	0.0%	1.7E-06	1.2E-06
Bissonnette	Short	9.6	---	3.6E-07	5.1E-04	0.1%	---	6.2E-04	---	100%	1.8E-06	6.8E-07
	Long	9.6	---	---	5.1E-04	0.0%	---	---	---	0.0%	1.7E-06	6.7E-07
Moldovan and Hendry	Short	9.7	---	6.2E-06	9.0E-04	0.7%	---	1.8E-03	3.1E-05	98.3%	1.6E-08	2.6E-10
	Long	9.7	---	6.2E-06	9.0E-04	0.7%	---	1.8E-03	3.3E-05	98.2%	1.6E-08	2.7E-10
Mahoney et al.	Short	7.6	---	---	2.2E-07	0.0%	---	---	---	0.0%	2.8E-06	4.8E-06
	Long	7.7	---	---	2.2E-07	0.0%	---	---	---	0.0%	2.8E-06	5.8E-06

The model predicts the dissolution of sulfide minerals (e.g., pyrite, chalcopyrite, and galena) in the oxic and alkaline conditions in the TMFs (and is observed in the JEB TMF as discussed in Chapter 6.6.3). The other primary minerals that dissolve are K-feldspar, illite, and pyroxene. As time progresses, crystalline minerals should begin to form in the tailings. Chlorite, kaolinite, muscovite, and quartz precipitate in the model, although amorphous $Al(OH)_3$ and hydrotalcite would need to dissolve to precipitate large amounts of these minerals. Predicting secondary mineral decomposition is difficult due to adsorption complexes inhibiting transformation and dissolution (Das et al., 2011a). As such, aging tests of tailings samples and long-term monitoring of TMF depth profiles are better suited for these predictions.

The general framework of the results of the geochemical modeling are mostly consistent with past geochemical studies of Athabasca Basin neutralization and tailings processes. We believe this model could be used in industrial and natural systems where acid neutralization occurs. Additions to the thermodynamic library with respect to layered double hydroxides are required to improve the output of the model as are the surface complexation constants for these layered double hydroxides. Modeling of the Fe-As system also needs to be improved to better predict the ferric arsenate and ferrihydrite precipitation system, especially when As concentrations are elevated.

6.8 Future Studies

The geochemistry and geochemical evolution of Athabasca Basin U tailings is well studied in many aspects such as primary and secondary mineral identification, mineralogical controls of EOCs (although heavily skewed towards As), hydrogeology, and porewater chemistry. Arguably, the body of literature on the geochemistry tailings is more extensive than for any other mill process or tailing worldwide. With that said, however, there are certain aspects that remain poorly understood. For example, the mechanism of Se sequestration in the tailings is not explicitly defined and is only inferred to be controlled by inner-sphere surface complexation with ferrihydrite. The stability of amorphous $Al(OH)_3$ and layered double hydroxides in the tailings is not known and can only be speculated on using studies with controlled chemical conditions that may not represent the tailings. The stability of the EOC controls of these Al and Mg phases should be further investigated. Additionally, laboratory aging tests of simulated and actual tailings emphasizing amorphous $Al(OH)_3$ and layered double hydroxide stability should be conducted to at least the same level of detail as the Fe(III)-As(V) system.

6.9 Applicability of Uranium Tailings Research to Other Mining Environments

6.9.1 Other Uranium Milling Facilities

Uranium tailings geochemistry is strongly influenced by the characteristics of the ore and host rock. The geochemical studies of Athabasca Basin tailings are highly applicable to other U milling operations that use an oxic acid leach process for similar ores. For example, the Ranger Mine in the Northern Territory, Australia mills U ore rich in chlorite, quartz, and sericite with minor amounts of galena, pyrite, chalcopyrite, dolomite, apatite, rutile, and hematite (Douglas et al., 2010; Sinclair et al., 2006). The Ranger process uses an acid leach to dissolve U minerals and a lime neutralization to treat raffinate, while tailings are disposed in an in-pit TMF above neutral pH (Sinclair et al., 2006). Ferrihydrite, hydrobasaluminite, amorphous $Al(OH)_3$, and hydrotalcite are observed as secondary minerals in the resulting tailings, suggesting that similar mineralogical controls exist in other facilities (Douglas et al., 2010; Sinclair et al., 2006). Another example of applicability is the transport of contaminants from the Schneckenstein U tailings dam in Germany (Merkel, 2006). Understanding the potential mineralogical controls (or lack thereof) of these contaminants could assist in remediation efforts, predicting the future mobility of the contaminants, and understanding the fate of the contaminants downstream from the dam.

6.9.2 General Applications

The geochemistry of U tailings is not unique to the geochemistry of other tailings systems, acid mine/rock drainage, or other contaminated sites. The most common process used to remove metals from industrial effluents is chemical precipitation with lime or NaOH (Blais et al., 2008). The neutralization chemistry of these processes is likely similar to the neutralization of U mill raffinate. Other metal processing industries, such as the gold industry, deposit As-rich tailings sub-aqueously (pH 6.2-8.0). As-bearing secondary phases (e.g., Ca-Fe arsenates and As-bearing Fe oxyhydroxides) are abundant in these tailings (Craigen, 2006). Acidic water generated by acid mine drainage is often rich in Fe derived from pyrite oxidation and Al from aluminosilicate dissolution (Blowes et al., 1991; Moncur et al., 2005). The Fe- and Al-rich acidic water is gradually neutralized by carbonate minerals in the natural environment as it migrates through the soils, resulting in amorphous $Fe(OH)_3$ and $Al(OH)_3$ precipitation (Bigham and Nordstrom, 2000; Cismasu et al., 2011; Moncur et al., 2005). These hydroxide precipitates adsorb metal(loid)s

liberated through the acid mine drainage process. This process of hydroxide precipitation and metal(loid) adsorption is chemically comparable to the raffinate neutralization in U mills; acid mine drainage neutralization simply occurs on greater time scales (Bigham and Nordstrom, 2000). The large scale and controlled environment of U mill tailings are valuable for scientific advances in environmental research. For example, adsorption capacity measurements of metal hydroxides and layered double hydroxides can be applied to disciplines interested in using these adsorbents as treatment methods (Robertson et al., 2016). Several EXAFS studies of U tailings have contributed to the understanding of metal(loid) co-precipitation and adsorption with metal hydroxides and layered double hydroxides (Bissonnette et al., 2016; Chen et al., 2009; Essilfie-Dughan et al., 2013; Moldovan et al., 2003; Robertson et al., 2017).

6.10 Acknowledgements

The long-term financial support provided by Cameco Corporation and the Natural Sciences and Engineering Research Council of Canada (NSERC) through a Senior Industrial Research Chair to MJH (grant 184573) is gratefully acknowledged, as is an NSERC CGS-M (JR). Numerous individuals from our research group contributed to this body of work over many years. These include (but are not limited to): Brett Moldovan, Jocelyn Bissonnette (Cameco Corporation), Krysta Shacklock, Ryan Frey, Soumya Das, Tom Bonli, Jianzhong Fan, Jing Chen, Fina Nelson, and Blaine Novakovski (University of Saskatchewan).

7.0 SUMMARY OF CONCLUSIONS AND RECOMMENDATIONS

Uranium ore deposits in the Athabasca Basin contain elevated concentrations of EOCs. Milling this ore results in the dissolution of EOCs into mill process water through strong acid leaching under oxic conditions. This water is treated in a lime neutralization process that decreases EOC concentrations through adsorption and co-precipitation mechanisms. The precipitates are discharged as a slurry to in-pit tailings management facilities.

Because of the uncertainty of the long-term mobility of EOCs in the tailings with respect to the surrounding groundwater regime, large amounts of research focus on the characteristics of the mechanisms of EOC removal in the neutralization process and the long-term stability of the mineralogical controls in the tailings management facilities. The mineralogical controls that Fe exerts on EOCs are well defined in the literature but do not completely describe the control of EOCs in U mill tailings. Uncharacterized masses of Al and Mg secondary minerals precipitate during the neutralization process. Other areas of study show certain Al and Mg mineral phases (e.g., $Al(OH)_3$ and layered double hydroxides) exert adsorption controls on oxyanions. Understanding the mineralogical characteristics of Al and Mg phases in Key Lake's neutralization process and tailings management facility will further define the fate of EOCs in this system.

The goal of this thesis was to define the Al and Mg secondary mineralogy in the Key Lake neutralization system and the mineralogical controls they exert on EOCs. The outcomes of each objective of the thesis (defined in Chapter 1.1) are addressed in this section.

7.1 Objective 1 - Characterize the Al and Mg mineralogy generated in the Key Lake bulk neutralization process

The mineralogy of Al and Mg secondary precipitates was characterized in Chapter 4.0. Acidic, metal(loid)-rich water (raffinate) neutralized with lime in steps of pH 4.0, 6.5, and 9.5 results in the precipitation of secondary minerals. At pH 4.0, Al precipitates as an amorphous $AlOHSO_4$ phase with the approximate stoichiometry of hydrobasaluminite

($Al_4(OH)_{10}(SO_4)\cdot 15H_2O$). Aluminum cations also substitute for Fe^{3+} in the ferrihydrite structure, producing an aluminous ferrihydrite phases. TEM images of these precipitates do not show discrete $AlOHSO_4$ and aluminous ferrihydrite phases. Therefore it is proposed that these two phases form an intimate mixture at the nanoscale. The pH 4.0 precipitates are removed from solution before further neutralization occurs. At pH 6.5, a mixture of $AlOHSO_4$ and amorphous $Al(OH)_3$ precipitates. At pH 9.5, a mixture of amorphous $Al(OH)_3$ (19-33%) and MgAl-hydrotalcite (63-70%) precipitates. There are residual amounts of $AlOHSO_4$ (0-11%) at pH 9.5; however, most $AlOHSO_4$ from the pH 6.5 step dissolves or transforms to either $Al(OH)_3$ or MgAl-hydrotalcite. The secondary Al and Mg mineralogy in the final tailings slurry (pH 10.5) is a mixture of amorphous $Al(OH)_3$ (26-43%), MgAl-hydrotalcite (57-61%), and aluminous ferrihydrite (not quantified).

7.2 Objective 2 - Determine if Al and Mg secondary minerals exert controls on EOC concentrations in the neutralization process

Mineralogical controls of As, Ni, Se, and Mo by Al and Mg secondary minerals were identified as discussed in Chapters 4.0 and 5.0. In raffinates devoid of Fe, precipitation of As, Ni, Se, and Mo still occurred, suggesting that Al and Mg minerals exert controls on EOC concentrations. Relative to raffinate with dissolved Fe, the decrease in EOC concentrations were: 100% (Ni), 99.9% (As), 95.0% (Se), and 61.0% (Mo). X-ray elemental mapping of the Al and Mg precipitates showed a distinct association of all EOCs with Al and Mg secondary phases. Amorphous $AlOHSO_4$ was associated with As, Ni, and Mo. Amorphous $Al(OH)_3$ and MgAl-hydrotalcite was associated with As, Ni, and Se. In the presence of Fe precipitates, amorphous $Al(OH)_3$ and MgAl-hydrotalcite were still associated with As and Ni. These results show that Al and Mg secondary minerals can exert controls on EOC concentrations during the neutralization process. From the decrease in aqueous concentrations, Al and Mg controls of As, Ni, and Se are comparable to Fe controls. Aluminum and Mg controls of aqueous Mo are relatively weak compared to Fe controls. Chapter 5.0 confirms the Al and Mg controls of As and Ni and determines the sequestration mechanism as discussed in the next section.

7.3 Objective 3 - Determine the magnitude of control exerted by the Al and Mg mineral phases on As and Ni concentrations with and without Fe mineral phases

The magnitude and mechanism of Al and Mg mineralogical controls of As and Ni in synthetic and mill samples were identified in Chapter 5.0. Arsenic adsorbs to both $AlOHSO_4$ (pH 4.0) and amorphous $Al(OH)_3$ (pH 9.5 and 10.5) as a corner-sharing bidentate-binuclear surface complex. Arsenic adsorbs to MgAl-hydrotalcite through a bidentate surface complex at pH 9.5 and 10.5. Nickel adsorbs to amorphous $Al(OH)_3$ as an edge-sharing bidentate-mononuclear surface complex at pH 4.0, 9.5, and 10.5. Nickel and Al co-precipitate as a Ni-Al layered double hydroxide at pH 9.5 and 10.5. In pH 4.0 precipitates with Fe, between 15-26% of solid phase As adsorbed to $AlOHSO_4$ and the remainder precipitated as ferric arsenate or adsorbed to ferrihydrite. All Ni at pH 4.0 was adsorbed to amorphous $Al(OH)_3$. In pH 9.5 precipitates, between 12-16% of As adsorbed to amorphous $Al(OH)_3$, 46-87% adsorbed to MgAl-hydrotalcite, and 26% of As in one sample was adsorbed to ferrihydrite. All Ni was associated with Al and Mg precipitates at pH 9.5; 19-53% of Ni adsorbed to amorphous $Al(OH)_3$ and 33-84% precipitated as a Ni-Al layered double hydroxide. In the final tailings precipitates (pH 10.5), 24-55% of As adsorbed to amorphous $Al(OH)_3$, 0-40% adsorbed to MgAl-hydrotalcite, and 34-54% adsorbed to ferrihydrite. The results show that Al and Mg phases are major controls or As and Ni in Key Lake mill tailings and work in concert with Fe phases to control aqueous concentrations of EOCs.

7.4 Objective 4 - Compile a complete review of the literature on U in-pit tailings management facilities of the Athabasca Basin

A review of all literature pertaining to in-pit U mill tailings in the Athabasca Basin was conducted in Chapter 6.0. The review discusses the effects of ore mineralogy and milling process on the tailings geochemistry, the differences in raffinate neutralization process in the three operational Athabasca Basin mills, the geochemistry of the raffinate neutralization processes, and the geochemistry and stability of the tailings bodies. Using the knowledge collected from the review, a geochemical model encompassing the neutralization and tailings geochemistry was developed to predict equilibrium porewater concentrations and mineralogy of the Athabasca Basin U mill tailings. The review synthesized the current state of the science into one document to better understand the total geochemistry of the tailings system.

7.5 Global Conclusions

Aluminum and Mg mineral phases, which comprise a major fraction of secondary minerals in Key Lake U mill tailings, were largely uncharacterized before this study. Neutralization of acidic Al and Mg-rich solutions resulted in precipitation of amorphous $AlOHSO_4$, amorphous $Al(OH)_3$, and MgAl-hydrotalcite at various pH values. These three phases exert controls on the solubility of As, Ni, Se, and Mo through adsorption and co-precipitation mechanisms. These Al and Mg mineralogical controls exist in concert with Fe mineralogical controls and improve the understanding of the geochemistry of these neutralization processes.

The most common process used to remove metals from industrial effluents is chemical precipitation with lime of NaOH (Blais et al., 2008). As such, the general chemistry of these neutralization processes can be described with much of the research of the Athabasca Basin U mills. Acidic water from acid mine drainage is often rich in Fe, Al, and other trace contaminants (Blowes et al., 1991; Moncur et al., 2005). Natural neutralization of these waters results in precipitation of amorphous $Fe(OH)_3$ and $Al(OH)_3$ capable of sequestering trace contaminants (Bigham and Nordstrom, 2000; Cismasu et al., 2011; Moncur et al., 2005). The results of this thesis improve the understanding of these precipitation and sequestration processes in both industrial and natural environments, and can be useful for designing geochemically stable waste repositories and natural remediation strategies.

7.6 Recommendations for Future Work

Most aspects of the mineralogical controls of EOCs in the DTMF and other U mill tailings are well understood. However, there are knowledge gaps in the literature that provide uncertainty with the long-term fate of certain EOCs. The following areas of study are recommended for future work:

1. Controls of Se concentrations in U mill tailings are poorly understood and should be investigated. Selenium likely adsorbs to ferrihydrite through both inner-sphere and outer-sphere complexation (Peak and Sparks, 2002); however, there is no literature that examines the mechanism of Se sequestration in acid neutralization processes.
2. The Al and Mg mineralogical controls of Se and Mo concentrations that were qualitatively observed in Chapter 4.0 should be investigated. Hydrotalcite was demonstrated to adsorb

Se and Mo at pH 9.6 on the same order of magnitude as literature values of ferrihydrite adsorption capacities. Aluminum and Mg minerals are shown to control Se and Mo concentrations and other studies and could be a factor in U mill tailings (Frost et al., 2005; Goldberg, 2013; Paikaray et al., 2013).

3. Aging or stability tests of the Al and Mg minerals should be conducted. The fate of amorphous $Al(OH)_3$ and hydrotalcite in the tailings is unclear. Amorphous $Al(OH)_3$ crystallizes to gibbsite over time (Goldberg et al., 2001), although the presence of surface complexes could inhibit crystallization. There is minimal research on the long-term stability of layered double hydroxides (Goh et al., 2008).
4. Aging tests of EOCs adsorbed to Al and Mg mineral should be conducted to determine the long-term porewater concentrations of EOCs in the tailings. These studies should be compared to aging tests performed with Fe mineralogical controls (Das et al., 2011a; Langmuir et al., 1999).
5. Studies should be conducted to maximize Al and Mg mineralogical controls in the neutralization process, especially when Fe concentrations in the raffinate are low or EOC concentrations are high. These studies could examine the feasibility of adding extra Al or Mg to the raffinate versus adding Fe to the raffinate.
6. Aqueous Si and Si precipitates are poorly characterized in the neutralization process. The dissolution of clays and silicates during the leaching process results in variable concentrations of Si in the raffinate. Silicon can incorporate into the structure ferrihydrite and negatively affect the adsorption capacity of ferrihydrite by promoting increased outer-sphere rather than inner-sphere complexation (Cismasu et al., 2013). Silicon also reacts with layered double hydroxides and may improve the stability of layered double hydroxides in the tailings (Scheckel et al., 2000).Understanding the secondary mineralogy of Si will further improve the understanding of the tailings geochemistry.

8.0 REFERENCES

Adams, F., Rawajfih, Z., 1977. Basaluminite and alunite: A possible cause of sulfate retention by acid soils. Soil Sci. Soc. Am. J. 47, 686–692.

Adra, A., Morin, G., Ona-Nguema, G., Brest, J., 2016. Arsenate and arsenite adsorption onto Al-containing ferrihydrites. Implications for arsenic immobilization after neutralization of acid mine drainage. Appl. Geochemistry 64, 2–9. doi:10.1016/j.apgeochem.2015.09.015

Adra, A., Morin, G., Ona-Nguema, G., Menguy, N., Maillot, F., Casiot, C., Bruneel, O., Lebrun, S., Juillot, F., Brest, J., 2013. Arsenic scavenging by aluminum-substituted ferrihydrites in a circumneutral pH river impacted by acid mine drainage. Environ. Sci. Technol. 47, 12784–12792. doi:10.1021/es4020234

Arai, Y., 2008. Spectroscopic evidence for Ni(II) surface speciation at the iron oxyhydroxides-water interface. Environ. Sci. Technol. 42, 1151–6.

Arai, Y., Elzinga, E.J., Sparks, D.L., 2001. X-ray absorption spectroscopic investigation of arsenite and arsenate adsorption at the aluminum oxide-water interface. J. Colloid Interface Sci. 235, 80–88. doi:10.1006/jcis.2000.7249

Arai, Y., Sparks, D.L., 2002. Residence time effects on arsenate surface speciation at the aluminum oxide-water interface. Soil Sci. 167, 303–314. doi:10.1097/00010694-200205000-00001

Beaulieu, B.T., Savage, K.S., 2005. Arsenate adsorption structures on aluminum oxide and phyllosilicate mineral surfaces in smelter-impacted soils. Environ. Sci. Technol. 39, 3571–3579. doi:10.1021/es048836f

Becze, L., Gomez, M.A., Petkov, V., Cutler, J.N., Demopoulos, G.P., 2010. The potential arsenic retention role of Ca-Fe(III)-AsO4 compounds in lime neutralized co-precipitation tailings, in: Lam, E.K., Rowson, J.W., Ozberk, E. (Eds.), Uranium 2010: Proceedings of the 3rd International Conference on Uranium. Saskatoon, SK, Canada, pp. 327–336.

Bertsch, P., Parker, B., 1996. Aqueous polynuclear aluminum species, in: Sposito, G. (Ed.), The Environmental Chemistry of Aluminum. CRC/Lewis Publishers, Boca Raton, Florida, pp. 117–168.

Bharadwaj, B., Moldovan, B., 2005. Cameco Corporation - the Key Lake Uranium Mill: Current status and vision for the future, in: Uranium Production and Raw Materials for the Nuclear Fuel Cycle - Supply and Demand, Economics, the Environment and Energy Security. pp. 205–212.

Bigham, J.M., Nordstrom, D.K., 2000. Iron and aluminum hydroxysulfates from acid sulfate

waters, in: Alpers, C.N., Jambor, J.L., Nordstrom, D.K. (Eds.), Sulfate Minerals: Crystallography, Geochemistry, and Environmental Significance. Mineralogical Society of America, pp. 351–403. doi:10.2138/rmg.2000.40.7

Bissonnette, J., Essilfie-Dughan, J., Moldovan, B.J., Hendry, M.J., 2016. Sequestration of As and Mo in uranium mill precipitates (pH 1.5–9.2): An XAS study. Appl. Geochemistry 72, 20–33. doi:10.1016/j.apgeochem.2016.06.007

Bissonnette, J.S., 2015. Sequestration of arsenic and molybdenum during the neutralization of uranium mill wastes: Key Lakemill, Saskatchewan, Canada. University of Saskatchewan.

Blais, J.F., Djedidi, Z., Cheikh, R. Ben, Tyagi, R.D., Mercier, G., 2008. Metals precipitation from effluents: review. Pract. Period. Hazardous, Toxic, Radioact. Waste Manag. 12, 135–149. doi:10.1061/(ASCE)1090-025X(2008)12:3(135)

Blanchard, P.E.R., Hayes, J.R., Grosvenor, A.P., Rowson, J., Hughes, K., Brown, C., 2015. Investigating the geochemical model for molybdenum mineralization in the JEB tailings management facility at McClean Lake, Saskatchewan: An x-ray absorption spectroscopy study. Environ. Sci. Technol. 49, 6504–6509. doi:10.1021/acs.est.5b00528

Blowes, D.W., Reardon, E.J., Jambor, J.L., Cherry, J.A., 1991. The formation and potential importance of cemented layers in inactive sulfide mine tailings. Geochim. Cosmochim. Acta 55, 965–978. doi:10.1016/0016-7037(91)90155-X

Burke, I.T., Peacock, C.L., Lockwood, C.L., Stewart, D.I., Mortimer, R.J.G., Ward, M.B., Renforth, P., Gruiz, K., Mayes, W.M., 2013. Behavior of aluminum, arsenic, and vanadium during the neutralization of red mud leachate by HCl, gypsum, or seawater. Environ. Sci. Technol. 47, 6527–6535. doi:10.1021/es4010834

Cameco, 2013. Key Lake - annual production [WWW Document]. URL http://www.cameco.com/mining/key_lake/annual_production/

Cameco, 2011. Rabbit Lake tailings north pit expansion project: project description.

Cameco, 2010. Key Lake extension project - project description [WWW Document]. URL http://www.cameco.com/common/pdf/responsibility/regulatory/key_lake/Cameco_Key_Lake_Extension_Project.pdf

Cameco Corporation, 2012. McArthur River Operation, Northern Saskatchewan, Canada - Technical Report. Saskatoon.

Carl, C., von Pechmann, E., Hohndorf, A., Ruhrmann, G., 1992. Mineralogy and U/Pb, Pb/Pb, and Sm/Nd geochronology of the Key Lake uranium deposit, Athabasca Basin, Saskatchewan, Canada. Can. J. Earth Sci. 29, 879–895.

Chen, N., Jiang, D.T., Cutler, J., Kotzer, T., Jia, Y.F., Demopoulos, G.P., Rowson, J.W., 2009. Structural characterization of poorly-crystalline scorodite, iron(III)–arsenate co-precipitates and uranium mill neutralized raffinate solids using X-ray absorption fine structure spectroscopy. Geochim. Cosmochim. Acta 73, 3260–3276. doi:10.1016/j.gca.2009.02.019

Cismasu, A.C., Levard, C., Michel, F.M., Brown, G.E., 2013. Properties of impurity-bearing ferrihydrite II: Insights into the surface structure and composition of pure, Al- and Si-bearing ferrihydrite from Zn(II) sorption experiments and Zn K-edge X-ray absorption spectroscopy. Geochim. Cosmochim. Acta 119, 46–60. doi:10.1016/j.gca.2013.05.040

Cismasu, A.C., Michel, F.M., Stebbins, J.F., Levard, C., Brown, G.E., 2012. Properties of impurity-bearing ferrihydrite I. Effects of Al content and precipitation rate on the structure of 2-line ferrihydrite. Geochim. Cosmochim. Acta 92, 275–291. doi:10.1016/j.gca.2012.06.010

Cismasu, A.C., Michel, F.M., Tcaciuc, A.P., Brown, G.E., 2014. Properties of impurity-bearing ferrihydrite III. Effects of Si on the structure of 2-line ferrihydrite. Geochim. Cosmochim. Acta 133, 168–185. doi:10.1016/j.gca.2014.02.018

Cismasu, A.C., Michel, F.M., Tcaciuc, A.P., Tyliszczak, T., Brown, G.E.J., 2011. Composition and structural aspects of naturally occurring ferrihydrite. Comptes Rendus Geosci. 343, 210–218. doi:10.1016/j.crte.2010.11.001

COGEMA, 2003. McClean Lake Operation Tailings Optimization and Validation Program - Status Report for 2002.

Corriveau, M.C., 2006. Characterization of arsenic-bearing near-surface and airborne particulates from gold-mine tailings in Nova Scotia, Canada. Queen's University.

Craigen, C.M., 2006. Controls on arsenic speciation in mine tailings and co-existing pore water in freshwater and marine settings from the lower Seal Harbour gold district, Nova Scotia, Canada. Queen's University.

d'Espinose de la Caillerie, J.-B., Kermarec, M., Clause, O., 1995. Impregnation of y-alumina with Ni(II) or Co(II) ions at neutral pH: hydrotalcite-type coprecipitate formation and characterization. J. Am. Chem. Soc. 11471–11481.

Das, J., Das, D., Dash, G.P., Parida, K.M., 2002. Studies on Mg/Fe hydrotalcite-like-compound (HTlc) I. Removal of inorganic selenite (SeO3(2-)) from aqueous medium. J. Colloid Interface Sci. 251, 26–32. doi:10.1006/jcis.2002.8319

Das, S., Hendry, M.J., 2011. Application of Raman spectroscopy to identify iron minerals commonly found in mine wastes. Chem. Geol. 290, 101–108. doi:10.1016/j.chemgeo.2011.09.001

Das, S., Hendry, M.J., Essilfie-Dughan, J., 2013. Adsorption of selenate onto ferrihydrite, goethite, and lepidocrocite under neutral pH conditions. Appl. Geochemistry 28, 185–193. doi:10.1016/j.apgeochem.2012.10.026

Das, S., Hendry, M.J., Essilfie-Dughan, J., 2011a. Effects of adsorbed arsenate on the rate of transformation of 2-line ferrihydrite at pH 10. Environ. Sci. Technol. 45, 5557–63. doi:10.1021/es200107m

Das, S., Hendry, M.J., Essilfie-Dughan, J., 2011b. Transformation of two-line ferrihydrite to goethite and hematite as a function of pH and temperature. Environ. Sci. Technol. 45, 268–275.

De Klerk, R.J., Jia, Y., Daenzer, R., Gomez, M.A., Demopoulos, G.P., 2012. Continuous circuit coprecipitation of arsenic(V) with ferric iron by lime neutralization: Process parameter effects on arsenic removal and precipitate quality. Hydrometallurgy 111–112, 65–72. doi:10.1016/j.hydromet.2011.10.004

Delaney, T.A., Hockley, D.E., Chapman, J.T., Holl, N.C., 1998. Geochemical characterization of tailings at the McArthur River Mine, Saskatchewan, in: Tailings and Mine Waste '98, Proceedings for the 5th International Conference. Fort Collins, Colorado.

Demopoulos, G.P., 2009. Aqueous precipitation and crystallization for the production of particulate solids with desired properties. Hydrometallurgy 96, 199–214. doi:10.1016/j.hydromet.2008.10.004

Dixit, S., Hering, J.G., 2003. Comparison of arsenic(V) and arsenic(III) sorption onto iron oxide minerals: implications for arsenic mobility. Environ. Sci. Technol. 37, 4182–9.

Djedidi, Z., Médard, B., Cheikh, R. Ben, Mercier, G., Tyagi, R.D., Blais, J.F., 2009. Comparative study of dewatering characteristics of metal precipitates generated during treatment synthetic polymetallic and AMD solutions. Hydrometallurgy 98, 247–256. doi:10.1016/j.hydromet.2009.05.010

Donahue, R., 2000. Geochemistry of arsenic in uranium mill tailings, Saskatchewan, Canada. University of Saskatchewan.

Donahue, R., Hendry, M.J., 2003. Geochemistry of arsenic in uranium mine mill tailings, Saskatchewan, Canada. Appl. Geochemistry 18, 1733–1750. doi:10.1016/S0883-2927(03)00106-9

Donahue, R., Hendry, M.J., Landine, P., 2000. Distribution of arsenic and nickel in uranium mill tailings, Rabbit Lake, Saskatchewan, Canada. Appl. Geochemistry 15, 1097–1119.

Douglas, G., Adeney, J., Johnston, K., Wendling, L., Coleman, S., 2012. Major element, trace element, nutrient, and radionuclide mobility in a mining by-product–amended soil. J. Environ. Qual. 41, 1818–1834. doi:10.2134/jeq2012.0139

Douglas, G., Shackleton, M., Woods, P., 2014. Hydrotalcite formation facilitates effective contaminant and radionuclide removal from acidic uranium mine barren lixiviant. Appl. Geochemistry 42, 27–37. doi:10.1016/j.apgeochem.2013.12.018

Douglas, G.B., Wendling, L. a., Pleysier, R., Trefry, M.G., 2010. Hydrotalcite formation for contaminant removal from Ranger Mine process water. Mine Water Environ. 29, 108–115. doi:10.1007/s10230-010-0106-4

Downs, R.T., 2006. The RRUFF Project: an integrated study of the chemistry, crystallography, Raman and infrared spectroscopy of minerals. [WWW Document]. URL http://rruff.info/

Doyle, C.S., Traina, S.J., Ruppert, H., Kendelewicz, T., Rehr, J.J., Brown, G.E., 1999. XANES studies at the Al K-edge of aluminium-rich surface phases in the soil environment. J. Synchrotron Radiat. 6, 621–623. doi:10.1107/S0909049598015568

Dzombak, D.A., Morel, F.M.M., 1990. Surface Complexation Modeling: Hydrous Ferric Oxide. Wiley, New York.

Essilfie-Dughan, J., Hendry, M.J., Pickering, I.J., George, G., Kotzer, T., 2010. Molybdenum and selenium speciation in uranium mine tailings using X-ray absorption spectroscopy, in: Uranium 2010: Proceedings of the 3rd International Conference on Uranium. Saskatoon, SK, Canada, pp. 401–408.

Essilfie-Dughan, J., Hendry, M.J., Warner, J., Kotzer, T., 2013. Arsenic and iron speciation in uranium mine tailings using X-ray absorption spectroscopy. Appl. Geochemistry 28, 11–18. doi:10.1016/j.apgeochem.2012.10.022

Essilfie-Dughan, J., Hendry, M.J., Warner, J., Kotzer, T., 2012. Microscale mineralogical characterization of As, Fe, and Ni in uranium mine tailings. Geochim. Cosmochim. Acta 96, 336–352. doi:10.1016/j.gca.2012.08.005

Essilfie-Dughan, J., Hendry, M.J., Warner, J., Kotzer, T., 2011a. Solubility controls of arsenic, iron, and nickel in uranium mine tailings, in: Merkel, B., Schipek, M. (Eds.), Proceedings of the International Conference 2011: Uranium Mining and Hydrogeology VI. Freiberg, Saxony, Germany, pp. 325–334.

Essilfie-Dughan, J., Pickering, I.J., Hendry, M.J., George, G.N., Kotzer, T., 2011b. Molybdenum speciation in uranium mine tailings using X-ray absorption spectroscopy. Environ. Sci. Technol. 45, 455–60. doi:10.1021/es102954b

Evans, D.G., Slade, C.T., 2006. Structural aspects of layered double hydroxides, in: Duan, X., Evans, D.G. (Eds.), Layered Double Hydroxides. Springer-Verlag, Berlin, Heidelberg, pp. 1–87.

Foster, A.L., 1999. Partitioning and transformation of arsenic and selenium in natural and laboratory systems, Ph.D Thesis, Department of Geological and Environmental Sciences. Stanford University. doi:10.16953/deusbed.74839

Foster, A.L., Brown Jr., G.E., Tingle, T.N., Parks, G. a., 1998. Quantitative arsenic speciation in mine tailings using X-ray absorption spectroscopy. Am. Mineral. 83, 553–568.

Foster, A.L., Kim, C.S., 2014. Arsenic speciation in solids using X-ray absorption spectroscopy. Rev. Mineral. Geochemistry 79, 257–369.

Frey, R., Rowson, J., Hughes, K., Rinas, C., Warner, J., 2010. Identification of poorly crystalline scorodite in uranium mill tailings, in: Lam, E., Rowson, J.W., Ozberk, E. (Eds.), Uranium 2010: Proceedings of the 3rd International Conference on Uranium. Saskatoon, SK, Canada, p. 389.

Frost, R.L., Musumeci, A.W., Martens, W.N., Adebajo, M.O., Bouzaid, J., 2005. Raman spectroscopy of hydrotalcites with sulphate, molybdate and chromate in the interlayer. J. Raman Spectrosc. 36, 925–931. doi:10.1002/jrs.1385

Frost, R.L., Spratt, H.J., Palmer, S.J., 2009. Infrared and near-infrared spectroscopic study of synthetic hydrotalcites with variable divalent/trivalent cationic ratios. Spectrochim. acta. Part

A 72, 984–8. doi:10.1016/j.saa.2008.12.018

Fukushi, K., Aoyama, K., Yang, C., Kitadai, N., Nakashima, S., 2013. Surface complexation modeling for sulfate adsorption on ferrihydrite consistent with in situ infrared spectroscopic observations. Appl. Geochemistry 36, 92–103. doi:10.1016/j.apgeochem.2013.06.013

Goh, K.-H., Lim, T.-T., Dong, Z., 2008. Application of layered double hydroxides for removal of oxyanions: a review. Water Res. 42, 1343–68. doi:10.1016/j.watres.2007.10.043

Goldberg, S., 2013. Modeling selenite adsorption envelopes on oxides, clay minerals, and soils using the triple layer model. Soil Sci. Soc. Am. J. 77, 64. doi:10.2136/sssaj2012.0205

Goldberg, S., 2002. Competitive adsorption of arsenate and arsenite on oxides and clay minerals. Soil Sci. Soc. Am. J. 66, 413–421.

Goldberg, S., Johnston, C.T., 2001. Mechanisms of arsenic adsorption on amorphous oxides evaluated using macroscopic measurements, vibrational spectroscopy, and surface complexation modeling. J. Colloid Interface Sci. 234, 204–216. doi:10.1006/jcis.2000.7295

Goldberg, S., Lebron, I., Suarez, D.L., Hinedi, Z.R., 2001. Surface characterization of amorphous aluminum oxides. Soil Sci. Soc. Am. J. 65, 78–86.

Gomez, M.A., Hendry, M.J., Hossain, A., Das, S., Elouatik, S., 2013. Abiotic reduction of 2-line ferrihydrite: effects on adsorbed arsenate, molybdate, and nickel. RSC Adv. 3, 25812. doi:10.1039/c3ra44769c

Gomez, M.A., Hendry, M.J., Koshinsky, J., Essilfie-Dughan, J., Paikaray, S., Chen, J., 2013. Mineralogical controls on aluminum and magnesium in uranium mill tailings: Key Lake, Saskatchewan, Canada. Environ. Sci. Technol. 47, 7883–7891.

Goulden, W.D., 1997. The geochemical distribution of radium-226 in Cluff Lake uranium mill tailings. University of Saskatchewan.

Green, D.W., Perry, R.H., 2008. Liquid-liquid reactors, in: Perry's Chemical Engineers' Handbook. McGraw-Hill.

Gunzler, H., Gremlich, H.-U., 2002. IR Spectroscopy, 1st ed. Wiley-VCH, Weinheim.

Gupta, C.K., Singh, H., 2003. Uranium Resource Processing: Secondary Resources. Springer-Verlag, Berlin.

Gustafsson, J.P., 2003. Modelling molybdate and tungstate adsorption to ferrihydrite. Chem. Geol. 200, 105–115.

Hayes, J.R., Grosvenor, A.P., Rowson, J., Hughes, K., Frey, R.A., Reid, J., 2014. Analysis of the Mo speciation in the JEB tailings management facility at McClean Lake, Saskatchewan. Environ. Sci. Technol. 48, 4460–4467. doi:10.1021/es404980x

Heinrich, G., Kyser, K., Chipley, D., Lam, E., 2010. The determination of selenium and molybdenum distribution in uranium ore and mill solids, in: Lam, E., Rowson, J.W., Ozberk, E. (Eds.), Uranium 2010: Proceedings of the 3rd International Conference on Uranium.

Saskatoon, SK, Canada, p. 609.

Hossain, M.A., 2014. Mineralogical characterization of uranium ores, blends and resulting leach residues from Key Lake pilot plant, Saskatchewan, Canada. University of Saskatchewan.

Hughes, K.A., Rinas, C., Frey, R., Rowson, J., 2010. The fate of entrained hydrocarbon materials in the McClean Lake operation mill tailings, in: Lam, E., Rowson, J.W., Ozberk, E. (Eds.), Uranium 2010: Proceedings of the 3rd International Conference on Uranium. Saskatoon, SK, Canada, pp. 317–326.

IAEA, 2004. The long term stabilization of uranium mill tailings.

Ildefonse, P., Cabaret, D., Sainctavit, P., Calas, G., Flank, A.-M., Lagarde, P., 1998. Aluminium X-ray absorption near edge structure in model compounds and Earth's surface minerals. Phys Chem Miner. 25, 112–121.

Jambor, J.L., Dutrizac, J.E., 1998. Occurrence and constitution of natural and synthetic ferrihydrite, a widespread iron oxyhydroxide. Chem. Rev. 98, 2549–2586.

Jamieson, B.W., Frost, S.E., 1997. The McArthur River project: high grade uranium mining, in: 22nd Annual International Symposium of the Uranium Institute. London, England.

Jefferson, C.W., Thomas, D.J., Gandhi, S.S., Ramaekers, P., Delaney, G., Brisbin, D., Cutts, C., Portella, P., Olson, R.A., 2007. Unconformity-associated uranium deposits of the Athabasca basin, Saskatchewan and Alberta, in: Jefferson, C.W., Delaney, G. (Eds.), EXTECH IV: Geology and Uranium Exploration Technology of the Proterozoic Athabasca Basin, Saskatchewan and Alberta. Geological Survey of Canada, Bulletin 588, pp. 23–67.

Jenner, G.A., Longerich, H.P., Jackson, S.E., Fryer, B.J., 1990. ICP-MS — A powerful tool for high-precision trace-element analysis in Earth sciences: Evidence from analysis of selected U.S.G.S. reference samples. Chem. Geol. 83, 133–148. doi:10.1016/0009-2541(90)90145-W

Jia, Y., Demopoulos, G.P., 2005. Adsorption of arsenate onto ferrihydrite from aqueous solution: influence of media (sulfate vs nitrate), added gypsum, and pH alteration. Environ. Sci. Technol. 39, 9523–7.

Jia, Y., Xu, L., Fang, Z., Demopoulos, G.P., 2006. Observation of surface precipitation of arsenate on ferrihydrite. Environ. Sci. Technol. 40, 3248–53.

Jia, Y., Xu, L., Wang, X., Demopoulos, G.P., 2007. Infrared spectroscopic and X-ray diffraction characterization of the nature of adsorbed arsenate on ferrihydrite. Geochim. Cosmochim. Acta 71, 1643–1654. doi:10.1016/j.gca.2006.12.021

Jobbágy, M., Regazzoni, A.E., 2013. Complexation at the edges of hydrotalcite: the cases of arsenate and chromate. J. Colloid Interface Sci. 393, 314–8. doi:10.1016/j.jcis.2012.10.069

Jones, A.M., Collins, R.N., Waite, T.D., 2011. Mineral species control of aluminum solubility in sulfate-rich acidic waters. Geochim. Cosmochim. Acta 75, 965–977. doi:10.1016/j.gca.2010.12.001

Kabengi, N.J., Daroub, S.H., Rhue, R.D., 2006. Energetics of arsenate sorption on amorphous aluminum hydroxides studied using flow adsorption calorimetry. J. Colloid Interface Sci. 297, 86–94. doi:10.1016/j.jcis.2005.10.050

Kappen, P., Webb, J., 2013. An EXAFS study of arsenic bonding on amorphous aluminium hydroxide. Appl. Geochemistry 31, 79–83. doi:10.1016/j.apgeochem.2012.12.007

Ladeira, A.C.Q., Ciminelli, V.S.T., Duarte, H.A., Alves, M.C.M., Ramos, A.Y., 2001. Mechanism of anion retention from EXAFS and density functional calculations: Arsenic(V) adsorbed on gibbsite. Geochim. Cosmochim. Acta 65, 1211–1217. doi:10.1016/S0016-7037(00)00581-0

Lane, M.D., 2007. Mid-infrared emission spectroscopy of sulfate and sulfate-bearing minerals. Am. Mineral. 92, 1–18. doi:10.2138/am.2007.2170

Langmuir, D., Mahoney, J., Rowson, J., 2006. Solubility products of amorphous ferric arsenate and crystalline scorodite (FeAsO4·2H2O) and their application to arsenic behavior in buried mine tailings. Geochim. Cosmochim. Acta 70, 2942–2956. doi:10.1016/j.gca.2006.03.006

Langmuir, D., Mahoney, J., Rowson, J., MacDonald, A., 1999. Predicting arsenic concentrations in the porewaters of buried uranium mill tailings. Geochim. Cosmochim. Acta 63, 3379–3394.

Langmuir, D., Melchior, D., 1985. The geochemistry of Ca, Sr, Ba and Ra sulfates in some deep brines from the Palo Duro Basin, Texas. Geochim. Cosmochim. Acta 49, 2423–2432. doi:10.1016/0016-7037(85)90242-X

Lazaridis, N.K., Hourzemanoglou, A., Matis, K. a, 2002. Flotation of metal-loaded clay anion exchangers. Part II: the case of arsenates. Chemosphere 47, 319–24.

Li, F., Duan, X., 2006. Applications of layered double hydroxides, in: Duan, X., Evans, D.G. (Eds.), Layered Double Hydroxides. Springer-Verlag, Berlin, Heidelberg, pp. 193–223.

Lieu, A., Zheng, J., Moldovan, B., Ko, K., Jarvi, J., Saruchera, T., Bergbusch, P., Paulsen, K., Tremblay, M., Bharadwaj, B., 2010. Selenium and molybdenum removal from contaminated mill process effluent: Cameco Key Lake Operation, in: Lam, E.K., Rowson, J.W., Ozberk, E. (Eds.), Uranium 2010: Proceedings of the 3rd International Conference on Uranium. MetSoc, pp. 749–759.

Liu, D.J., Hendry, M.J., 2011. Controls on 226Ra during raffinate neutralization at the Key Lake uranium mill, Saskatchewan, Canada. Appl. Geochemistry 26, 2113–2120. doi:10.1016/j.apgeochem.2011.07.009

Livi, K.J.T., Senesi, G.S., Scheinost, A.C., Sparks, D.L., 2009. Microscopic examination of nanosized mixed Ni-Al hydroxide surface precipitates on pyrophyllite. Environ. Sci. Technol. 43, 1299–1304. doi:10.1021/es8015606

Longerich, H.P., Jenner, G.A., Fryer, B.J., Jackson, S.E., 1990. Inductively coupled plasma-mass spectrometric analysis of geological samples: A critical evaluation based on case studies. Chem. Geol. 83, 105–118. doi:10.1016/0009-2541(90)90143-U

Lottermoser, B., 2003. Mine Wastes. Springer-Verlag Berlin Heidelberg New York.

Lowson, R.T., Comarmond, M.C.J., Rajaratnam, G., Brown, P.L., 2005. The kinetics of the dissolution of chlorite as a function of pH and at 25°C. Geochim. Cosmochim. Acta 69, 1687–1699. doi:10.1016/j.gca.2004.09.028

Luo, L., Zhang, S., Shan, X.-Q., Jiang, W., Zhu, Y.-G., Liu, T., Xie, Y.-N., McLaren, R.G., 2006. Arsenate sorption on two Chinese red soils evaluated with macroscopic measurements and extended X-ray absorption fine-structure spectroscopy. Environ. Toxicol. Chem. 25, 3118–3124.

Mahoney, J., Langmuir, D., Gosselin, N., Rowson, J., 2005. Arsenic readily released to pore waters from buried mill tailings. Appl. Geochemistry 20, 947–959. doi:10.1016/j.apgeochem.2004.11.012

Mahoney, J., Slaughter, M., Langmuir, D., Rowson, J., 2007. Control of As and Ni releases from a uranium mill tailings neutralization circuit: Solution chemistry, mineralogy and geochemical modeling of laboratory study results. Appl. Geochemistry 22, 2758–2776. doi:10.1016/j.apgeochem.2007.06.021

Malinowski, E.R., 1991. Factor Analysis in Chemistry, 2nd ed. Wiley Interscience.

Manceau, A., Lanson, M., Geoffroy, N., 2007. Natural speciation of Ni, Zn, Ba, and As in ferromanganese coatings on quartz using X-ray fluorescence, absorption, and diffraction. Geochim. Cosmochim. Acta 71, 95–128. doi:10.1016/j.gca.2006.08.036

Manceau, A., Marcus, M.A., Tamura, N., 2002. Quantitative speciation of heavy metals in soils and sediments by synchrotron X-ray techniques. Rev. Mineral. Geochemistry 49, 341–428. doi:10.2138/gsrmg.49.1.341

Manning, B., 2005. Arsenic speciation in As(III)- and As(V)-treated soil using XANES spectroscopy. Microchim. Acta 151, 181–188. doi:10.1007/s00604-005-0398-4

Martin, M., Yu, G., Barberis, E., Violante, A., Kozak, L.M., Huang, P.M., 2009. Impact of structural perturbation of aluminum hydroxides by tannate on arsenate adsorption. Soil Sci. Soc. Am. 73, 1664–1675.

Mazzetti, L., Thistlethwaite, P.J., 2002. Raman spectra and thermal transformations of ferrihydrite and schwertmannite. J. Raman Spectrosc. 33, 104–111.

Merkel, B.J., 2006. Long term fate of uranium tailings in mountain areas, in: Merkel, B.J., Hasche-Berger, A. (Eds.), Uranium in the Environment: Mining Impact and Consequences. Springer Berlin Heidelberg New York, pp. 47–56.

Merritt, R.C., 1971. The Extractive Metallurgy of Uranium. Johnson Publishing Company, Boulder, CO.

Moldovan, B.J., 2006. Fate and transport of arsenic in uranium mine tailings: Rabbit Lake Mine, Saskatchewan, Canada. University of Saskatchewan.

Moldovan, B.J., Hendry, M.J., 2005. Characterizing and quantifying controls on arsenic solubility over a pH range of 1 - 11 in a uranium mill-scale experiment. Environ. Sci. Technol. 39, 4913–4920.

Moldovan, B.J., Hendry, M.J., Harrington, G.A., 2008. The arsenic source term for an in-pit uranium mine tailings facility and its long-term impact on the regional groundwater. Appl. Geochemistry 23, 1437–1450. doi:10.1016/j.apgeochem.2007.12.037

Moldovan, B.J., Jiang, D.T., Hendry, M.J., 2003. Mineralogical characterization of arsenic in uranium mine tailings precipitated from iron-rich hydrometallurgical solutions. Environ. Sci. Technol. 37, 873–879.

Moncur, M.C., Ptacek, C.J., Blowes, D.W., Jambor, J.L., 2005. Release, transport and attenuation of metals from an old tailings impoundment. Appl. Geochemistry 20, 639–659. doi:10.1016/j.apgeochem.2004.09.019

Morimoto, K., Anraku, S., Hoshino, J., Yoneda, T., Sato, T., 2012. Surface complexation reactions of inorganic anions on hydrotalcite-like compounds. J. Colloid Interface Sci. 384, 99–104. doi:10.1016/j.jcis.2012.06.072

Müller, K., Ciminelli, V.S.T., Dantas, M.S.S., Willscher, S., 2010. A comparative study of As(III) and As(V) in aqueous solutions and adsorbed on iron oxy-hydroxides by Raman spectroscopy. Water Res. 44, 5660–72. doi:10.1016/j.watres.2010.05.053

Natural Resources Canada, 2014. About Uranium [WWW Document]. URL http://www.nrcan.gc.ca/energy/uranium-nuclear/7695 (accessed 3.7.17).

Nkongolo, K.K., Spiers, G., Beckett, P., Narendrula, R., Theriault, G., Tran, A., Kalubi, K.N., 2013. Long-term effects of liming on soil chemistry in stable and eroded upland areas in a mining region. Water. Air. Soil Pollut. 224. doi:10.1007/s11270-013-1618-x

Nordstrom, D.K., 2011. Hydrogeochemical processes governing the origin, transport and fate of major and trace elements from mine wastes and mineralized rock to surface waters. Appl. Geochemistry 26, 1777–1791. doi:10.1016/j.apgeochem.2011.06.002

Nordstrom, D.K., 1982. The effect of sulfate on aluminum concentrations in natural waters: some stability relations in the system Al2O3-SO3-H2O at 298 K. Geochim. Cosmochim. Acta 46, 681–692.

Nordstrom, D.K., Ball, J.W., 1986. The Geochemical Behavior of Aluminum in Acidified Surface Waters. Science (80-.). 232, 54–56.

Opiso, E.M., Sato, T., Morimoto, K., Asai, A., Anraku, S., Numako, C., Yoneda, T., 2010. Incorporation of arsenic during the formation of Mg-bearing minerals at alkaline condition. Miner. Eng. 23, 230–237. doi:10.1016/j.mineng.2009.08.005

Paikaray, S., Gomez, M.A., Hendry, M.J., Essilfie-Dughan, J., 2014. Formation Mechanism of Layered Double Hydroxides in Mg2+, Al3+ and Fe3+-rich Aqueous Media: Implications in Mine Tailing Neutralization Process. Appl. Clay Sci. 101, 579–590.

Paikaray, S., Gomez, M.A., Jim Hendry, M., Essilfie-Dughan, J., 2014. Formation mechanism of layered double hydroxides in Mg2+-, Al3+-, and Fe3+-rich aqueous media: Implications for neutralization in acid leach ore milling. Appl. Clay Sci. 101, 579–590. doi:10.1016/j.clay.2014.09.022

Paikaray, S., Hendry, M.J., 2012. The role of trivalent cations and interlayer anions on the formation of layered double hydroxides in an oxic-CO2 medium. Appl. Surf. Sci. 263, 633–639. doi:10.1016/j.apsusc.2012.09.125

Paikaray, S., Hendry, M.J., Essilfie-Dughan, J., 2013. Controls on arsenate, molybdate, and selenate uptake by hydrotalcite-like layered double hydroxides. Chem. Geol. 345, 130–138. doi:10.1016/j.chemgeo.2013.02.015

Paktunc, D., 2015. Phase transformations in the system Fe-AsO4-SO4 and the structure of amorphous ferric arsenate: Implications for arsenic stabilization in mine drainage and industrial effluents. Can. Mineral. 53, 921–936. doi:10.3749/canmin.1500040

Paktunc, D., Bruggeman, K., 2010. Solubility of nanocrystalline scorodite and amorphous ferric arsenate: Implications for stabilization of arsenic in mine wastes. Appl. Geochemistry 25, 674–683. doi:10.1016/j.apgeochem.2010.01.021

Paktunc, D., Dutrizac, J., Gertsman, V., 2008. Synthesis and phase transformations involving scorodite, ferric arsenate and arsenical ferrihydrite: Implications for arsenic mobility. Geochim. Cosmochim. Acta 72, 2649–2672. doi:10.1016/j.gca.2008.03.012

Paktunc, D., Majzlan, J., Huang, A., Thibault, Y., Johnson, M.B., White, M.A., 2015. Synthesis, characterization, and thermodynamics of arsenates forming in the Ca-Fe(III)-As(V)-NO3 system: Implications for the stability of Ca-Fe arsenates. Am. Mineral. 100, 1803–1820. doi:10.2138/am-2015-5199

Palmer, S.J., Frost, R.L., 2011. Effect of pH on the uptake of arsenate and vanadate by hydrotalcites in alkaline solutions: a Raman spectroscopic study. J. Raman Spectrosc. 42, 224–229. doi:10.1002/jrs.2680

Palmer, S.J., Soisonard, A., Frost, R.L., 2009. Determination of the mechanism(s) for the inclusion of arsenate, vanadate, or molybdate anions into hydrotalcites with variable cationic ratio. J. Colloid Interface Sci. 329, 404–9. doi:10.1016/j.jcis.2008.09.065

Park, Y.-J., Yang, J.-K., Lee, S.-M., Choi, S.-I., 2011. Applicability of poorly crystalline aluminum oxide for adsorption of arsenate. J. Environ. Sci. Health. A. Tox. Hazard. Subst. Environ. Eng. 46, 1376–84. doi:10.1080/10934529.2011.606707

Parker, L.M., Milestone, N.B., Newman, R.H., 1995. The Use of Hydrotalcite as an Anion Adsorbent. Ind. Eng. Chem. Res. 34, 1196–1202.

Parkhurst, D.L., Appelo, C.A.J., 2013. Description of input and examples for PHREEQC version 3 - A computer program for speciation, batch-reaction, one-dimensional transport, and inverse geochemical calculations, in: U.S. Geological Survey Techniques and Methods, Book 6. p. 497.

Peak, D., Sparks, D.L., 2002. Mechanisms of selenate adsorption on iron oxides and hydroxides. Environ. Sci. Technol. 36, 1460–1466. doi:10.1021/es0156643

Peltier, E., Allada, R., Navrotsky, A., Sparks, D.L., 2006. Nickel solubility and precipitation in soils: a thermodynamic study. Clays Clay Miner. 54, 153–164. doi:10.1346/CCMN.2006.0540202

Pichler, T., Hendry, M.J., Hall, G.E.., 2001. The mineralogy of arsenic in uranium mine tailings at the Rabbit Lake In-pit Facility, northern Saskatchewan, Canada. Environ. Geol. 40, 495–506.

Puigdomenech, I., 2010. Chemical Equilibrium Diagrams [WWW Document]. URL https://sites.google.com/site/chemdiagr/ (accessed 3.12.17).

Rajapaksha, A.U., Vithanage, M., Weerasooriya, R., Dissanayake, C.B., 2012. Surface complexation of nickel on iron and aluminum oxides: A comparative study with single and dual site clays. Colloids Surfaces A Physicochem. Eng. Asp. 405, 79–87. doi:10.1016/j.colsurfa.2012.05.001

Ravel, B., Newville, M., 2005. ATHENA, ARTEMIS, HEPHAESTUS: data analysis for X-ray absorption spectroscopy using IFEFFIT. J. Synchrotron Radiat. 12, 537–41. doi:10.1107/S0909049505012719

Raven, K.P., Jain, A., Loeppert, R.H., 1998. Arsenite and arsenate adsorption on ferrihydrite: kinetics, equilibrium, and adsorption envelopes. Environ. Sci. Technol. 32, 344–349. doi:10.1021/es970421p

Regier, T., Paulsen, J., Wright, G., Coulthard, I., Tan, K., Sham, T.K., Blyth, R.I.R., 2007. Commissioning of the spherical grating monochromator soft X-ray spectroscopy beamline at the Canadian Light Source. AIP Conf. Proc. 879, 473–476. doi:10.1063/1.2436101

Rinas, C., Rowson, J., Frey, R., Hughes, K., 2010. Aging of reduced arsenic minerals in uranium mill tailings at the McClean Lake operation, in: Lam, E., Rowson, J.W., Ozberk, E. (Eds.), Uranium 2010: Proceedings of the 3rd International Conference on Uranium. Saskatoon, SK, Canada, p. 377.

Robertson, J., Essilfie-Dughan, J., Lin, J., Hendry, M.J., 2017. SI - Coordination of arsenic and nickel to aluminum and magnesium phases in uranium mill raffinate precipitates. Appl. Geochemistry In press.

Robertson, J., Hendry, M.J., Essilfie-Dughan, J., Chen, J., 2016. Precipitation of aluminum and magnesium secondary minerals from uranium mill raffinate (pH 1.0–10.5) and their controls on aqueous contaminants. Appl. Geochemistry 64, 30–42. doi:10.1016/j.apgeochem.2015.09.002

Robertson, J., Shacklock, K., Frey, R., Gomez, M.A., Essilfie-Dughan, J., Hendry, M.J., 2014. Modeling the Key Lake uranium mill's bulk neutralization process using a pilot-scale model. Hydrometallurgy 149, 210–219.

Rozov, K., Berner, U., Taviot-Gueho, C., Leroux, F., Renaudin, G., Kulik, D., Diamond, L.W., 2010. Synthesis and characterization of the LDH hydrotalcite–pyroaurite solid-solution

series. Cem. Concr. Res. 40, 1248–1254. doi:10.1016/j.cemconres.2009.08.031

Sánchez-España, J., Yusta, I., Diez-Ercilla, M., 2011. Schwertmannite and hydrobasaluminite: A re-evaluation of their solubility and control on the iron and aluminium concentration in acidic pit lakes. Appl. Geochemistry 26, 1752–1774. doi:10.1016/j.apgeochem.2011.06.020

Saskatchewan Mining Association, 2014. Uranium in Saskatchewan [WWW Document]. URL http://www.saskmining.ca/uploads/general_files/24/uranium-fact-sheets-2014-final-iii-april-29.pdf (accessed 10.28.16).

Scheckel, K.G., Scheinost, A.C., Ford, R.G., Sparks, D.L., 2000. Stability of layered Ni hydroxide surface precipitates - A dissolution kinetics study. Geochim. Cosmochim. Acta 64, 2727–2735. doi:10.1016/S0016-7037(00)00385-9

Scheidegger, A.M., Lamble, G.M., Sparks, D.L., 1997. Spectroscopic evidence for the formation of mixed-cation hydroxide phases upon metal sorption on clays and aluminum oxides. J. Colloid Interface Sci. 128, 118–128.

Scheidegger, A.M., Strawn, D.G., Lamble, G.M., Sparks, D.L., 1998. The kinetics of mixed Ni-Al hydroxide formation on clay and aluminum oxide minerals: A time-resolved XAFS study. Geochim. Cosmochim. Acta 62, 2233–2245.

Scheinost, A.C., Sparks, D.L., 2000. Formation of layered single- and double-metal hydroxide precipitates at the mineral/water interface: a multiple-scattering XAFS analysis. J. Colloid Interface Sci. 223, 167–178. doi:10.1006/jcis.1999.6638

Schindler, M., Durocher, J.L., Kotzer, T.G., Hawthorne, F.C., 2013. Uranium-bearing phases in a U-mill disposal site in Northern Canada: Products of the interaction between leachate/raffinate and tailings material. Appl. Geochemistry 29, 151–161. doi:10.1016/j.apgeochem.2012.11.007

Schindler, M., Legrand, C. a., Hochella, M.F., 2015. Alteration, adsorption and nucleation processes on clay–water interfaces: Mechanisms for the retention of uranium by altered clay surfaces on the nanometer scale. Geochim. Cosmochim. Acta 153, 15–36. doi:10.1016/j.gca.2014.12.020

Shaw, S.A., Hendry, M.J., Wallschläger, D., Kotzer, T., Essilfie-Dughan, J., 2011. Distribution, characterization, and geochemical controls of elements of concern in uranium mine tailings, Key Lake, Saskatchewan, Canada. Appl. Geochemistry 26, 2044–2056. doi:10.1016/j.apgeochem.2011.07.002

Sinclair, G., Taylor, G., Paul, B., 2006. The Effects of Weathering and Diagenetic Processes on the Geochemical Stability of Uranium Mill Tailings, in: Merkel, B.J., Hasche-Berger, A. (Eds.), Uranium in the Environment: Mining Impact and Consequences. Springer Berlin Heidelberg New York, pp. 27–46.

Stollenwerk, K.G., 1994. Geochemical interactions between constituents in acidic groundwater and alluvium in an aquifer near Globe, Arizona. Appl. Geochemistry 9, 353–369.

Su, C., Suarez, D.L., 2000. Selenate and selenite sorption on iron oxides: an infrared and

electrophoretic study. Soil Sci. Soc. Am. J. 64, 101–111.

Tang, G., Luo, W., Watson, D.B., Brooks, S.C., Gu, B., 2013. Prediction of aluminum, uranium, and co-contaminants precipitation and adsorption during titration of acidic sediments. Environ. Sci. Technol. 47, 5787–93. doi:10.1021/es400169y

Violante, A., Gaudio, S.D., Pigna, M., Ricciardella, M., Banerjee, D., 2009. Coprecipitation of arsenate with metal oxides. 3. Nature, mineralogy, and reactivity of iron(III)-aluminum precipitates. Environ. Sci. Technol. 43, 1515–1521.

von Pechmann, E., 1981. Mineralogy of the Key Lake U-Ni orebodies, Saskatchewan, Canada: evidence for their formation by the hypogene hydrothermal processes, in: Geology of Uranium Deposits, Proceedings of CIM-SEG Uranium Symposium. pp. 27–37.

Wang, S.L., Liu, C.H., Wang, M.K., Chuang, Y.H., Chiang, P.N., 2009. Arsenate adsorption by Mg/Al-NO3 layered double hydroxides with varying the Mg/Al ratio. Appl. Clay Sci. 43, 79–85. doi:10.1016/j.clay.2008.07.005

Warner, J., Rowson, J., 2007. In-situ Monitoring and Validation of a Uranium Mill Tailings Management Facility Design Using X-ray Absorption Near Edge Structure (XANES) Spectroscopy. Synchrotron Radiat. News 20, 14–17. doi:10.1080/08940880701401128

Waychunas, G.., Rea, B.., Fuller, C.., Davis, J.., 1993. Surface chemistry of ferrihydrite: Part 1. EXAFS studies of the geometry of coprecipitated and adsorbed arsenate. Geochim. Cosmochim. Acta 57, 2251–2269. doi:10.1016/0016-7037(93)90567-G

Webb, S.M., 2005. SIXPack: a graphical user interface for XAS analysis using IFEFFIT. Phys. Scr. T115, 1011–1014. doi:10.1238/Physica.Topical.115a01011

World Nuclear Association, 2016a. World Uranium Mining Production [WWW Document]. URL http://www.world-nuclear.org/information-library/nuclear-fuel-cycle/mining-of-uranium/world-uranium-mining-production.aspx

World Nuclear Association, 2016b. Nuclear Power in the World Today [WWW Document]. URL http://www.world-nuclear.org/information-library/current-and-future-generation/nuclear-power-in-the-world-today.aspx (accessed 10.28.16).

World Nuclear Association, 2016c. Uranium in Canada [WWW Document]. URL http://www.world-nuclear.org/information-library/country-profiles/countries-a-f/canada-uranium.aspx (accessed 10.28.16).

Yang, L., Shahrivari, Z., Liu, P.K.T., Sahimi, M., Tsotsis, T.T., 2005. Removal of trace levels of arsenic and selenium from aqueous solutions by calcined and uncalcined layered double hydroxides (LDH). Ind. Eng. Chem. Res. 44, 6804–6815.

A.1 SUPPLEMENTARY INFORMATION FOR CHAPTER 3.0

Table A.1. Raw ICP-MS data of the filtrate from washed solids. W1, W2, and W3 represent the first, second, and third washes, respectively.

	Concentration (mg/L)									
	Na	**Mg**	**Al**	**Si**	**Ca**	**Fe**	**Ni**	**As**	**Se**	**Mo**
L1										
Se-Mo W1	4.27	5.71	8.61	1.46	628	0.32	1.16	0.01	0.03	0.06
W2	0.51	0.18	1.72	1.64	285	0.18	0.04	0.01	0.01	0.04
W3	0.27	0.08	1.30	1.13	2.58	0.13	0.01	0.00	0.00	0.01
Lamella W1	5.07	18.2	0.20	0.14	176	0.01	0.01	0.01	0.05	0.68
W2	0.31	3.43	1.41	0.11	25.8	0.01	0.00	0.01	0.03	0.15
W3	0.13	3.25	1.18	0.02	14.6	0.02	0.00	0.01	0.02	0.10
Combined W1	6.26	11.5	0.56	0.07	601	0.01	0.04	0.06	0.36	5.41
W2	0.33	3.29	0.43	0.16	41.5	0.01	0.00	0.04	0.21	0.94
W3	2.13	2.85	0.41	ud [a]	16.1	0.06	0.01	0.02	0.16	0.27
L2										
Se-Mo W1	5.22	9.65	7.44	--	522	0.04	--	0.13	0.05	0.15
W2	0.14	0.67	4.34	--	7.62	0.02	--	0.04	0.01	0.03
W3	0.11	0.47	2.75	--	1.99	0.02	--	0.02	0.01	0.02
Lamella W1	5.79	62.7	0.06	--	101	ud	--	ud	0.01	0.01
W2	0.28	6.05	0.15	--	26.0	ud	--	ud	0.01	0.01
W3	0.13	2.72	0.22	--	13.0	ud	--	ud	ud	0.01
Combined W1	5.94	0.72	17.3	--	290	ud	--	0.01	0.39	1.36
W2	0.23	0.08	26.9	--	99.0	ud	--	0.08	0.52	0.45
W3	0.08	0.07	19.1	--	62.6	ud	--	0.07	0.39	0.31

[a] ud = undetected

Table A.2. Averaged raw ICP-MS data of aqueous samples (n = 3 for L1 and L2, one sample from each day of steady state operation) from the SRNS experiments and KLBN. KL1 data published by Gomez et al. (2013b). Dilution effects due to lime addition were not taken into account because KL1 lime addition rates were not available.

		Concentration (mg/L)											
	pH	**Mg**		**Al**		**Fe**		**Ni**		**As**		**Se**		**Mo**	
L1															
Raffinate	1.0	1148	±19	1791	±14	1321	±71	223	±5	324	±6	27.3	±0.5	83.4	±12.6
P2	3.5	862	±20	1223	±33	3.50	±0.33	160	±3	0.19	±0.02	0.22	±0.01	0.36	±0.06
Se-Mo O/F [a]	3.5	867	±9	1238	±25	3.26	±1.36	159	±5	0.23	±0.12	0.20	±0.02	0.42	±0.04
P3	6.5	690	±1	1.13	±0.71	0.054	±0.007	16.9	±6.9	0.018	±0.009	0.139	±0.004	0.68	±0.01
Lamella O/F	9.5	43.5	±11.4	6.34	±1.04	0.086	±0.041	0.22	±0.01	0.034	±0.014	0.17	±0.02	1.99	±0.78
L2															
Raffinate	1.0	1074	±62	1758	±103	1310	±37	205	±9	299	±15	27.8	±1.2	89.5	±24.8
P2	4.4	746	±80	67.2	±22.2	0.89	±0.27	87.8	±10.4	0.20	±0.07	0.21	±0.02	0.39	±0.11
Se-Mo OF	4.4	687	±7	47.3	±10.1	0.36	±0.07	83.5	±2.3	0.10	±0.02	0.20	±0.01	0.23	±0.01
P3	6.5	674	±21	0.13	±0.02	0.072	±0.036	60.0	±0.7	0.023	±0.002	0.18	±0.01	0.27	±0.07
Lamella O/F	10.1	326	±13	0.038	±0.004	0.018	±0.005	0.20	±0.02	0.015	±0.001	0.147	±0.005	0.051	±0.016
KL1															
Raffinate	1.4	1044		1635		1428		23.3		27.8		0.40		3.14	
P2	4.3	604		116		396		10.3		0.45		0.16		0.14	
Se-Mo O/F	4.4	649		62.8		445		12.7		0.32		0.21		0.05	
P3	6.4	602		0.07		8.51		4.38		0.01		0.02		0.01	
Lamella O/F	10.1	2.38		0.49		0.06		0.03		0.01		0.010		0.01	

[a] O/F - overflow

Table A.3. ICP-MS results of elemental solid compositions of Se-Mo (pH 3.5/4.4) and Lamella (pH 9.5/10.1) Thickener underflows expressed in mole percent. Only the elements tabulated were considered when converting to mole percent.

		Mole Percent						
	pH	**Mg**	**Al**	**Fe**	**Ni**	**As**	**Se**	**Mo**
L1	3.5	0.03%	7.58%	75.1%	0.04%	12.7%	1.17%	3.35%
L2	4.4	0.19%	62.0%	29.8%	0.90%	5.23%	0.47%	1.48%
KL1	4.4	6.80%	89.8%	2.76%	0.15%	0.44%	0.00%	0.06%
L1	9.5	37.5%	53.7%	4.63%	3.44%	0.65%	0.05%	0.04%
L2	10.1	71.9%	17.3%	0.27%	10.4%	0.04%	0.01%	0.02%
KL1	10.1	63.2%	18.8%	17.6%	0.46%	0.01%	0.00%	0.00%

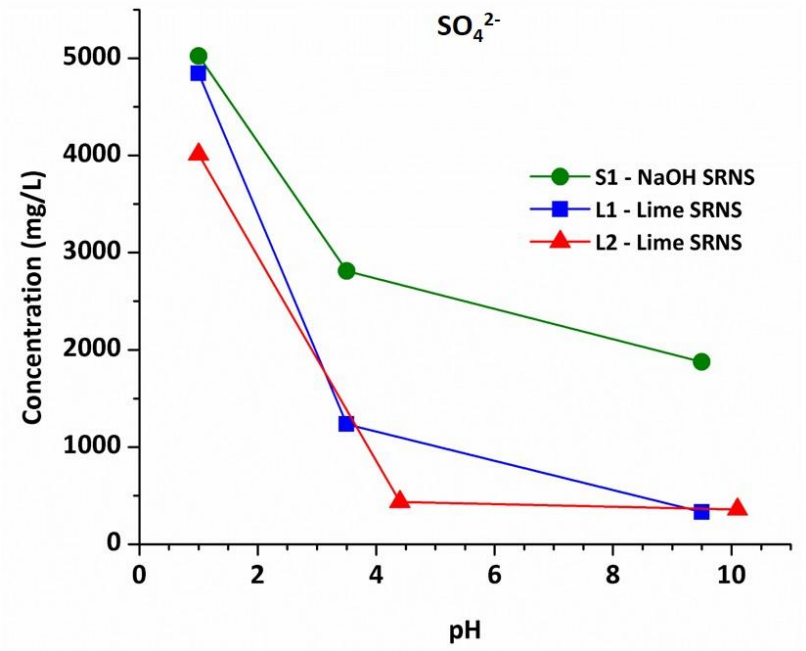

Figure A.1. Sulfate concentrations in the raffinate (pH 1), Se-Mo Thickener overflow (pH 3.5 - 4.4), and Lamella Thickener overflow (pH 9.5 - 10.1) for three SRNS experiments (S1, L1, and L2). Experiment S1 (not presented in this paper) was conducted under the same conditions as L1, but was neutralized using NaOH instead of lime. This shows the effect of SO_4^{2-} removal by gypsum precipitation, as no gypsum was formed in S1.

B.1 SUPPLEMENTARY INFORMATION FOR CHAPTER 4.0

Table B.1. ICP-MS data used to calculate the percentage of each element removed from solution at each stage. The data has been corrected for dilution by the addition of lime.

R1	pH	Mg	Al	Si	Ca	Fe	Ni	As	Se	Mo	S
Raffinate	1	1110	1660	357	43.1	0.43	0.03	0.01	< 0.01	0.25	12400
P2	4	1020	704	110	890	0.62	0.07	< 0.01	< 0.01	0.06	3910
SeMo	4	1060	763	124	957	0.72	0.07	< 0.01	< 0.01	0.03	3980
P3	6.5	933	0.17	3.06	969	0.03	0.05	< 0.01	< 0.01	0.05	2190
P4	9.5	37.0	7.61	0	1211	0.02	0.1	< 0.01	< 0.01	0.05	1090
Lamella	9.5	41.5	6.63	0	1213	0.03	0.05	< 0.01	< 0.01	0.04	1070
R2											
Raffinate	1	1070	1610	244	46.3	1270	1.03	0.04	< 0.01	0.09	12900
P2	4	1030	644	94	743	28.4	0.86	< 0.01	< 0.01	< 0.01	3740
SeMo	4	1060	574	85.8	775	24.9	0.84	< 0.01	< 0.01	< 0.01	3660
P3	6.5	1040	19.7	6.43	901	0.24	0.26	< 0.01	< 0.01	< 0.01	2410
P4	9.5	21.9	3.6	0.45	1080	0.07	0.04	< 0.01	< 0.01	< 0.01	1100
Lamella	9.5	23.8	3.48	0.39	1090	0.03	0.03	< 0.01	< 0.01	0.01	1090
R3											
Raffinate	1	973	1580	209	41.8	0.63	258	336	44.9	140	13000
P2	4	900	560	44.7	685	0.14	185	7.9	3.98	86.9	3430
SeMo	4	890	538	46.4	663	0.1	176	6.43	3.13	78.6	3280
P3	6.5	803	0.57	2.52	743	0.02	17.7	0.11	0.45	28.7	2100
P4	9.5	12.0	3.92	0	1180	0.02	0.07	0.33	2.65	59.7	1020
Lamella	9.5	12.7	4.1	0	1120	0.02	0.06	0.28	2.37	55.9	1000
R4											
Raffinate	1	1160	1930	293	48.7	1300	217	307	33.6	94.5	13400
P2	4	1050	607	117	901	25.1	179	0.84	0.17	1.59	4060
SeMo	4	1070	558	118	1020	23.3	171	0.41	0.14	1.67	4140
P3	6.5	1010	0.18	9.42	1020	0.13	41.6	0.01	0.09	1.27	3220
P4	9.5	55.1	1.95	0.32	1900	0.18	0.18	0.01	0.18	2.32	1610
Lamella	9.5	45.2	2.29	0.56	1440	0.11	0.19	0.01	0.11	1.58	1470

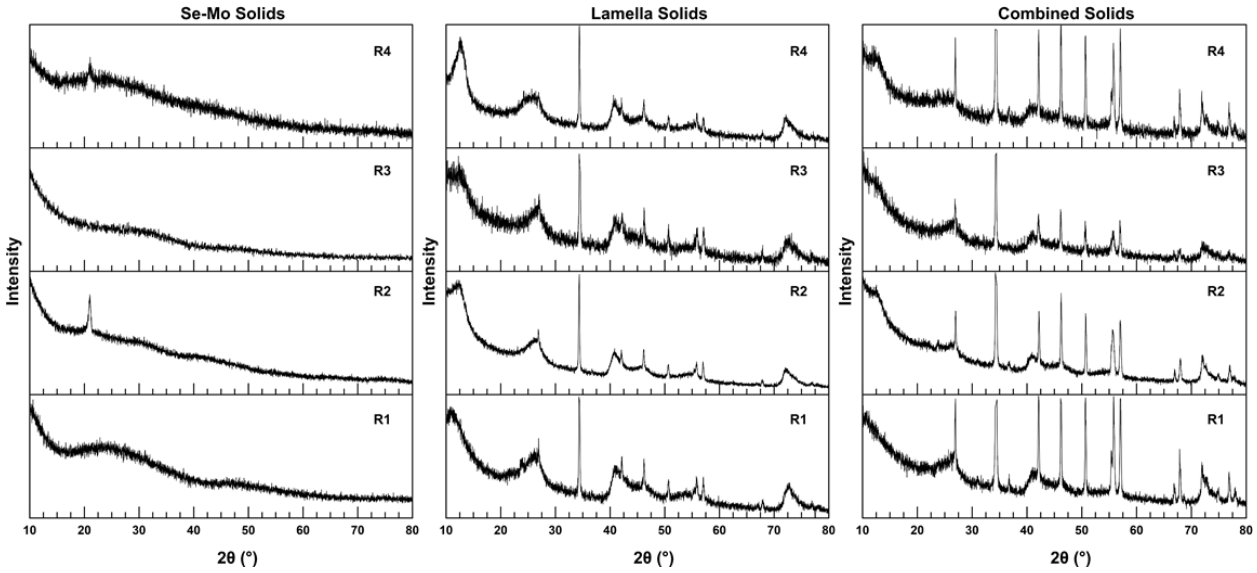

Figure B.1. X-ray diffractograms of Se-Mo (pH 4.0), Lamella (pH 9.5), and Combined (pH 10.5) solids collected from each experiment.

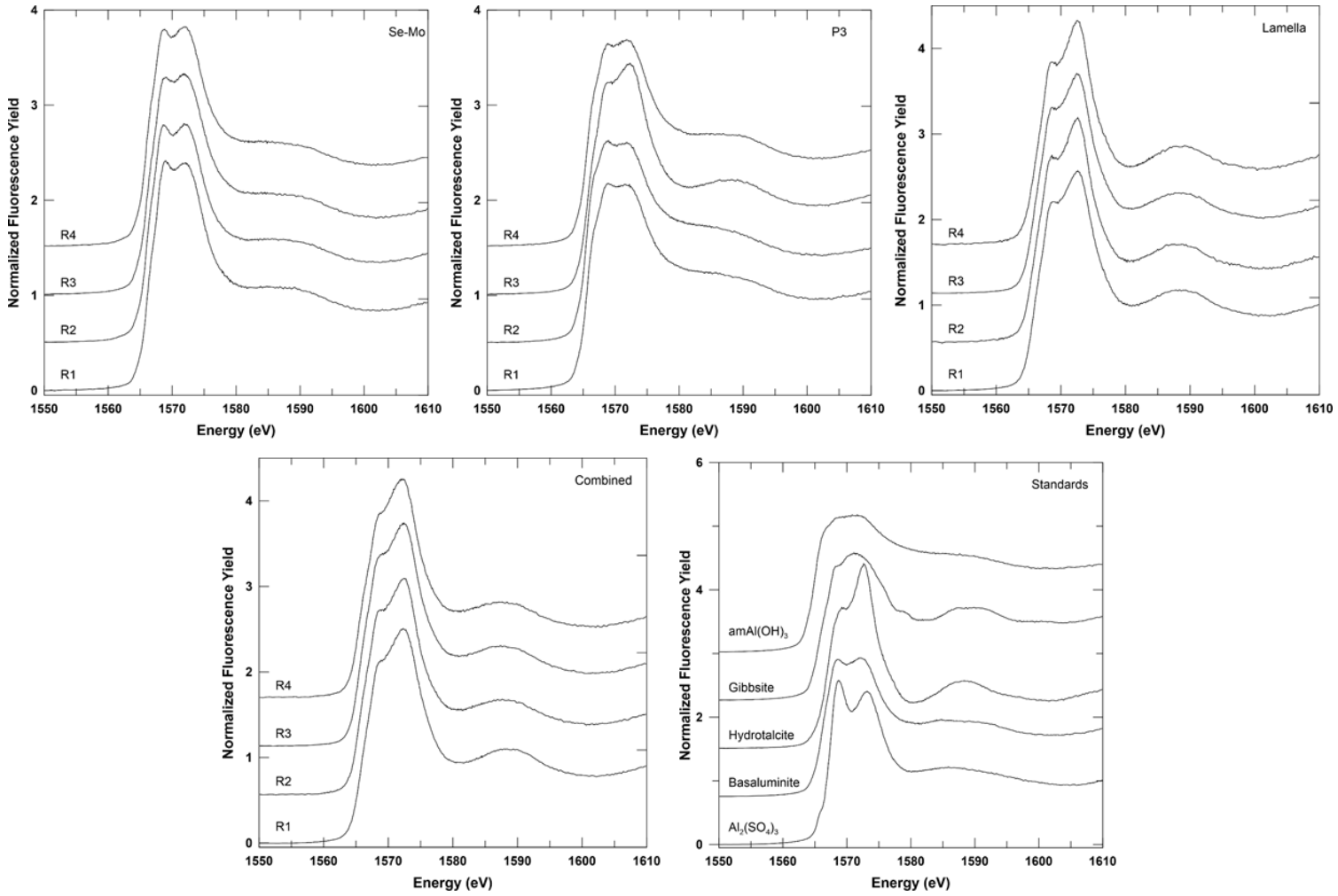

Figure B.2. Al K-edge X-ray absorption near-edge structure spectra of the Se-Mo (pH 4.0), P3 (pH 6.5), Lamella (pH 9.5), and Combined (pH 10.5) samples for all experiments. Spectra of standard compounds are presented in the bottom right.

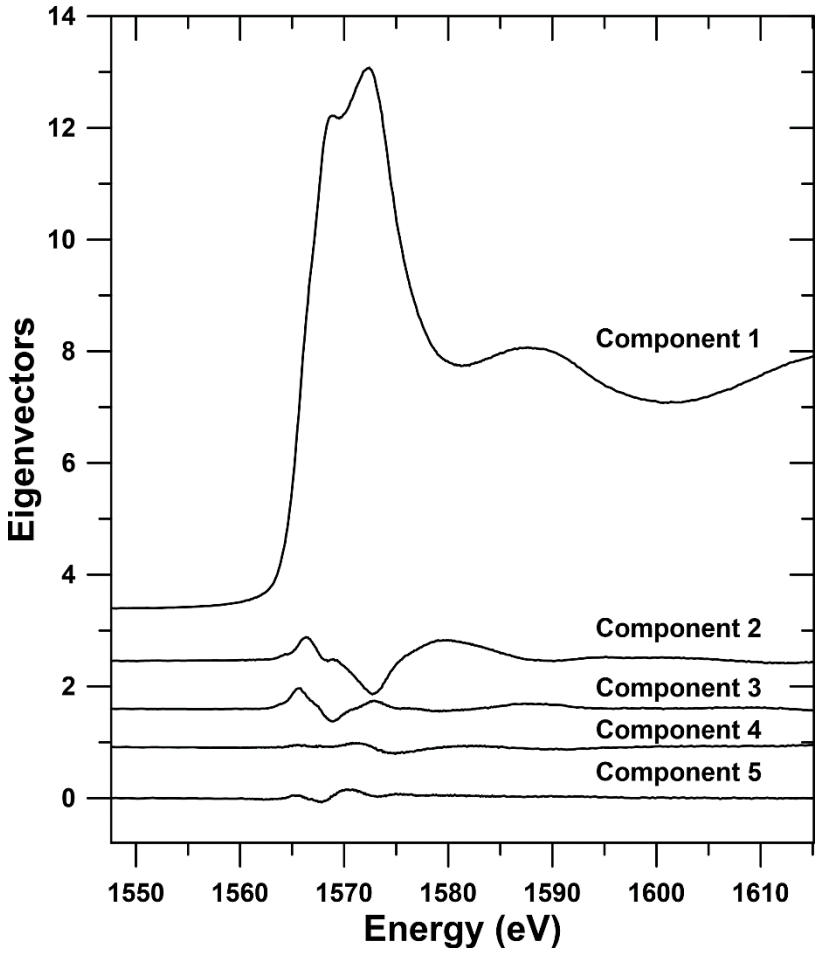

Figure B.3. Principle component analysis of the 16 samples scanned by Al K-edge XAS. The cumulative variance for three components was 0.999, indicating that the samples could be represented well by the first three components. This was the basis for choosing three standards for LCF. Five of the 16 components are shown for emphasis on the minimal variance after three components.

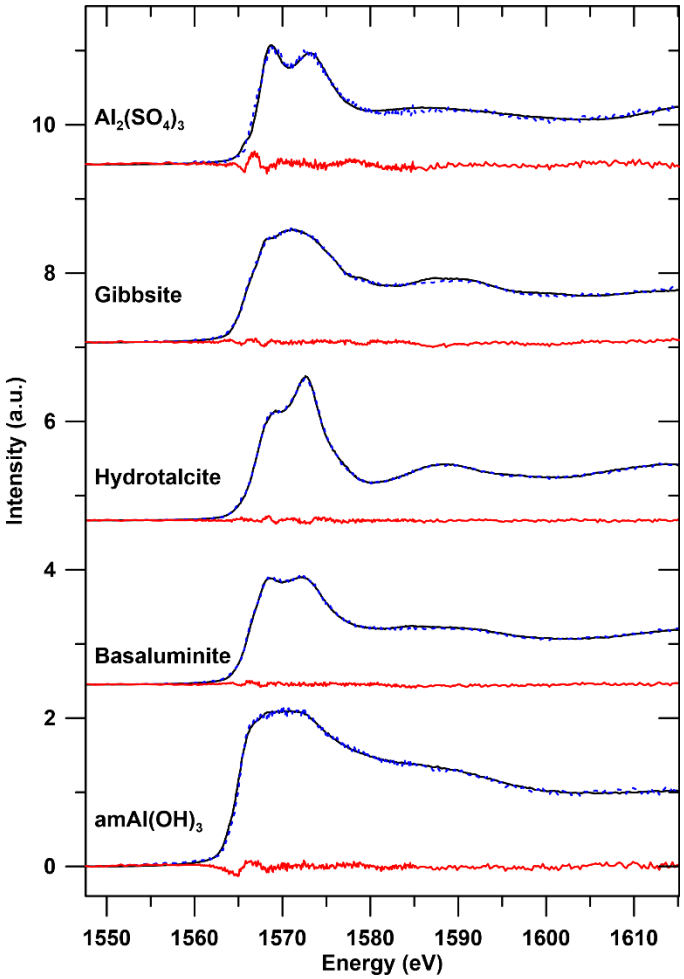

Figure B.4. Target transformations of the standard compounds using the PCA results (solid black = standard compound spectra, dashed blue = target transformation, solid red = residual).

Table B.2. Chi square, R value, and SPOIL value calculated using the program SixPACK. Chi square and R values indicate the target transforms of hydrotalcite, amAl(OH)$_3$, and basaluminite are three components that comprise the set of samples. SPOIL values, as described by Essilfie-Dughan et al. (2011) indicate the targets are all potential candidates (values less than 1.5 indicate excellent candidates, and between 1.5 - 3.0 indicate good candidates). Combined with XRD results, it was decided that Gibbsite and $Al_2(SO_4)_3$ could not be in the samples.

	Chi Square	R Value	SPOIL
Hydrotalcite	0.23	3.0E-04	2.14
amAl(OH)$_3$	0.57	4.4E-04	1.41
Basaluminite	0.25	2.9E-04	1.26
Gibbsite	0.70	6.2E-04	1.44
$Al_2(SO_4)_3$	1.69	1.8E-03	1.88

C.1 SUPPLEMENTARY INFORMATION FOR CHAPTER 5.0

Fitting Results of β-$Ni(OH)_2$ and Amorphous $Ni(OH)_2$

The fitting parameters of β-$Ni(OH)_2$ and amorphous $Ni(OH)_2$ are given in Table 5.4 and the fitted $\chi(k)\cdot k^3$ and radial structure functions are given in Figure C.7. Crystalline β-$Ni(OH)_2$ was fit with an octahedral first shell (CN = 6.3, R = 2.06Å) of Ni-O, followed by a six-coordinate (CN = 5.9) Ni-Ni second shell at 3.12 Å. The first shell of am$Ni(OH)_2$ appeared to be distorted as two separate Ni-O paths were required for a good fit. The $CN_{Ni\text{-}O,1}$ was 2.1 with $R_{Ni\text{-}O,1}$ = 1.81 Å, while the $CN_{Ni\text{-}O,2}$ was 4.3 with $R_{Ni\text{-}O,2}$ = 2.08 Å; these two paths potentially represent axial and equatorial O of the octahedron, respectively. Similarly, two separate Ni-Ni paths were required for the second shell, which indicates that both face-sharing (a shorter bond distance, $R_{Ni\text{-}Ni,1}$ = 2.90 Å) and edge-sharing bonds (a longer bond distance, $R_{Ni\text{-}Ni,2}$ = 3.10 Å) potentially formed. The total CN of the Ni-Ni paths was 5.1 and less than that of β-$Ni(OH)_2$ (5.9), which can be attributed to the amorphous nature of am$Ni(OH)_2$.

Table C.1. ICP-MS data of aqueous samples collected at various stages of neutralization in the synthetic and field samples. R3 and R4 (data from Robertson et al., 2016) KL data was not collected for P2, P3, and P4. All units are in mg/L.

R3	**pH**	**Mg**	**Al**	**Si**	**Ca**	**Fe**	**Ni**	**As**	**Se**	**Mo**	**S**
Raffinate	1.0	973	1580	209	41.8	0.63	258	336	44.9	140	13000
P2	4.0	900	560	44.6	685	0.14	185	7.90	3.98	86.9	3430
SeMo	4.0	890	538	46.4	663	0.10	176	6.43	3.13	78.6	3280
P3	6.5	803	0.57	2.52	743	0.03	17.7	0.11	0.45	28.7	2100
P4	9.5	12.0	3.92	< 0.01	1180	0.02	0.07	0.33	2.65	59.7	1020
Lamella	9.5	12.7	4.10	< 0.01	1120	0.02	0.06	0.28	2.37	55.9	1000
R4											
Raffinate	1.0	1160	1920	293	48.7	1300	217	307	33.6	94.5	13400
P2	4.0	1050	607	117	901	25.1	179	0.84	0.17	1.59	4060
SeMo	4.0	1070	558	118	1010	23.3	171	0.41	0.14	1.67	4140
P3	6.5	1010	0.18	9.42	1020	0.13	41.6	< 0.01	0.09	1.27	3220
P4	9.5	55.1	1.95	0.32	1900	0.18	0.18	0.01	0.18	2.32	1610
Lamella	9.5	45.2	2.29	0.56	1440	0.11	0.19	< 0.01	0.11	1.58	1460
KL											
Raffinate	1.4	2330	378	20700	n.d.	4460	129	127	0.28	1.91	20700
Se-Mo	4.6	852	17.0	11.0	424	760	34.4	0.15	0.29	0.03	n/a
Lamella	9.9	9.32	0.0200	n.d.	543	< 0.01	0.03	0.01	0.02	0.03	n/a
Combined	10.9	0.23	0.57	6.13	577	< 0.01	0.04	0.11	0.03	1.29	n/a
Detection Limit		1E-3	2E-4	5E-2	5E-3	2E-3	2E-5	1E-4	5E-4	5E-5	2E-2
RSD[a]		1%	1%	2%	0.9%	6%	3%	2%	0.9%	2%	1%

[a] The relative standard deviation (RSD) was calculated from replicate samples of the raffinate.

Table C.2. Statistical parameters of the principal component analyses for the set of As and Ni samples. Arsenic and Ni PCA was performed on the $\chi(k)\cdot k^3$ spectra over the range k = 1-13 $Å^{-1}$ and k = 1 - 6.8 $Å^{-1}$, respectively.

As Principal Component Analysis				**Ni Principal Component Analysis**			
Component	**Variance**	**Cumulative Variance**	**IND[a]**	**Component**	**Variance**	**Cumulative Variance**	**IND[a]**
1	0.781	0.781	0.128	1	0.832	0.832	0.114
2	0.054	0.835	0.141	2	0.072	0.904	0.100
3	0.047	0.882	0.149	3	0.035	0.939	0.119
4	0.027	0.909	0.963	4	0.026	0.965	0.147
5	0.025	0.934	0.271	5	0.015	0.98	0.267
6	0.020	0.954	0.429	6	0.011	0.991	0.663
7	0.018	0.972	0.819	7	0.005	0.996	
8	0.014	0.986	2.720				
9	0.010	0.996					

[a] The IND function (Malinowski number) indicates the minimum number of components in the sample set when the function is minimized.

Table C.3. Statistical parameters of the target transformations of As and Ni reference compounds to the principal components of the sample sets.

As Target Transformation			Ni Target Transformation		
Reference	**Residual**	**SPOIL[a]**	**Reference**	**Residual**	**SPOIL[a]**
As-amAl(OH)$_3$	0.004	1.9	Ni-amAl(OH)$_3$	0.007	3.0
As-HT	0.005	1.4	Ni-HT	0.024	3.0
As-Fh	0.006	2.1	Ni-Fh	0.080	6.0
As-AlOHSO$_4$	0.009	1.3	Ni(OH)$_2$	0.130	4.0
Ferric Arsenate	0.011	1.3	amNi(OH)$_2$	0.254	10.8
Scorodite	0.025	2.3			

[a] A SPOIL value <1.5 indicates excellent matches, 1.5-3 is good, 3-4.5 is fair, 4.5-6 is poor, and >6 is unacceptable

Table C.4. Summary of linear combination fitting of As K-edge XAS spectra for all samples, expressed as a percentage ± estimated standard deviation as calculated by ATHENA.

Sample	**As-amAl(OH)$_3$**	**As-AlOHSO$_4$**	**As-FH**	**Ferric Arsenate**	**As-HT**	**Sum**	**R-factor[a]**
R3Se-Mo	-	88(±0)%	-	-	-	88%	0.028
R4Se-Mo	-	15(±5)%	61(±3)%	26(±6)%	-	102%	0.006
KLSe-Mo	-	26(±5)%	56(±3)%	13(±5)%	-	95%	0.006
R3Lam	12(±6)%	-	-	-	76(±6)%	88%	0.015
R4Lam	12(±7)%	-	-	-	87(±7)%	99%	0.014
KLLam	16(±12)%	-	26(±8)%	-	46(±17)%	88%	0.043
R3Combined	55(±3)%	-	-	-	40(±3)%	95%	0.004
R4Combined	42(±4)%	-	54(±3)%	-	<5%[b]	101%	0.004
KLCombined	24(±5)%	-	34(±3)%	-	35(±5)%	93%	0.007

Fitting was performed in k-space from 1.0 to 13.0 Å^{-1} and components were not required to sum to 100%.

[a] R-factor defined as $\Sigma((\text{Data-Fit})^2)/\Sigma(\text{Data}^2)$.

[b] Components fit to <5% are not considered significant but were included as they contribute to the total sum.

Table C.5. Summary of Ni K-edge EXAFS fitting parameters of β-$Ni(OH)_2$ and amorphous $Ni(OH)_2$. The amplitude reduction factor, S_0^2, was fixed at 0.9. Fitting was performed over a range from k_{min} = 2.3 $Å^{-1}$ to k_{max} = 9.8-12.6 $Å^{-1}$.

	E_o (eV)	CN	R (Å)	σ^2 ($Å^2$)	R-Factor	χ_v^2
β-$Ni(OH)_2$						
Ni-O	-5.9(9)	6.0[a]	2.06(1)	0.006(1)	0.017	701
Ni-Ni	-5.9(9)	6.0(7)	3.12(1)	0.006(1)		
amNi$(OH)_2$						
Ni-O_1	-7(2)	2.1[a]	1.81(2)	0.001(2)	0.016	22897
Ni-O_2	-7(2)	4.3[a]	2.08(2)	0.001(3)		
Ni-Ni_1	-7(2)	1.4[a]	2.90(3)	0.003(3)		
Ni-Ni_2	-7(2)	3.7[a]	3.10(5)	0.004(5)		

Fitting was performed over a range from k_{min} = 2.3 $Å^{-1}$ to k_{max} = 9.8-12.6 $Å^{-1}$. The amplitude reduction factor, S_0^2, was fixed at 0.9. E_o = energy shift. R = interatomic distance. σ^2 = Debye-Waller factor. χ_v^2 = reduced chi-square. The numbers in parentheses are the errors of the fitting parameters, calculated from the diagonal of the covariance matrix and scaled by the square-root of χ_v^2.

[a]Parameter held constant in the fitting procedure

Table C.6. Summary of linear combination fitting of Ni K-edge XAS spectra for all samples, expressed as a percentage ± estimated standard deviation as calculated by ATHENA. Fitting was performed in k-space from 1.0 to 10.9 $Å^{-1}$ and components were not required to sum to 100%.

Sample	Ni-HT	Ni-am$Al(OH)_3$	Sum	R-Factor[a]
KLSe-Mo[b]	-	100(±0)%	100%	0.042
R3Lam	33(±3)%	53(±3)%	86%	0.032
R4Lam	37(±3)%	51(±3)%	88%	0.032
KLLam[b]	84(±10)%	19(±10)%	103%	0.056
R3Combined	52(±6)%	49(±7)%	101%	0.13
R4Combined	33(±3)%	64(±3)%	97%	0.031
KLCombined[b]	72(±7)%	33(±7)%	105%	0.033

[a]R-factor defined as $\Sigma((Data-Fit)^2)/\Sigma(Data^2)$

[b]KL samples were fit from 1.0-6.8 $Å^{-1}$ due to interference from the Dy L_2- and Cu K-edges above this energy.

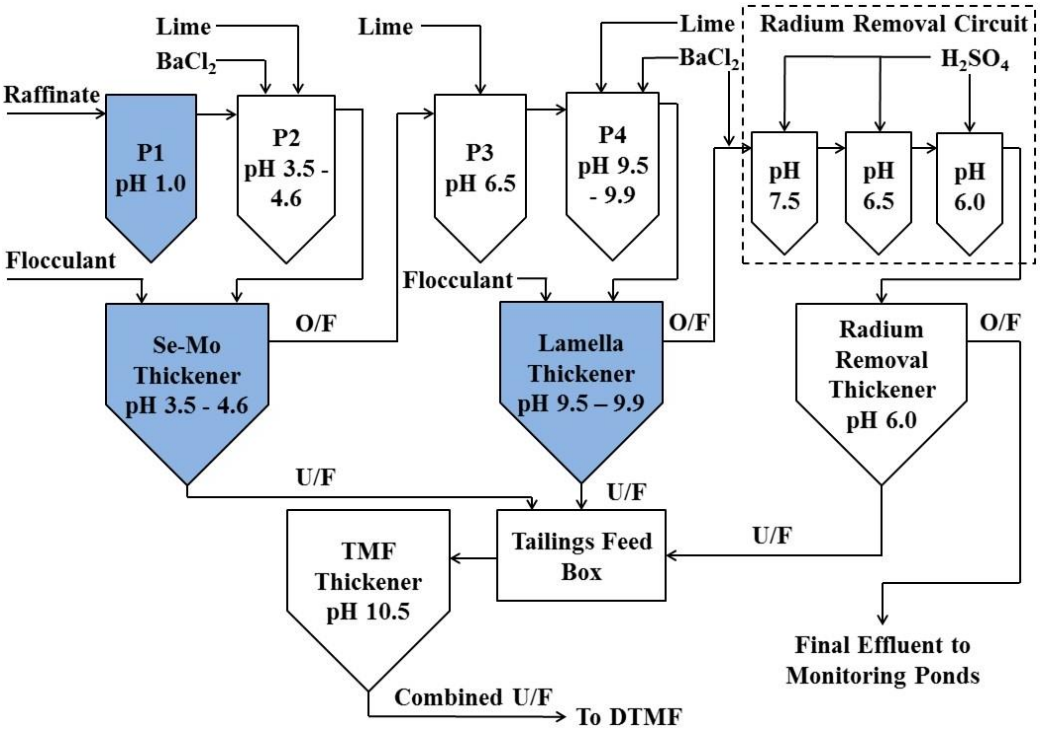

Figure C.1. Process flow diagram of the Key Lake bulk neutralization process. Field samples were collected from the raffinate stream (P1), Se-Mo thickener underflow, and Lamella thickener underflow (U/F) and are labelled in blue. The pH set point in each Pachuca (P1, P2, P3, and P4) is a nominal value. The Radium Removal Circuit is beyond scope of this study. Reproduced from Robertson et al. (2014).

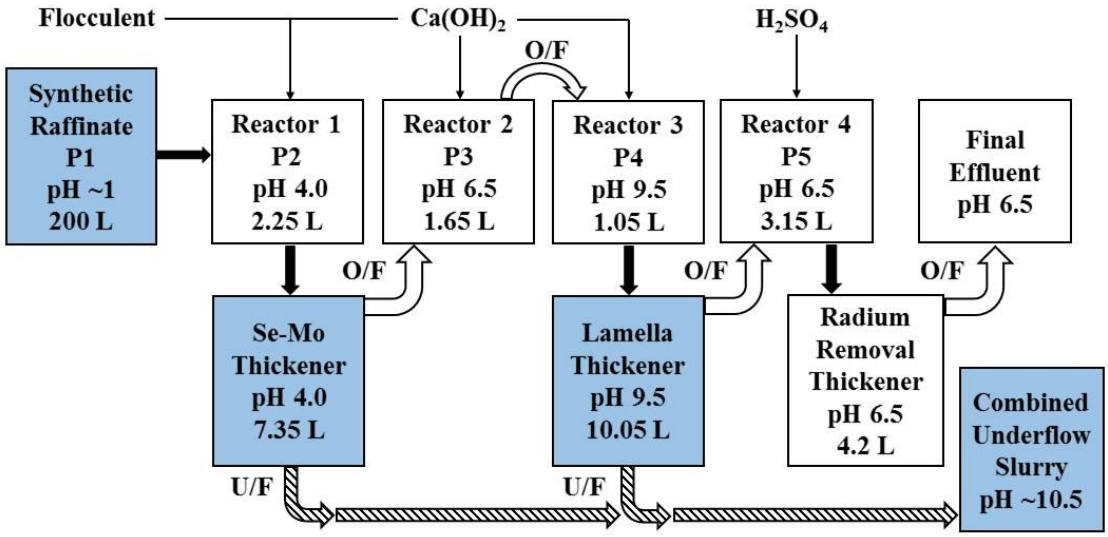

Figure C.2. Process flow diagram of the synthetic raffinate neutralization system based on the flow paths of the Key Lake bulk neutralization process. White boxes represent solution sampling points and blue boxes represent solution and solid sampling points. Black arrows represent pumped flow, white arrows represent gravity flow, and hatched arrows represent intermittent flow controlled by valves. Reproduced from Robertson et al. (2014).

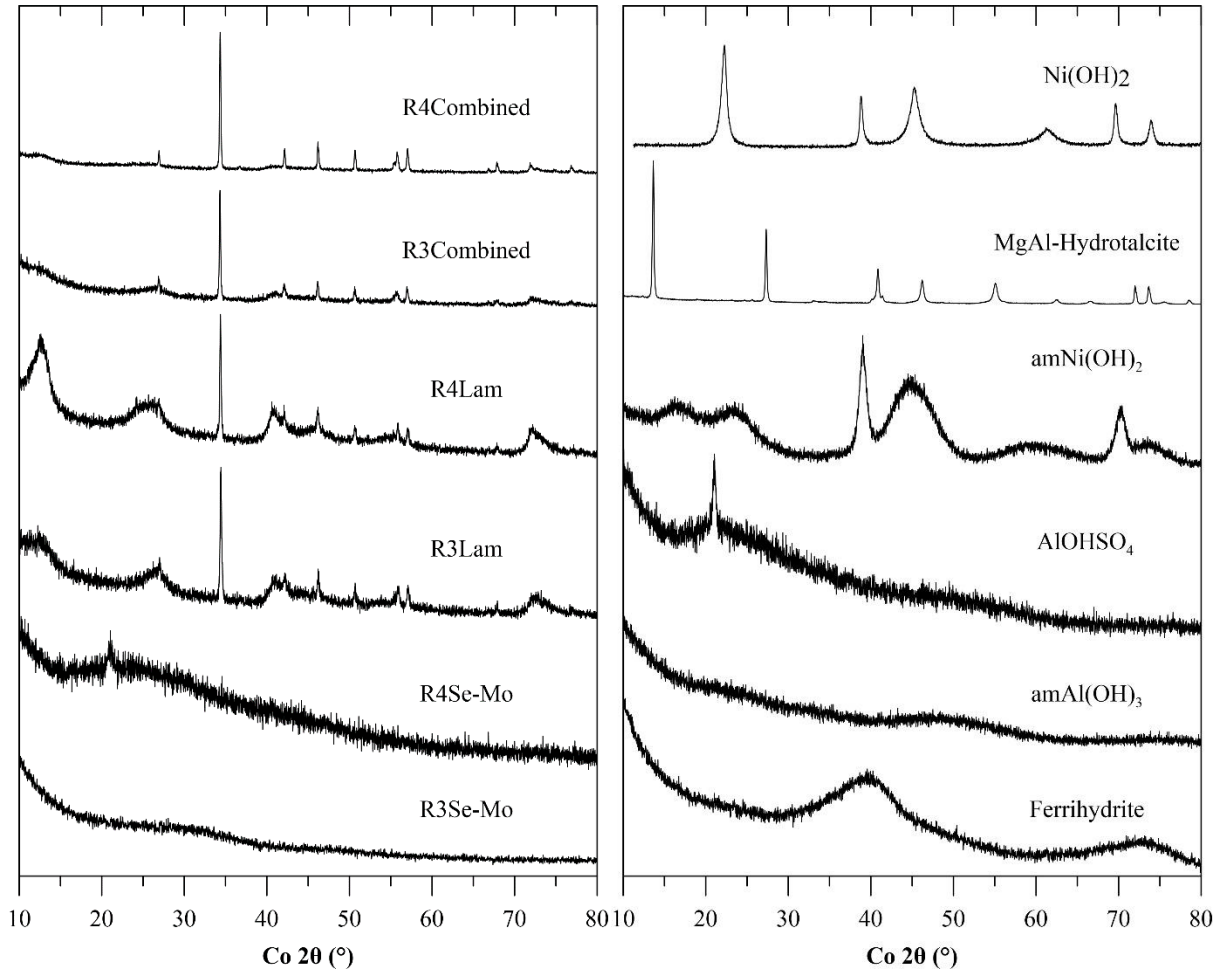

Figure C.3. Powder X-ray diffraction data of the synthetic samples (left) and select standard compounds (right). The diffraction patterns of each sample and standard are presented to show the bulk crystalline character of the samples and standards that are characterized via XAS in the main text. The positions of the standards are not intended to match the positions of the samples in the figure. Diffraction patterns were collected using an Empyrean Pro PANalytical diffractometer equipped with a Co target (Co $K_{\alpha 1}$ = 1.7902 Å). Additional details on the experimental setup for the synthetic samples are given in Robertson et al. (2016).

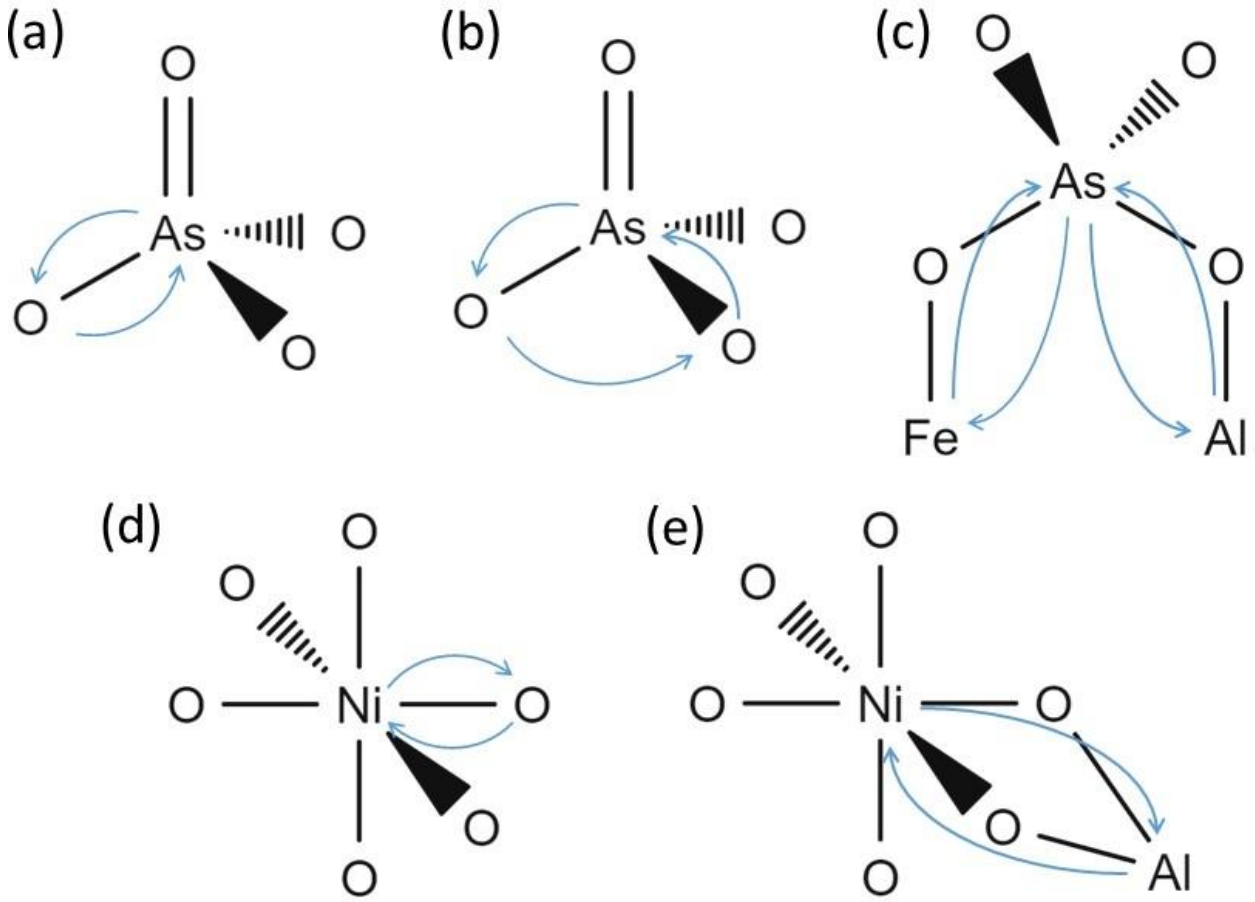

Figure C.4. Schematic of the backscattering paths used in the fitting of As and Ni EXAFS. These structures do not represent the exact chemical structures discussed in the text but are used to illustrate the paths used by FEFF: (a) As-O path, (b) As-O-O multiple scattering path, (c) As-Fe or As-Al path, (d) Ni-O path, and (e) Ni-Al path (analogous to Ni-Fe and Ni-Ni paths).

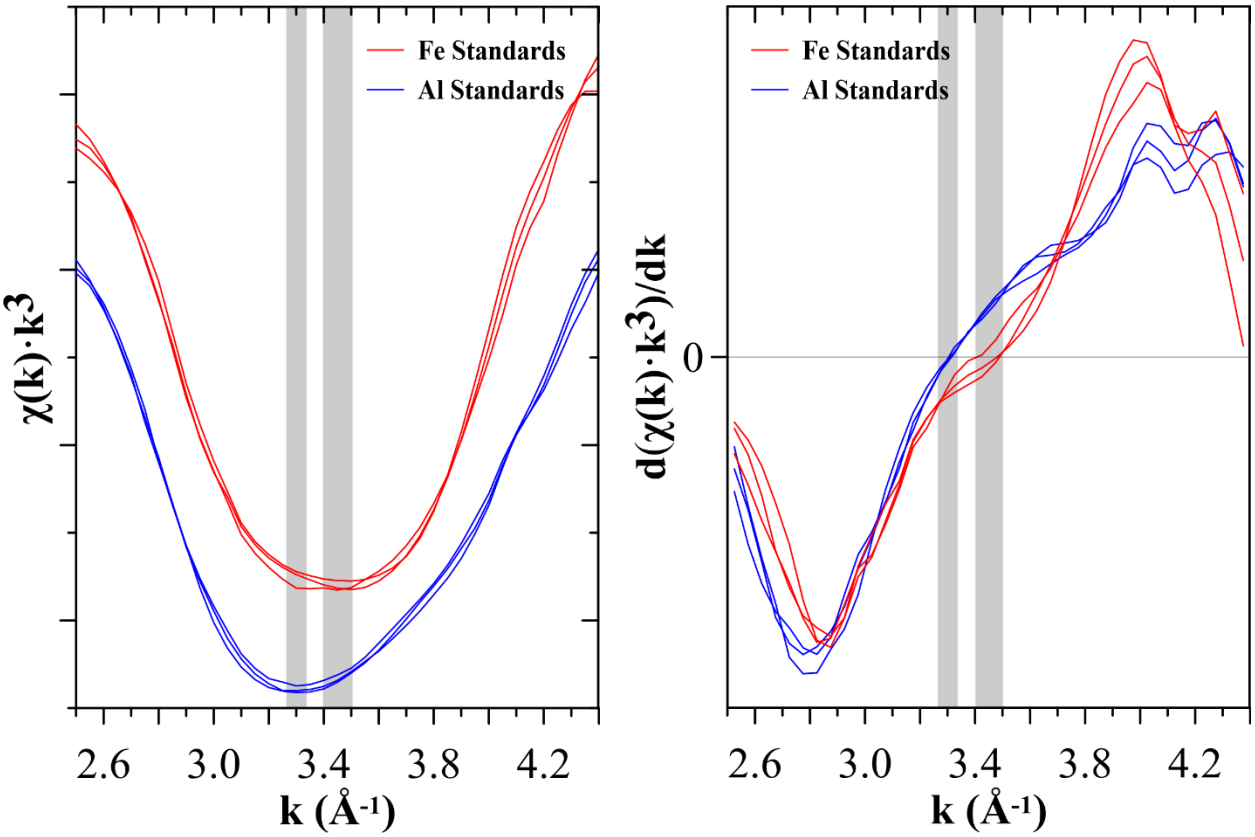

Figure C.5. A focused view of the 2.5-4.4 $Å^{-1}$ range (left) of the Al and Fe standards to show the offset consistent with the type of second shell As coordination. The zero-crossings of the smoothed, first derivative spectra (right) show the minima of Al standards occur at 3.3 $Å^{-1}$ and the minima of Fe standards occur between 3.4-3.5 $Å^{-1}$. This offset can be used as a fingerprint for samples to determine the predominant type of second shell coordination (As-Al/Fe).

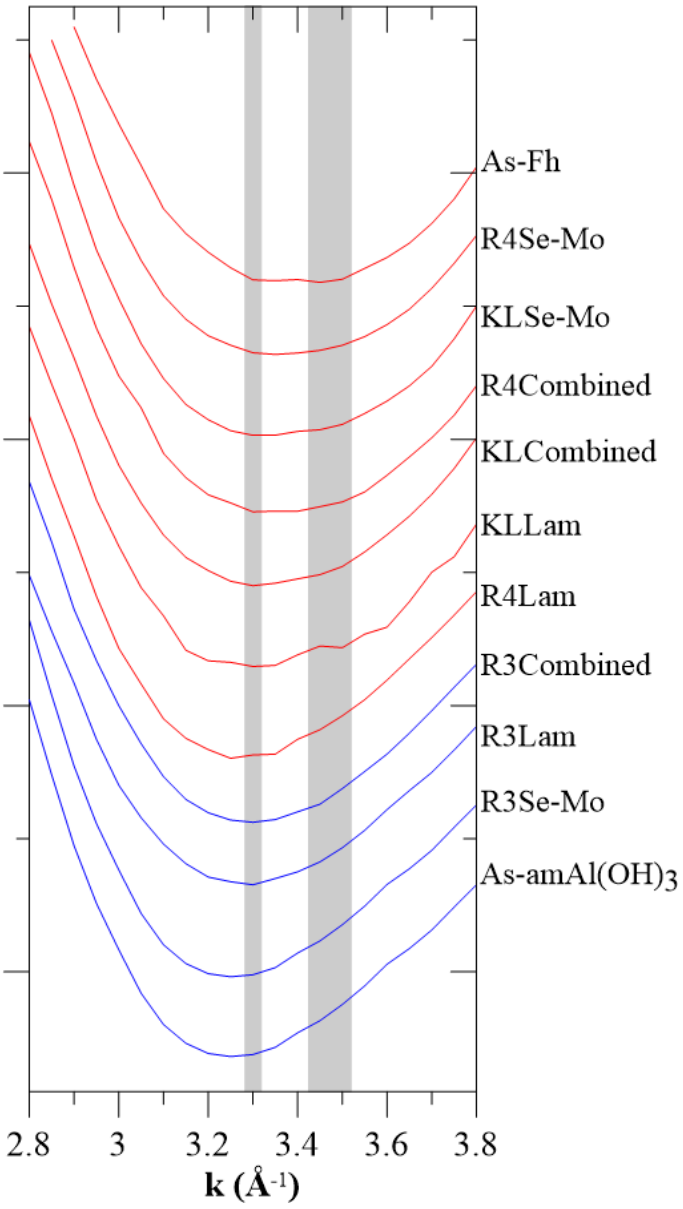

Figure C.6. Arsenic K-edge $\chi(k)\cdot k^3$ spectra between 2.8 and 3.8 $Å^{-1}$ and arranged from the least amount of Fe in the sample (bottom) to the most (top) to emphasize the change in trough position as the coordination of As with Fe increases. Samples containing As-O-Al bonds are characterized by an asymmetric peak minima at 3.3 $Å^{-1}$ and samples containing As-O-Fe bonds were shifted upwards with a symmetric minima around 3.5 $Å^{-1}$ (see grey regions). As the Fe content increases, the minima shift closer to 3.5 $Å^{-1}$ and greater peak symmetry. The blue trace represents samples with no Fe and the red trace represents samples with Fe.

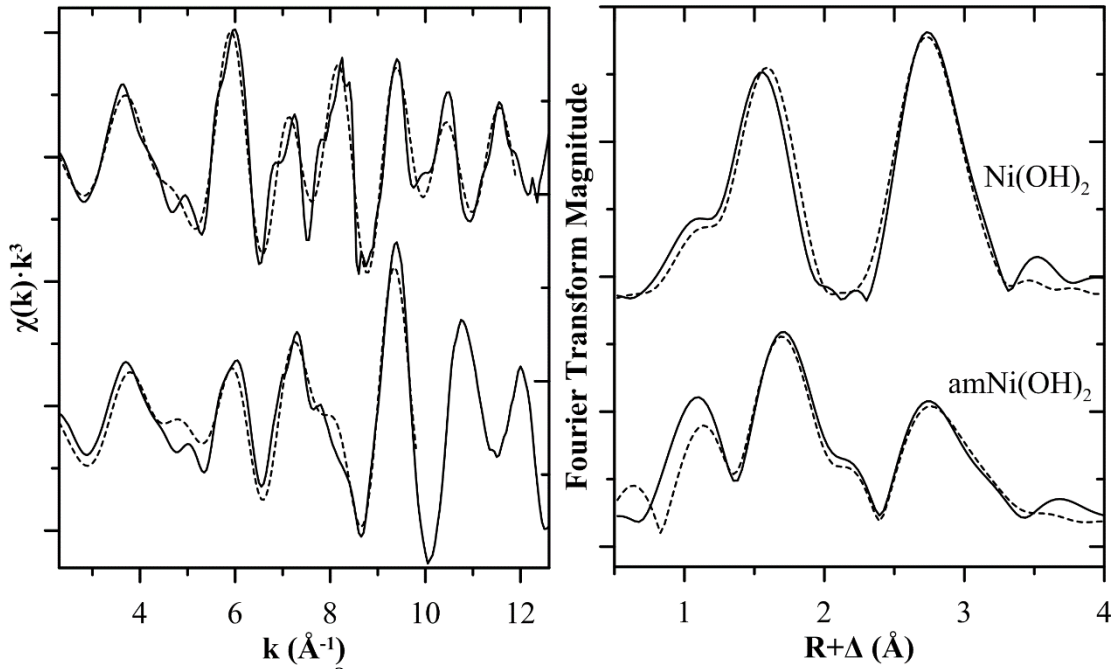

Figure C.7. Nickel K-edge k^3-weighted $\chi(k)$ spectra of the Ni standard compounds and the corresponding RSFs. Whole lines represent data and dashed lines represent fits.

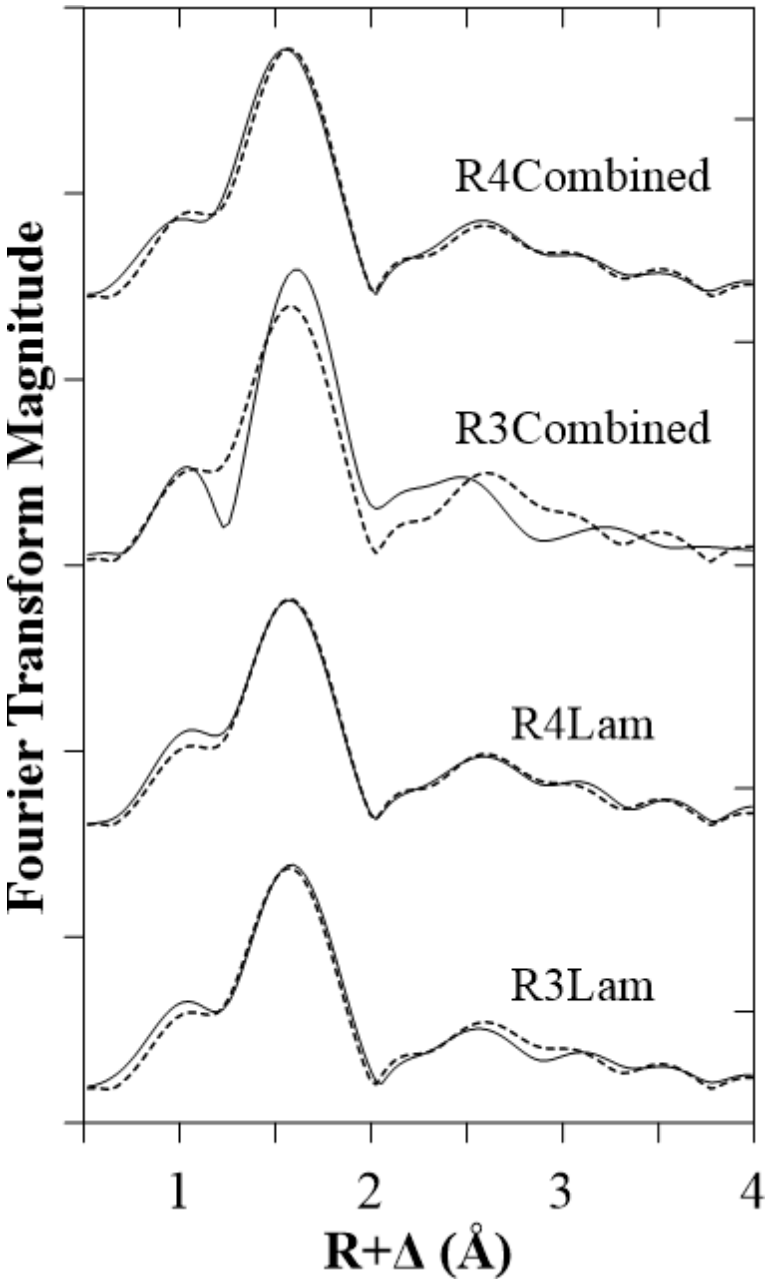

Figure C.8. Nickel K-edge k^3-weighted Fourier transforms of the synthetic samples (R3 and R4). Whole lines represent data and dashed lines represent results from LCF. The Fourier transform range was 2.3 to 10.9 $Å^{-1}$. Field samples (KL) are not presented because the data range only extends to 6.8 $Å^{-1}$ due to interference from other elements (discussed in text).

D.1 SUPPLEMENTARY INFORMATION FOR CHAPTER 6.0

Table D.1. Compilation of studies using in-situ or laboratory experiments related to Athabasca Basin milling operations and the corresponding types of performed analyses.

	Rabbit Lake	Key Lake	McClean Lake
In situ studies	**Donahue et al. (2000)** - Tailings cores from eight RLITMF boreholes; whole-rock chemical analysis **Pichler et al. (2001)** - Tailings cores from the RLITMF - Samples from neutralization circuit and the leach residue - Samples subjected to sequential extractions, TEM, SEM, and XRD **Donahue and Hendry (2003)** - Tailings cores from the RLITMF; subjected to sequential extractions and porewater analysis - Collection of raffinate, leach residue, and tailings discharge samples **Moldovan et al. (2003)** - Six tailings samples subjected to XAS analysis; As K-edge XAS **Moldovan and Hendry (2005)** - Aqueous solutions from the raffinate neutralization circuit over three months under three different pH regimes; solution chemistry modeled	**Shaw et al. (2011)** - Tailings cores from the DTMF from four separate years spanning Deilmann and McArthur orebodies; subjected to sequential extractions and porewater analysis - Monthly composite of as-discharged tailings since 1996 **Essilfie-Dughan et al. (2011)** - Tailings cores from the DTMF; Mo K-edge XAS **Essilfie-Dughan et al. (2012)** - Additional analysis from samples collected by Shaw et al. (2011); Fe, As, and Ni μXRF and XAS **Essilfie-Dughan et al. (2013)** - Additional analysis from samples collected by Shaw et al. (2011); Fe and As K-edge XAS **Gomez et al. (2013b)** - Aqueous and solid samples collected from the raffinate neutralization circuit - Two tailings samples from the DTMF - Solid samples subjected to XRD and TEM **Bissonnette et al. (2016)** - Aqueous and solid samples collection from the raffinate neutralization circuit; Mo and As K-edge XAS **Robertson et al. (2017**) - Solid samples collected from the raffinate neutralization circuit; Ni and As K-edge XAS	**Frey et al. (2010)** - One tailings sample subjected to As K-edge XAS **Rinas et al. (2010)** - Tailings cores from the JEB TMF over the course of five sampling campaigns - Sample slurry from the tailings thickener - Samples subjected to As K-edge XAS and aging tests **Hayes et al. (2014)** - Tailings cores from two JEB TMF boreholes subjected to XRD, μXRF, and Mo K-edge XANES **Blanchard et al. (2015**) - Tailings cores spanning the depth of two JEB TMF boreholes; subjected to Mo K-edge XANES and porewater analyses
Laboratory Batch		**Lieu et al. (2010)** - Mill raffinate solutions neutralized with various reagents; measured effectiveness of Se and Mo precipitation **Liu and Hendry (2011)** - Mill raffinate solution titrated; precipitation of ^{226}Ra was measured under various conditions **Robertson et al. (2016)** - High pH synthetic raffinate precipitates subjected to As, Se, and Mo adsorption tests	**Langmuir et al. (1999)** - Raffinates from multiple ore types created and neutralized; solid samples subjected to XRD and electron microprobe methods - Thermodynamic modeling of aqueous samples - Aging tests of neutralized slurries **Mahoney et al. (2005)** - Neutralized tailings slurry equilibrated with a leaching solution to measure As desorption **Mahoney et al. (2007)** - Mill raffinate solution neutralized by various methods; solid samples subjected to XRD, SEM, and electron microprobe methods - Thermodynamic modeling of aqueous samples **Chen et al. (2009)**

			- Mill raffinate solution neutralized; two solid samples (from Mahoney et al. 2007) subjected to As and Fe K-edge XAS
Laboratory Continuous		**Robertson et al. (2014)** - Neutralization of synthetic raffinates; aqueous and solid phase chemistry compared to mill samples via XRD, ATR-IR, and Raman spectroscopy **Bissonnette et al. (2016)** - Neutralization of pilot plant generated raffinates from multiple ore blends; XRD, SEM, and As and Mo K-edge XAS **Robertson et al. (2016)** -Neutralization of synthetic raffinates; solids subjected to TEM, XRD, and Al K-edge XAS **Robertson et al. (2017)** - Synthetic raffinate precipitates subjected to As and Ni K-edge XAS	**De Klerk et al. (2012)** - Neutralization of synthetic raffinates in a circuit operating under similar conditions of the McClean Lake mill; precipitates subjected to XRD and Raman spectroscopy

Geochemical Modeling

Below is the PHREEQC code used for the Bissonnette (2015) model, using the adjusted LLNL(D2) thermodynamic database.

```
SOLUTION 1 Raffinate
       temp           40
       pH             1.6
       pe             10.07
       redox          pe
       units          mg/kgw
       density        1
       Al             737.7
       As(5)          47.3
       Ca             179.41
       Fe(3)          242.8
       Fe(2)          304
       Mg             511
       Mo             0.5
       Na             57.2
       Ni             34.7
       S              13372 as S charge
       Si             2000
       Se             0.25
       C(4)           137 as HCO3
       Ba             10 # placeholder
       -water         1 # kg

SOLUTION 3 Initial leach residue aqueous phase
       temp           30
       pH             1.6
       pe             10.07
       redox          pe
       units          mg/kgw
       density        1
       Al             819.25
       As(5)          52.5
       Ca             199.25
       Fe             607.5
       Mg             567.5
       Mo             0.56
       Ni             38.5
       S              3343 as S charge
       Si             500
       Se             0.1
       C(4)           137 as HCO3
       Ba             0.25 # placeholder
       -water         1 # kg

USE solution none
PHASES
       Fix_H+
              H+ = H+
              log_k          0
       Fix_pe
              e- = e-
              log_k          0
END

USE solution 1
EQUILIBRIUM_PHASES 1 Initialization of raffinate for output file
       Fix_H+  -1.6    Ca(OH)2 10.0
END

USE solution 1
EQUILIBRIUM_PHASES 1
       Fix_H+  -2.3    Ca(OH)2 10.00
       Al(OH)3(am)     0 0
```

```
        Barite          0 0
        Calcite         0 0
        CaMoO4          0 0
        FeAsO4:2H2O             0 0
        Ferrihydrite    0 0
        Gypsum          0 0
        Hydrobasaluminite       0 0
        Hydrotalcite    0 0
        Mg(OH)2         0 0
        Ni3(AsO4)2:8H2O         0 0
        Ni(OH)2         0 0
        NiMoO4          0 0
        SiO2(am)                0 0
        CO2(g)          -3.5 0.0000132
SURFACE 1
        Alumina_sOH Hydrobasaluminite equilibrium_phases 0.197      5.15e4
        Hfo_sOH Ferrihydrite   equilibrium_phases 0.005      5.34e4
        Hfo_wOH Ferrihydrite   equilibrium_phases 0.5        5.34e4
END

USE solution 1
EQUILIBRIUM_PHASES 1
        Fix_H+  -2.5    Ca(OH)2 10.0
        Al(OH)3(am)     0 0
        Barite          0 0
        Calcite         0 0
        CaMoO4          0 0
        FeAsO4:2H2O             0 0
        Ferrihydrite    0 0
        Gypsum          0 0
        Hydrobasaluminite       0 0
        Hydrotalcite    0 0
        Mg(OH)2         0 0
        Ni3(AsO4)2:8H2O         0 0
        Ni(OH)2         0 0
        NiMoO4          0 0
        SiO2(am)                0 0
        CO2(g)          -3.5 0.0000132
SURFACE 1
        Alumina_sOH Hydrobasaluminite equilibrium_phases 0.197      5.15e4
        Hfo_sOH Ferrihydrite   equilibrium_phases 0.005      5.34e4
        Hfo_wOH Ferrihydrite   equilibrium_phases 0.5        5.34e4
END

USE solution 1
EQUILIBRIUM_PHASES 1
        Fix_H+  -3.0    Ca(OH)2 10.0
        Al(OH)3(am)     0 0
        Barite          0 0
        Calcite         0 0
        CaMoO4          0 0
        FeAsO4:2H2O             0 0
        Ferrihydrite    0 0
        Gypsum          0 0
        Hydrobasaluminite       0 0
        Hydrotalcite    0 0
        Mg(OH)2         0 0
        Ni3(AsO4)2:8H2O         0 0
        Ni(OH)2         0 0
        NiMoO4          0 0
        SiO2(am)                0 0
        CO2(g)          -3.5 0.0000132
SURFACE 1
        Alumina_sOH Hydrobasaluminite equilibrium_phases 0.197      5.15e4
        Hfo_sOH Ferrihydrite   equilibrium_phases 0.005      5.34e4
        Hfo_wOH Ferrihydrite   equilibrium_phases 0.5        5.34e4
END

USE solution 1
EQUILIBRIUM_PHASES 1
```

```
        Fix_H+  -3.5    Ca(OH)2 10.0
        Al(OH)3(am)      0 0
        Barite           0 0
        Calcite          0 0
        CaMoO4           0 0
        FeAsO4:2H2O              0 0
        Ferrihydrite     0 0
        Gypsum           0 0
        Hydrobasaluminite        0 0
        Hydrotalcite     0 0
        Mg(OH)2          0 0
        Ni3(AsO4)2:8H2O          0 0
        Ni(OH)2          0 0
        NiMoO4           0 0
        SiO2(am)                 0 0
        CO2(g)           -3.5 0.0000132
SURFACE 1
        Alumina_sOH Hydrobasaluminite equilibrium_phases 0.197      5.15e4
        Hfo_sOH Ferrihydrite   equilibrium_phases 0.005      5.34e4
        Hfo_wOH Ferrihydrite   equilibrium_phases 0.5        5.34e4
END

USE solution 1
EQUILIBRIUM_PHASES 1
        Fix_H+  -4.0    Ca(OH)2 10.0
        Al(OH)3(am)      0 0
        Barite           0 0
        Calcite          0 0
        CaMoO4           0 0
        FeAsO4:2H2O              0 0
        Ferrihydrite     0 0
        Gypsum           0 0
        Hydrobasaluminite        0 0
        Hydrotalcite     0 0
        Mg(OH)2          0 0
        Ni3(AsO4)2:8H2O          0 0
        Ni(OH)2          0 0
        NiMoO4           0 0
        SiO2(am)                 0 0
        CO2(g)           -3.5 0.0000132
SURFACE 1
        Alumina_sOH Hydrobasaluminite equilibrium_phases 0.197      5.15e4
        Hfo_sOH Ferrihydrite   equilibrium_phases 0.005      5.34e4
        Hfo_wOH Ferrihydrite   equilibrium_phases 0.5        5.34e4
END

USE solution 1
EQUILIBRIUM_PHASES 1
        Fix_H+  -4.2    Ca(OH)2 10.0
        Al(OH)3(am)      0 0
        Barite           0 0
        Calcite          0 0
        CaMoO4           0 0
        FeAsO4:2H2O              0 0
        Ferrihydrite     0 0
        Gypsum           0 0
        Hydrobasaluminite        0 0
        Hydrotalcite     0 0
        Mg(OH)2          0 0
        Ni3(AsO4)2:8H2O          0 0
        Ni(OH)2          0 0
        NiMoO4           0 0
        SiO2(am)                 0 0
        CO2(g)           -3.5 0.0000132
SURFACE 1
        Alumina_sOH Hydrobasaluminite equilibrium_phases 0.197      5.15e4
        Hfo_sOH Ferrihydrite   equilibrium_phases 0.005      5.34e4
        Hfo_wOH Ferrihydrite   equilibrium_phases 0.5        5.34e4
SAVE solution 2 #This solution is the overflow from the thickener and the equilibrium porewater of
the underflow slurry
```

```
END

USE solution 2
EQUILIBRIUM_PHASES 1
       Fix_H+  -4.5    Ca(OH)2 10.0
       Fix_pe  -8.03   O2      10.0
       Al(OH)3(am)      0 0
       Barite           0 0
       Calcite          0 0
       CaMoO4           0 0
       FeAsO4:2H2O              0 0
       Ferrihydrite     0 0
       Gypsum           0 0
       Hydrobasaluminite        0 0
       Hydrotalcite     0 0
       Mg(OH)2          0 0
       Ni3(AsO4)2:8H2O          0 0
       Ni(OH)2          0 0
       NiMoO4           0 0
       SiO2(am)                 0 0
       CO2(g)           -3.5 0.0000132
SURFACE 1
       Alumina_sOH Hydrobasaluminite equilibrium_phases 0.197      5.15e4
       Hydro_sOH Hydrotalcite equilibrium_phases 0.197      5.15e4
       Hfo_sOH Ferrihydrite   equilibrium_phases 0.005      5.34e4
       Hfo_wOH Ferrihydrite   equilibrium_phases 0.5        5.34e4
END

USE solution 2
EQUILIBRIUM_PHASES 1
       Fix_H+  -5.0    Ca(OH)2 10.0
       Fix_pe  -8.03   O2      10.0
       Al(OH)3(am)      0 0
       Barite           0 0
       Calcite          0 0
       CaMoO4           0 0
       FeAsO4:2H2O              0 0
       Ferrihydrite     0 0
       Gypsum           0 0
       Hydrobasaluminite        0 0
       Hydrotalcite     0 0
       Mg(OH)2          0 0
       Ni3(AsO4)2:8H2O          0 0
       Ni(OH)2          0 0
       NiMoO4           0 0
       SiO2(am)                 0 0
       CO2(g)           -3.5 0.0000132
SURFACE 1
       Alumina_sOH Hydrobasaluminite equilibrium_phases 0.197      5.15e4
       Hydro_sOH Hydrotalcite equilibrium_phases 0.197      5.15e4
       Hfo_sOH Ferrihydrite   equilibrium_phases 0.005      5.34e4
       Hfo_wOH Ferrihydrite   equilibrium_phases 0.5        5.34e4
END

USE solution 2
EQUILIBRIUM_PHASES 1
       Fix_H+  -5.5    Ca(OH)2 10.0
       Fix_pe  -8.03   O2      10.0
       Al(OH)3(am)      0 0
       Barite           0 0
       Calcite          0 0
       CaMoO4           0 0
       FeAsO4:2H2O              0 0
       Ferrihydrite     0 0
       Gypsum           0 0
       Hydrobasaluminite        0 0
       Hydrotalcite     0 0
       Mg(OH)2          0 0
       Ni3(AsO4)2:8H2O          0 0
       Ni(OH)2          0 0
```

```
        NiMoO4          0 0
        SiO2(am)                0 0
        CO2(g)          -3.5 0.0000132
SURFACE 1
        Alumina_sOH Hydrobasaluminite equilibrium_phases 0.197      5.15e4
        Hydro_sOH Hydrotalcite equilibrium_phases 0.197      5.15e4
        Hfo_sOH Ferrihydrite   equilibrium_phases 0.005      5.34e4
        Hfo_wOH Ferrihydrite   equilibrium_phases 0.5        5.34e4
END

USE solution 2
EQUILIBRIUM_PHASES 1
        Fix_H+  -6.0    Ca(OH)2 10.0
        Fix_pe  -8.03   O2      10.0
        Al(OH)3(am)     0 0
        Barite          0 0
        Calcite         0 0
        CaMoO4          0 0
        FeAsO4:2H2O             0 0
        Ferrihydrite    0 0
        Gypsum          0 0
        Hydrobasaluminite       0 0
        Hydrotalcite    0 0
        Mg(OH)2         0 0
        Ni3(AsO4)2:8H2O         0 0
        Ni(OH)2         0 0
        NiMoO4          0 0
        SiO2(am)                0 0
        CO2(g)          -3.5 0.0000132
SURFACE 1
        Alumina_sOH Hydrobasaluminite equilibrium_phases 0.197      5.15e4
        Hydro_sOH Hydrotalcite equilibrium_phases 0.197      5.15e4
        Hfo_sOH Ferrihydrite   equilibrium_phases 0.005      5.34e4
        Hfo_wOH Ferrihydrite   equilibrium_phases 0.5        5.34e4
END

USE solution 2
EQUILIBRIUM_PHASES 1
        Fix_H+  -6.5    Ca(OH)2 10.0
        Fix_pe  -8.03   O2      10.0
        Al(OH)3(am)     0 0
        Barite          0 0
        Calcite         0 0
        CaMoO4          0 0
        FeAsO4:2H2O             0 0
        Ferrihydrite    0 0
        Gypsum          0 0
        Hydrotalcite    0 0
        Mg(OH)2         0 0
        Ni3(AsO4)2:8H2O         0 0
        Ni(OH)2         0 0
        NiMoO4          0 0
        SiO2(am)                0 0
        CO2(g)          -3.5 0.0000132
SURFACE 1
        Alumina_sOH Al(OH)3(am)       equilibrium_phases 0.197      5.15e4
        Hydro_sOH Hydrotalcite equilibrium_phases 0.197      5.15e4
        Hfo_sOH Ferrihydrite   equilibrium_phases 0.005      5.34e4
        Hfo_wOH Ferrihydrite   equilibrium_phases 0.5        5.34e4
END

USE solution 2
EQUILIBRIUM_PHASES 1
        Fix_H+  -7.0    Ca(OH)2 10.0
        Fix_pe  -7.54   O2      10.0
        Al(OH)3(am)     0 0
        Barite          0 0
        Calcite         0 0
        CaMoO4          0 0
        FeAsO4:2H2O             0 0
```

```
        Ferrihydrite    0 0
        Gypsum          0 0
        Hydrotalcite    0 0
        Mg(OH)2         0 0
        Ni3(AsO4)2:8H2O         0 0
        Ni(OH)2         0 0
        NiMoO4          0 0
        SiO2(am)                0 0
        CO2(g)          -3.5 0.0000132
SURFACE 1
        Alumina_sOH Al(OH)3(am)       equilibrium_phases 0.197      5.15e4
        Hydro_sOH Hydrotalcite equilibrium_phases 0.197      5.15e4
        Hfo_sOH Ferrihydrite   equilibrium_phases 0.005      5.34e4
        Hfo_wOH Ferrihydrite   equilibrium_phases 0.5        5.34e4
END

USE solution 2
EQUILIBRIUM_PHASES 1
        Fix_H+  -7.2    Ca(OH)2 10.0
        Fix_pe  -7.54   O2      10.0
        Al(OH)3(am)     0 0
        Barite          0 0
        Calcite         0 0
        CaMoO4          0 0
        FeAsO4:2H2O             0 0
        Ferrihydrite    0 0
        Gypsum          0 0
        Hydrotalcite    0 0
        Mg(OH)2         0 0
        Ni3(AsO4)2:8H2O         0 0
        Ni(OH)2         0 0
        NiMoO4          0 0
        SiO2(am)                0 0
        CO2(g)          -3.5 0.0000132
SURFACE 1
        Alumina_sOH Al(OH)3(am)       equilibrium_phases 0.197      5.15e4
        Hydro_sOH Hydrotalcite equilibrium_phases 0.197      5.15e4
        Hfo_sOH Ferrihydrite   equilibrium_phases 0.005      5.34e4
        Hfo_wOH Ferrihydrite   equilibrium_phases 0.5        5.34e4
END

USE solution 2
EQUILIBRIUM_PHASES 1
        Fix_H+  -7.5    Ca(OH)2 10.0
        Fix_pe  -7.54   O2      10.0
        Al(OH)3(am)     0 0
        Barite          0 0
        Calcite         0 0
        CaMoO4          0 0
        FeAsO4:2H2O             0 0
        Ferrihydrite    0 0
        Gypsum          0 0
        Hydrotalcite    0 0
        Mg(OH)2         0 0
        Ni3(AsO4)2:8H2O         0 0
        Ni(OH)2         0 0
        NiMoO4          0 0
        SiO2(am)                0 0
        CO2(g)          -3.5 0.0000132
SURFACE 1
        Alumina_sOH Al(OH)3(am) equilibrium_phases 0.197     5.15e4
        Hydro_sOH Hydrotalcite equilibrium_phases 0.197      5.15e4
        Hfo_sOH Ferrihydrite   equilibrium_phases 0.005      5.34e4
        Hfo_wOH Ferrihydrite   equilibrium_phases 0.5        5.34e4
END

USE solution 2
EQUILIBRIUM_PHASES 1
        Fix_H+  -8.0    Ca(OH)2 10.0
        Fix_pe  -7.54   O2      10.0
```

```
        Al(OH)3(am)     0 0
        Barite          0 0
        Calcite         0 0
        CaMoO4          0 0
        FeAsO4:2H2O     0 0
        Ferrihydrite    0 0
        Gypsum          0 0
        Hydrotalcite    0 0
        Mg(OH)2         0 0
        Ni3(AsO4)2:8H2O         0 0
        Ni(OH)2         0 0
        NiMoO4          0 0
        SiO2(am)                0 0
        CO2(g)          -3.5 0.0000132
SURFACE 1
        Alumina_sOH Al(OH)3(am) equilibrium_phases 0.197    5.15e4
        Hydro_sOH Hydrotalcite equilibrium_phases 0.197     5.15e4
        Hfo_sOH Ferrihydrite   equilibrium_phases 0.005     5.34e4
        Hfo_wOH Ferrihydrite   equilibrium_phases 0.5       5.34e4
END

USE solution 2
EQUILIBRIUM_PHASES 1
        Fix_H+  -8.5    Ca(OH)2 10.0
        Fix_pe  -7.54   O2      10.0
        Al(OH)3(am)     0 0
        Barite          0 0
        Calcite         0 0
        CaMoO4          0 0
        FeAsO4:2H2O             0 0
        Ferrihydrite    0 0
        Gypsum          0 0
        Hydrotalcite    0 0
        Hydrotalcite(NiAl) 0 0
        Mg(OH)2         0 0
        Ni3(AsO4)2:8H2O         0 0
        Ni(OH)2         0 0
        NiMoO4          0 0
        SiO2(am)                0 0
        CO2(g)          -3.5 0.0000132
SURFACE 1
        Alumina_sOH Al(OH)3(am) equilibrium_phases 0.197    5.15e4
        Hydro_sOH Hydrotalcite equilibrium_phases 0.197     5.15e4
        Hfo_sOH Ferrihydrite   equilibrium_phases 0.005     5.34e4
        Hfo_wOH Ferrihydrite   equilibrium_phases 0.5       5.34e4
END

USE solution 2
EQUILIBRIUM_PHASES 1
        Fix_H+  -9.0    Ca(OH)2 10.0
        Fix_pe  -7.54   O2      10.0
        Al(OH)3(am)     0 0
        Barite          0 0
        Calcite         0 0
        CaMoO4          0 0
        FeAsO4:2H2O             0 0
        Ferrihydrite    0 0
        Gypsum          0 0
        Hydrotalcite    0 0
        Hydrotalcite(NiAl) 0 0
        Mg(OH)2         0 0
        Ni3(AsO4)2:8H2O         0 0
        Ni(OH)2         0 0
        NiMoO4          0 0
        SiO2(am)                0 0
        CO2(g)          -3.5 0.0000132
SURFACE 1
        Alumina_sOH Al(OH)3(am) equilibrium_phases 0.197    5.15e4
        Hydro_sOH Hydrotalcite equilibrium_phases 0.197     5.15e4
        Hfo_sOH Ferrihydrite   equilibrium_phases 0.005     5.34e4
```

```
       Hfo_wOH Ferrihydrite   equilibrium_phases 0.5        5.34e4
END

USE solution 2
EQUILIBRIUM_PHASES 1
       Fix_H+  -9.5    Ca(OH)2 10.0
       Fix_pe  -6.86   O2      10.0
       Al(OH)3(am)      0 0
       Barite           0 0
       Calcite          0 0
       CaMoO4           0 0
       FeAsO4:2H2O              0 0
       Ferrihydrite     0 0
       Gypsum           0 0
       Hydrotalcite     0 0
       Hydrotalcite(NiAl) 0 0
       Mg(OH)2          0 0
       Ni3(AsO4)2:8H2O          0 0
       Ni(OH)2          0 0
       NiMoO4           0 0
       SiO2(am)                 0 0
       CO2(g)           -3.5 0.0000132
SURFACE 1
       Alumina_sOH Al(OH)3(am) equilibrium_phases 0.197     5.15e4
       Hydro_sOH Hydrotalcite equilibrium_phases 0.197      5.15e4
       Hfo_sOH Ferrihydrite   equilibrium_phases 0.005      5.34e4
       Hfo_wOH Ferrihydrite   equilibrium_phases 0.5        5.34e4
END

USE solution 2
EQUILIBRIUM_PHASES 1
       Fix_H+  -9.7    Ca(OH)2 10.0
       Fix_pe  -6.86   O2      10.0
       Al(OH)3(am)      0 0
       Barite           0 0
       Calcite          0 0
       CaMoO4           0 0
       FeAsO4:2H2O              0 0
       Ferrihydrite     0 0
       Gypsum           0 0
       Hydrotalcite     0 0
       Hydrotalcite(NiAl) 0 0
       Mg(OH)2          0 0
       Ni3(AsO4)2:8H2O          0 0
       Ni(OH)2          0 0
       NiMoO4           0 0
       SiO2(am)                 0 0
       CO2(g)           -3.5 0.0000132
SURFACE 1
       Alumina_sOH Al(OH)3(am) equilibrium_phases 0.197     5.15e4
       Hydro_sOH Hydrotalcite equilibrium_phases 0.197      5.15e4
       Hfo_sOH Ferrihydrite   equilibrium_phases 0.005      5.34e4
       Hfo_wOH Ferrihydrite   equilibrium_phases 0.5        5.34e4
SAVE solution 10 #This solution is the overflow from the thickener and is currently the final
effluent
END

USE solution 2
EQUILIBRIUM_PHASES 1
       Fix_H+  -10.1   Ca(OH)2 10.0
       Fix_pe  -6.86   O2      10.0
       Al(OH)3(am)      0 0
       Barite           0 0
       Calcite          0 0
       CaMoO4           0 0
       FeAsO4:2H2O              0 0
       Ferrihydrite     0 0
       Gypsum           0 0
       Hydrotalcite     0 0
       Hydrotalcite(NiAl) 0 0
```

```
        Mg(OH)2         0 0
        Ni3(AsO4)2:8H2O         0 0
        Ni(OH)2         0 0
        NiMoO4          0 0
        SiO2(am)                0 0
        CO2(g)          -3.5 0.0000132
SURFACE 1
        Alumina_sOH Al(OH)3(am) equilibrium_phases 0.197    5.15e4
        Hydro_sOH Hydrotalcite equilibrium_phases 0.197     5.15e4
        Hfo_sOH Ferrihydrite   equilibrium_phases 0.005     5.34e4
        Hfo_wOH Ferrihydrite   equilibrium_phases 0.5       5.34e4
SAVE solution 10 #This solution is the overflow from the thickener and is currently the final
effluent
END

USE solution 2
EQUILIBRIUM_PHASES 1
        Fix_H+  -10.5   Ca(OH)2 10.0
        Fix_pe  -6.86   O2      10.0
        Al(OH)3(am)     0 0
        Barite          0 0
        Calcite         0 0
        CaMoO4          0 0
        FeAsO4:2H2O             0 0
        Ferrihydrite    0 0
        Gypsum          0 0
        Hydrotalcite    0 0
        Hydrotalcite(NiAl) 0 0
        Mg(OH)2         0 0
        Ni3(AsO4)2:8H2O         0 0
        Ni(OH)2         0 0
        NiMoO4          0 0
        SiO2(am)                0 0
        CO2(g)          -3.5 0.0000132
SURFACE 1
        Alumina_sOH Al(OH)3(am) equilibrium_phases 0.197    5.15e4
        Hydro_sOH Hydrotalcite equilibrium_phases 0.197     5.15e4
        Hfo_sOH Ferrihydrite   equilibrium_phases 0.005     5.34e4
        Hfo_wOH Ferrihydrite   equilibrium_phases 0.5       5.34e4
END

## Start of tailings model

MIX 1 Mixing leach residue and raffinate
        1       0.25  # Raffinate
        3       0.5   # Leach Residue
SAVE solution 4
END

USE solution 4
EQUILIBRIUM_PHASES 1 Initial simulation of the as-discharged tailings
        Fix_H+  -9.6    Ca(OH)2 10.0
        Fix_pe  -3.72   O2      10.0
SAVE solution 5
END

USE solution 5
EQUILIBRIUM_PHASES 1 Initial simulation of the as-discharged tailings
        Fix_H+  -9.6    Ca(OH)2 10.0
        Fix_pe  -3.72   O2      10.0
        # Secondary Minerals
        Al(OH)3(am)     0 0
        Barite          0 0
        Calcite         0 0
        CaMoO4          0 0
        FeAsO4:2H2O             0 0
        Ferrihydrite    0 0
        Gypsum          0 0
        Hydrotalcite    0 0
        Hydrotalcite(NiAl) 0 0
```

```
        Mg(OH)2         0 0
        Ni3(AsO4)2:8H2O         0 0
        Ni(OH)2         0 0
        NiMoO4          0 0
        SiO2(am)                0 0
        CO2(g)          -3.5 0.0000132
        # Primary Minerals
        Barite          0 0.0024 dissolve_only
        Chalcopyrite    0 0.0013 dissolve_only
        Clinochlore-14A         0 0.0043 dissolve_only
        K-Feldspar              0 0.035 dissolve_only
        Galena          0 0.0003 dissolve_only
        Hematite                0 0.0042 dissolve_only
        Illite          0 0.019 dissolve_only
        Kaolinite               0 0.0088 dissolve_only
        Muscovite               0 0.051 dissolve_only
        Pyrite          0 0.0061 dissolve_only
        Ca-Al_Pyroxene  0 0.034 dissolve_only
        Quartz          0 4.2 dissolve_only
SURFACE 1
        Alumina_sOH Al(OH)3(am)       equilibrium_phases 0.197      5.15e4
        Hydro_sOH Hydrotalcite equilibrium_phases 0.197      5.15e4
        Hfo_sOH Ferrihydrite   equilibrium_phases 0.005      5.34e4
        Hfo_wOH Ferrihydrite   equilibrium_phases 0.5        5.34e4
SAVE solution 20
END

USE solution 5
EQUILIBRIUM_PHASES 1 Equilibrium simulation of the final tailings
        Fix_H+  -9.6    Ca(OH)2 10.0
        Fix_pe  -3.72   O2      10.0
        # Secondary Minerals
        Al(OH)3(am)     0 0
        Barite          0 0
        Calcite         0 0
        CaMoO4          0 0
        FeAsO4:2H2O             0 0
        Ferrihydrite    0 0
        Gypsum          0 0
        Hydrotalcite    0 0
        Hydrotalcite(NiAl) 0 0
        Mg(OH)2         0 0
        Ni3(AsO4)2:8H2O         0 0
        Ni(OH)2         0 0
        NiMoO4          0 0
        SiO2(am)                0 0
        CO2(g)          -3.5 0.0000132
        # Primary Minerals
        Barite          0 0.0024
        Chalcopyrite    0 0.0013
        Clinochlore-14A         0 0.0043
        K-Feldspar              0 0.035
        Galena          0 0.0003
        Hematite                0 0.0042 dissolve_only
        Illite          0 0.019
        Kaolinite               0 0.0088
        Muscovite               0 0.051
        Pyrite          0 0.0061
        Ca-Al_Pyroxene  0 0.034
        Quartz          0 4.2
SURFACE 1
        Alumina_sOH Al(OH)3(am)       equilibrium_phases 0.197      5.15e4
        Hydro_sOH Hydrotalcite equilibrium_phases 0.197      5.15e4
        Hfo_sOH Ferrihydrite   equilibrium_phases 0.005      5.34e4
        Hfo_wOH Ferrihydrite   equilibrium_phases 0.5        5.34e4
SAVE solution 30
END
```